UNIVERSIDAD DE CHILE
FACULTAD DE CIENCIAS FÍSICAS Y MATEMÁTICAS
DEPARTAMENTO DE INGENIERÍA ELÉCTRICA

CONTROL SYSTEMS FOR HIGH-POWER MEDIUM-VOLTAGE MODULAR MULTILEVEL CONVERTER-BASED DRIVES

TESIS PARA OPTAR AL GRADO DE
DOCTOR EN INGENIERÍA ELÉCTRICA

MAURICIO ANTONIO ESPINOZA BOLAÑOS

PROFESOR GUÍA:
ROBERTO CÁRDENAS DOBSON
PROFESOR GUÍA 2:
JON CLARE

MIEMBROS DE LA COMISIÓN:
DORIS SÁEZ HUEICHAPAN
CESAR SILVA JIMÉNEZ
MARCELO PÉREZ LEIVA

SANTIAGO DE CHILE
2018

RESUMEN DE LA MEMORIA PARA OPTAR
AL TÍTULO DE DOCTOR EN INGENIERÍA ELÉCTRICA
POR: MAURICIO ANTONIO ESPINOZA BOLAÑOS
FECHA: 2018
PROF. GUÍA: ROBERTO CÁRDENAS DOBSON JON CLARE

CONTROL SYSTEMS FOR HIGH-POWER MEDIUM-VOLTAGE MODULAR MULTILEVEL CONVERTER-BASED DRIVES

Hoy en día, la construcción de maquinaria y plantas industriales exigen soluciones de accionamiento con un diseño flexible y escalable. En sectores industriales como la petroquímica, la minería, la generación de energía, etc., existe una demanda de soluciones con alta eficiencia, seguridad integrada y respaldo de las compañías proveedoras. En este contexto, el Convertidor Multinivel Modular (MMC) ha aparecido como una opción prometedora para accionamientos de media tensión de alta potencia debido a sus características, como modularidad total, flexibilidad de control, niveles de media tensión, calidad de potencia y posible operación sin transformador. Por lo tanto, esta tesis discute la aplicación del MMC para accionamientos de máquinas. El modelado del MMC y sus sistemas de control asociados para esta aplicación son analizados ampliamente en este documento. Específicamente, se ha propuesto un nuevo modelado basado en coordenadas *dq* y su sistema correspondiente sistema de control para regular el valor instantáneo de las tensiones de los condensadores del MMC. Además, se ha propuesto la integración de los sistemas de control de la máquina y del MMC para mejorar el rendimiento general del sistema. Por ejemplo, se demostró que las corrientes circulantes requeridas durante bajas frecuencias ac se reducen al considerar la interacción de ambos sistemas de control.

La efectividad de las estrategias de control propuestas se validó a través de extensos resultados experimentales, que se han publicado en dos artículos (IEEE Transactions on Industrial Electronics) y seis artículos de conferencia (indexados en la base de datos Scopus), así como contribuciones importantes en otros proyectos relacionados con el control de convertidores multinivel modulares. El prototipo utilizado se compone de 18 celdas de potencia. El sistema se controla utilizando un procesador de señales digitales y dos FPGAs. Un segundo MMC con 12 celdas de potencia también se usó para algunas pruebas, conformando una unidad Back-to-Back MMC. Se probó el rendimiento dinámico y en estado estable de las metodologías de control propuestas, considerando el arranque del MMC, cambios escalón tanto en el par y las corrientes de magnetización, rampas de velocidad, pruebas de cruce por velocidad cero, operación de rotor bloqueado, operación con flujo debilitado, diferentes condiciones de carga, manipulación de la tensión dc del MMC, etc. En todos los casos, el rendimiento alcanzado es consistente con los resultados esperados.

RESUMEN DE LA MEMORIA PARA OPTAR
AL TÍTULO DE DOCTOR EN INGENIERÍA ELÉCTRICA
POR: MAURICIO ANTONIO ESPINOZA BOLAÑOS
FECHA: 2018
PROF. GUÍA: ROBERTO CÁRDENAS DOBSON JON CLARE

CONTROL SYSTEMS FOR HIGH-POWER MEDIUM-VOLTAGE MODULAR MULTILEVEL CONVERTER-BASED DRIVES

Nowadays, machinery and plant construction are demanding drive solutions with flexible and scalable design. In industrial sectors such as petrochemical, mining, power generation, etc., there is a demand for solutions with high efficiency, integrated safety and support from the supplier companies. In this context, the Modular Multilevel Converter (MMC) has appeared as a promising option for high-power medium-voltage drives due to their characteristics, such as full modularity, control flexibility, medium-voltage levels, power quality and possible transformer-less operation. Thereby, this thesis discusses the application of the MMC as a machine drive. The modelling and control systems required for this application are extensively analysed and discussed in this document. Specifically, a novel *dq*-based modelling of the MMC and its associated control system has been proposed to regulate the instantaneous value of the MMC capacitor voltages. Additionally, the integration of the machine and MMC control systems has been proposed to enhance the performance of the overall system. For example, it was demonstrated that the required circulating currents during low-ac frequencies are reduced by considering the interaction of both control systems.

The effectiveness of the proposed control strategies is validated through extensive experimental results, which have been published in two journal papers (IEEE Transaction on Industrial Electronics) and six conference papers (indexed in the Scopus database), as well as important contributions in other projects related to the control of modular multilevel converters. The downscaled prototype utilised is composed of 18 power cells. The system is controlled using a Digital Signal Processor and two Field Programmable Gate Arrays (FPGAs). A second MMC with 12 power cells was also used for some tests, conforming a Back-to-Back MMC-based drive. The dynamic and steady-state performance of the proposed control methodologies were tested, considering the MMC starting-up, step changes in both the torque and magnetising currents, speed-ramps, zero-speed crossing test, rotor-locked operation, flux-weakening operation, different loading conditions, manipulation of the input voltage of the MMC, etc. In all cases, the achieved performance is consistent with the expected results.

acknowledgement

Este trabajo no hubiera sido posible sin la ayuda y el apoyo de mi supervisor, colegas, amigos y familia. A todos ellos, mi más sincera gratitud, de verdad.

Primeramente, me gustaría agradecerle al profesor Roberto Cárdenas. Gracias por su ayuda, orientación y empatía a la hora de trabajar, pero más importante, por tratar de enseñarme a trabajar como un profesional sin perder la esencia de ser personas.

A la gente de los labs, esa gente que se notó desde el primer momento que me querían hacer sentir bien durante mi estadía en Chile. Todos y cada uno me han enseñado un poquito de electrónica de potencia, control, máquinas, etc., pero mucho de cómo ser personas de bien y hacer sentir bien a los demás. Lo bonito es que no puedo mencionar a uno solo. Me llevo recuerdos muy bonitos de tod@s. Tendría que poner una página si menciono nombres, así que paso. Como dijo uno de ellos: "No somos el laboratorio más eficiente, pero sí el más feliz" (igual publicamos un montón...).

A lo largo de estos años también tuve mucho contacto con distintos grupos de trabajo en varias áreas del mundo (Magallanes, USACH, Alemania, Inglaterra, la Antártica). El factor común es que siempre me trataron bien. Muchas gracias a todos, en particular al grupo de la Universidad de Santiago de Chile, el INACH, y la Universidad de Newcastle.

Me gustaría agradecer a mi familia (Edith, Éricka, Fran, Mari, Sandra, Álvaro, Alejandro) y a mis amigos de Costa Rica y alrededor del mundo y a mis colegas Aramis y Oscar. Gracias a todos por aguantar mi mal genio.

Finalmente, agradezco a mis patrocinadores, la Comisión Nacional de Ciencia y Tecnología (CONICYT) de Chile, quienes me han brindado la oportunidad de estudiar en Chile. El apoyo de Fondecyt grant Nr. 1180879 "Modular Multilevel Technologies For Future Generations of High Power Machines" y el Proyecto Basal AC3E FB0008 es amablemente agradecido. Además, los fondos provistos por CONICYT-PCHA/Doctorado Nacional/2014-63140233 y la Universidad de Costa Rica son también reconocidos.

Contents

Part I

Introduction

Chapter 1

Introduction

1.1 Basis of this Ph.D. Submission

This thesis document is elaborated by using the "thesis by published papers" format of the University of Chile. In this format, the Ph.D. candidate must have at least two accepted journal papers. Each paper is then used as a chapter, removing the paper abstract and copying the rest of the information as is published. Because each paper is in a self-contained format, where repeated information or material could be discussed, even briefly, some repetition between chapters could be expected. Additional chapters or appendices can be added depending on the supervisor requirements.

Therefore, this thesis document is composed of chapters related with two journal papers (both of them were published on IEEE Transactions on Industrial Electronics, Q1 journal, impact factor 7.168), one journal paper to be submitted and three selected conference papers (indexed in the Scopus database). Due to the thesis format, the hypotheses, contributions and general conclusions of this project are closely related to the papers used as chapters. This relation is depicted in Table 1.1 (see the following sections for details).

In this context, the remainder of this work is divided into the following parts, each of them composed of chapters:

Table 1.1: Structure and relation of this thesis submission

Chapter	Related paper	Hypothesis			Contribution			Conclusion		
		1	2	3	1	2	3	1	2	3
2	[1] (Journal paper)	✓			✓			✓		
3	[2] (Journal paper)		✓			✓			✓	
4	[3] (To be submitted)			✓			✓			✓
5	[4] (Conference paper)	✓			✓			✓		
6	[5] (Conference paper)			✓			✓			✓
7	[6] (Conference paper)			✓			✓			✓

- **Part II: Journal Papers** Two journal papers are utilised as Chapters 2 and 3 of this document. Both of them were published on the IEEE Transactions on Industrial Electronics (Q1 journal, impact factor 7.168). In Chapter 2, the journal paper "An Enhanced *dq*-Based Vector Control System for Modular Multilevel Converters Feeding Variable-Speed Drives" is presented [1]. Furthermore, the journal paper "An Integrated Converter and Machine Control System for MMC-Based High Power Drives" [2] is utilised in Chapter 3.
- **Part III: Journal Paper to be Submitted**. Chapter 4 composes this part, which is related to the paper "Modelling and Control of the MMC-Based Drive with a Time-Variable dc-Port Voltage" [3]. The paper has already been almost completely written and it is expected to submit this work to the IEEE Transactions on Power Electronics (Q1 journal, impact factor 7.151).
- **Part IV: Selected Conference Papers**. Although this thesis project generated six conference papers (see Section 1.2), three of them were selected to compose this part. Chapter 5 is based on the conference paper "Improved Control Strategy of the Modular Multilevel Converter for High Power Drive Applications in Low Frequency Operation" [4]. The information of the paper "Modelling and Control of the Modular Multilevel Converter in Back to Back Configuration for High Power Induction Machine Drives" [5] is presented in Chapter 6. Finally, Chapter 7 is composed of the paper "Control and Operation of the MMC-Based Drive with Reduced Capacitor Voltage Fluctuations" [6].
- **Part V: Appendices**. Chapter 8 composes this part, and describes the implementation of the experimental system utilised to validate the proposed control strategies of this Ph.D. project.

1.2 Published Works

At this moment, the author of this Ph.D. project has participated in 26 published papers (all of them indexed in the Scopus database, with four papers published in journals indexed also in the ISI database). Three journal papers are also in the revision process. For presentation purposes, all these works are classified into the following categories.

- **Papers as first author presented in this document**. The abstract and information of these papers are presented in the following list.

  Published journal papers:

  1. M. Espinoza, R. Cárdenas, M. Díaz, and J. C. Clare. An Enhanced *dq*-Based Vector Control System for Modular Multilevel Converters Feeding Variable-Speed Drives. *Industrial Electronics, IEEE Transactions on*, 64(4):2620–2630, April 2017. ISSN 0278-0046. **Q1 journal paper. Impact Factor: 7.168.**

     Abstract: Modular Multilevel Converters (MMC) are considered an attractive solution for high power drive applications. However, energy balancing within the converter is complex to achieve, particularly when the machine is operating at low rotational speeds. In this paper a new control system, based on cascaded control loops and a vector-power-voltage (vPV) model of the MMC, is proposed. The control system is implemented in a *dq*-synchronous frame rotating at ω_e rad/s

with the external loop regulating the capacitor voltages using PI controllers. The internal loop controls the converter currents using PI and resonant controllers. In addition the control systems required to operate the machine at other points, i.e. at medium and high rotational speeds, are also discussed in this work. Experimental results obtained with a MMC-based drive laboratory prototype with eighteen power cells are presented in this paper.

2. M. Espinoza, R. Cardenas, J. Clare, D. Soto, M. Diaz, E. Espina, and C. Hackl. An integrated converter and machine control system for mmc-based high power drives. *IEEE Transactions on Industrial Electronics*, PP(99):1–1, 2018. ISSN 0278-0046. doi: 10.1109/TIE.2018.2801839. **Q1 journal paper. Impact Factor: 7.168.**

   Abstract: The Modular Multilevel Converter (MMC) is a promising topology for high power drive applications. However, large voltage fluctuations are produced in the floating capacitors when the machine is operating with high stator currents at low rotational speed. To compensate these oscillations, relatively large mitigation currents are required to keep the capacitor voltages within an acceptable range. In this paper, a new integrated control scheme is discussed to regulate the voltage fluctuations. The strategy is based on closed-loop vector-control of the voltage fluctuations, maintaining them inside a pre-defined threshold. The proposed control system is also augmented using flux weakening operation of the machine at low rotational speeds. An experimental prototype composed of eighteen power cells, feeding a vector-controlled induction machine in the whole speed range, is used to validate the effectiveness and feasibility of the proposed control strategies.

Journal paper to be submitted:

1. M. Espinoza, R. Cardenas, M. Diaz, F. Donoso, and A. Mora. Modelling and Control of the MMC-Based Drive with a Time-Variable dc-Port Voltage. *IEEE Transactions on Power Electronics*, 2019. **Q1 journal paper. Impact Factor: 7.151.**

   Abstract: The Modular Multilevel Converter (MMC) is a topology suitable for high-power medium-voltage variable-speed drives. However, the behaviour of this converter is highly affected by the power fluctuations of its modules. This paper analyses the influence of the dc-port voltage on these power fluctuations. It is demonstrated that the manipulation of this voltage offers several advantages for the operation of the drive. For example, it is possible to reduce: the voltage fluctuations in the capacitors, the capacitance of each cell or the application of mitigating variables during low machine speeds. Additionally, a reduction in the required common-mode voltage during low-speed operation is also feasible. The effectiveness of the proposed control schemes is demonstrated through simulation studies and experimental validation tests conducted with an 18-cell-7.5 kW MMC prototype in the whole frequency range.

Selected conference papers:

1. M. Espinoza, E. Espina, M. Diaz, A. Mora, and R. Cárdenas. Improved control strategy of the Modular Multilevel Converter for high power drive applications in low frequency operation. In *Power Electronics and Application (EPE), 2016 18th European Conference on*, pages 5–9, Karlsruhe, Germany, September 2016

   Abstract: Modular Multilevel Converters (MMC) are considered an attractive solution for high power drives. However, its operation during low rotational speeds

can produce undesired voltage fluctuations in the MMC capacitors. In this paper, two methodologies to improve the converter performance in this speed range are analysed and tested. The first strategy proposes the control of the inner converter currents combining a synchronous *dq* rotating frame and resonant controllers to improve the current tracking and to reduce the voltage fluctuations. The second strategy achieves the reduction of the voltage fluctuations by adjusting the DC Port voltage as a function of the machine frequency. Both methods are validated by simulation and experimental work, where a 18 cell MMC prototype is applied to drive an induction machine.

2. M. Espinoza, R. Cárdenas, M. Diaz, A. Mora, and Soto. D. Modelling and Control of the Modular Multilevel Converter in Back to Back Configuration for High Power Induction Machine Drives. In *IEEE Industrial Electronics Society (IECON), 2016 42nd Annual Conference of*, pages 24–27, Florence, Italy, October 2016

   Abstract: Drives based on modular multilevel topologies are the next generation of high-power/voltage converters. In this paper, the Modular Multilevel Converter model is extended to the Back to Back scheme, allowing its control as an unique system, instead two separated converters. Additionally, the proposed control strategy is able to regulate the ac ports and to perform the voltage balancing in both converters by using circulating currents and common mode voltage, providing independence between the converters and the ac ports. Extensive computer simulation and a laboratory prototype of a Modular Multilevel Converter with eighteen power cells feeding an induction machine validate the effectiveness of the presented control algorithm.

3. M. Espinoza, F. Donoso, M. Diaz, A. Letelier, and R. Cardenas. Control and Operation of the MMC-Based Drive with Reduced Capacitor Voltage Fluctuations. In *Power Electronics, Machines and Drives (PEMD), 9th International Conference on*, Liverpool, UK., 17-19, April 2018

   Abstract: The Modular Multilevel Converter has emerged as a suitable topology for high power drive applications. However, the voltage fluctuations of its floating capacitors increase the control complexity of the converter. In this paper, the MMC dc-port voltage is manipulated to regulate the amplitude of these fluctuations to a constant value during the whole frequency range. The proposed approach has several advantages when compared with the conventional ones since it minimises the voltage fluctuation in the capacitor cells. Additionally, it decreases the common-mode voltage at low-frequencies and the capacitor rms current, increasing their expected lifespan and reducing the winding insulation damages and the leakage currents in the bearing of the machine. The effectiveness of the proposed control strategy is validated with a laboratory-based prototype composed of eighteen power cells, feeding a vector-controlled induction machine.

- **Papers as first author not presented in this document, but directly related with this Ph.D. project**

1. M. Espinoza, A. Mora, M. Diaz, and R. Cárdenas. Balancing energy and low frequency operation of the Modular Multilevel Converter in Back to Back configuration. In *Ecological Vehicles and Renewable Energies (EVER), 2015 Tenth International Conference on*, pages 1–9, March 2015
2. M. Espinoza, E. Espina, M. Diaz, and R. Cárdenas. Control Strategies for Mod-

ular Multilevel Converters Driving Cage Machines. In *IEEE 3rd Southern Power Electronics Conference (SPEC), 2017*, pages 1–6, Puerto Varas, Chile, Diciembre 2017

3. M. Espinoza, E. Espina, M. Diaz, F. Donoso, and R. Cárdenas. A Control Strategy for Modular Multilevel-Based Drives Considering the System Operating Point. In *Power Electronics and Application (EPE), 2018 20th European Conference on*, pages 17–21, Riga, Latvia, September 2018

- **Papers as co-author related with this research topic, but not directly to this project**. They are classified as follows:

  Published journal papers:

  1. M. Diaz, R. Cardenas, M. Espinoza, F. Rojas, A. Mora, J. C. Clare, and P. Wheeler. Control of Wind Energy Conversion Systems Based on the Modular Multilevel Matrix Converter. *IEEE Transactions on Industrial Electronics*, 64(11):8799–8810, Nov 2017. ISSN 0278-0046. doi: 10.1109/TIE.2017.2733467. **Q1 journal paper. Impact Factor: 7.168.**
  2. A. Mora, M. Urrutia, R. Cardenas, A. Angulo, M. Espinoza, M. Diaz, and P. Lezana. Model predictive control based capacitor voltage balancing strategies for modular multilevel converters. *IEEE Transactions on Industrial Electronics*, pages 1–1, 2018. ISSN 0278-0046. doi: 10.1109/TIE.2018.2844842. **Q1 journal paper. Impact Factor: 7.168.**
  3. M. Diaz, R. Cardenas, M. Espinoza, F. Rojas, C. Hackl, J. Clare, and P. Wheeler. Vector Control of a Modular Multilevel Matrix Converter Operating in the Full Output-Frequency Range. *IEEE Transactions on Industrial Electronics*, 2019. **Q1 journal paper. Impact Factor: 7.168.**

  Conference papers:

  1. M. Díaz, M. Espinoza, A. Mora, F. Rojas, and R. Cárdenas. A Novel LVRT Control Strategy for Modular Multilevel Matrix Converter based High-Power Wind Energy Conversion Systems. In *Tenth International Conference and Exhibition on Ecological Vehicles and Renewable Energies EVER15*, Monte-Carlo, Monaco, March 31-, April 01 2015.
  2. A. Mora, M. Espinoza, M. Díaz, and R. Cárdenas. Model Predictive Control of Modular Multilevel Matrix Converter. In *2015 IEEE 24th International Symposium on Industrial Electronics (ISIE)*, pages 1074–1079, June 2015.
  3. M. Diaz, M. Espinoza, A. Mora, R. Cárdenas, and P. Wheeler. Modelling and Control of the Modular Multilevel Matrix Converter and its application to Wind Energy Conversion Systems. In *IEEE Industrial Electronics Society (IECON), 2016 42nd Annual Conference of*, pages 24–27, Florence, Italy, October 2016.
  4. M. Díaz, M. Espinoza, A. Mora, R. Cárdenas, and P. Wheeler. The Application of the Modular Multilevel Matrix Converter in High-PowerWind Turbines. In *2016 18th European Conference on Power Electronics and Applications (EPE'16 ECCE Europe)*, pages 1–11, Sept 2016. doi: 10.1109/EPE.2016.7695437.
  5. A. Mora, R. Cárdenas, M. Espinoza, and M. Díaz. Active power oscillation elimination in 4-leg grid-connected converters under unbalanced network conditions. In *IECON 2016 - 42nd Annual Conference of the IEEE Industrial Electronics Society*, pages 2229–2234, Oct 2016. doi: 10.1109/IECON.2016.7792960.

6. M. Diaz, F. Rojas, M. Espinoza, A. Mora, P. Wheeler, and R. Cardenas. Closed loop vector control of the modular multilevel matrix converter for equal input-output operating frequencies. In *2017 IEEE Southern Power Electronics Conference (SPEC)*, pages 1–6, Dec 2017. doi: 10.1109/SPEC.2017.8333629.
7. F. Rojas, M. Díaz, M. Espinoza, and R. Cárdenas. A solid state transformer based on a three-phase to single-phase modular multilevel converter for power distribution networks. In *2017 IEEE Southern Power Electronics Conference (SPEC)*, pages 1–6, Dec 2017. doi: 10.1109/SPEC.2017.8333627.
8. M. Diaz, M. Espinoza, F. Rojas, R. Cardenas, and P. Wheeler. Vector Control Strategies to enable equal frequency operation of the Modular Multilevel Matrix Converter. In *Power Electronics, Machines and Drives (PEMD), 9th International Conference on*, Liverpool, UK., 17-19, April 2018.
9. M. Diaz, F. Rojas, F. Donoso, R. Cardenas, M. Espinoza, A. Mora, and P. Wheeler. Control of modular multilevel cascade converters for offshore wind energy generation and transmission. In *2018 Thirteenth International Conference on Ecological Vehicles and Renewable Energies (EVER)*, pages 1–10, April 2018. doi: 10.1109/EVER.2018.8362406.
10. F. Donoso, M. Espinoza, M. Diaz, A. Letelier, and R. Cardenas. Back-to-Back Modular Multilevel Converter for Drive Applications Under Unbalance Grid Conditions. In *Power Electronics and Application (EPE), 2018 20th European Conference on*, Riga, Latvia, 17-19, September 2018.

- **Additional papers published during these Ph.D. studies**

  Conference papers as first author:

  1. M. Espinoza, J.D. Rojas, R. Vilanova, and O. Arrieta. Identification and Control of Chemical Processes Using the Anisochronic Modeling Paradigm. *IFAC-PapersOnLine*, 48(8):361–366, 2015. ISSN 2405-8963. 9th IFAC Symposium on Advanced Control of Chemical Processes ADCHEM 2015 Whistler, Canada, 7-10 June 7-10, 2015.
  2. M. Espinoza, J. D. Rojas, R. Vilanova, and O. Arrieta. Robustness/performance tradeoff for anisochronic plants with two degrees of freedom PID controllers. In *2015 IEEE Conference on Control Applications (CCA)*, pages 1230–1235, Sept 2015.

  Conference papers as co-author:

  1. E. Espina, M. Espinoza, and R. Cárdenas. Active power angle droop control per phase for unbalanced 4-wire microgrids. In *2017 IEEE Southern Power Electronics Conference (SPEC)*, pages 1–6, Dec 2017. doi: 10.1109/SPEC.2017.8333637.
  2. S. McDonald, N. Baker, M. Espinoza, and O. Pickert. Power electronic topology assessment for wave energy converters. In *International Conference on Renewable Power Generation (RPG)*, 2018.
  3. C. Contreras, D. Guajardo, M. Diaz, F. Rojas, M. Espinoza, and R. Cardenas. Fast Delayed Signal Cancellation Based PLL for Unbalanced Grid Conditions. In *22th Congress of the Chilean ACCA Automatic Control Association, IEEE International Conference on Automation*, Concepcion, Chile, 17-19, October 2018.

1.3 Motivation

Nowadays, machinery and plant construction are demanding automation and drive solutions with high flexible and scalable design. Regarding to energy efficiency, electric machines represent the major energy consumption worldwide with around 29% of global electric power consumption [28]. Consequently, machines across all the world are being equipped with variable-speed drives to achieve better performance and reduction of electric consumption [29, 30]. What is more, in industrial sectors such as petrochemical, mining, power generation, marine, etc., there is a demand for individual easy to use solutions, with high efficiency, integrated safety and support from the supplier companies [31, 32]. To name a few, the electrical machines are used in a wide range of industry and energy generation applications, such as:

1. **Mining**. In the Chilean context, mining is the main economic activity, which has approximately 72.000 motors. For itself, the mining industry represents 33% of the total electric power consumption of Chile [33].

2. **Wind Energy Conversion Systems (WECSs)**. The wind energy has presented the fastest relative growth reaching almost 540 GW of installed capacity worldwide by 2017 [34]. The high-power requirements of WECSs have driven the power electronics technology towards the medium-voltage (MV) operation. Accordingly, MV-power converters will be dominant in the next generation of Multi-MW WECSs and Drives [35, 36].

3. **Marine**. The rising energy costs, the increasing environmental regulation and the accelerating demand for larger and multi-use ships, have become design challenges for vessel and offshore applications [37]. In this context, all vessel types and floating structures can benefit from using medium voltage drives due to its flexibility, energy efficiency and superior performance in propulsion and auxiliary applications [38].

4. **Traction Systems**. The market for drives in the rail industry has a growing interest in new technologies. For example, there are desired several improvements in technological aspects, such as a smooth and robust traction control systems, a much better energy-efficiency trade-off, a better power/weight ratio, as well as modern diagnostics and modular design [39, 40].

Currently, Voltage Source Converters (VSCs), such as the Neutral-Point-Clamped (NPC) Converter and the Cascaded Full-Bridge (CFB) Converter, are well-established technology for drive applications up to 15 MW [36]. Additionally, Current Source Converters (CSCs), such as Cycloconverter, PWM Current Source Inverter and the Load-Commutated Inverter, are used for high-power applications of tens of MW [41]. Although the benefits of the VSC and CSC are undeniable over low-voltage converters, they have important drawbacks in the medium-voltage range, such as requirements of isolated dc-sources and multi-winding transformers (CHB), complicated control for more than five levels (NPC), and low-power quality and filters requirements (CSC) [41].

Alternatively, the Modular Multilevel Converter (MMC), which was proposed by Mar-

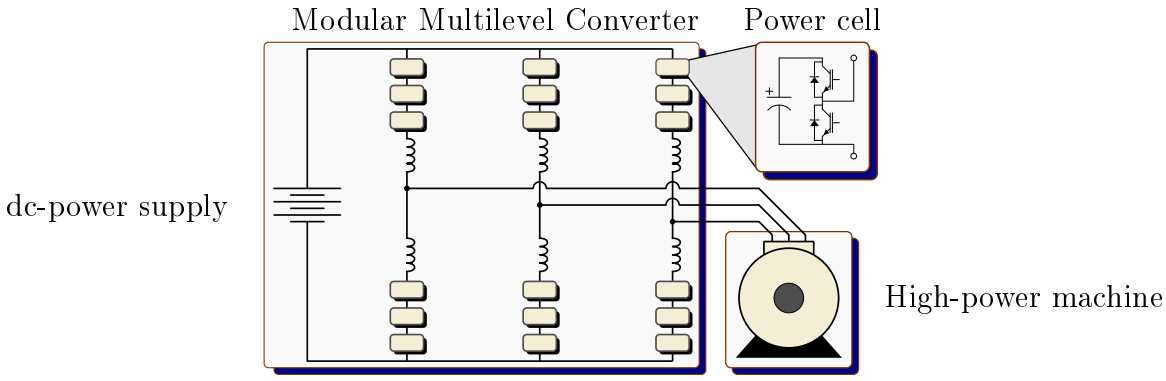

Figure 1.1: High-power/voltage drive based on Modular Multilevel topology

quardt in 2001 [42], is an emerging converter topology suitable for Medium/High voltage applications.When compared with the VSC or CSC, the MMC exhibits several advantages, for instance, full modularity, redundancy, control flexibility, easy extensibility to high-voltage levels, power quality and possible transformer-less operation. These features place the MMC above the conventional power converters for medium-voltage drives [43–45]. For these reasons, it has been proposed for applications such as rail train [46–48], power quality improvement [49, 50], high-voltage dc-transmission (HVDC) [51–54] and machine drives [55–74].

A better performance of the MMC-based drive has been reported for applications such as pumps, fans, marine propulsion, oil and gas transportation when compared with others modular converters (e.g. the Modular Multilevel Matrix Converter (M^3C) [75, 76] and the Hexverter [77–79]) [44, 62, 80]. Consequently, a commercial solution, the driver SINAMICS SM120 CM of Siemens, has been offered for the medium-voltage range since 2015 (up to 30 MVA @ 7.2 kV). This solution integrates the MMC technology either as grid module, motor module or both [81–84].

The MMC-based drive topology is shown in Fig. 1.1. It is composed of an ac-port that feeds the machine, a dc-port and six "clusters" (also called "arms" or "branches"). Each cluster has n cascaded cells and an inductor L. The cells are composed of a half-bridge or chopper circuit with a "flying" capacitor C. The commercial solution offered by Siemens is shown in Fig. 1.2. In the figure, a 42-power cell MMC is shown. In this case, two chopper cells as the one depicted in Fig. 1.1 are combined into the one illustrated in Fig. 1.2b (i.e. the converter has 84 floating capacitors).

Notice that this topology requires an additional device acting as dc-source to transform the ac-grid voltage. The dc-source could be implemented by using front-end rectifiers. Particularly, 12-, 18-, 24-, and 36-pulses rectifiers are available in the commercial version of the MMC drive [81–84]. However, these rectifiers require a phase-shifted multi-winding transformer to meet the grid guidelines [85]; that increases the converter weight and losses for high power/voltage applications. For example, for a 24 MW @ 7.2 kV drive, the required transformer for marine applications could weigh 4500 kg or more and take up more than 5 m^3 of ship space [37]. A suitable option to avoid the use of transformers is presented in Fig. 1.3, where the dc-source is obtained by using a grid-side MMC, creating a Back-to-Back (BTB) scheme that does not require the use of an input transformer. Moreover, this topology has other advantages, e.g. the converter is able to create an ac-voltage higher than the grid volt-

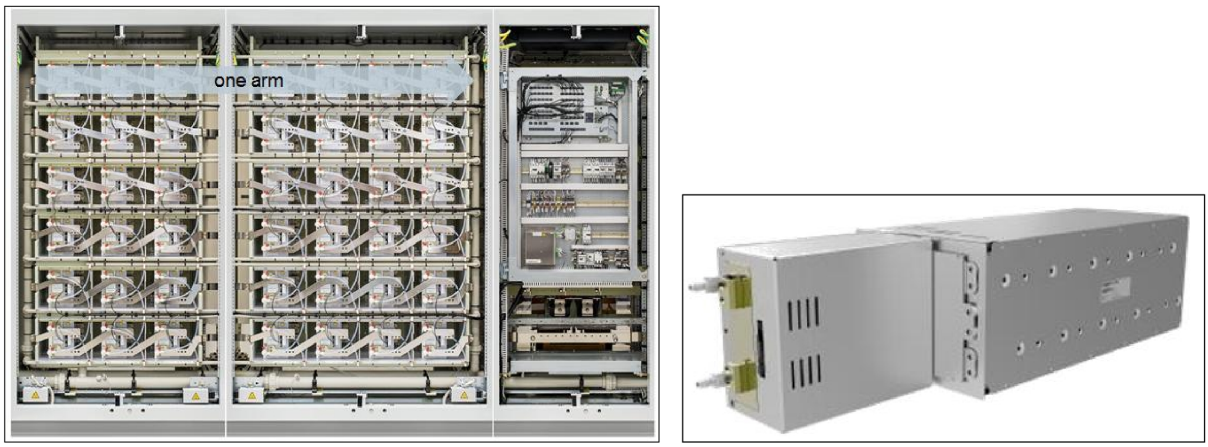

(a) Converter enclosure (42 power cells) (b) Power cell

Figure 1.2: Commercial solution of the MMC-based drive [81]

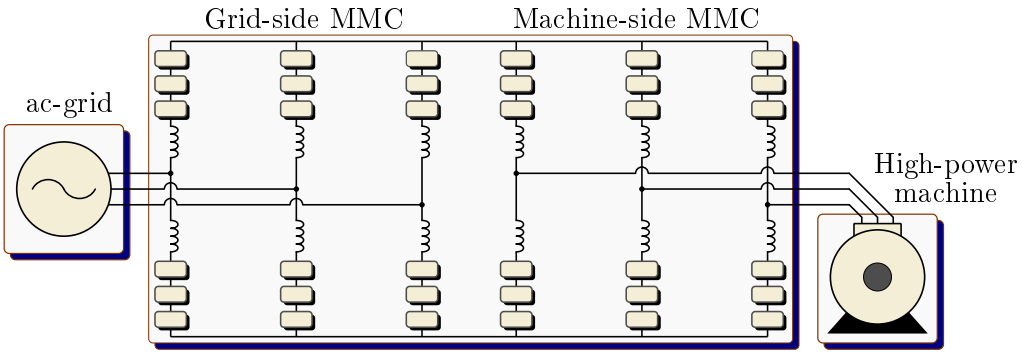

Figure 1.3: Back-To-Back Modular Multilevel Converter for drive applications

age (because the dc-port voltage can be easily controlled), and the bidirectional power flow is feasible, allowing the regenerative operation. The MMC-based drive in BTB configuration is also offered by Siemens [82, 83].

1.4 Problem Description

Although the modularity of the clusters provides good quality in the output variables and medium-voltage capabilities, the control system to achieve the operation of the MMC is more complex than the used one in other non-multilevel topologies. The reason is that the capacitors of the MMC are not connected to an external source (see the power cell in Fig. 1.1), as usual in other converter topologies for low-voltage applications. In this manner, the control system of the MMC-based drive must be able to provide the required voltages and currents to the machine, as well as to fulfil the following objectives:

- To regulate the mean value of the voltage in the MMC capacitors as desired, which is defined in this document as the balancing task.
- To mitigate any large voltage fluctuation in the capacitors, which is defined in this

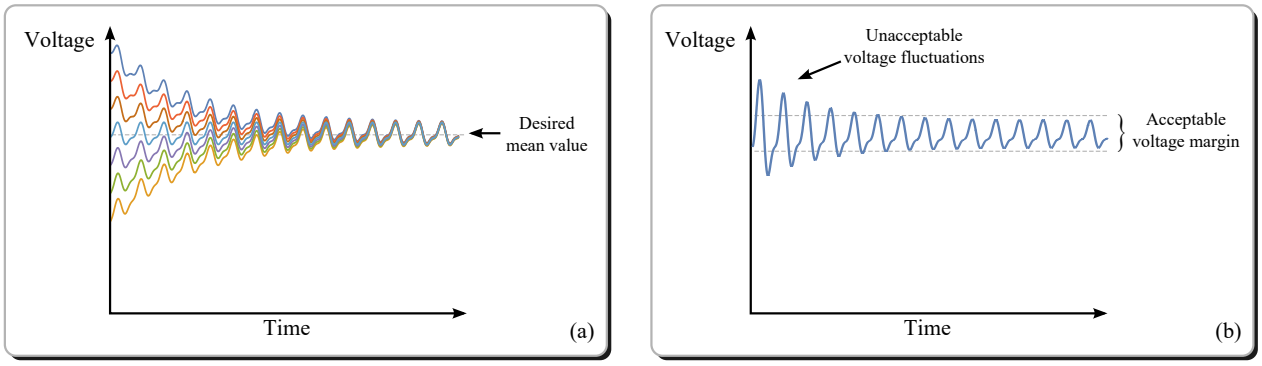

Figure 1.4: Control tasks for regulating the capacitor voltages properly. (a) Balancing task, (b) Mitigation task.

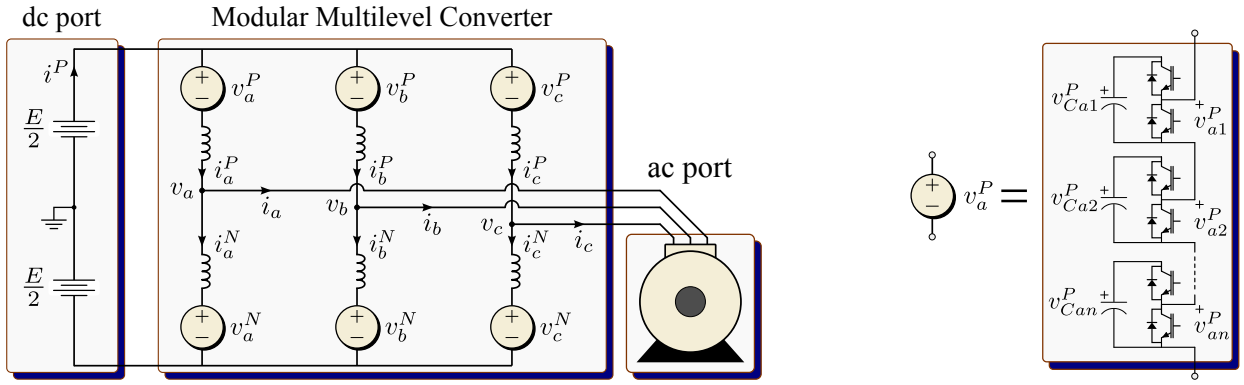

(a) Electrical representation (b) Cluster model

Figure 1.5: Model of the Modular Multilevel Converter

document as the mitigation task.

An illustrative example of both tasks is shown in Fig. 1.4. In Fig. 1.4(a), the balancing task is carried out to regulate the voltage of seven capacitors in the same cluster (usually, they are regulated to the same mean value). Notice that there are fluctuations in the voltage of the capacitors; however, this task is focussed on achieving an equal mean voltage value in each of them. As shown in Fig. 1.4(b), the mitigation task must be enabled if the fluctuations exceed a predefined margin (e.g. 10% of the mean value [61, 65]).

Although the balancing task is well known for grid-connected MMC (e.g. HVDC systems [51–54]), the mitigation task is more related with drive applications because the capacitors are highly affected by the machine frequency. The electrical model of the MMC is used to analyse this issue. As shown in Fig. 1.5, the clusters of the MMC can be modelled as controllable voltage sources. Therefore, using the cluster "Pa" as an example [see Fig. 1.5(a)], its instantaneous power and energy are related as follows:

$$\frac{dW_c}{dt} = p_a^P = v_a^P i_a^P \tag{1.1}$$

where W_c is the stored energy in the cluster, p_a^P is the instantaneous power, v_a^P is the output cluster voltage and i_a^P is the cluster current. For energy storage calculations, the inductor voltage drop can be neglected. On the other hand, the cluster current can be related with

the port currents i^P and i_a supposing a homogeneous current distribution between the MMC clusters. Accordingly, the instantaneous power is approximated as follows [see Fig. 1.5(a)]:

$$\begin{aligned} p_a^P &\approx \underbrace{\left(\frac{1}{2}E - v_a\right)}_{\approx v_a}\underbrace{\left(\frac{1}{2}i_a + \frac{1}{3}i^P\right)}_{i_a} \\ &= \frac{1}{6}Ei^P - \frac{1}{2}v_a i_a + \frac{1}{4}Ei_a - \frac{1}{3}v_a i^P \end{aligned} \tag{1.2}$$

Therefore, if that the machine voltage and current are given by:

$$v_a = V_a \sin(\omega_e t), \quad i_a = I_a \sin(\omega_e t + \theta), \tag{1.3}$$

the dynamic relation defined in (1.1) results in:

$$\frac{dW_c}{dt} = \frac{Ei^P}{6} - \frac{V_a I_a}{4}\cos(\theta) + \frac{V_a I_a}{4}\cos(2\omega_e t + \theta) + \frac{EI_a}{4}\sin(\omega_e t + \theta) - \frac{i^P V_a}{3}\sin(\omega_e t) \tag{1.4}$$

Analysing the right-side of (1.4), it is concluded that the first two components must cancel each other to maintain constant the mean value of the cluster energy. Additionally, the energy pulsations produced by the oscillating components can be determined as follows:

$$\begin{aligned} W_{c1} &= \int \left[\frac{EI_a}{4}\sin(\omega_e t + \theta) - \frac{i^P V_a}{3}\sin(\omega_e t)\right] dt \\ &= -\frac{EI_a\cos(\omega_e t + \theta)}{4\omega_e} + \frac{i^P V_a \cos(\omega_e t)}{3\omega_e} \end{aligned} \tag{1.5}$$

$$\begin{aligned} W_{c2} &= \int \left[\frac{V_a I_a}{4}\cos(2\omega_e t + \theta)\right] dt \\ &= \frac{V_a I_a}{8\omega_e}\sin(2\omega_e t + \theta) \end{aligned} \tag{1.6}$$

Based on (1.5) and (1.6), it is concluded that energy pulsations of frequency ω_e and $2\omega_e$ are presented in the MMC clusters. Both of them have a peak amplitude which is inversely proportional to the machine frequency ω_e and directly proportional to the magnitude of the machine currents and voltages. Therefore, if no corrective actions are taken, large energy fluctuations (and consequently voltage fluctuations) appear when the machine is operating with low-frequency stator currents and voltages, which is typically produced at low-rotational speed. Moreover, if the starting current is high, the low-frequency power pulsations could be very high [61, 62, 64, 65]. For this reason, two operating modes are commonly defined to design the control systems of the MMC-based drive:

1. The Low-Frequency Mode (LFM), where additional electrical variables are required to perform the mitigation task [i.e. to mitigate or eliminate the large voltage fluctuations in the cell capacitors, see Fig. 1.5(b)]. These variables are the machine common-mode voltage and the circulating currents (defined as a current that only flows through the MMC clusters and is not reflected in any port [80].

2. The High-Frequency Mode (HFM), where the oscillations in the capacitor voltages are within an acceptable range without using any mitigating variable.

Several control systems for operating the MMC-based drive have been experimentally validated in [55–74]. However, in most of those papers the control systems are implemented using P or PI controllers. As well known, these controllers are not appropriate for regulating, with zero steady-state error, the high-frequency sinusoidal currents and voltages found in the MMC [86]. Another drawback of the reported control systems, is that most of them are based on the original coordinate system of the MMC (e.g. using the electrical variables shown in Fig. 1.5), producing coupling between different control systems or limitations in the dynamic response. What is more, in all these publications, the set point values for the mitigation variables are predefined with feed-forward signals. Therefore, these variables do not have any sort of closed loop adaptation capability, which is required to compensate for possible changes in the parameters or operating points of the MMC-based drive.

In this context, this Ph.D. project is aimed to investigate and to propose novel modelling and control methods to enhance the operation of the MMC as a machine drive. Mainly, it is proposed to enhance the performance of the mitigating task during LFM by proposing new control methodologies, such as closed-loop based control systems, the integration of the machine information into the MMC control schemes, modifications of the input voltage of the MMC, etc. Computational simulations, as well as an experimental laboratory prototype composed of 18 power modules driving an induction machine, have been utilised to validate all the proposals of this project.

1.5 Project Objectives

The main objective of this Ph.D. project is to propose, analyse and validate experimentally novel modelling and control methodologies to allow the operation of the MMC as a high-power medium-voltage machine drive in the full frequency range (0 to nominal speed and zero-crossing speed).

The research described in this thesis pursues also to accomplish the following specific objectives:

1. To obtain a novel and compact model of the MMC dynamics suitable for implementing high-dynamic performance control systems (e.g. vector- or resonant-based control systems).

2. To consider the interaction between the variables of the electrical machine (e.g. currents and electrical frequency) and the converter (e.g. cluster voltages) to propose closed-loop control structures to enhance the mitigating task in the converter.

3. To analyse the impact of a non-constant dc-port voltage in the MMC-based drive, particularly in the required mitigating variables during LFM, the capacitance of each cell and their voltages fluctuations.

4. To implement a downscaled prototype to validate the proposed modelling and control strategies for MMC-based drives in an experimental rig.

1.6 Hypotheses

The following hypotheses are stated for this research project. As discussed above, each of them is closely related with the papers presented in the following chapters (see Table 1.1):

1. By applying vector modelling approaches, it could be possible to represent and regulate the dynamics of the MMC-based drive with high-dynamic control systems with zero steady-state error. Mainly, closed-loop regulation of the capacitor voltages is desired to ensure the proper operation of the drive.

2. The regulation of the capacitor voltages in the MMC could be improved by considering the interaction between the machine currents and the cluster voltages of the converter. For example, new mitigating methods can be proposed. Transition algorithms between the converter modes or modifications in the machine currents to improve the converter operation can be also proposed.

3. The dc-port voltage of the MMC could be manipulated to propose new control schemes for affecting the mitigating variables during LFM, the capacitance of each cell or their voltage fluctuations.

1.7 Summary of Contributions

After performing an extensive literature review, where several control algorithms were analysed, simulated and experimentally validated in some cases, it became evident that it is possible to significantly improve some of the control algorithms previously published in the literature or to propose completely new control methodologies. Therefore, the following contributions were obtained at the end of this Ph.D. work:

1. A comprehensive vector-based model and control system of the MMC is developed in this work (see Chapter 2, [1]). With the proposed control strategy, the voltage of the MMC clusters is directly controlled as demanded, improving the performance of the mitigation task. High-dynamic control systems, with zero steady-state error, have been proposed and experimentally validated. A novel control scheme for the fast regulation of the circulating currents is also proposed and discussed (see Chapter 5, [4]). With these enhancements, the disturbances produced in the system, changes in the operating point, etc. are compensated.

2. The operation of the MMC-based drive has been analysed using an integrated approach to analyse the interaction between the machine and converter variables. (see Chapter 3 and [2]). It was experimentally validated that a seamless transition between the drive operating modes is feasible when the voltage oscillations in the MMC capacitors are maintained within a predefined margin (e.g. $\pm 10\%$ of the mean value of the capacitor voltage). This transition considers the machine loading conditions, and not only the machine frequency, as usual in previous works. Additionally, the machine flux weakening operation was combined with the control systems of the MMC to reduce

significantly the required circulating currents during LFM.

3. The behaviour of the MMC-based drive has been studied when the dc-port voltage is manipulated (see Chapters 4 and 7, which are based on [3] and [6], respectively). Three operating schemes are proposed depending on the MMC parameters and applied signals. Each of them offers advantages for operating the drive, for example, they can reduce 1) the voltage fluctuations of the cell capacitor (in the both, low- and high-frequency modes), 2) the required capacitance in each cell, or 3) the duration of the LFM. The obtained experimental results show that an important reduction in the mitigating common-mode voltage was achieved when the dc-port voltage is manipulated as proposed in this work, reducing problems such as the insulation damage or leakage currents in the machine bearings. To the best of the author knowledge, this is the first work where the zero-crossing speed and the machine starting-up are tested in an MMC-based drive considering modifications in the dc-port voltage. Additionally, the control system for an MMC-based drive in BTB configuration has been proposed and analysed (see Chapter 6 and [5]). A decoupled control of both MMC is feasible with the presented control strategy. This configuration was used to validate the proposed control schemes presented in Chapter 4.

1.8 General Conclusions

The dynamic and steady-state performance of the proposed control methodologies have been tested, considering the operation of the MMC-based drive during starting up of the electrical machine, step changes in both the torque and magnetising currents, speed-ramps variations, zero-speed crossing test, motoring and generating operation, rotor-locked operation, flux-weakening operation, different loading conditions, etc. In all the cases the performance achieved is consistent with the expected results. Consequently, the following general conclusions are established based on the published works of this project [1–9], the hypotheses presented in Section 1.6 and the experimental and simulation results of this work:

1. Using the proposed vector-based model for the MMC, it is simple to analyse the converter dynamics and it can be used to design and implement vector control strategies to balance the cluster voltages, mitigate large voltage oscillations, regulate the input/output energy transfer, etc. Using the model, a novel dq-based vector control strategy for LFM operation has been presented, analysed and experimentally validated. This control methodology balances the voltage in the MMC clusters, as well as mitigates their large oscillations (i.e. the mitigation and balancing tasks are carried out).

2. It has been demonstrated that an integral control system design approach, considering the dynamics of the converter and induction machine is advantageous to enhance the performance and design of MMC-based drives. A novel algorithm has been proposed to develop a seamless transition between the converter operating modes. The presented algorithm achieves high dynamic behaviour and robustness against changes in the loading conditions.

The proposed control system to maintain the voltage of the MMC capacitors within a predefined margin is highly advantageous when compared with the current state of the art and this has been experimentally and analytically demonstrated in this work. For example, an important reduction in the mitigating currents during LFM has been experimentally demonstrated. A further reduction was also achieved by applying flux weakening operation in the machine during LFM.

3. In this work, the influence of the dc-port voltage on the MMC behaviour has been analysed for both, low- and high-frequency modes. During LFM, it has been demonstrated that a low value of E is advantageous for the operation of the machine drive. For example, a low dc-port value leads to a reduction of three parameters: 1) the voltage fluctuation in the MMC capacitors, 2) the cell capacitance or 3) the duration of the LFM.

   Additionally, the problems produced by the application of common-mode voltages in the machine are reduced by applying low values of the dc-port voltage during LFM. What is more, the peak value of the circulating currents is not affected severely for the proposed control schemes. In HFM, a state-space model was proposed to represent the dynamics of the voltage in the MMC clusters as a function of the dc-port voltage; consequently, a closed-loop control system, that manipulates the voltage E, was proposed to regulate them properly.

Bibliography

[1] M. Espinoza, R. Cárdenas, M. Díaz, and J. C. Clare. An Enhanced *dq*-Based Vector Control System for Modular Multilevel Converters Feeding Variable-Speed Drives. *Industrial Electronics, IEEE Transactions on*, 64(4):2620–2630, April 2017. ISSN 0278-0046.

[2] M. Espinoza, R. Cardenas, J. Clare, D. Soto, M. Diaz, E. Espina, and C. Hackl. An integrated converter and machine control system for mmc-based high power drives. *IEEE Transactions on Industrial Electronics*, PP(99):1–1, 2018. ISSN 0278-0046. doi: 10.1109/TIE.2018.2801839.

[3] M. Espinoza, R. Cardenas, M. Diaz, F. Donoso, and A. Mora. Modelling and Control of the MMC-Based Drive with a Time-Variable dc-Port Voltage. *IEEE Transactions on Power Electronics*, 2019.

[4] M. Espinoza, E. Espina, M. Diaz, A. Mora, and R. Cárdenas. Improved control strategy of the Modular Multilevel Converter for high power drive applications in low frequency operation. In *Power Electronics and Application (EPE), 2016 18th European Conference on*, pages 5–9, Karlsruhe, Germany, September 2016.

[5] M. Espinoza, R. Cárdenas, M. Diaz, A. Mora, and Soto. D. Modelling and Control of the Modular Multilevel Converter in Back to Back Configuration for High Power Induction Machine Drives. In *IEEE Industrial Electronics Society (IECON), 2016 42nd Annual Conference of*, pages 24–27, Florence, Italy, October 2016.

[6] M. Espinoza, F. Donoso, M. Diaz, A. Letelier, and R. Cardenas. Control and Operation of the MMC-Based Drive with Reduced Capacitor Voltage Fluctuations. In *Power Electronics, Machines and Drives (PEMD), 9th International Conference on*, Liverpool, UK., 17-19, April 2018.

[7] M. Espinoza, A. Mora, M. Diaz, and R. Cárdenas. Balancing energy and low frequency operation of the Modular Multilevel Converter in Back to Back configuration. In *Ecological Vehicles and Renewable Energies (EVER), 2015 Tenth International Conference on*, pages 1–9, March 2015.

[8] M. Espinoza, E. Espina, M. Diaz, and R. Cárdenas. Control Strategies for Modular Multilevel Converters Driving Cage Machines. In *IEEE 3rd Southern Power Electronics Conference (SPEC), 2017*, pages 1–6, Puerto Varas, Chile, Diciembre 2017.

[9] M. Espinoza, E. Espina, M. Diaz, F. Donoso, and R. Cárdenas. A Control Strategy for Modular Multilevel-Based Drives Considering the System Operating Point. In *Power Electronics and Application (EPE), 2018 20th European Conference on*, pages 17–21, Riga, Latvia, September 2018.

[10] M. Diaz, R. Cardenas, M. Espinoza, F. Rojas, A. Mora, J. C. Clare, and P. Wheeler. Control of Wind Energy Conversion Systems Based on the Modular Multilevel Matrix Converter. *IEEE Transactions on Industrial Electronics*, 64(11):8799–8810, Nov 2017. ISSN 0278-0046. doi: 10.1109/TIE.2017.2733467.

[11] A. Mora, M. Urrutia, R. Cardenas, A. Angulo, M. Espinoza, M. Diaz, and P. Lezana. Model predictive control based capacitor voltage balancing strategies for modular multilevel converters. *IEEE Transactions on Industrial Electronics*, pages 1–1, 2018. ISSN 0278-0046. doi: 10.1109/TIE.2018.2844842.

[12] M. Diaz, R. Cardenas, M. Espinoza, F. Rojas, C. Hackl, J. Clare, and P. Wheeler. Vector Control of a Modular Multilevel Matrix Converter Operating in the Full Output-Frequency Range. *IEEE Transactions on Industrial Electronics*, 2019.

[13] M. Díaz, M. Espinoza, A. Mora, F. Rojas, and R. Cárdenas. A Novel LVRT Control Strategy for Modular Multilevel Matrix Converter based High-Power Wind Energy Conversion Systems. In *Tenth International Conference and Exhibition on Ecological Vehicles and Renewable Energies EVER15*, Monte-Carlo, Monaco, March 31-, April 01 2015.

[14] A. Mora, M. Espinoza, M. Díaz, and R. Cárdenas. Model Predictive Control of Modular Multilevel Matrix Converter. In *2015 IEEE 24th International Symposium on Industrial Electronics (ISIE)*, pages 1074–1079, June 2015.

[15] M. Diaz, M. Espinoza, A. Mora, R. Cárdenas, and P. Wheeler. Modelling and Control of the Modular Multilevel Matrix Converter and its application to Wind Energy Conversion Systems. In *IEEE Industrial Electronics Society (IECON), 2016 42nd Annual Conference of*, pages 24–27, Florence, Italy, October 2016.

[16] M. Díaz, M. Espinoza, A. Mora, R. Cárdenas, and P. Wheeler. The Application of the Modular Multilevel Matrix Converter in High-PowerWind Turbines. In *2016 18th European Conference on Power Electronics and Applications (EPE'16 ECCE Europe)*, pages 1–11, Sept 2016. doi: 10.1109/EPE.2016.7695437.

[17] A. Mora, R. Cárdenas, M. Espinoza, and M. Díaz. Active power oscillation elimination in 4-leg grid-connected converters under unbalanced network conditions. In *IECON 2016 - 42nd Annual Conference of the IEEE Industrial Electronics Society*, pages 2229–2234, Oct 2016. doi: 10.1109/IECON.2016.7792960.

[18] M. Diaz, F. Rojas, M. Espinoza, A. Mora, P. Wheeler, and R. Cardenas. Closed loop vector control of the modular multilevel matrix converter for equal input-output operating frequencies. In *2017 IEEE Southern Power Electronics Conference (SPEC)*, pages 1–6, Dec 2017. doi: 10.1109/SPEC.2017.8333629.

[19] F. Rojas, M. Díaz, M. Espinoza, and R. Cárdenas. A solid state transformer based on a three-phase to single-phase modular multilevel converter for power distribution networks. In *2017 IEEE Southern Power Electronics Conference (SPEC)*, pages 1–6, Dec 2017. doi: 10.1109/SPEC.2017.8333627.

[20] M. Diaz, M. Espinoza, F. Rojas, R. Cardenas, and P. Wheeler. Vector Control Strategies to enable equal frequency operation of the Modular Multilevel Matrix Converter. In *Power Electronics, Machines and Drives (PEMD), 9th International Conference on*, Liverpool, UK., 17-19, April 2018.

[21] M. Diaz, F. Rojas, F. Donoso, R. Cardenas, M. Espinoza, A. Mora, and P. Wheeler. Control of modular multilevel cascade converters for offshore wind energy generation and transmission. In *2018 Thirteenth International Conference on Ecological Vehicles and Renewable Energies (EVER)*, pages 1–10, April 2018. doi: 10.1109/EVER.2018.8362406.

[22] F. Donoso, M. Espinoza, M. Diaz, A. Letelier, and R. Cardenas. Back-to-Back Modular Multilevel Converter for Drive Applications Under Unbalance Grid Conditions. In *Power Electronics and Application (EPE), 2018 20th European Conference on*, Riga, Latvia, 17-19, September 2018.

[23] M. Espinoza, J.D. Rojas, R. Vilanova, and O. Arrieta. Identification and Control of Chemical Processes Using the Anisochronic Modeling Paradigm. *IFAC-PapersOnLine*, 48(8):361–366, 2015. ISSN 2405-8963. 9th IFAC Symposium on Advanced Control of Chemical Processes ADCHEM 2015 Whistler, Canada, 7-10 June 7-10, 2015.

[24] M. Espinoza, J. D. Rojas, R. Vilanova, and O. Arrieta. Robustness/performance tradeoff for anisochronic plants with two degrees of freedom PID controllers. In *2015 IEEE Conference on Control Applications (CCA)*, pages 1230–1235, Sept 2015.

[25] E. Espina, M. Espinoza, and R. Cárdenas. Active power angle droop control per phase for unbalanced 4-wire microgrids. In *2017 IEEE Southern Power Electronics Conference (SPEC)*, pages 1–6, Dec 2017. doi: 10.1109/SPEC.2017.8333637.

[26] S. McDonald, N. Baker, M. Espinoza, and O. Pickert. Power electronic topology assessment for wave energy converters. In *International Conference on Renewable Power Generation (RPG)*, 2018.

[27] C. Contreras, D. Guajardo, M. Diaz, F. Rojas, M. Espinoza, and R. Cardenas. Fast Delayed Signal Cancellation Based PLL for Unbalanced Grid Conditions. In *22th Congress of the Chilean ACCA Automatic Control Association, IEEE International Conference on Automation*, Concepcion, Chile, 17-19, October 2018.

[28] Paul Waide and Conrad-U. Brunner. Energy-Efficiency Policy Opportunities for Electric Motor-Driven Systems InternatIonal energy agency Energy Efficiency Series, 2011. URL `https://www.iea.org/publications/freepublications/publication/EE_for_ElectricSystems.pdf`.

[29] OIEA. Energy Efficiency Roadmap for Electric Motors and Motor Systems, 2010. URL `https://euagenda.eu/publications/`

energy-efficiency-roadmap-for-electric-motors-and-motor-systems.

[30] WEG-Group. MVW01: Medium Voltage Variable Speed Drive, 2015. URL http://www.weg.net/files/products/WEG-mvw01-medium-voltage-drive-50019088-brochure-english.pdf.

[31] ABB. ABB drives in power generation: Medium voltage drives for more efficient and reliable plant operation, 2010. URL https://library.e.abb.com/public/77f49845159e2e5cc12579c7003d688c/Power%20brochure%20RevB_lowres.pdf.

[32] Siemens-AG. For every destination, the optimum drive SINAMICS: the seamless and integrated drives family for every application, 2011. URL https://www.industry.usa.siemens.com/drives/us/en/electric-drives/Documents/DRV-Brochure-SINAMICS-Seamless_Integrated.pdf.

[33] AETS. Estudio de Mercado de Motores Eléctricos en Chile, 2010. URL http://dataset.cne.cl/Energia_Abierta/Estudios/Minerg/10.Estudio%20Motores%20El%C3%A9ctricos%20en%20Chile_Final%20(1045).pdf.

[34] The European Wind Energy Association. Wind in Power: 2013 European Statistics. The European Wind Energy Association, August 2014. URL http://www.ewea.org/fileadmin/files/library/publications/statistics/EWEA-Annual-Statistics-2013.pdf.

[35] L.G. Franquelo, J. Rodriguez, J.I. Leon, S. Kouro, R. Portillo, and M.A.M. Prats. The Age of Multilevel Converters Arrives. *Industrial Electronics Magazine, IEEE*, 2(2):28–39, June 2008. ISSN 1932-4529.

[36] S. Kouro, M. Malinowski, K. Gopakumar, J. Pou, L.G. Franquelo, Bin Wu, J. Rodriguez, M.A. Perez, and J.I. Leon. Recent Advances and Industrial Applications of Multilevel Converters. *Industrial Electronics, IEEE Transactions on*, 57(8):2553–2580, Aug 2010. ISSN 0278-0046.

[37] Allen-Bradley. Medium Voltage Solutions for Marine Applications: Driving Efficiency Aboard Your Vessel. Technical report, Rockwell Automation, Inc., 2011. URL http://literature.rockwellautomation.com/idc/groups/literature/documents/br/marine-br003_-en-p.pdf.

[38] ABB. ABB drives for marine Medium voltage drives for reliable and efficient operations at sea, 2011. URL https://library.e.abb.com/public/2e7b508ea530471ac125785b00446c95/Marine%20brochure%20RevB_lowres.pdf.

[39] Arnold Aranjo. ABB traction, 2018. URL http://abbcustomerworldaustralia.com/wp-content/uploads/2018/03/6.-ABB-Customer-World-Workshop-Traction.pdf.

[40] Andreas Fuchs. Siemens: Modern Electrical Propulsion Systems for Rolling Stock, 2005. URL https://pdfs.semanticscholar.org/presentation/9e77/3aec4b2fe43905afb44278a147b2ffc4f4b2.pdf.

[41] B. Wu, J. Pontt, J. Rodriguez, S. Bernet, and S. Kouro. Current-Source Converter and Cycloconverter Topologies for Industrial Medium-Voltage Drives. *IEEE Transactions on Industrial Electronics*, 55(7):2786–2797, July 2008. ISSN 0278-0046. doi: 10.1109/TIE.2008.924175.

[42] R. Marquardt. Stromrichterschaltungen mit verteilten energiespeichern, 2001.

[43] H. Akagi. Classification, terminology, and application of the modular multilevel cascade converter (mmcc). *IEEE Transactions on Power Electronics*, 26(11):3119–3130, Nov 2011. ISSN 0885-8993. doi: 10.1109/TPEL.2011.2143431.

[44] Y. Okazaki, W. Kawamura, M. Hagiwara, H. Akagi, T. Ishida, M. Tsukakoshi, and R. Nakamura. Experimental Comparisons Between Modular Multilevel DSCC Inverters and TSBC Converters for Medium-Voltage Motor Drives. *IEEE Transactions on Power Electronics*, PP(99):1–1, 2016. ISSN 0885-8993.

[45] M.A. Perez, S. Bernet, J. Rodriguez, S. Kouro, and R. Lizana. Circuit Topologies, Modeling, Control Schemes, and Applications of Modular Multilevel Converters. *Power Electronics, IEEE Transactions on*, 30(1):4–17, Jan 2015. ISSN 0885-8993.

[46] M. Glinka and R. Marquardt. A new AC/AC-multilevel converter family applied to a single-phase converter,. In *Power Electronics and Drive Systems, 2003. PEDS 2003. The Fifth International Conference on*, volume 1, pages 16–23, November 2003.

[47] M. Glinka. Prototype of multiphase modular-multilevel-converter with 2 MW power rating and 17-level-output-voltage. In *Power Electronics Specialists Conference, 2004. PESC 04. 2004 IEEE 35th Annual*, volume 4, pages 2572–2576 Vol.4, 2004.

[48] M. Glinka and R. Marquardt. A new AC/AC multilevel converter family. *Industrial Electronics, IEEE Transactions on*, 52(3):662–669, June 2005. ISSN 0278-0046.

[49] L. Baruschka and A. Mertens. Comparison of Cascaded H-Bridge and Modular Multilevel Converters for BESS application. In *2011 IEEE Energy Conversion Congress and Exposition*, pages 909–916, Sept 2011.

[50] J. Mei, B. Xiao, K. Shen, L. M. Tolbert, and J. Y. Zheng. Modular Multilevel Inverter with New Modulation Method and Its Application to Photovoltaic Grid-Connected Generator. *IEEE Transactions on Power Electronics*, 28(11):5063–5073, Nov 2013. ISSN 0885-8993.

[51] M. Saeedifard and R. Iravani. Dynamic Performance of a Modular Multilevel Back-to-Back HVDC System. *Power Delivery, IEEE Transactions on*, 25(4):2903–2912, Oct 2010. ISSN 0885-8977.

[52] Shukai Xu, Hong Rao, Qiang Song, Wenhua Liu, and Xiongguang Zhao. Experimental research of MMC based VSC-HVDC system for wind farm integration. In *Industrial Electronics (ISIE), 2013 IEEE International Symposium on*, pages 1–5, May 2013.

[53] Siemens. HVDC PLUS-Basics and Principle of Operation. `http://www.`

energy.siemens.com/br/pool/br/transmissao-de-energia/transformadores/hvdc-plus-basics-and-principle-of-operation.pdf, 2013.

[54] K. Sekiguchi, P. Khamphakdi, M. Hagiwara, and H. Akagi. A Grid-Level High-Power BTB (Back-To-Back) System Using Modular Multilevel Cascade Converters Without-Common DC-Link Capacitor. *IEEE Transactions on Industry Applications*, 50(4):2648–2659, July 2014. ISSN 0093-9994.

[55] B. Tai, C. Gao, X. Liu, and Z. Chen. A Novel Flexible Capacitor Voltage Control Strategy for Variable-Speed Drives with Modular Multilevel Converters. *IEEE Transactions on Power Electronics*, PP(99):1–1, 2016. ISSN 0885-8993.

[56] J. J. Jung, H. J. Lee, and S. K. Sul. Control Strategy for Improved Dynamic Performance of Variable-Speed Drives With Modular Multilevel Converter. *IEEE Journal of Emerging and Selected Topics in Power Electronics*, 3(2):371–380, June 2015. ISSN 2168-6777.

[57] Makoto Hagiwara and Hirofumi Akagi. Control and Experiment of Pulsewidth Modulated Modular Multilevel Converters. *IEEE Transactions on Power Electronics*, 24(7): 1737–1746, July 2009.

[58] Makoto Hagiwara, Kazutoshi Nishimura, and Hirofumi Akagi. A Medium-Voltage Motor Drive With a Modular Multilevel PWM Inverter. *IEEE Transactions on Power Electronics*, 25(7):1786–1799, July 2010.

[59] M. Hagiwara, R. Maeda, and H. Akagi. Control and Analysis of the Modular Multilevel Cascade Converter Based on Double-Star Chopper-Cells (MMCC-DSCC). *Power Electronics, IEEE Transactions on*, 26(6):1649–1658, June 2011. ISSN 0885-8993.

[60] H. Akagi. New trends in medium-voltage power converters and motor drives. In *Industrial Electronics (ISIE), 2011 IEEE International Symposium on*, pages 5–14, June 2011.

[61] Makoto Hagiwara, Isamu Hasegawa, and Hirofumi Akagi. Start-Up and Low-Speed Operation of an Electric Motor Driven by a Modular Multilevel Cascade Inverter. *IEEE Transactions on Industry Applications*, 49(4):1556–1565, July-August 2013.

[62] Y. Okazaki, H. Matsui, M. Muhoro, M. Hagiwara, and H. Akagi. Enhancement on capacitor voltage balancing capability of a modular multilevel cascade inverter for medium-voltage synchronous-motor drives. In *2015 IEEE Energy Conversion Congress and Exposition (ECCE)*, pages 6352–6359, Sept 2015.

[63] Y. Okazaki, H. Matsui, M. Muhoro, M. Hagiwara, and H. Akagi. Enhancement on capacitor voltage balancing capability of a modular multilevel cascade inverter for medium-voltage synchronous-motor drives. In *2015 IEEE Energy Conversion Congress and Exposition (ECCE)*, pages 6352–6359, Sept 2015. doi: 10.1109/ECCE.2015.7310550.

[64] N. Thitichaiworakorn, M. Hagiwara, and H. Akagi. Experimental Verification of a Modular Multilevel Cascade Inverter Based on Double-Star Bridge Cells. *IEEE Transactions on Industry Applications*, 50(1):509–519, Jan 2014. ISSN 0093-9994.

[65] Arthur J. Korn, Manfred Winkelnkemper, and Peter Steimer. Low Output Frequency Operation of the Modular Multi-Level Converter. In *Energy Conversion Congress and Exposition (ECCE), 2010 IEEE*. IEEE, 12-16 September 2010.

[66] A. Antonopoulos, K. Ilves, L. Ängquist, and H.-P. Nee. On interaction between internal converter dynamics and current control of high-performance high-power AC motor drives with modular multilevel converters. In *Energy Conversion Congress and Exposition (ECCE), 2010 IEEE*, pages 4293–4298, Sept 2010.

[67] A. Antonopoulos, L. Ängquist, S. Norrga, K. Ilves, and H.-P. Nee. Modular multilevel converter ac motor drives with constant torque form zero to nominal speed. In *Energy Conversion Congress and Exposition (ECCE), 2012 IEEE*, pages 739–746, Sept 2012.

[68] A. Antonopoulos, L. Ängquist, S. Norrga, K. Ilves, L. Harnefors, and H.-P. Nee. Modular Multilevel Converter AC Motor Drives With Constant Torque From Zero to Nominal Speed. *Industry Applications, IEEE Transactions on*, 50(3):1982–1993, May 2014. ISSN 0093-9994.

[69] A. Antonopoulos, L. Ängquist, L. Harnefors, and H. P. Nee. Optimal Selection of the Average Capacitor Voltage for Variable-Speed Drives With Modular Multilevel Converters. *IEEE Transactions on Power Electronics*, 30(1):227–234, Jan 2015. ISSN 0885-8993.

[70] B. Li, S. Zhou, D. Xu, D. Xu, and W. Wang. Comparative study of the sinusoidal-wave and square-wave circulating current injection methods for low-frequency operation of the modular multilevel converters. In *Energy Conversion Congress and Exposition (ECCE), 2015 IEEE*, pages 4700–4705, Sept 2015.

[71] S. Debnath, J. Qin, B. Bahrani, M. Saeedifard, and P. Barbosa. Operation, Control, and Applications of the Modular Multilevel Converter: A Review. *IEEE Transactions on Power Electronics*, 30(1):37–53, Jan 2015. ISSN 0885-8993.

[72] J. Kolb, F. Kammerer, and M. Braun. Dimensioning and design of a Modular Multilevel Converter for drive applications. In *Power Electronics and Motion Control Conference (EPE/PEMC), 2012 15th International*, pages LS1a–1.1–1–LS1a–1.1–8, Sept 2012.

[73] J. Kolb, F. Kammerer, M. Gommeringer, and M. Braun. Cascaded Control System of the Modular Multilevel Converter for Feeding Variable-Speed Drives. *Power Electronics, IEEE Transactions on*, 30(1):349–357, Jan 2015. ISSN 0885-8993.

[74] B. Li, S. Zhou, D. Xu, R. Yang, D. Xu, C. Buccella, and C. Cecati. An Improved Circulating Current Injection Method for Modular Multilevel Converters in Variable-Speed Drives. *Industrial Electronics, IEEE Transactions on*, 63(11):7215–7225, Nov 2016. ISSN 0278-0046.

[75] F. Kammerer, D. Braeckle, M. Gommeringer, M. Schnarrenberger, and M. Braun. Operating performance of the modular multilevel matrix converter in drive applications. In *PCIM Europe 2015; International Exhibition and Conference for Power Electronics, Intelligent Motion, Renewable Energy and Energy Management; Proceedings of*, pages 1–8, May 2015.

[76] W. Kawamura, M. Hagiwara, and H. Akagi. Control and experiment of a 380-v, 15-kw motor drive using modular multilevel cascade converter based on triple-star bridge cells (mmcc-tsbc). In *2014 International Power Electronics Conference (IPEC-Hiroshima 2014 - ECCE ASIA)*, pages 3742–3749, May 2014.

[77] L. Baruschka and A. Mertens. A New Three-Phase AC/AC Modular Multilevel Converter With Six Branches in Hexagonal Configuration. *IEEE Transactions on Industry Applications*, 49(3):1400–1410, May 2013. ISSN 0093-9994. doi: 10.1109/TIA.2013.2252593.

[78] L. Baruschka, D. Karwatzki, M. von Hofen, and A. Mertens. Low-speed drive operation of the modular multilevel converter Hexverter down to zero frequency. In *2014 IEEE Energy Conversion Congress and Exposition (ECCE)*, pages 5407–5414, Sept 2014. doi: 10.1109/ECCE.2014.6954142.

[79] D. Karwatzki, L. Baruschka, and A. Mertens. Survey on the Hexverter topology: A modular multilevel AC/AC converter. In *2015 9th International Conference on Power Electronics and ECCE Asia (ICPE-ECCE Asia)*, pages 1075–1082, June 2015. doi: 10.1109/ICPE.2015.7167914.

[80] K. Ilves, L. Bessegato, and S. Norrga. Comparison of cascaded multilevel converter topologies for AC/AC conversion. In *Power Electronics Conference (IPEC-Hiroshima 2014 - ECCE-ASIA), 2014 International*, pages 1087–1094, May 2014.

[81] Marc Hiller, Stephan Busse, and Ahd-H. Gheeth. Modular Multilevel Converter (M2C) Medium Voltage Drives: Working Principle. Technical report, Siemens, 2016.

[82] Siemens. SINAMICS SM120 Cabinet Modules. `https://www.industry.siemens.com/drives/global/en/converter/mv-drives/Pages/sinamics-sm120-cm.aspx`, July 2016.

[83] P. Himmelmann, M. Hiller, D. Krug, and M. Beuermann. A new modular multilevel converter for medium voltage high power oil gas motor drive applications. In *2016 18th European Conference on Power Electronics and Applications (EPE'16 ECCE Europe)*, pages 1–11, Sept 2016. doi: 10.1109/EPE.2016.7695692.

[84] S. Busse, M. Hiller, K. Kahlen, and P. Himmelmann. MTBF comparison of cutting edge medium voltage drive topologies for oil gas applications. In *2015 Petroleum and Chemical Industry Conference Europe (PCIC Europe)*, pages 1–13, June 2015. doi: 10.1109/PCICEurope.2015.7790028.

[85] IEEE. Recommended Practice and Requirements for Harmonic Control in Electric Power Systems. *IEEE Std 519-2014 (Revision of IEEE Std 519-1992)*, pages 1–29, June 2014.

[86] R. Cardenas, C. Juri, R. Pena, J. Clare, and P. Wheeler. Analysis and Experimental Validation of Control Systems for Four-Leg Matrix Converter Applications. *IEEE Transactions on Industrial Electronics*, 59(1):141–153, Jan 2012. ISSN 0278-0046.

Part II

Journal Papers

Chapter 2

An Enhanced *dq*-Based Vector Control System for Modular Multilevel Converters Feeding Variable Speed Drives

This chapter is based on the journal paper:

M. Espinoza, R. Cárdenas, M. Díaz, and J. C. Clare. An Enhanced *dq*-Based Vector Control System for Modular Multilevel Converters Feeding Variable-Speed Drives. *Industrial Electronics, IEEE Transactions on*, 64(4):2620–2630, April 2017. ISSN 0278-0046. **Q1 journal paper. Impact Factor: 7.168.**

Abstract: Modular Multilevel Converters (MMC) are considered an attractive solution for high power drive applications. However, energy balancing within the converter is complex to achieve, particularly when the machine is operating at low rotational speeds. In this paper a new control system, based on cascaded control loops and a vector-power-voltage (vPV) model of the MMC, is proposed. The control system is implemented in a *dq*-synchronous frame rotating at ω_e'rad·s^{-1} with the external loop regulating the capacitor voltages using PI controllers. The internal loop controls the converter currents using PI and resonant controllers. In addition the control systems required to operate the machine at other points, i.e. at medium and high rotational speeds, are also discussed in this work. Experimental results obtained with a MMC-based drive laboratory prototype with eighteen power cells are presented in this paper.

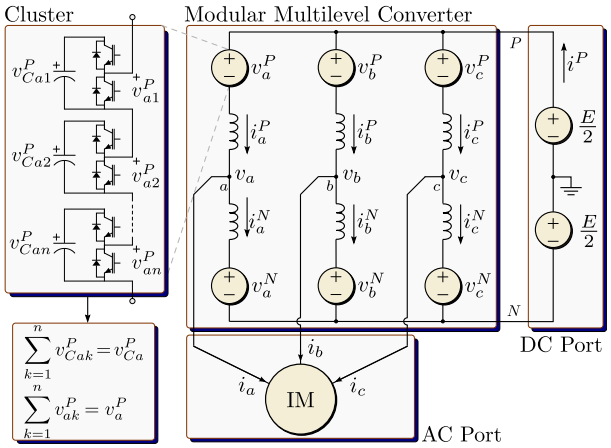

Figure 2.1: Modular Multilevel Converter topology

2.1 Introduction

THE Modular Multilevel Converter (MMC) is a relatively new power converter topology originally proposed for high voltage dc (HVDC) transmission [1–4]. However, for drive applications, the MMC has several advantages when compared to other high-power converters, particularly for quadratic torque-speed profile loads, where a better performance has been reported [5, 6]. Several publications, where experimental results are presented, have been discussed in the literature [7–18, 20, 21]. The topology of a high power drive based on a MMC is shown in Fig. 2.1. It is composed of an ac port, a dc port and six "clusters". Each cluster has n cascaded cells and an inductor L. Each cell is composed of a half bridge circuit and its associated "flying" capacitor C.

Because of the large number of flying capacitors, one of the important tasks of the control systems is to maintain the voltage in each capacitor operating within an acceptable range. This control target is difficult to fulfil when the electrical machine is operating at zero or low rotational speed [12, 13]. Therefore, for control purposes, the operating range of the MMC is usually divided into two modes: The High-Frequency Mode (HFM) and the Low-Frequency Mode (LFM).

Control systems for both, HFM and LFM, have been presented and experimentally validated in [9–12]. However, in these papers the control systems are not decoupled. Therefore, cross-couplings between control loops is possible, affecting the overall system performance. Moreover, in [9–12, 20] the regulation of the currents and voltages is realized using P or PI controllers. As is well known, these controllers are not appropriate for regulating the ac currents and voltages found in the MMC with zero steady state error [19]. In [20] a decoupled model of the MMC is proposed using a six-dimensional transformation of the converter signals to regulate the variables at each port and to perform the energy balance of the MMC. However, the effectiveness of the algorithms proposed in [20] is difficult to evaluate because the presented experimental results do not show the tracking achieved for these signals in the proposed six-dimensional domain.

To balance the converter energy in the LFM, the use of circulating currents and common

mode voltages has been proposed and analysed in several publications [12–16, 22]. The waveforms proposed in the literature for the common mode voltage and mitigation currents are sinusoidal signals with or without third harmonic injection [12, 13], square wave [12] and hybrid mitigation signals [16, 22]. In all these publications, the set points for the regulation of the mitigation currents are predefined off-line. Therefore, the predetermined mitigation currents do not have any sort of closed loop adaptation capability which is required to compensate for possible changes in the parameters or operating points of the MMC-based drive. For instance off-line predefined mitigation signals cannot compensate non-idealities or simplifications in the power converter model (e.g. neglected inductor voltage in the energy model); the difficulties associated with measuring the stator voltage at low rotational speeds, etc. Moreover in [12–16, 20, 22] P or PI controllers, implemented in the stationary frame, are utilised. As mentioned before, these controllers are not appropriate to regulate sinusoidal signals with zero steady state error.

To solve the aforementioned problems, this paper proposes a new control system for the operation of the MMC-based drive. Moreover, to analyse the control system a vector-Power-Voltage (vPV) model is presented in this work. This model represents the dynamics of the topology shown in Fig. 2.1 using a compact notation with only four vector equations being required. Moreover, it is simpler to use this 4-equation modelling to propose, analyse, and implement conventional dq-based vector control systems.

The proposed dq vector control system is based on a cascaded architecture, where the outer loop drives the imbalances in the capacitor voltages to zero by modifying the set-point value for the circulating currents, which are regulated with resonant controllers implemented in a synchronous rotating frame. Using some minor modifications the proposed control scheme is suitable for operation in both the LFM and HFM.

The rest of this paper is organised as follows. Section 2.2 briefly discusses the conventional modelling of the MMC drive topology shown in Fig. 2.1. Section 2.3 discussed the proposed vPV model and the vector control systems for operating at LFM and HFM. Section 2.4 presents the experimental results obtained with a laboratory prototype. Finally, an appraisal of the proposed control systems is presented in the conclusions.

2.2 Analysis of the MMC

2.2.1 Voltage-Current Model of the MMC

As often occurs in applications related to power converters, it is simpler to analyse the system using a different coordinate space. In this section the $\Sigma\Delta\alpha\beta 0$ transformation (which is partly based on the work presented in [23]) is discussed. Considering the MMC shown in Fig. 2.1, the following currents can be obtained as a function of the cluster currents by using the $[C]_{\Sigma\Delta}$

matrix, which considers the interaction of electrical variables among the converter poles:

$$\begin{bmatrix} i_a^\Sigma & i_b^\Sigma & i_c^\Sigma \\ i_a & i_b & i_c \end{bmatrix} = \underbrace{\begin{bmatrix} \frac{1}{2} & \frac{1}{2} \\ 1 & -1 \end{bmatrix}}_{[C]_{\Sigma\Delta}} \cdot \begin{bmatrix} i_a^P & i_b^P & i_c^P \\ i_a^N & i_b^N & i_c^N \end{bmatrix} \tag{2.1}$$

where the lower row of the resultant current matrix contains the ac port currents and the upper row contains currents that do not appear at the ac port, usually referred to as circulating currents [12, 24]. However, (2.1) can be post-multiplied by the transpose Clarke-transformation, $[C]^\intercal_{\alpha\beta 0}$, to consider the interaction of the electrical variables among the converter phases of the MMC and to get the independent components of each kind of current, resulting in:

$$\begin{bmatrix} i_\alpha^\Sigma & i_\beta^\Sigma & i_0^\Sigma \\ i_\alpha & i_\beta & i_0 \end{bmatrix} = \begin{bmatrix} \frac{1}{2} & \frac{1}{2} \\ 1 & -1 \end{bmatrix} \cdot \begin{bmatrix} i_a^P & i_b^P & i_c^P \\ i_a^N & i_b^N & i_c^N \end{bmatrix} \cdot \underbrace{\begin{bmatrix} \frac{2}{3} & -\frac{1}{3} & -\frac{1}{3} \\ 0 & \frac{1}{\sqrt{3}} & -\frac{1}{\sqrt{3}} \\ \frac{1}{3} & \frac{1}{3} & \frac{1}{3} \end{bmatrix}^\intercal}_{[C]^\intercal_{\alpha\beta 0}} = \begin{bmatrix} i_\alpha^\Sigma & i_\beta^\Sigma & \frac{1}{3}i^P \\ i_\alpha & i_\beta & 0 \end{bmatrix} \tag{2.2}$$

where $i_0^\Sigma = \frac{1}{3}i^P$ and the zero sequence current is $i_0 = 0$.

The $\Sigma\Delta\alpha\beta 0$ transformation applied to (2.2) could be used to transform any 2×3 matrix from *PNabc* coordinates to $\Sigma\Delta\alpha\beta 0$ coordinates. Mathematically this is written as:

$$[X]^{\Sigma\Delta}_{\alpha\beta 0} \doteq [C]_{\Sigma\Delta} \cdot [X]^{PN}_{abc} \cdot [C]^\intercal_{\alpha\beta 0} \tag{2.3}$$

Hence, Kirchhoff's voltage law for every loop of Fig. 2.1 is applied to obtain the dynamic model of the cluster currents:

$$\tfrac{E}{2}\begin{bmatrix} 1 & 1 & 1 \\ 1 & 1 & 1 \end{bmatrix} = \begin{bmatrix} v_a^P & v_b^P & v_c^P \\ v_a^N & v_b^N & v_c^N \end{bmatrix} + L\frac{d}{dt}\begin{bmatrix} i_a^P & i_b^P & i_c^P \\ i_a^N & i_b^N & i_c^N \end{bmatrix} + \begin{bmatrix} v_a & v_b & v_c \\ -v_a & -v_b & -v_c \end{bmatrix} \tag{2.4}$$

and applying the $\Sigma\Delta\alpha\beta 0$ transformation to (2.4) yields:

$$\begin{bmatrix} 0 & 0 & \frac{1}{2}E \\ 0 & 0 & 0 \end{bmatrix} = \begin{bmatrix} v_\alpha^\Sigma & v_\beta^\Sigma & v_0^\Sigma \\ v_\alpha^\Delta & v_\beta^\Delta & v_0^\Delta \end{bmatrix} + L\frac{d}{dt}\begin{bmatrix} i_\alpha^\Sigma & i_\beta^\Sigma & \frac{1}{3}i^P \\ i_\alpha & i_\beta & 0 \end{bmatrix} + 2\begin{bmatrix} 0 & 0 & 0 \\ v_\alpha & v_\beta & v_0 \end{bmatrix} \tag{2.5}$$

where v_α, v_β, i_α and i_β are the $\alpha\beta$ coordinates of the voltages and currents in the electrical machine, v_0 is the common mode voltage and i_α^Σ and i_β^Σ are circulating currents which are not present at any port. Using (2.5) it is simpler to propose and analyse an appropriate control system to regulate each independent current of the MMC shown in Fig. 2.1.

2.2.2 Power-Voltage Model of the MMC

The sum of the capacitor voltages in a cluster (i.e. the available cluster voltage) is related with its instantaneous power by the following expression [10, 25]:

$$\frac{d}{dt}\underbrace{\begin{bmatrix} v_{Ca}^P & v_{Cb}^P & v_{Cc}^P \\ v_{Ca}^N & v_{Cb}^N & v_{Cc}^N \end{bmatrix}}_{[V]^{PN}_{Cabc}} \approx \frac{1}{Cv_C^*}\underbrace{\begin{bmatrix} p_a^P & p_b^P & p_c^P \\ p_a^N & p_b^N & p_c^N \end{bmatrix}}_{[P]^{PN}_{abc}} \tag{2.6}$$

where v_C^* is the voltage reference for the capacitor voltage in each cell. Notice that the powers in (2.6) (in a-b-c coordinates) are calculated using the current and voltage of each cluster (e.g. $p_a^P = v_a^P i_a^P$, $p_a^N = v_a^N i_a^N$, etc.). Moreover, in (2.6) it is assumed that the capacitor voltages are well regulated with instantaneous values close to v_C^*.

The $\Sigma\Delta\alpha\beta 0$ transformation can be applied to (2.6) to relate the total cluster voltage and the power flow in each cluster among the converter poles and phases [see (2.3)] as follows:

$$\frac{d}{dt}\underbrace{\begin{bmatrix} v_{C\alpha}^{\Sigma} & v_{C\beta}^{\Sigma} & v_{C0}^{\Sigma} \\ v_{C\alpha}^{\Delta} & v_{C\beta}^{\Delta} & v_{C0}^{\Delta} \end{bmatrix}}_{[V]_{C\alpha\beta 0}^{\Sigma\Delta}} \approx \frac{1}{Cv_C^*}\underbrace{\begin{bmatrix} p_{\alpha}^{\Sigma} & p_{\beta}^{\Sigma} & p_{0}^{\Sigma} \\ p_{\alpha}^{\Delta} & p_{\beta}^{\Delta} & p_{0}^{\Delta} \end{bmatrix}}_{[P]_{\alpha\beta 0}^{\Sigma\Delta}} \tag{2.7}$$

where the powers in $\Sigma\Delta\alpha\beta 0$ coordinates could be derived from (2.5). After some manipulations yields:

$$p_{\alpha}^{\Sigma} = \tfrac{1}{2}Ei_{\alpha}^{\Sigma} - \tfrac{1}{4}i_{\alpha}v_{\alpha} + \tfrac{1}{4}i_{\beta}v_{\beta} - \tfrac{1}{2}i_{\alpha}v_0 \tag{2.8a}$$

$$p_{\beta}^{\Sigma} = \tfrac{1}{2}Ei_{\beta}^{\Sigma} + \tfrac{1}{4}i_{\beta}v_{\alpha} + \tfrac{1}{4}i_{\alpha}v_{\beta} - \tfrac{1}{2}i_{\beta}v_0 \tag{2.8b}$$

$$p_{0}^{\Sigma} = \tfrac{1}{6}Ei^{P} - \tfrac{1}{4}i_{\alpha}v_{\alpha} - \tfrac{1}{4}i_{\beta}v_{\beta} \tag{2.8c}$$

$$p_{\alpha}^{\Delta} = \tfrac{1}{2}Ei_{\alpha} - \tfrac{2}{3}i^{P}v_{\alpha} - i_{\alpha}^{\Sigma}v_{\alpha} + i_{\beta}^{\Sigma}v_{\beta} - 2i_{\alpha}^{\Sigma}v_0 \tag{2.8d}$$

$$p_{\beta}^{\Delta} = \tfrac{1}{2}Ei_{\beta} - \tfrac{1}{3}2i^{P}v_{\beta} + i_{\beta}^{\Sigma}v_{\alpha} + i_{\alpha}^{\Sigma}v_{\beta} - 2i_{\beta}^{\Sigma}v_0 \tag{2.8e}$$

$$p_{0}^{\Delta} = -i_{\alpha}^{\Sigma}v_{\alpha} - i_{\beta}^{\Sigma}v_{\beta} - \tfrac{2}{3}i^{P}v_0 \tag{2.8f}$$

The meaning of these variables is discussed in next sections.

2.3 Proposed control system

2.3.1 Vector Power-Voltage Model of the MMC

In this paper a new Vector-Power-Voltage (vPV) model of the MMC is proposed. This model allows a simple analysis and implementation of control strategies using vector control algorithms. Defining the power flows and the total cluster voltages as vectors, e.g. $\underline{p}_{\alpha\beta}^{\Sigma} = p_{\alpha}^{\Sigma} + jp_{\beta}^{\Sigma}$, $\underline{v}_{C\alpha\beta}^{\Sigma} = v_{C\alpha}^{\Sigma} + jv_{C\beta}^{\Sigma}$, etc., and using the conventional vector notation for the currents and voltages, the vector model of (2.8a)-(2.8f) is obtained as:

$$\underline{p}_{\alpha\beta}^{\Sigma} = \tfrac{1}{2}E\underline{i}_{\alpha\beta}^{\Sigma} - \tfrac{1}{4}\left(\underline{i}_{\alpha\beta}\underline{v}_{\alpha\beta}\right)^{c} - \tfrac{1}{2}v_0\underline{i}_{\alpha\beta} \tag{2.9a}$$

$$\underline{p}_{\alpha\beta}^{\Delta} = \tfrac{1}{2}E\underline{i}_{\alpha\beta} - \tfrac{2}{3}i^{P}\underline{v}_{\alpha\beta} - \left(\underline{v}_{\alpha\beta}\underline{i}_{\alpha\beta}^{\Sigma}\right)^{c} - 2v_0\underline{i}_{\alpha\beta}^{\Sigma} \tag{2.9b}$$

$$p_{0}^{\Sigma} = \tfrac{1}{6}Ei^{P} - \tfrac{1}{4}\left(\underline{v}_{\alpha\beta} \circ \underline{i}_{\alpha\beta}\right) \tag{2.9c}$$

$$p_{0}^{\Delta} = -\left(\underline{v}_{\alpha\beta} \circ \underline{i}_{\alpha\beta}^{\Sigma}\right) - \tfrac{2}{3}i^{P}v_0 \tag{2.9d}$$

where the symbol "$\circ$" represents the dot product between vectors and the superscript "c" stands for the complex conjugated operator. In (2.9a), the vector $\underline{p}^{\Sigma}_{\alpha\beta}$ represents the power flows between the converter phases. On the other hand the vector power $\underline{p}^{\Delta}_{\alpha\beta}$ [see (2.9b)] and the zero sequence power p^{Δ}_{0} [see (2.9d)] represents power flows between the upper and lower poles of the converter. Finally the zero sequence power, p^{Σ}_{0} [see (2.9c)] is proportional to the power flow between the dc and ac ports and defines the change in the MMC total stored energy. The relationship between the powers of (2.9) and the voltages in $\Sigma\Delta\alpha\beta 0$ coordinates is obtained from (2.7).

If the control systems of the MMC-based drive depicted in Fig. 2.1 achieve perfect regulation of the capacitor voltages, then it is concluded from (2.6) and (2.7) that in steady state the vector voltages in $\Sigma\Delta\alpha\beta 0$ coordinates converge to:

$$\left|\underline{v}^{\Sigma *}_{C\alpha\beta}\right| = \left|\underline{v}^{\Delta *}_{C\alpha\beta}\right| = v^{\Delta *}_{C0} = 0, \qquad v^{\Sigma *}_{C0} = nv^{*}_{C} \tag{2.10}$$

where * represents the set-point value of a signal.

2.3.2 Analysis of the System Using the vPV Model for LFM

When the machine is operating at $\omega_e \approx 0$ rad·s^{-1}, the stator voltage applied is low. Using (2.7) and (2.9b) yields:

$$Cv^{*}_{C}\frac{d\underline{v}^{\Delta}_{C\alpha\beta}}{dt} \approx \underline{p}^{\Delta}_{\alpha\beta} \approx \tfrac{1}{2}E\underline{i}_{\alpha\beta} - 2v_0\underline{i}^{\Sigma}_{\alpha\beta} \tag{2.11}$$

Analysing (2.11) is concluded that most of the low frequency ω_e power oscillations are produced by the term $E\underline{i}_{\alpha\beta}$, particularly when high motor starting current is required. Moreover, if the stator voltage is not negligible, additional low frequency power oscillations are produced by the term $i^{P}\underline{v}_{\alpha\beta}$ in $\underline{p}^{\Delta}_{\alpha\beta}$.

To avoid large voltage variations in the MMC capacitors, the low frequency power oscillations produced by $E\underline{i}_{\alpha\beta}$ and $i^{P}\underline{v}_{\alpha\beta}$ have to be mitigated or eliminated from $\underline{p}^{\Delta}_{\alpha\beta}$. Therefore, in this work a hybrid control strategy, based on the ac component of the common mode voltage (i.e. $\tilde{v}_0$) and the circulating current (i.e. $\underline{\tilde{i}}^{\Sigma}_{\alpha\beta}$), is proposed to reduce the amplitude of $\underline{v}^{\Delta}_{C\alpha\beta}$ during LFM operation. Thus, the set point value of the circulating current $\underline{\tilde{i}}^{\Sigma}_{\alpha\beta}$ is defined as:

$$\underline{\tilde{i}}^{\Sigma *}_{\alpha\beta} = ke^{j(\theta_e - \theta_0)}f(t) \tag{2.12}$$

where k is a constant, $\theta_e = \int \omega_e dt$, with ω_e as the output frequency and θ_0 a phase angle. The term $f(t)$ is defined as:

$$f(t) = A\sin(\omega_m t) \tag{2.13}$$

where the value of ω_m is a degree of freedom, usually selected to be relatively high compared to ω_e (see [12, 13] for details). Additionally, $\tilde{v}^{*}_{0}$ is defined as a square waveform of frequency ω_m, i.e.:

$$\tilde{v}^{*}_{0} = V_0\mathrm{sgn}\left[f(t)\right] \tag{2.14}$$

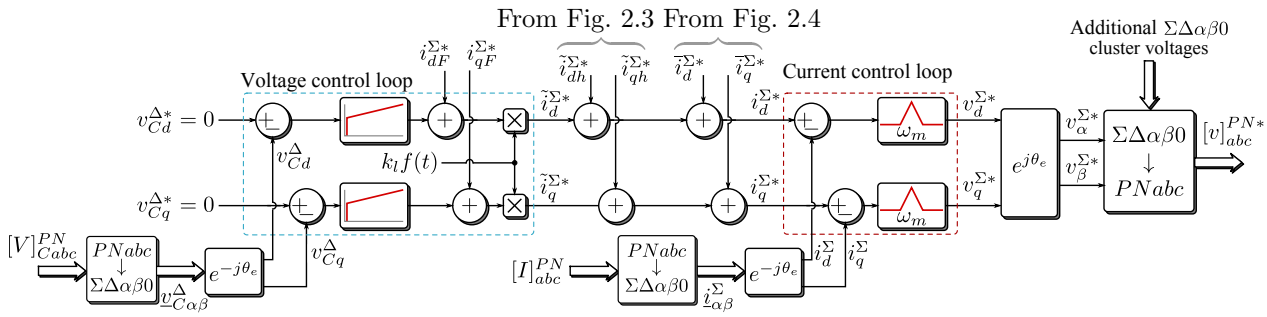

Figure 2.2: Proposed control system for the voltage vector $\underline{v}_{C\alpha\beta}^{\Delta}$ at LFM

Using (2.12) and (2.14) is relatively simple to demonstrate that $\tilde{v}_0^* \underline{\tilde{i}}_{\alpha\beta}^{\Sigma *}$ has a power term of frequency ω_e which could be used to mitigate the low frequency power pulsations produced by the terms $E\underline{i}_{\alpha\beta}$ and $\underline{v}_{\alpha\beta}$ in (2.9b). Ideally, these low frequency signals are completely eliminated when:

$$\underline{\tilde{i}}_{\alpha\beta}^{\Sigma} = k e^{j(\theta_e - \theta_0)} f(t) = \tfrac{1}{2V_0}\left(\tfrac{1}{2} E \underline{i}_{\alpha\beta} - \tfrac{2}{3} i^P \underline{v}_{\alpha\beta}\right) f(t) \tag{2.15}$$

where A=1.57 is used in (2.13) as is discussed elsewhere [22].

In the following subsections the control systems required for voltage balancing and mitigation of the power oscillations are going to be discussed. They are analysed and designed using the vPV model depicted in (2.9a)-(2.9d).

2.3.3 Vector control of the $\underline{v}_{C\alpha\beta}^{\Delta}$ voltage

At low rotational speed (LFM)

As discussed in several publications [12–16, 22] the most critical operating point of a MMC-drive is when the electrical frequency is low and the machine is operating with a relatively high current. Moreover, if $\underline{\tilde{i}}_{\alpha\beta}^{\Sigma *}$ is off-line calculated using (2.15), there are several issues which can potentially hinder the correct mitigation of the low frequency voltage pulsation in the MMC capacitors. Some of these issues have been discussed at Section 2.1. Therefore, in this operating conditions a control systems with good dynamic response and zero steady state error is fundamental to achieve a proper regulation of the capacitor voltages. To fulfil these requirements, in this paper a closed loop vector control system for real time regulation of $\underline{\tilde{i}}_{\alpha\beta}^{\Sigma *}$ is proposed. As demonstrate below, the performance of this control system is better than the conventional solutions considering the high dynamic typically achievable with vector control techniques.

To analyse the proposed nested control loops in dq-coordinates, the dynamics of the system is referred to a synchronous frame. Therefore, replacing (2.7) in (2.9b) and referring to a dq-axis rotating at ω_e yields:

$$C v_C^* \left[\frac{d\underline{v}_{Cdq}^{\Delta}}{dt} + j\omega_e \underline{v}_{Cdq}^{\Delta}\right] \approx \tfrac{1}{2} E \underline{i}_{dq} - \tfrac{2}{3} i^P \underline{v}_{dq} - 2 v_0 \underline{i}_{dq}^{\Sigma} \tag{2.16}$$

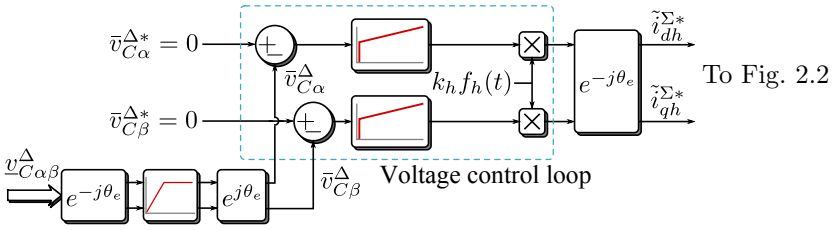

Figure 2.3: Proposed control system for the voltage $\underline{v}^{\Delta}_{C\alpha\beta}$ at HFM

Notice that in (2.16) one term producing relatively high frequency power oscillations has not been considered. These oscillations are almost completely filtered out by the MMC capacitors and its effects are negligible.

The proposed nested control system is shown in Fig. 2.2. The slower outer control loop regulates $\underline{v}^{\Delta}_{Cdq}$, and the internal faster control loop regulates the circulating current $\underline{\tilde{i}}^{\Sigma *}_{dq}$. The voltage vector $\underline{v}^{\Delta}_{Cdq}$, is controlled, with zero steady state error, using PI controllers. The output of the external control loop is used to calculate the set-point for the circulating currents $\underline{\tilde{i}}^{\Sigma}_{dq}$. For simplicity, the dq decoupling terms have not been considered in Fig. 2.2, but they can be added to both control loops.

In the external loop at the output of the PI controllers, two feed-forward compensation terms are considered. These terms are obtained by transforming (2.15) to the dq frame yielding:

$$\underline{\tilde{i}}^{\Sigma *}_{dqF} = \frac{1}{2V_0}\left(\frac{1}{2}E\underline{i}_{dq} - \frac{2}{3}i^{P}\underline{v}_{dq}\right)f(t) \tag{2.17}$$

and they correspond to the conventional feed-forward terms used in the control strategies reported in [12]. In this work these terms are used only to improve the dynamic performance of the voltage control loop. However, if (for instance) some of the components in (2.17) are misidentified, the PI controllers still ensure zero steady state error driving $\underline{v}^{\Delta}_{Cdq}$ to zero (i.e. eliminating the ω_e frequency component in $\underline{v}^{\Delta}_{C\alpha\beta}$).

Analysing (2.13) and (2.17) is concluded that the dq circulating currents have sinusoidal components of frequency ω_m. Therefore, in this work resonant controllers are utilised to regulated these currents (see Fig. 2.2). Notice that the magnitude and phase of $\underline{\tilde{i}}^{\Sigma *}_{\alpha\beta}$ (i.e. k and θ_0) are modified by the voltage control loop. This is certainly an advantage over the conventional mitigation algorithm, where $\underline{\tilde{i}}^{\Sigma *}_{\alpha\beta}$ is predetermined in advance and P or PI controllers, implemented in the stationary frame, are used in the control system to balance the capacitor voltages [12, 20].

The output of the cascaded control systems shown in Fig. 2.2 are the clusters voltages in $\Sigma\Delta\alpha\beta 0$ coordinates. These voltages are referred to the $PNabc$ frame using the inverse $\Sigma\Delta\alpha\beta 0$ transformation in order to be processed by the cell balancing algorithm (see [28]). In this work the angle θ_e is the rotor-flux angle of the vector controlled induction machine. However, the control system proposed in Fig. 2.2 can be orientated along any other vector rotating at ω_e rad·s^{-1}.

Operation at high rotational speed (HFM)

The MMC is operating in the HFM when the voltage oscillations in $\underline{v}^{\Delta}_{C\alpha\beta}$ are relatively small and the circulation of the mitigation currents is not longer required to maintain this voltage bounded.

In the HFM only the dc components of $\underline{v}^{\Delta}_{C\alpha\beta}$ are regulated to zero. Hence, PI controllers implemented in the stationary frame are used, as is shown in the control system in Fig. 2.3. To eliminate the components of frequency ω_e from $\underline{v}^{\Delta}_{Cdq}$, a filter is applied. Good performance and implementation simplicity have been obtained by using a high-pass filter implemented in a synchronous frame rotating at ω_e (see Fig. 2.3). Notice that high pass filters implemented in a *dq*-frame are equivalent to notch filters in the stationary frame.

In previous work [20] it was proposed to add a positive and negative sequence current of frequency ω_e to $\underline{i}^{\Sigma}_{\alpha\beta}$, to produce a manipulable power flow in $(\underline{v}_{\alpha\beta}\underline{i}^{\Sigma}_{\alpha\beta})^c$ and $(\underline{v}_{\alpha\beta}\circ\underline{i}^{\Sigma}_{\alpha\beta})$. These power flows were used to control the voltages $\underline{v}^{\Delta}_{C\alpha\beta}$ and v^{Δ}_{C0} [see (2.9b) and (2.9d)]. However, when that methodology is used, the MMC control system could be affected by sudden variations of the machine stator voltage, $\underline{v}_{\alpha\beta}$. In fact, cross-couplings between the control systems could be introduced when $\underline{v}_{\alpha\beta}$ is affected by intermittent load perturbations.

Hence, in this paper the power term $v_0\underline{i}^{\Sigma}_{\alpha\beta}$ in (2.9b) is used to balance the voltage vector $\underline{v}^{\Delta}_{C\alpha\beta}$ at HFM operation. Moreover, the common mode voltage $\tilde{v}_0$ is used to increase the maximum modulation index of the MMC using third harmonic injection. Then, for the operation in the high frequency mode the voltage $\tilde{v}_0$ and the function $f_h(t)$ are defined as:

$$\tilde{v}_0 = V_{0h}\sin\left(3\theta^{\Delta}_{\alpha\beta}\right), \qquad f_h(t) = 2\sin\left(3\theta^{\Delta}_{\alpha\beta}\right) \tag{2.18}$$

where $\theta^{\Delta}_{\alpha\beta}$ is defined as the electrical angle of the vector $\underline{v}^{\Delta}_{\alpha\beta} = v^{\Delta}_{\alpha} + jv^{\Delta}_{\beta}$. It is important to clarify that the electrical angle used to generate the common mode voltage $(3\theta^{\Delta}_{\alpha\beta})$ is not directly derived from the voltages applied to the machine stator. This is because the phase shift introduced by the voltage drop in the cluster inductances is not negligible.

Transition between modes

A simple method is used to switch between the low frequency and high frequency operating modes. Assuming that ω_l is the highest frequency at which (only) the LFM is used and the transition zone is from ω_l to ω_h, the following weighting factors are defined:

$$k_l = 1 - k_h = \begin{cases} 1 & \text{if } |\omega_e| < \omega_l \\ \frac{\omega_h - |\omega_e|}{\omega_h - \omega_l} & \text{if } \omega_l \leq |\omega_e| \leq \omega_h \\ 0 & \text{if } \omega_h < |\omega_e| \end{cases} \tag{2.19}$$

These weighting factors are used to select the reference for current $\underline{i}^{\Sigma *}_{dq}$ for either HFM or LFM (see Fig. 2.2 and Fig. 2.3). For the experimental work presented in Section IV, the value of ω_l is 20π rad·s^{-1} ($\omega_r \approx 500$rpm) and ω_h is equal to 30π rad·s^{-1} ($\omega_r \approx 750$rpm).

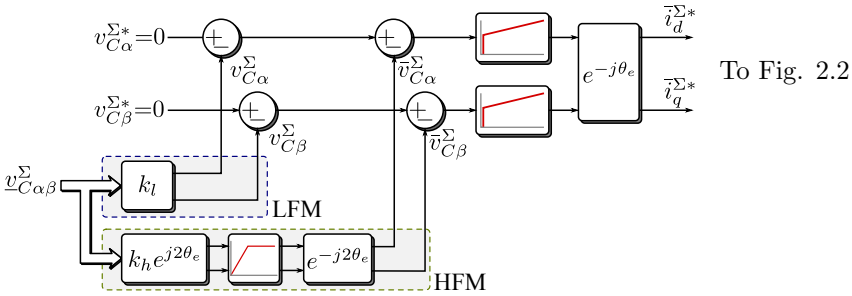

Figure 2.4: Control system to regulate the voltage $\underline{v}^{\Sigma}_{\alpha\beta}$

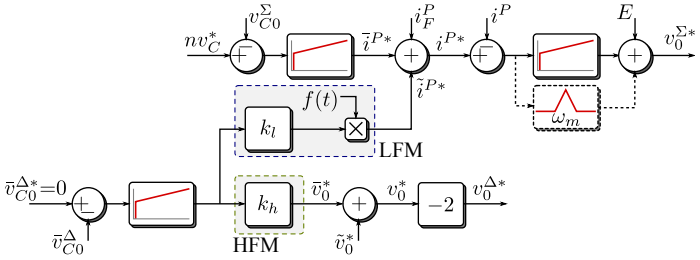

Figure 2.5: Proposed control system for the voltages v^{Σ}_{C0} and v^{Δ}_{C0}

2.3.4 Control of $\underline{v}^{\Sigma}_{\alpha\beta}$ for the whole speed operating range

The voltage $\underline{v}^{\Sigma}_{C\alpha\beta}$ is regulated by manipulating $\underline{p}^{\Sigma}_{\alpha\beta}$ of (2.9a). However, in $\underline{p}^{\Sigma}_{\alpha\beta}$ there are not large low frequency power oscillation when the machine is operating at $\omega_e \approx 0$ and a single control loop (see Fig. 2.4) with some minor modifications could suffice to operate in the LFM as well as the HFM.

The regulation of $\underline{v}^{\Sigma}_{C\alpha\beta}$ is achieved by introducing a dc component in the circulating currents, $\underline{i}^{\Sigma *}_{\alpha\beta}$, which affects the power $E\underline{i}^{\Sigma}_{\alpha\beta}$ in (2.9a). The proposed control system is shown in Fig. 2.4. At LFM, the voltage $\underline{v}^{\Sigma}_{C\alpha\beta}$ is directly used as a feedback signal, because most of its ac components are in the high frequency range which are filtered out by the cell capacitors. The only exception is the term $(\underline{v}_{\alpha\beta}\underline{i}_{\alpha\beta})^c$ that produce a power component of frequency $2\omega_e$. However, for LFM operation, the magnitude of the stator voltage $\underline{v}_{\alpha\beta}$ is small and the effects produced by this power term are typically negligible.

To avoid the oscillations introduced by the $2\omega_e$ frequency component at HFM operation, a notch filter (implemented synchronously) is applied to the feedback signal. The transition between modes is also realised using the weighting factors k_l and k_h. The output of the PI controllers is a dc component added to the circulating current reference $\underline{i}^{\Sigma *}_{\alpha\beta}$ (see Fig. 2.2).

2.3.5 Control of the voltages v^{Σ}_{C0} and v^{Δ}_{C0}

The voltages v^{Σ}_{C0} and v^{Δ}_{C0} are controlled by manipulating the current i^P and the common mode voltage, $\overline{v}_0$. The proposed control system, for both voltages, is shown in Fig. 2.5.

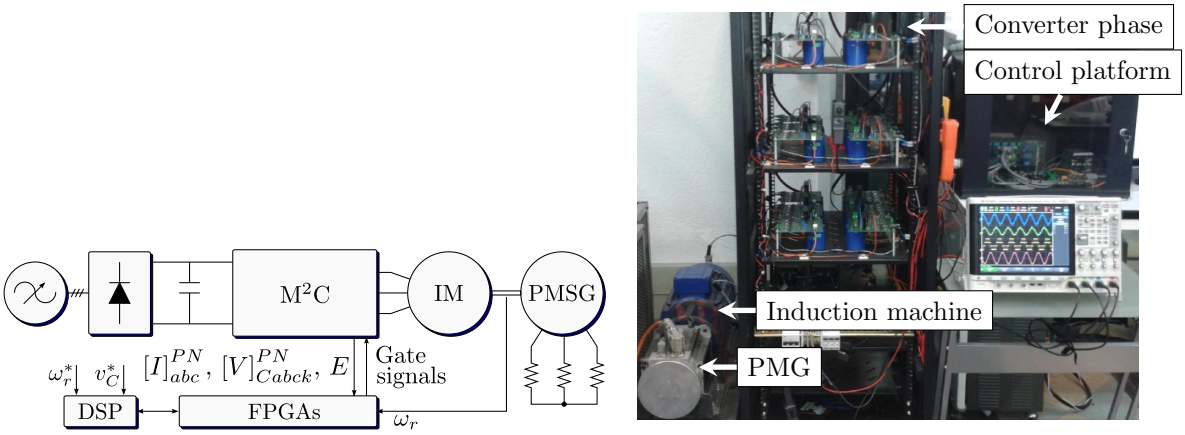

(a) System configuration (b) Experimental system

Figure 2.6: Description of the laboratory prototype

The voltage v_{C0}^{Σ} is controlled by regulating the power produced by the term Ei^P using the current i^P [see (2.9c)] as shown in the top side of Fig. 2.5. A feed-forward i_F^P term could be included to improve the dynamic response when sudden variations in the ac output power are produced. This output power is represented by the term $\frac{1}{4}(\underline{v}_{\alpha\beta} \circ \underline{i}_{\alpha\beta})$ in (2.9c).

The voltage v_{C0}^{Δ} is regulated by manipulating the power produced by the term $i^P v_0$ in (2.9d). This is achieved by introducing a dc component in the common mode voltage v_0 as shown at the bottom of Fig. 2.5. However, when the machine is operating at low rotational speed, the input power is negligible and the current i^P is very low. Therefore in this case the regulation of v_{C0}^{Δ} could require a large dc component in the common mode voltage v_0. To avoid this problem, in this paper an alternative control method for LFM operation is proposed.

It is relatively simple, with a low control effort, to add an ac ($\tilde{i}^P$) current superimposed to the main dc input current. If the current $\tilde{i}^P$ has the same frequency and phase of $f(t)$ [see (2.13)], then the voltage v_{C0}^{Δ} could be regulated by manipulating the amplitude of ($\tilde{i}^P$) and the mean value of the power term $\tilde{i}^P v_0$ in (2.9d). The proposed control system is shown in Fig. 2.5. Notice that a resonant controller tuned at ω_m could be required to regulate $\tilde{i}^P$. Moreover the use of an ac component superimposed to the main dc input current is dependant on the capacity of the dc power supply (feeding the MMC) to withstand operation with ac current components.

The selection of the control systems for HFM/LFM operation is again realised by using the weighting factors of (2.19).

2.4 Experimental set-up and results

In Fig. 2.6a the experimental system implemented to validate the proposed control strategy is shown. In addition a picture of the experimental prototype is shown in Fig. 2.6b.

Table 2.1: Set-up parameters for the 18 cells MMC-drive

Parameter	Symbol	Value	Unit
dc port voltage	E	450	V
Cluster inductor	L_1	2,5	mH
Cell capacitor	C	4700	μF
Cell dc voltage	V_C	160	V
Switching frequency	f_s	5000	Hz
Mitigating frequency	ω_m	314	rad/s

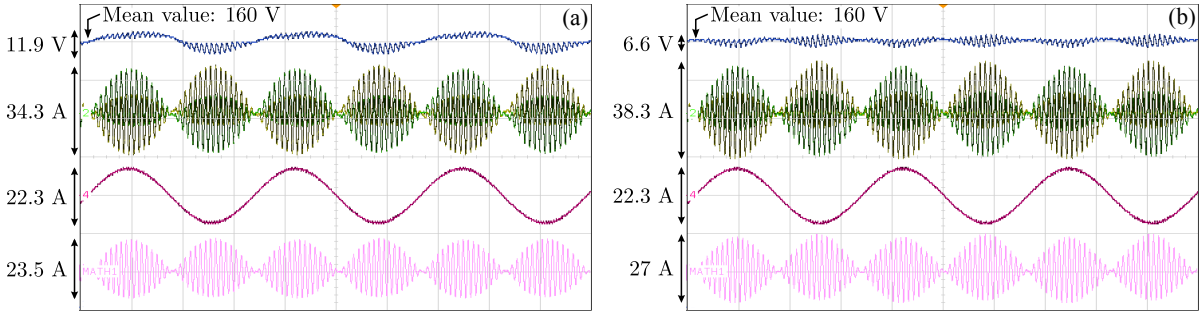

Figure 2.7: MMC static performance at LFM. (a) stationary frame controllers (conventional methodology). (b) proposed control system. Blue: capacitor voltage (20 V/Div), yellow and green: cluster currents (15 A/Div), red: machine current (15 A/Div), pink: phase a circulating current (15 A/Div).

The MMC prototype is fed by a dc-link created by a six-pulse diode rectifier bridge and filter capacitors. The MMC output port is connected to a 3kW, 2910rpm, 2-pole vector-controlled induction machine driving a Permanent Magnet Generator (PMG). The PMG is feeding a 3ϕ resistor bank emulating a quadratic torque-speed load. For the implementation of the indirect vector-control system [29], a position encoder of 10.000 pulses per revolution is affixed to the induction machine. Hall effect transducers are used to measure the dc-link voltage, the capacitor voltage of the 18 cells and the cluster currents. To control the system a platform based on two FPGA boards (Actel ProASIC3), 40 14-bit AD channels and the DSP Texas Instrument TMS320C6713 is used. Optical fibres are used to transmit the switching signals. The experimental parameters are summarized in Table 2.1. All the control systems have been tuned using frequency domain linear control tools. The controllers are designed with the same tuning parameters to allow a fair comparison between different control methodologies.

2.4.1 Experimental results considering operation at $\omega_r = 0$

For this test the rotor of the induction machine is mechanically locked and the stator currents are regulated to $i_d \approx 2.2$A and $i_q = 10$A. This is a very demanding condition for the MMC control system considering that the electrical frequency (close to 1.6 Hz) is equal to the slip frequency. Two control system have been implemented to obtain the experimental results shown in Fig. 2.7. In both cases, the function $f(t)$ was defined as in (2.13) and the common

mode voltage waveform was changed to a trapezoidal shape, with the edges of the 50Hz trapezoidal wave varying between -100% to 100% of the peak value in approximately 1ms. With this modification, the performance of the proposed control systems to operate when variations are produced in the MMC system is validated.

To allow a fair comparison between different control methodologies, all the nested control loops discussed in this work have been designed using identical tuning algorithms. Firstly, for the inner control loops (see Fig. 2.2), the controller parameters have been calculated by solving the following constrained optimisation problem:

$$\min_{\underline{\lambda}} \sum_{h=0}^{\infty} |e(hT_s)| \text{ such that: } M_S = 2 \tag{2.20}$$

where $\underline{\lambda}$ is the vector that contains the controller parameters, e is the tracking error, T_s the sampling time and M_s is the sensitivity function [26]. Notice that a system with $M_S \leq 2$ is usually considered very robust [26, 27].

Secondly, the parameters of the outer controllers are calculated by solving the following constrained optimisation problem:

$$\min_{\underline{\lambda}} \sum_{h=0}^{\infty} |y(hT_s) - y^*(hT_s)| \text{ such that: } M_S = 2 \tag{2.21}$$

where $y(hT_s)$ is the system response and $y^*(hT_s)$ is the desired response, which is usually selected to fulfil a pre-defined control bandwidth. The main advantage of using the tuning procedures depicted in (2.20) and (2.21), is that identical loop robustness is achieved for both, the conventional and the proposed methodology.

In Fig. 2.7a the results obtained by implementing the conventional control strategy reported in [12, 20] are shown. In this case the mitigation currents are off-line calculated using (2.15) and the control systems are based on PI controllers implemented in the stationary frame. On the other hand, the results obtained by the mitigation currents regulated using the proposed control strategy are shown in Fig. 2.7b.

As shown in Fig. 2.7, the peak to peak value of each capacitor voltage is reduced in 55% from approximately 11.9V to 6.6V when the proposed mitigating method is applied. Notice that this reduction produces an increase of 11% in the cluster peak-to-peak currents (from 34.4A to 38.3A), because in this case the feed-forward currents of (2.15) were underestimated. Both stator machine currents depicted in Fig. 2.7 (22.3A peak-to-peak) shows little distortion and are well regulated.

As mentioned before, to test the performance of the proposed control systems some of the experimental results have been obtained considering a trapezoidal waveform in the common mode voltage. In this case the values of dv/dt are reduced and the cluster voltage does not have hard voltage transitions between levels. This is depicted in Fig. 2.8 (yellow signal), with the line-to-line voltage corresponding to the green signal. Notice that in Fig. 2.7 and Fig. 2.8 it is shown that the proposed control system is able to reduce the capacitor voltage oscillations even if the waveform of $\tilde{v}_0$ defined in (2.14) is modified. As explained before the

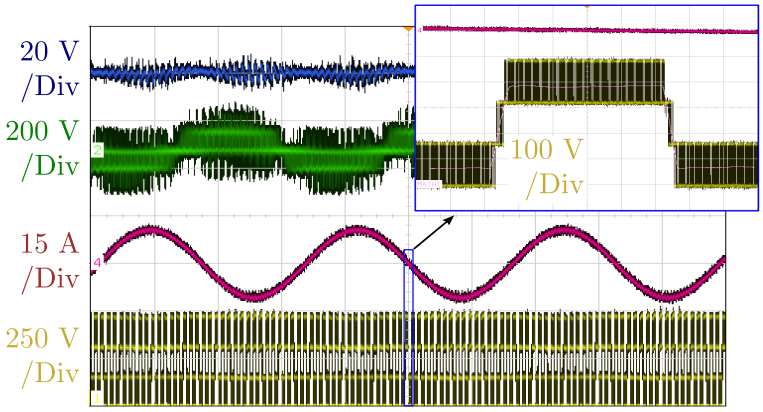

Figure 2.8: MMC signals applying the proposed control system. Blue: capacitor voltage (20 V/Div). green: line to line voltage (200 V/Div), red: machine current (15 A/Div), yellow: cluster voltage (250 V/Div).

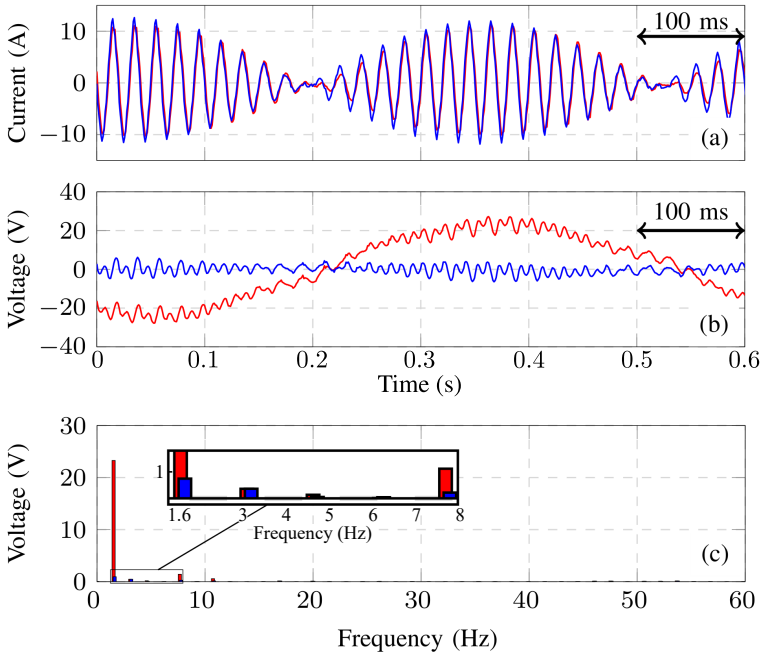

Figure 2.9: Comparison of mitigation schemes. (a) i_{α}^{Σ}. (b) $v_{C\alpha}^{\Delta}$. (c) $v_{C\alpha}^{\Delta}$ Fourier Spectrum. Blue: dq-based control, red: stationary frame control.

dq-based voltage control loop regulates with zero steady state error the signals of frequency ω_e present in the voltage $\underline{v}^{\Delta}_{C\alpha\beta}$, even if variations in the MMC system are produced.

Finally an amplify view of some of the signals corresponding to the test of Fig. 2.7 are shown in Fig. 2.9. In Fig. 2.9a both circulating currents are shown, i.e. that obtained from the conventional control method and the one obtained with the proposed control method of Fig. 2.2. The circulating currents have similar phase and different peak values. Fig. 2.9 (b) shows the voltage $v^{\Delta}_{C\alpha}$ achieved with both control methodologies. Notice that for the conventional control system, the 1.6 Hz oscillations are not eliminate from the capacitor voltage. The Fourier analysis of the frequency components in $v^{\Delta}_{C\alpha}$, for both control methodologies, is shown in Fig. 2.9. For the conventional control methodology there is a 20 V component at $f\approx$1.6 Hz, on the other hand the proposed control method has a 0.7 V component at the same frequency.

2.4.2 Dynamic performance of the proposed control system

Performance considering step changes in the machine currents

The experimental results considering step changes in the machine currents are shown in Fig. 2.10. For this test is considered that initially all the capacitors are discharged and the control and start-up of the MMC is realised in four stages (t_0=0s, t_1=0.1s, t_2=0.6s, t_3=1.1s). In the first stage,$[t_0 \rightarrow t_1]$ (see at top of Fig. 2.10), the eighteen MMC cells (3 per cluster) are charged to 150V imposing a duty cycle of 50%, (E = 450V). During the second stage, $[t_1 \rightarrow t_2]$, the control loops to regulate the voltages $\underline{v}^{\Sigma}_{C\alpha\beta}$, $\underline{v}^{\Delta}_{C\alpha\beta}$, v^{Σ}_{C0} and v^{Δ}_{C0} are enabled and the cell voltage set-point is changed linearly from 150V to 160V (see Fig. 2.10(b)). In this stage a small sinusoidal component of 50Hz is superimposed in the dc input current to facilitate the regulation of v^{Δ}_{C0}. Moreover, as shown in Fig. 2.10(c) and Fig. 2.10(d), circulating current and common mode voltage are imposed in the system.

A step in the the reference of the machine magnetisating current is realised in the third stage, $[t_2 \rightarrow t_3]$ and i^*_d is set to 2.2 A (see Fig. 2.10(e) and Fig. 2.10(f)). After this step change, the proposed mitigating algorithm increases the common mode voltage and the magnitude of the circulating currents to maintain the MMC capacitor voltages well regulated.

The last stage, $[t_3 \rightarrow t_4]$, is the machine start-up by imposing a constant torque current of 8.5A, as is shown in Fig. 2.10(e) and Fig. 2.10(f). In this stage the machine speed is increased to approximately 1600 rpm (see Fig. 2.10(a)). Notice that during LFM operation, which was defined below 10 Hz (close to 500 rpm), the magnitude of $\underline{i}^{\Sigma}_{\alpha\beta}$ is increased as the common mode voltage is reduced (see Fig. 2.10(c) and Fig. 2.10(d)).

The transition mode (TM) is defined between 10Hz-15Hz. In this mode the amplitude of $\underline{i}^{\Sigma}_{\alpha\beta}$ is reduced and the magnitude of the capacitor voltage oscillations increases to approximately $\pm$4.44% of the nominal value (160V). When HFM operation is achieved, the circulating currents required are of relatively small amplitude balancing the energy in the MMC cells. In addition, for HFM operation the current i^P is relatively large and, due to this, a low dc component in the common-mode voltage is enough to maintain the voltage v^{Δ}_{C0}

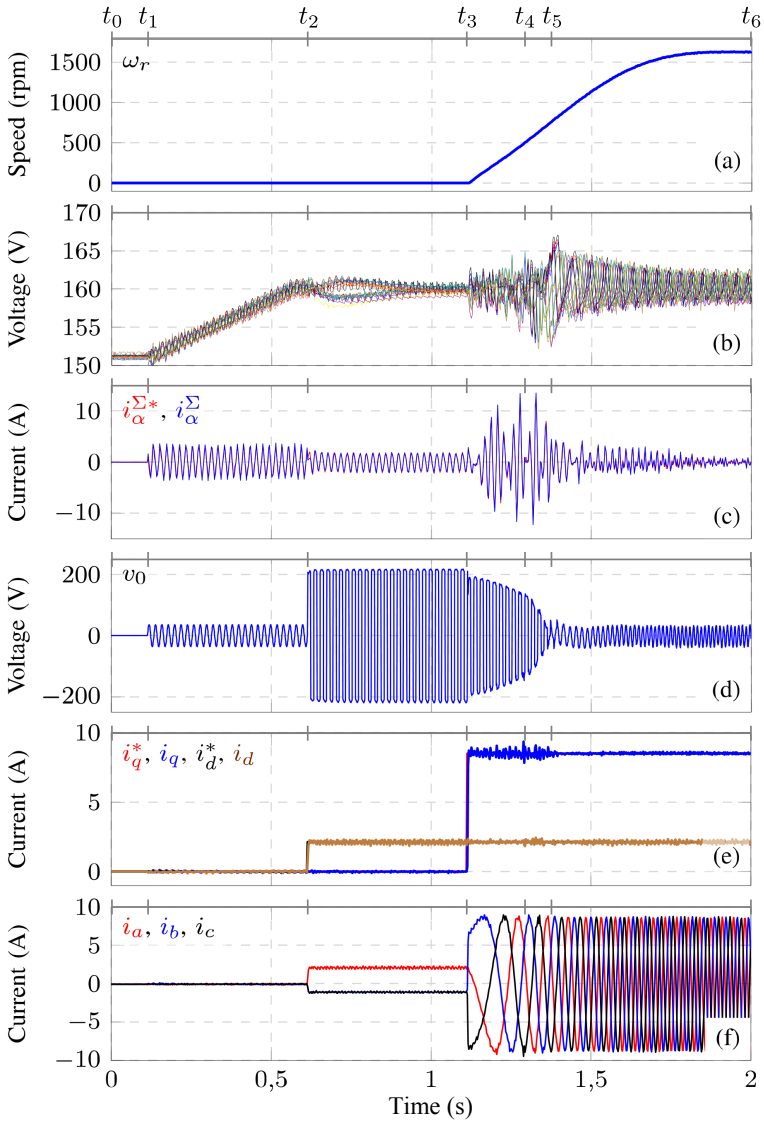

Figure 2.10: Set-up response to step changes in the machine currents. (a) Machine speed, (b) capacitor voltages, (c) Circulating current i_α^Σ, (d) desired common mode voltage, (e) ac port current (dq-frame), (f) ac port current (abc-frame).

well regulated (see (2.9d)).

Dynamic performance considering a ramp variation in ω_r^*

To test the performance of the MMC-based drive in the whole speed range, including zero-speed crossing operation, the rotational speed profile shown in Fig. 2.11(a) is applied to the induction machine. The machine is accelerated from 0 to ±1700 rpm with a slope of ±1800 rpm/s (see Fig. 2.11(a)). During LFM operation (below 10 Hz), a small ac component is superimposed in the dc input current to facilitate the regulation of v_{C0}^{Δ} (see Fig. 2.11(c) and Fig. 2.11(i)). Therefore some noise and oscillations are present in this current which are also related to the application of the common mode voltage. However, this is not a problem since the motor currents are not affected (see Fig. 2.11(d) and Fig. 2.11(e)). Moreover, in this work is assumed that the dc port power supply can safely operate with (small) ac signals superimposed in i^P.

In Fig. 2.11(g) the $\alpha\beta$ components of the voltage vector $\underline{v}_{C\alpha\beta}^{\Delta}$ are depicted. These voltage components are well regulated during LFM operation, showing the effectiveness and good dynamic response of the proposed control system. Moreover, the voltages $\underline{v}_{C\alpha\beta}^{\Sigma}$ and v_{C0}^{Σ} are also tightly regulated (see Fig. 2.11(f) and Fig. 2.11(h)); hence, the total cluster voltages are well controlled for LFM operation, as shown in Fig. 2.11(b).

When the transition zone is reached, the output signals of the LFM/HFM control systems are weighted up by the factors k_l and k_h defined in (2.19). During this transition the oscillations of the cluster voltages are less than 30V peak-to-peak, representing a variation of ±3.1% respect to the nominal value ($3v_C^* = 480$V). During HFM operation, neither the ac component in i^P nor the mitigating signals of (2.15) are applied. Therefore, only the dc components of the $\Sigma\Delta\alpha\beta 0$ voltages are regulated. Moreover, the amplitude of the oscillations in the $\Sigma\Delta\alpha\beta 0$ voltages decreases when ω_r increases. Therefore they are relatively simpler to control. This is shown in Fig. 2.11(f) to Fig. 2.11(h) (depicting the voltages $\underline{v}_{C\alpha\beta}^{\Sigma}$, $\underline{v}_{C\alpha\beta}^{\Delta}$, v_{C0}^{Σ} and v_{C0}^{Δ}).

From the experimental results depicted in Fig. 2.11 is also concluded that the magnitudes of the oscillations produced when the machine is regenerating energy to the dc-link power source are smaller than those produce when the machine is motoring. This is because, for this test, the amplitudes of the machine currents and i^P current are reduced during regeneration.

To the best of our knowledge this is the first time that regenerative and zero-speed crossing operation of a MMC-based drive are experimentally implemented using a vector-controlled induction machine fed by a MMC.

2.5 Conclusion

In this paper a new and comprehensive vector-power-voltage (vPV) model of the MMC-based drive has been presented. Using this model is simple to analyse the converter dynamics and it can be used to design and implement vector control strategies to balance the power converter, mitigate low frequency voltage oscillations, regulate the input/output energy transfer, etc.

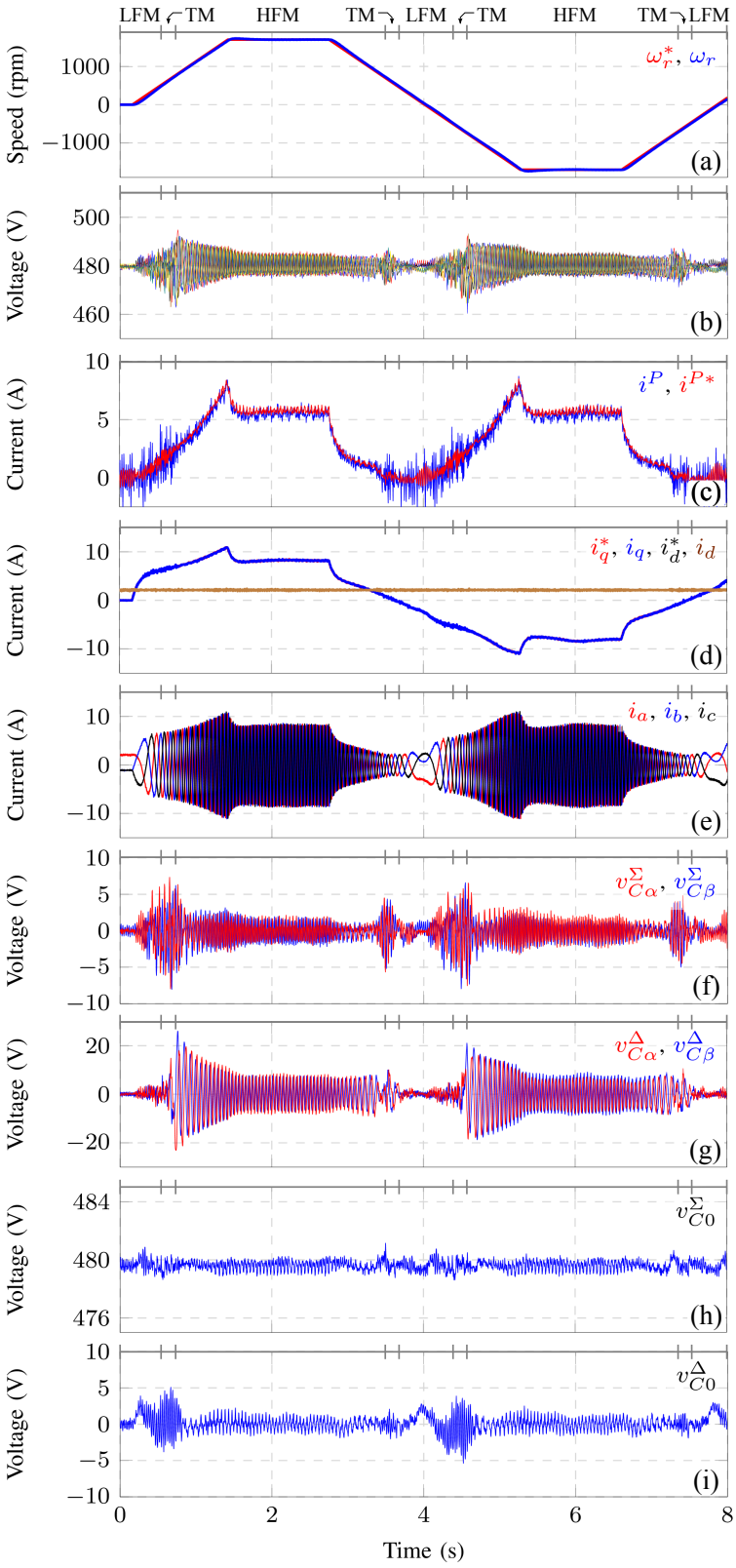

Figure 2.11: System response to a ramp speed variation. (a) machine speed, (b) Total cluster voltages, (c) dc port current, (d) ac port current (dq frame), (e) ac port currents (abc frame), (f) $v_{C\alpha}^{\Sigma}$ and $v_{C\beta}^{\Sigma}$ voltages, (g) $v_{C\alpha}^{\Delta}$ and $v_{C\beta}^{\Delta}$ voltages, (h) v_{C0}^{Σ} voltage, (i) v_{C0}^{Δ} voltage.

Using the vPV model, a novel dq-based vector control strategy for LFM operation has been presented, analysed and experimentally validated in this paper. This control methodology balances the capacitor voltages, as well as mitigates the low frequency (ω_e) capacitor voltage oscillations using nested control loops implementing PI and resonant controllers.

The proposed modelling and vector control systems have also been applied to HFM operation. In all the cases, i.e. LFM and HFM operation, decoupled control of the voltages in the $\Sigma\Delta\alpha\beta 0$-space is achieved by using circulating currents and common mode voltage of different frequencies. All the control strategies proposed in this paper have been analytically discussed and experimentally validated using a MMC-based drive prototype. The dynamic and steady state performance of the proposed control methodologies have been tested, considering MMC starting-up, step changes in both the torque and magnetising currents, speed-ramps, zero-speed crossing test, motoring and generating operation, rotor-locked operation, etc. In all the cases the performance achieved has been excellent.

When compared to the control strategies reported in the literature, the proposed control system produces a higher computational burden, which is mostly required to implement several controllers, and to transform current and voltage signals from abc coordinates to $\Sigma\Delta\alpha\beta 0$ and dq coordinates. However this extra computational burden can be easily handled by a modern DSP, e.g. in this work the implementation of the whole control system for an 18-cell converter, has been relatively simple to realise using a low cost commercial DSP augmented by FPGA boards.

Bibliography

[1] M. Glinka and R. Marquardt, "A new AC/AC-multilevel converter family applied to a single-phase converter," in *The Fifth International Conference on Power Electronics and Drive Systems, 2003. PEDS 2003.*, vol. 1, DOI 10.1109/PEDS.2003.1282669, pp. 16–23 Vol.1, Nov. 2003.

[2] M. Glinka and R. Marquardt, "A new AC/AC multilevel converter family," *IEEE Trans. Ind. Electron.*, vol. 52, no. 3, pp. 662–669, Jun. 2005.

[3] S. Debnath, J. Qin, and M. Saeedifard, "Control and Stability Analysis of Modular Multilevel Converter Under Low-Frequency Operation," *IEEE Trans. Ind. Electron.*, vol. 62, no. 9, pp. 5329–5339, Sep. 2015.

[4] M. Perez, S. Bernet, J. Rodriguez, S. Kouro, and R. Lizana, "Circuit Topologies, Modeling, Control Schemes, and Applications of Modular Multilevel Converters," *IEEE Trans. Power Electron.*, vol. 30, no. 1, pp. 4–17, Jan. 2015.

[5] Y. Okazaki, W. Kawamura, M. Hagiwara, H. Akagi, T. Ishida, M. Tsukakoshi, and R. Nakamura, "Experimental Comparisons Between Modular Multilevel DSCC Inverters and TSBC Converters for Medium-Voltage Motor Drives," *IEEE Trans. Power Electron.*, vol. PP, DOI 10.1109/TPEL.2016.2562103, no. 99, pp. 1–1, 2016.

[6] K. Ilves, L. Bessegato, and S. Norrga, "Comparison of cascaded multilevel converter topologies for AC/AC conversion," in *Power Electronics Conference (IPEC-Hiroshima 2014 - ECCE-ASIA), 2014 International*, DOI 10.1109/IPEC.2014.6869722, pp. 1087–1094, May. 2014.

[7] B. Tai, C. Gao, X. Liu, and Z. Chen, "A Novel Flexible Capacitor Voltage Control Strategy for Variable-Speed Drives With Modular Multilevel Converters," *IEEE Trans. Power Electron.*, vol. 32, no. 1, pp. 128–141, Jan. 2017.

[8] J. J. Jung, H. J. Lee, and S. K. Sul, "Control Strategy for Improved Dynamic Performance of Variable-Speed Drives With Modular Multilevel Converter," *IEEE Journal of Emerging and Selected Topics in Power Electronics*, vol. 3, no. 2, pp. 371–380, Jun. 2015.

[9] M. Hagiwara, K. Nishimura, and H. Akagi, "A Medium-Voltage Motor Drive With a Modular Multilevel PWM Inverter," *IEEE Trans. Power Electron.*, vol. 25, DOI

10.1109/TPEL.2010.2042303, no. 7, pp. 1786–1799, Jul. 2010.

[10] H. Akagi, "New trends in medium-voltage power converters and motor drives," in *Industrial Electronics (ISIE), 2011 IEEE International Symposium on*, DOI 10.1109/ISIE.2011.5984128, pp. 5–14, Jun. 2011.

[11] N. Thitichaiworakorn, M. Hagiwara, and H. Akagi, "Experimental Verification of a Modular Multilevel Cascade Inverter Based on Double-Star Bridge Cells," *IEEE Trans. Ind. Appl.*, vol. 50, DOI 10.1109/TIA.2013.2269896, no. 1, pp. 509–519, Jan. 2014.

[12] M. Hagiwara, I. Hasegawa, and H. Akagi, "Start-Up and Low-Speed Operation of an Electric Motor Driven by a Modular Multilevel Cascade Inverter," *IEEE Trans. Ind. Appl.*, vol. 49, DOI 10.1109/TIA.2013.2256331, no. 4, pp. 1556–1565, July-August 2013.

[13] A. J. Korn, M. Winkelnkemper, and P. Steimer, "Low Output Frequency Operation of the Modular Multi-Level Converter," in *Energy Conversion Congress and Exposition (ECCE), 2010 IEEE*, DOI 10.1109/ECCE.2010.5617802. IEEE, 12-16 September 2010.

[14] A. Antonopoulos, L. Ängquist, S. Norrga, K. Ilves, L. Harnefors, and H.-P. Nee, "Modular Multilevel Converter AC Motor Drives With Constant Torque From Zero to Nominal Speed," *IEEE Trans. Ind. Appl.*, vol. 50, DOI 10.1109/TIA.2013.2286217, no. 3, pp. 1982–1993, May. 2014.

[15] B. Li, S. Zhou, D. Xu, D. Xu, and W. Wang, "Comparative study of the sinusoidal-wave and square-wave circulating current injection methods for low-frequency operation of the modular multilevel converters," in *Energy Conversion Congress and Exposition (ECCE), 2015 IEEE*, DOI 10.1109/ECCE.2015.7310324, pp. 4700–4705, Sep. 2015.

[16] S. Debnath, J. Qin, B. Bahrani, M. Saeedifard, and P. Barbosa, "Operation, Control, and Applications of the Modular Multilevel Converter: A Review," *IEEE Trans. Power Electron.*, vol. 30, DOI 10.1109/TPEL.2014.2309937, no. 1, pp. 37–53, Jan. 2015.

[17] A. Antonopoulos, L. Ängquist, L. Harnefors, and H. P. Nee, "Optimal Selection of the Average Capacitor Voltage for Variable-Speed Drives With Modular Multilevel Converters," *IEEE Trans. Power Electron.*, vol. 30, DOI 10.1109/TPEL.2014.2316273, no. 1, pp. 227–234, Jan. 2015.

[18] J. Kolb, F. Kammerer, and M. Braun, "Dimensioning and design of a Modular Multilevel Converter for drive applications," in *Power Electronics and Motion Control Conference (EPE/PEMC), 2012 15th International*, pp. LS1a–1.1–1–LS1a–1.1–8, Sep. 2012.

[19] R. Cardenas, C. Juri, R. Pena, J. Clare, and P. Wheeler, "Analysis and Experimental Validation of Control Systems for Four-Leg Matrix Converter Applications," *IEEE Transactions on Industrial Electronics*, vol. 59, no. 1, pp. 141–153, Jan 2012.

[20] J. Kolb, F. Kammerer, M. Gommeringer, and M. Braun, "Cascaded Control System of the Modular Multilevel Converter for Feeding Variable-Speed Drives," *IEEE Trans. Power Electron.*, vol. 30, DOI 10.1109/TPEL.2014.2299894, no. 1, pp. 349–357, Jan. 2015.

[21] S. Du, B. Wu, K. Tian, N. Zargari, and Z. Cheng, "An Active Cross-Connected Modular Multilevel Converter (AC-MMC) for Medium-voltage Motor Drive," *IEEE Trans. Ind. Electron.*, vol. PP, no. 99, pp. 1–1, 2016.

[22] M. Espinoza, A. Mora, M. Diaz, and R. Cárdenas, "Balancing energy and low frequency operation of the Modular Multilevel Converter in Back to Back configuration," in *Ecological Vehicles and Renewable Energies (EVER), 2015 Tenth International Conference on*, pp. 1–9, Mar. 2015.

[23] F. Kammerer, M. Gommeringer, J. Kolb, and M. Braun, "Energy balancing of the Modular Multilevel Matrix Converter based on a new transformed arm power analysis," in *Power Electronics and Applications (EPE'14-ECCE Europe), 2014 16th European Conference on*, pp. 1–10, Aug. 2014.

[24] Y. Wan, S. Liu, and J. Jiang, "Generalised analytical methods and current-energy control design for modular multilevel cascade converter," *Power Electronics, IET*, vol. 6, no. 3, pp. 495–504, Mar. 2013.

[25] H. Akagi, S. Inoue, and T. Yoshii, "Control and Performance of a Transformerless Cascade PWM STATCOM With Star Configuration," *IEEE Trans. Ind. Appl.*, vol. 43, DOI 10.1109/TIA.2007.900487, no. 4, pp. 1041–1049, Jul. 2007.

[26] A. G. Yepes, F. D. Freijedo, Ó. Lopez, and J. Doval-Gandoy, "Analysis and Design of Resonant Current Controllers for Voltage-Source Converters by Means of Nyquist Diagrams and Sensitivity Function," *IEEE Trans. Ind. Electron.*, vol. 58, no. 11, pp. 5231–5250, Nov. 2011.

[27] B. Kristiansson and B. Lennartson, "Robust and optimal tuning of PI and PID controllers," *IEE Proceedings - Control Theory and Applications*, vol. 149, no. 1, pp. 17–25, Jan. 2002.

[28] Y. Okazaki, H. Matsui, M. M. Muhoro, M. Hagiwara, and H. Akagi, "Enhancement on capacitor-voltage-balancing capability of a modular multilevel cascade inverter for medium-voltage synchronous-motor drives," in *2015 IEEE Energy Conversion Congress and Exposition (ECCE)*, Sept 2015, pp. 6352–6359.

[29] R. Cardenas, R. Pena, J. Clare, and P. Wheeler, "Analytical and Experimental Evaluation of a WECS Based on a Cage Induction Generator Fed by a Matrix Converter," *IEEE Transactions on Energy Conversion*, vol. 26, no. 1, pp. 204–215, March 2011.

Chapter 3

An Integrated Converter and Machine Control System for MMC-Based High Power Drives

This chapter is based on the early access journal paper:

M. Espinoza, R. Cardenas, J. Clare, D. Soto, M. Diaz, E. Espina, and C. Hackl. An integrated converter and machine control system for mmc-based high power drives. *IEEE Transactions on Industrial Electronics*, PP(99):1–1, 2018. ISSN 0278-0046. doi: 10.1109/TIE.2018.2801839. **Q1 journal paper. Impact Factor: 7.168.**

Abstract: The Modular Multilevel Converter (MMC) is a promising topology for high power drive applications. However, large voltage fluctuations are produced in the floating capacitors when the machine is operating with high stator currents at low rotational speed. To compensate these oscillations, relatively large mitigation currents are required to keep the capacitor voltages within an acceptable range. In this paper, a new integrated control scheme is discussed to regulate the voltage fluctuations. The strategy is based on closed-loop vector-control of the voltage fluctuations, maintaining them inside a pre-defined threshold. The proposed control system is also augmented using flux weakening operation of the machine at low rotational speeds. An experimental prototype composed of eighteen power cells, feeding a vector-controlled induction machine in the whole speed range, is used to validate the effectiveness and feasibility of the proposed control strategies.

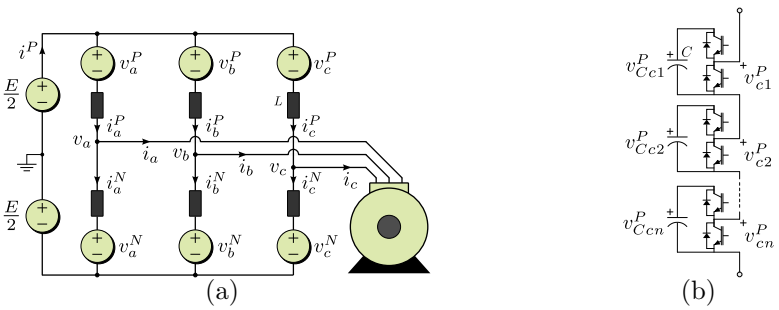

Figure 3.1: MMC-based drive (a): Converter topology. (b): Cluster.

3.1 Introduction

Since the invention of the Modular Multilevel Converter (MMC), it has been proposed for applications such as railway traction [1, 2], high voltage dc transmission (HVDC) [3, 4] and machine drives [5–18]. Since this topology has several advantages when compared to other high-power converters (e.g. for quadratic torque-speed profile loads [6, 7]), a commercial solution based on the MMC has been recently made available in the market for medium-voltage drive applications [19]. However, significant efforts are still required to improve the performance of the control systems for MMC-based drives, particularly for some operating points where this topology is prone to instability [11].

A typical MMC topology to drive a cage induction machine, is shown in Fig. 3.1. The converter is composed of six "clusters" connected to form a three-phase ac port and a dc port (see Fig. 3.1a). Each cluster has an inductor L and n cascaded half bridge cells. The energy in each cell is stored in a "flying" capacitor C (see Fig. 3.1b). Consequently, satisfactory operation of an MMC requires a control system to regulate the floating voltages across the capacitors. This task is more difficult to achieve when the machine operates with relatively large stator currents and at low rotational speed since, at this operating point, large voltage fluctuations may be produced in the capacitors. Therefore, in the so-called "Low-Frequency Mode" (LFM), mitigation is required to reduce the capacitor voltage fluctuations using quantities such as additional circulating currents and common-mode voltages (hereafter called "mitigating variables"). Conversely, when the mitigation is no longer required, the "High-Frequency Mode" (HFM) is usually enabled [10, 11, 15, 20].

Several control systems have been proposed for both operating modes [6, 12, 14, 16]. However, in those papers only the electrical frequency ω_e is utilised to define the operating mode of the converter, neglecting the influence of any additional operating conditions (such as the torque for example). If ω_e is used alone to define the operating point, the mitigation variables may be applied even when they are not required, degrading the converter efficiency and performance. Another drawback with the control systems reported in the literature [6,12,14,16], is that the mitigating currents typically increase with the machine frequency, which could lead to oversizing of some converter components. Moreover, it is important to notice that in most of the control systems discussed previously, the mitigation variables are designed to drive the capacitor voltage fluctuations to zero. This is not strictly necessary, since restricting the voltage fluctuations inside a suitable band, e.g. 5%-10% of the nominal voltage, is enough to ensure appropriate performance [10, 11].

In a recent paper a control algorithm to partially mitigate the capacitor voltage oscillations [17] was proposed. Although a reduction of the required circulating currents was achieved with the method reported, only simulation results were used to validate the proposed methodology for drive applications. The experimental results provided in [17] were obtained using a passive RL load, considering operation only in the low speed mode. Moreover the mitigation signals are calculated off-line and lack the necessary adaptation capability to compensate for possible changes in the operating point of the drive [16].

In this paper, a new control strategy to regulate the voltage fluctuations is proposed. This algorithm implements a fast-dynamic closed loop vector control strategy which regulates the measured capacitor voltage fluctuations inside a predefined threshold. The stator electrical frequency ω_e is not the only criterion to define the converter operating mode. Moreover, in contrast to previous works, seamless operation, without a large transition zone, is achieved using the proposed control methodology. Elimination of the transition zone is a very important contribution of this work since the largest circulating currents are typically reached during this transition [6]. This paper also proposes to combine vector control of the voltage fluctuations with flux weakened operation of the cage machine. Moreover, because closed loop control is proposed, variations and perturbations in the system, e.g. changes in the common mode voltage waveform, mechanical load changes, etc. can be compensated using the proposed control methodology.

The remainder of this paper is organized as follows. Modelling of the MMC-based drive is briefly discussed in Section 3.2. An analysis of the capacitor voltage fluctuations is presented in Section 3.3, while the proposed control systems and the implementation of the converter operating modes are discussed in Section 3.4. Experimental results obtained from an 18-cell MMC-based drive prototype, operating over the full speed range, are discussed in Section 3.5. Finally, Section 3.6 presents the conclusions of this work.

3.2 Modelling of the MMC

Recently, a new model for the MMC has been reported in [14,16]. In these papers, a $\Sigma\Delta\alpha\beta 0$-transformation is used to represent the MMC currents and total cluster voltages (the sum of the capacitor voltages in a cluster) in a coordinate system that simplifies decoupled control of the MMC. A brief review of this modelling approach is given here to provide the required context for the further developments.

The dynamics of the MMC-based drive are obtained from Fig. 3.1 as follows [14]:

$$L\frac{d}{dt}\overbrace{\begin{bmatrix} i_a^P & i_b^P & i_c^P \\ i_a^N & i_b^N & i_c^N \end{bmatrix}}^{\doteq \mathbf{I}_{abc}^{PN}} = -\overbrace{\begin{bmatrix} v_a^P & v_b^P & v_c^P \\ v_a^N & v_b^N & v_c^N \end{bmatrix}}^{\doteq \mathbf{V}_{abc}^{PN}} - \frac{E}{2}\begin{bmatrix} 1 & 1 & 1 \\ 1 & 1 & 1 \end{bmatrix} + \begin{bmatrix} -v_a & -v_b & -v_c \\ v_a & v_b & v_c \end{bmatrix} \tag{3.1}$$

$$C\bar{v}_C\frac{d}{dt}\underbrace{\begin{bmatrix} v_{Ca}^P & v_{Cb}^P & v_{Cc}^P \\ v_{Ca}^N & v_{Cb}^N & v_{Cc}^N \end{bmatrix}}_{\doteq \mathbf{V}_{Cabc}^{PN}} \approx \underbrace{\begin{bmatrix} p_a^P & p_b^P & p_c^P \\ p_a^N & p_b^N & p_c^N \end{bmatrix}}_{\doteq \mathbf{P}_{abc}^{PN}} \tag{3.2}$$

where $\bar{v}_C$ is the algebraic mean value of the voltage in all capacitors of the MMC, $p_a^P{=}i_a^P v_a^P$, $p_b^P{=}i_b^P v_b^P$, etc., are the cluster power fluctuations and $v_{Ca}^P{=}v_{Ca1}^P{+}v_{Ca2}^P{+}...{+}v_{Can}^P$, $v_{Ca}^N{=}v_{Ca1}^N{+}v_{Ca2}^N+...+v_{Can}^N$, etc., are the total cluster voltages. Equation (3.1) is obtained by applying Kirchhoff's voltage law to the converter depicted in Fig. 3.1. On the other hand, (3.2) denotes the energy balance in the MMC clusters, assuming that the total cluster voltages are maintained around the reference voltage, with relatively small ripple.

As discussed before, to achieve decoupled control of the converter currents and voltages, the $\Sigma\Delta\alpha\beta0$-transformation is utilised. This transformation is given by:

$$\mathbf{X}_{\alpha\beta0}^{\Sigma\Delta} \doteq \mathbf{C}^{\Sigma\Delta} \cdot \mathbf{X}_{abc}^{PN} \cdot \mathbf{C}_{\alpha\beta0}^{\intercal} \tag{3.3}$$

where $\mathbf{X}_{abc}^{PN}$ represents the matrix to be transformed (e.g. $\mathbf{I}_{abc}^{PN}$ or $\mathbf{V}_{abc}^{PN}$) and the matrices $\mathbf{C}^{\Sigma\Delta}$ and $\mathbf{C}_{\alpha\beta0}^{\intercal}$ are:

$$\mathbf{C}^{\Sigma\Delta} = \begin{bmatrix} \frac{1}{2} & \frac{1}{2} \\ 1 & -1 \end{bmatrix}, \quad \mathbf{C}_{\alpha\beta0}^{\intercal} = \begin{bmatrix} \frac{2}{3} & \frac{-1}{3} & \frac{-1}{3} \\ 0 & \frac{1}{\sqrt{3}} & \frac{-1}{\sqrt{3}} \\ \frac{1}{3} & \frac{1}{3} & \frac{1}{3} \end{bmatrix}^{\intercal} \tag{3.4}$$

Therefore, applying (3.3) to (3.1) and (3.2) yields:

$$L\frac{d}{dt}\overbrace{\begin{bmatrix} i_\alpha^\Sigma & i_\beta^\Sigma & \frac{1}{3}i^P \\ i_\alpha & i_\beta & 0 \end{bmatrix}}^{\doteq \mathbf{I}_{\alpha\beta0}^{\Sigma\Delta}} = -\overbrace{\begin{bmatrix} v_\alpha^\Sigma & v_\beta^\Sigma & v_0^\Sigma \\ v_\alpha^\Delta & v_\beta^\Delta & v_0^\Delta \end{bmatrix}}^{\doteq \mathbf{V}_{\alpha\beta0}^{\Sigma\Delta}} - 2\begin{bmatrix} 0 & 0 & -\frac{1}{4}E \\ v_\alpha & v_\beta & v_0 \end{bmatrix} \tag{3.5}$$

$$C\bar{v}_C\frac{d}{dt}\underbrace{\begin{bmatrix} v_{C\alpha}^\Sigma & v_{C\beta}^\Sigma & v_{C0}^\Sigma \\ v_{C\alpha}^\Delta & v_{C\beta}^\Delta & v_{C0}^\Delta \end{bmatrix}}_{\doteq \mathbf{V}_{C\alpha\beta0}^{\Sigma\Delta}} \approx \underbrace{\begin{bmatrix} p_\alpha^\Sigma & p_\beta^\Sigma & p_0^\Sigma \\ p_\alpha^\Delta & p_\beta^\Delta & p_0^\Delta \end{bmatrix}}_{\doteq \mathbf{P}_{\alpha\beta0}^{\Sigma\Delta}} \tag{3.6}$$

where the machine currents (i_α and i_β) and voltages (v_α, v_β and v_0) are expressed in $\alpha\beta0$-coordinates, i_α^Σ and i_β^Σ are the circulating currents and i^P is the dc port current. Based on (3.5), each current in $\mathbf{I}_{\alpha\beta0}^{\Sigma\Delta}$ can be controlled by manipulating only one component of the matrix $\mathbf{V}_{\alpha\beta0}^{\Sigma\Delta}$, which is composed of the output cluster voltages of the MMC in the $\Sigma\Delta\alpha\beta0$-coordinate system. Moreover, the machine common-mode voltage, v_0, is defined by modifying v_0^Δ [$v_0^\Delta{=}-2v_0$, see (3.5)]. As discussed in Section 3.3.1, decoupled control of the circulating currents i_α^Σ, i_β^Σ and the common-mode voltage v_0, is useful since these variables are utilised to mitigate the otherwise large fluctuations of the capacitor voltages in the LFM.

The vector representation of (3.6) is more appropriate for the implementation of high-dynamic performance vector control strategies. Defining the power flows and the total cluster voltages as vectors (e.g. $\mathbf{p}_{\alpha\beta}^\Sigma = p_\alpha^\Sigma + jp_\beta^\Sigma$, $\mathbf{v}_{C\alpha\beta}^\Sigma = v_{C\alpha}^\Sigma + jv_{C\beta}^\Sigma$, etc.), the vector model of (3.6) is obtained as (see [16]):

$$C\bar{v}_C\frac{d\mathbf{v}_{C\alpha\beta}^\Sigma}{dt} \approx \mathbf{p}_{\alpha\beta}^\Sigma \approx \tfrac{1}{2}E\mathbf{i}_{\alpha\beta}^\Sigma - \tfrac{1}{4}(\mathbf{i}_{\alpha\beta}\mathbf{v}_{\alpha\beta})^c - \tfrac{1}{2}v_0\mathbf{i}_{\alpha\beta} \tag{3.7a}$$

$$C\bar{v}_C\frac{d\mathbf{v}_{C\alpha\beta}^\Delta}{dt} \approx \mathbf{p}_{\alpha\beta}^\Delta \approx \tfrac{1}{2}E\mathbf{i}_{\alpha\beta} - \tfrac{2}{3}i^P\mathbf{v}_{\alpha\beta} - (\mathbf{v}_{\alpha\beta}\mathbf{i}_{\alpha\beta}^\Sigma)^c - 2v_0\mathbf{i}_{\alpha\beta}^\Sigma \tag{3.7b}$$

$$C\bar{v}_C\frac{dv_{C0}^{\Sigma}}{dt} \approx p_0^{\Sigma} \approx \tfrac{1}{6}Ei^P - \tfrac{1}{4}\Re\left[\mathbf{v}_{\alpha\beta}\left(\mathbf{i}_{\alpha\beta}\right)^c\right] \tag{3.7c}$$

$$C\bar{v}_C\frac{dv_{C0}^{\Delta}}{dt} \approx p_0^{\Delta} \approx -\Re\left[\mathbf{v}_{\alpha\beta}\left(\mathbf{i}_{\alpha\beta}^{\Sigma}\right)^c\right] - \tfrac{2}{3}i^P v_0 \tag{3.7d}$$

where " ^{c} " stands for the complex conjugation operator.

3.3 Analysis of the MMC-based drive

3.3.1 Voltage fluctuations in the converter capacitors

If $\mathbf{i}_{\alpha\beta}^{\Sigma}$ and v_0 are zero (i.e. no mitigation variables are applied), the steady-state total cluster voltages in the $\Sigma\Delta\alpha\beta 0$-domain can be obtained from (3.7a)-(3.7d) as:

$$\mathbf{v}_{C\alpha\beta}^{\Delta} \approx \frac{1}{j\omega_e C\bar{v}_C}\left(\tfrac{1}{2}E\mathbf{i}_{\alpha\beta} - \tfrac{2}{3}i^P\mathbf{v}_{\alpha\beta}\right) \tag{3.8a}$$

$$\mathbf{v}_{C\alpha\beta}^{\Sigma} \approx \frac{-1}{j8\omega_e C\bar{v}_C}\left(\mathbf{i}_{\alpha\beta}\mathbf{v}_{\alpha\beta}\right)^c \tag{3.8b}$$

$$v_{C0}^{\Sigma} \approx n\bar{v}_C, \qquad v_{C0}^{\Delta} \approx 0 \tag{3.8c}$$

Based on the inverse $\Sigma\Delta\alpha\beta 0$-transformation, the total capacitor voltages in $PNabc$-coordinates can be expressed using the vector voltages previously defined. For example, it can be demonstrated that the voltages v_{Ca}^P and v_{Ca}^N are given as follows:

$$v_{Ca}^P = \tfrac{1}{2}\Re\left[\mathbf{v}_{C\alpha\beta}^{\Delta}\right] + \Re\left[\mathbf{v}_{C\alpha\beta}^{\Sigma}\right] + \tfrac{1}{2}v_{C0}^{\Delta} + v_{C0}^{\Sigma} \tag{3.9a}$$

$$v_{Ca}^N = -\tfrac{1}{2}\Re\left[\mathbf{v}_{C\alpha\beta}^{\Delta}\right] + \Re\left[\mathbf{v}_{C\alpha\beta}^{\Sigma}\right] - \tfrac{1}{2}v_{C0}^{\Delta} + v_{C0}^{\Sigma} \tag{3.9b}$$

Considering (3.8a)-(3.8c) and (3.9a)-(3.9b), it is concluded that the total cluster voltages are mainly composed of a mean value given by v_{C0}^{Σ}, a fundamental fluctuation of frequency ω_e defined by $\mathbf{v}_{C\alpha\beta}^{\Delta}$ and a double frequency term given by $\mathbf{v}_{C\alpha\beta}^{\Sigma}$. Therefore, considering the worst case situation, the maximum amplitude of the oscillating component of the total cluster voltages, $|\tilde{v}_{Cx}^X|$, can be related with the vector voltages $\mathbf{v}_{C\alpha\beta}^{\Delta}$ and $\mathbf{v}_{C\alpha\beta}^{\Sigma}$ as follows:

$$|\tilde{v}_{Cx}^X| = \tfrac{1}{2}|\mathbf{v}_{C\alpha\beta}^{\Delta}| + |\mathbf{v}_{C\alpha\beta}^{\Sigma}| \tag{3.10}$$

where the symbol "˜" denotes the oscillating (ac) component of a variable, $x \in \{a, b, c\}$ and $X \in \{P, N\}$.

As discussed in [10, 11], the voltage fluctuation defined in (3.10) can exceed an acceptable amplitude depending on the converter operating point. Notice that the vector $\mathbf{v}_{C\alpha\beta}^{\Delta}$ contributes the most to the large fluctuations at machine start-up, mainly if high currents are required [16].

As depicted in (3.8a), in steady state, the voltage $\mathbf{v}_{C\alpha\beta}^{\Delta}$ has an oscillating component of frequency ω_e. Considering the advantages of vector control systems for the regulation of

power converters and electrical machines (see [16, 21]), in this work the voltage fluctuations of (3.7b) are referred to a synchronous dq-frame rotating at ω_e, where ω_e is the frequency of the signals applied to the stator of the induction machine. Therefore in this paper, a complex vector $\mathbf{x}_{\alpha\beta}{=}x_\alpha{+}jx_\beta$, expressed in the $\alpha\beta$-coordinate system, is referred into the dq-coordinate system applying the following complex transformation:

$$\mathbf{x}_{dq} = \mathbf{x}_{\alpha\beta} e^{-j\theta_e} \tag{3.11}$$

where $\theta_e{=}\int \omega_e dt$.

For drive applications, both θ_e and ω_e are defined by the machine control system. Therefore, applying (3.11) to (3.7b) and reordering yields:

$$C\bar{v}_C \frac{d\mathbf{v}^{\Delta}_{Cdq}}{dt} \approx \underbrace{\tfrac{1}{2}E\mathbf{i}_{dq} - \tfrac{2}{3}i^P\mathbf{v}_{dq}}_{\doteq \mathbf{p}_{\omega_e}} - \underbrace{jC\bar{v}_C\omega_e\mathbf{v}^{\Delta}_{Cdq}}_{\doteq \mathbf{p}_m} - \underbrace{2v_0\mathbf{i}^{\Sigma}_{dq}}_{\doteq \mathbf{p}_c} \tag{3.12}$$

where the term $(\mathbf{v}_{\alpha\beta}\mathbf{i}^{\Sigma}_{\alpha\beta})^c$ in (3.7b) has been neglected, since it produces small fluctuations in the capacitor voltages if the frequency of $\mathbf{i}^{\Sigma}_{\alpha\beta}$ is high in comparison with the frequency ω_e of $\mathbf{v}_{\alpha\beta}$. In (3.12), the power fluctuation $\mathbf{p}_{\omega_e}$ can produce large fluctuations in $\mathbf{v}^{\Delta}_{Cdq}$ depending on the drive operating point, the vector $\mathbf{p}_m$ is a coupling term and $\mathbf{p}_c$ is a degree of freedom. For example, the common-mode voltage and the circulating currents can be in-phase to manipulate the power $\mathbf{p}_c$ in order to regulate $\mathbf{v}^{\Delta}_{Cdq}$ as required to eliminate $\mathbf{p}_{\omega_e}$ and $\mathbf{p}_m$ during the LFM. To perform this task, high frequency components are utilised in $\mathbf{p}_c{=}2v_0\mathbf{i}^{\Sigma}_{dq}$ to avoid the generation of any low-frequency power pulsations in (3.7a)-(3.7d). In steady-state and considering ideal conditions, the required set-point values of $\tilde{\mathbf{i}}^{\Sigma}_{dq}$ and $\tilde{v}_0$, are defined as:

$$\tilde{\mathbf{i}}^{\Sigma *}_{dq} = \frac{1}{2V_0}\left(\mathbf{p}_{\omega_e} - \mathbf{p}_m\right) f(t), \tag{3.13}$$

$$\tilde{v}^*_0 = V_0 \text{sign}\left[f(t)\right] \tag{3.14}$$

where " * " stands for the desired value of a variable and V_0 is the amplitude of the common-mode voltage. Consequently, the resultant power $\mathbf{p}_c$ is:

$$\mathbf{p}_c = \left(\mathbf{p}_{\omega_e} - \mathbf{p}_m\right)|f(t)| \tag{3.15}$$

Hence, $\mathbf{p}_{\omega_e}$ and $\mathbf{p}_m$ are eliminated from (3.12) if $f(t)$ is a high frequency signal compared to ω_e during LFM, such that the mean value of $|f(t)|{=}1$ (considering one period of $f(t)$). In the experimental results of Section 3.5, a function $f(t){=}1.57\sin(100\pi t)$ is utilised. Additional discussions regarding the function $f(t)$ and other options to define the common-mode voltage are presented in [10, 11, 15].

3.3.2 Influence of the vector $\mathbf{v}^{\Delta}_{Cdq}$ on the mitigating variables

Conventionally, the set-point value of $\mathbf{v}^{\Delta}_{Cdq}$ is assigned to zero in the LFM to eliminate any fundamental voltage fluctuation in the MMC capacitors. This procedure generates high

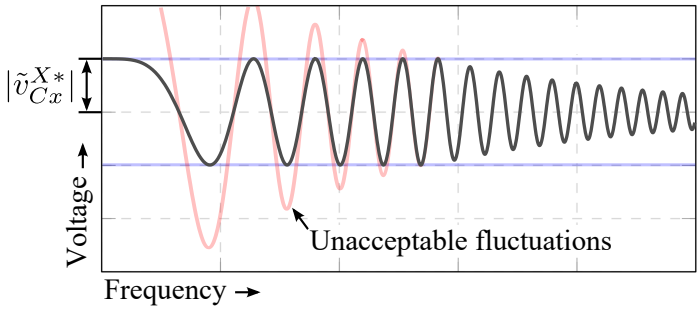

Figure 3.2: Expected behaviour of the total cluster voltage using the proposed strategy (black) and without mitigating variables (red).

circulating currents as ω_e increases, because the available cluster voltage has to be used to synthesise the machine voltage, reducing the value of V_0 [see (3.13)]. However, in this paper a methodology to reduce the circulating currents by using a specific non-zero set-point value for $\mathbf{v}_{Cdq}^{\Delta}$ is proposed.

From (3.13), it can be concluded that the magnitudes of the circulating currents are minimised if the vectors $\mathbf{p}_{\omega_e}$ and $\mathbf{p}_m$ have the same phase shift. This condition is fulfilled if $\mathbf{p}_m$ is defined in terms of $\mathbf{p}_{\omega_e}$ as:

$$\mathbf{p}_m^* = jC\bar{v}_C^*\omega_e\mathbf{v}_{Cdq}^{\Delta*} = C\bar{v}_C^*|\omega_e||\mathbf{v}_{Cdq}^{\Delta*}|\hat{\mathbf{p}}_{\omega_e} \tag{3.16}$$

where $\hat{\mathbf{p}}_{\omega_e}=\frac{\mathbf{p}_{\omega_e}}{|\mathbf{p}_{\omega_e}|}$ is a unit vector in-phase with $\mathbf{p}_{\omega_e}$. Thus, assuming $\mathbf{p}_m^*=\mathbf{p}_m$ and inserting (3.16) into (3.13) yields:

$$\tilde{\mathbf{i}}_{dq}^{\Sigma*} = \tfrac{1}{2V_0}(|\mathbf{p}_{\omega_e}| - C\bar{v}_C^*|\omega_e||\mathbf{v}_{Cdq}^{\Delta*}|)\hat{\mathbf{p}}_{\omega_e}f(t). \tag{3.17}$$

Based on (3.17), it can be concluded that the amplitude of the resultant circulating currents will be less or equal (at $\omega_e{\approx}0$) to that obtained if $\mathbf{v}_{Cdq}^{\Delta*}$, and consequently $\mathbf{p}_m^*$, are set to zero during the LFM [see (3.13)]. This improvement represents an important contribution to the performance and efficiency of MMC-based drives. However, $|\mathbf{v}_{Cdq}^{\Delta*}|$ must be related to the maximum fluctuations of the total cluster voltages to maintain their amplitudes inside an acceptable threshold. Using (3.10) and considering $|\mathbf{v}_{Cdq}^{\Delta}|=|\mathbf{v}_{C\alpha\beta}^{\Delta}|$, $|\mathbf{v}_{Cdq}^{\Delta*}|$ is expressed as follows:

$$|\mathbf{v}_{Cdq}^{\Delta*}| = 2\left(|\tilde{v}_{Cx}^{X*}| - |\mathbf{v}_{C\alpha\beta}^{\Sigma}|\right) \tag{3.18}$$

Finally, from (3.18) and (3.16), $\mathbf{v}_{Cdq}^{\Delta*}$ is calculated as:

$$\mathbf{v}_{Cdq}^{\Delta*} = -j2\text{sign}[\omega_e]\left(|\tilde{v}_{Cx}^{X*}| - |\mathbf{v}_{C\alpha\beta}^{\Sigma}|\right)\hat{\mathbf{p}}_{\omega_e} \tag{3.19}$$

Accordingly, the set-point value of $\tilde{\mathbf{i}}_{dq}^{\Sigma}$ can be automatically defined by an MMC control system that regulates $\mathbf{v}_{Cdq}^{\Delta}$ to follow $\mathbf{v}_{Cdq}^{\Delta*}$ given by (3.19). Furthermore, the circulating currents of (3.17) could be used as a feed-forward term to improve the dynamic response if required. A control system implementing this algorithm is presented in Section 3.4. Moreover, any non-linearity or change in the drive parameters is compensated by the closed-loop control system, while the fluctuations of the total cluster voltages are well regulated and are inside

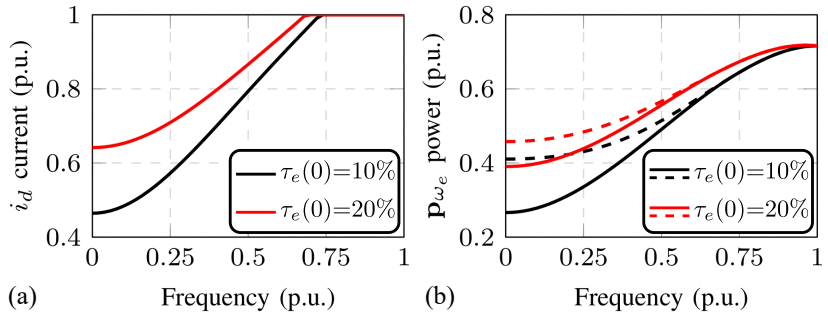

Figure 3.3: MMC variables as a function of the electrical frequency and torque loads (a): Optimal d-axis current. (b): Amplitude of the vector $\mathbf{p}_{\omega_e}$ (solid-lines: optimal $|\mathbf{p}_{\omega_e}|$, dashed-lines: nominal $|\mathbf{p}_{\omega_e}|$).

the voltage threshold defined by $|\tilde{v}_{Cx}^{X*}|$. This is illustrated in Fig. 3.2, where an example total cluster voltage is shown, considering that a non-zero $|\tilde{v}_{Cx}^{X*}|$ is regulated by the control system (see the black line). The expected voltage fluctuation in the cluster when no mitigating variables are used is also shown in Fig. 3.2, illustrating clearly the need for mitigation.

3.3.3 Flux-weakening operation of the MMC-based drive

Another option to reduce the amplitude of the circulating currents is to minimise $|\mathbf{p}_{\omega_e}|$ [see (3.17)]. Notice that $\mathbf{p}_{\omega_e}$ can be represented as a function of E and $\mathbf{i}_{dq}$ (i.e. $\mathbf{p}_{\omega_e}$=$\mathbf{p}_{\omega_e}(E, i_d, i_q)$) using the machine model (including saturation effects) and the power balance between the input and output converter ports. Therefore, if the dc port voltage is considered constant and the torque current i_q is defined by the speed control system, it is possible to define the following constrained optimisation problem to minimise $|\mathbf{p}_{\omega_e}|$ varying the flux current i_d:

$$\min_{i_d} |\mathbf{p}_{\omega_e}(E, i_d, i_q)| \text{ s.t. } \begin{cases} p\frac{L_m^2}{L_r} i_d i_q = \tau_e(\omega_e), \\ \sqrt{i_d^2 + i_q^2} < i_{\max} \end{cases} \tag{3.20}$$

where p is the number of pole-pairs, L_m and L_r are the magnetising and rotor inductances respectively (which are not constant due to flux-weakening) and $i_{\max}$ is the maximum machine current. Two constraints have been defined in (3.20) to obtain the required electrical torque in the machine, $\tau_e(\omega_e)$, while keeping the stator current magnitude below $i_{\max}$.

Fig. 3.3(a) shows the optimal values of i_d obtained when the parameters of the MMC-based drive utilised in this work are used to solve the optimisation problem of (3.20), showing that the magnitude of $\mathbf{p}_{\omega_e}$ is reduced (particularly for low ω_e values) when flux weakening operation is applied. To obtain this figure, the electrical torque chracteristic was defined as:

$$\tau_e(\omega_{e(\text{p.u.})}) = \tau_e(0) + [1 - \tau_e(0)]\, \omega_{e(\text{p.u.})}^2 \tag{3.21}$$

where $\omega_{e(\text{p.u.})} \leq 1$ is the per unit machine frequency and $\tau_e(0) < 1$ is the initial torque load.

A comparison of the magnitude of $\mathbf{p}_{\omega_e}$ when the optimal (solid-lines) and nominal (dashed-lines) values of i_d are used is depicted in Fig. 3.3(b). As shown in this graphic, the flux

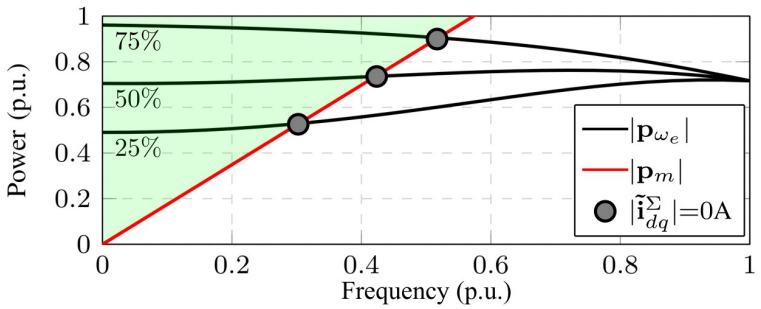

Figure 3.4: $|\mathbf{p}_{\omega_e}|$ and $|\mathbf{p}_m|$ as a function of the MMC operating point.

weakening operation at the machine start-up is an attractive option for mechanical loads requiring low torques at low rotational speeds [e.g. see the variation in $\mathbf{p}_{\omega_e}$ for $\tau_e(0)$=10% in Fig. 3.3(b)], such as blowers, fans, pumps and wind energy conversion systems. A discussion of some issues related to the implementation of vector control strategies for cage induction machines in flux weakening operation, e.g the variation of the machine inductances due to saturation effects, are presented in [21].

3.3.4 Transition between operating modes

The transition between the low- and high-frequency modes when the proposed strategies are used can be explained using Fig. 3.4. In the figure, the magnitude of $\mathbf{p}_{\omega_e}$ and $\mathbf{p}_m$ is depicted when a drive is feeding a machine such as that used in Section 3.5 (Experimental Results) for three different values of $\tau_e(0)$ [see (3.21)]. As the figure shows, the LFM has to be enabled when $|\mathbf{p}_{\omega_e}|>|\mathbf{p}_m|$ (see the green area of Fig. 3.4) since the power $\mathbf{p}_c$ is required to regulate the voltage fluctuations of the total cluster voltages within the threshold defined by $|\tilde{v}_{Cx}^{X*}|$ [see (3.12)]. However, when $|\mathbf{p}_{\omega_e}|\leq|\mathbf{p}_m|$ the mitigating variables are no longer required because the tendency of the total capacitor voltage fluctuation is to decrease as ω_e increases [see (3.12) and (3.8a)] and the HFM is then enabled. During the HFM, $\mathbf{p}_c$=$2v_0\tilde{\mathbf{i}}_{dq}^{\Sigma}$ is used only to ensure a zero-mean value in the voltages $v_{C\alpha}^{\Delta}$ and $v_{C\beta}^{\Delta}$. Therefore, v_0 can be defined to reduce the peak value of the output cluster voltage by injecting a third harmonic voltage, while the circulating currents have a component in-phase with v_0 (further details are in [14, 16]). In a practical implementation, the comparison between $|\mathbf{p}_{\omega_e}|$ and $|\mathbf{p}_m|$ can be performed by using software implemented switches, adding a small hysteresis band to avoid shattering between transitions. Finally, notice that the operating region of the LFM can be manipulated by varying the slope of $|\mathbf{p}_m|$ (e.g. by choosing $|\tilde{v}_{Cx}^{X*}|$ or C) and it is also affected by the machine torque, demonstrating the importance to consider more information other than only the frequency ω_e in the selection of the converter mode.

3.4 Proposed control systems

In this Section the control systems required to operate the MMC-based drive are presented and discussed. They are based on a cascaded structure, where the outer control loops regulate

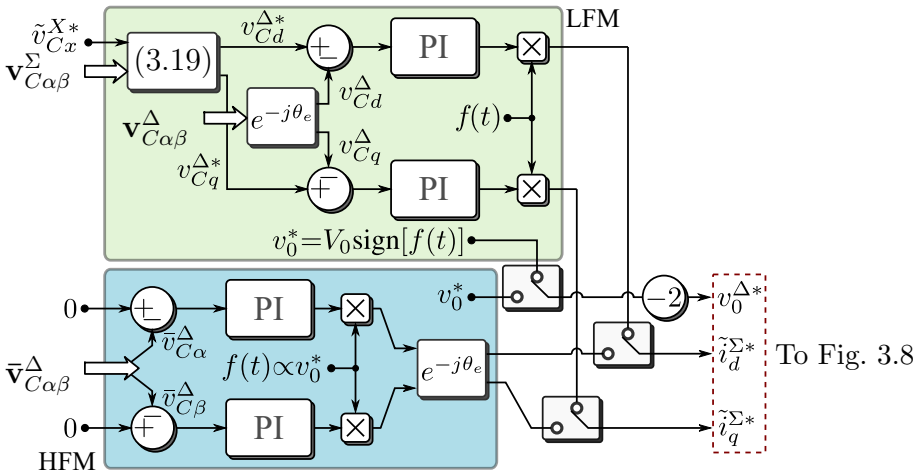

Figure 3.5: Control of the vector $\mathbf{v}^{\Delta}_{C\alpha\beta}$

the $\Sigma\Delta\alpha\beta 0$ capacitor voltages defined in (3.6). Meanwhile, the inner controllers regulate the cluster currents by manipulating the output cluster voltages $\mathbf{V}^{PN}_{abc}$ [see (3.5)].

3.4.1 Vector control of $\mathbf{v}^{\Delta}_{C\alpha\beta}$

The control system utilised to regulate the vector $\mathbf{v}^{\Delta}_{C\alpha\beta}$ is shown in Fig. 3.5 (further details are discussed in [16]). In both operating modes (LFM and HFM) $\mathbf{v}^{\Delta}_{C\alpha\beta}$ is regulated by manipulating the power fluctuation $\mathbf{p}_c{=}2\tilde{\mathbf{i}}^{\Sigma}_{dq}\tilde{v}_0$.

During the LFM (see the green area of Fig 3.5), $\mathbf{v}^{\Delta}_{Cdq}$ is regulated with zero steady-state error using two PI controllers, whose outputs are multiplied by the function $f(t)$ to create the desired ac component of the circulating currents in dq-coordinates. One of the most important contributions and differences of this work when compared with the most recent approaches reported in the literature [16], is that the set-point value of the voltage vector $\mathbf{v}^{\Delta}_{Cdq}$, $\mathbf{v}^{\Delta *}_{Cdq}{=}v^{\Delta *}_{Cd}{+}jv^{\Delta *}_{Cq}$ is a non-zero vector. Moreover using the value of $\mathbf{v}^{\Delta *}_{Cdq}$ calculated from (3.19), it is ensured that the fluctuations of the total cluster voltages are maintained inside the band defined by $\tilde{v}^{X*}_{Cx}$ (see Section 3.3.2). Additionally, a reduction in the magnitude of the circulating currents, as the machine frequency increases, is also achieved. It is not possible to obtain this reduction when a null vector $\mathbf{v}^{\Delta *}_{Cdq}$ is applied to the control system.

The control system depicted in the light-blue area of Fig. 3.5 is used to regulate $\mathbf{v}^{\Delta}_{C\alpha\beta}$ in the HFM. This is achieved by regulating its average value, $\bar{\mathbf{v}}^{\Delta}_{C\alpha\beta}$ (which is obtained by applying filters to $\mathbf{v}^{\Delta}_{C\alpha\beta}$) to zero. A dq-synchronous frame transformation is then used at the output of the control system to generate the desired values of the ac circulating currents.

Notice that $v_0^*{=}{-}\frac{1}{2}v_0^{\Delta}$ [see (3.5)] and $f(t)$ have different design methodologies in each mode [14, 16]. For the LFM, v_0^* and $f(t)$ are defined as high frequency signals with the magnitude of v_0^* as high as possible to reduce the circulating currents [see (3.13)]. Meanwhile, in the HFM they can be configured to inject third harmonic components in the modulation stage, maximising the modulation index [14]. The tuning of the PI parameters is robust

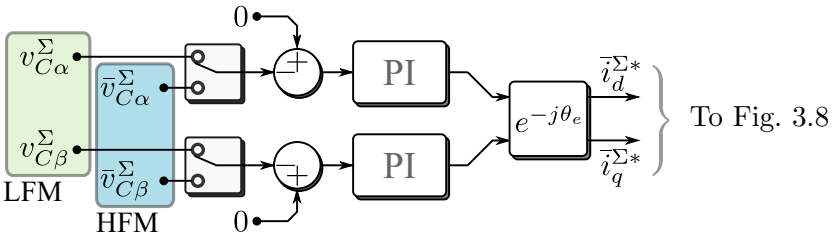

Figure 3.6: Control of the vector $\mathbf{v}_{C\alpha\beta}^{\Sigma}$

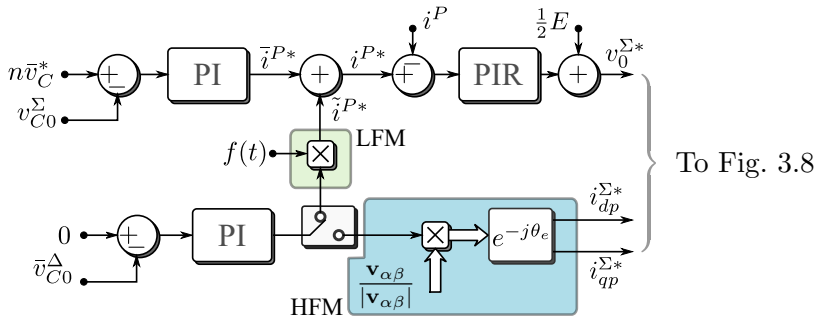

Figure 3.7: Control of the voltages v_{C0}^{Σ} and v_{C0}^{Δ}

against variations in the induction machine load, because the manipulated power $\mathbf{p}_c$ is not affected much by the loading conditions [see (3.12)]. This is further corroborated by the experimental results discussed in Section 3.5.2.

An additional difference to recent approaches reported in the literature [14, 16, 22], is that the proposed control system uses software-implemented switches to achieve a fast transition between the operating modes, avoiding the use of weighting factors to change the control system from the low-frequency to the high-frequency modes. In this work a seamless transition is possible because the circulating currents become null at the end of the LFM (see Fig. 3.4). This is certainly an advantage over previous works (see [14, 16, 22]), where a transition zone with relatively large circulating currents is typically produced, degrading the converter efficiency.

3.4.2 Control of the vector $\mathbf{v}_{C\alpha\beta}^{\Sigma}$

The regulation of $\mathbf{v}_{C\alpha\beta}^{\Sigma}$ is realised by adding a dc component in the circulating currents to create a manipulable power with the dc port voltage E [see (3.7a)]. As shown in the green area of Fig. 3.6, two PI controllers are required to generate this dc circulating current in the LFM. In this mode the vector $\mathbf{v}_{C\alpha\beta}^{\Sigma}$ is directly regulated. However, when the switches enable the HFM (see the light-blue area of Fig. 3.6) only the low-frequency components of $\mathbf{v}_{C\alpha\beta}^{\Sigma}$ ($\bar{\mathbf{v}}_{C\alpha\beta}^{\Sigma}$) are regulated avoiding the presence of circulating currents in steady-state.

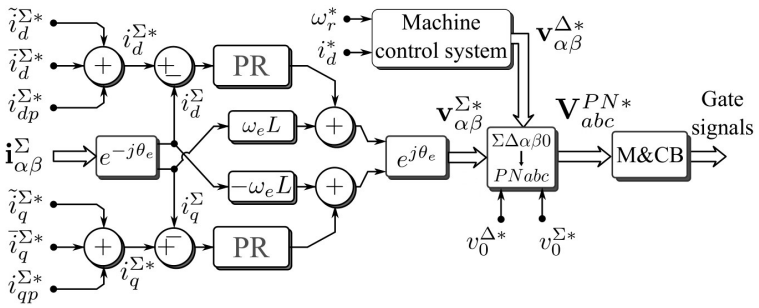

Figure 3.8: Circulating current controller and gate signal generation

3.4.3 Control of the voltages v_{C0}^{Σ} and v_{C0}^{Δ}

The voltage v_{C0}^{Σ} is regulated by using a dc component in i^P, as shown at the top of Fig. 3.7 [see (3.7c)]. The voltage v_{C0}^{Δ} [see (3.7d)] can be regulated using: 1) an ac component in i^P which produces a non-zero mean power with the common-mode voltage (i.e. a proportional-integral-resonant (PIR) controller could be required) or 2) a component of the circulating currents in phase with the machine back-emf [see (3.7d)]. Considering that during the LFM the common-mode voltage is high, the first option is used in this mode (see the green area of Fig. 3.7). The second option is utilised during the HFM considering that the back-emf is high enough in this operating mode (see the light-blue area of Fig. 3.7).

3.4.4 Circulating current controller and signal generator

In the LFM, the dq-circulating currents have the same frequency components as $f(t)$ [see (3.13)]. Hence, proportional-resonant controllers (PR) are appropriate to regulate them, as shown in the control diagram of Fig. 3.8, which is based on (3.5). Moreover, the proportional part of the controllers can regulate other components in $\mathbf{i}_{dq}^{\Sigma}$, even in the HFM [22]. At the output of the controller, the inverse dq- and $\Sigma\Delta\alpha\beta 0$-transformations are applied to the desired output cluster voltages in $\Sigma\Delta\alpha\beta 0$-coordinates to obtain $\mathbf{V}_{abc}^{PN*}$. This matrix is then processed by the modulator and cell balancing algorithm (M&CB block in Fig. 3.8) to determinate the transistor gate signals. In this work, the cell balancing algorithm presented in [22] and the machine control system discussed in [23] are used.

3.5 Experimental results

Experimental results for the proposed control methodology have been obtained using an 18-power cell MMC-based drive. A photograph of the system is presented in Fig. 3.9, while its parameters are given in Table 3.1. The MMC drives a 7.5kW vector-controlled induction machine (see Table 3.2) connected to a Permanent Magnet Generator (PMG). A resistor bank has been connected to the PMG output to provide an electrical load. Hall effect transducers are used to measure the dc port voltage, the capacitor voltages and the cluster currents. A position encoder of 10000 pulses per revolution is affixed to the induction machine. The

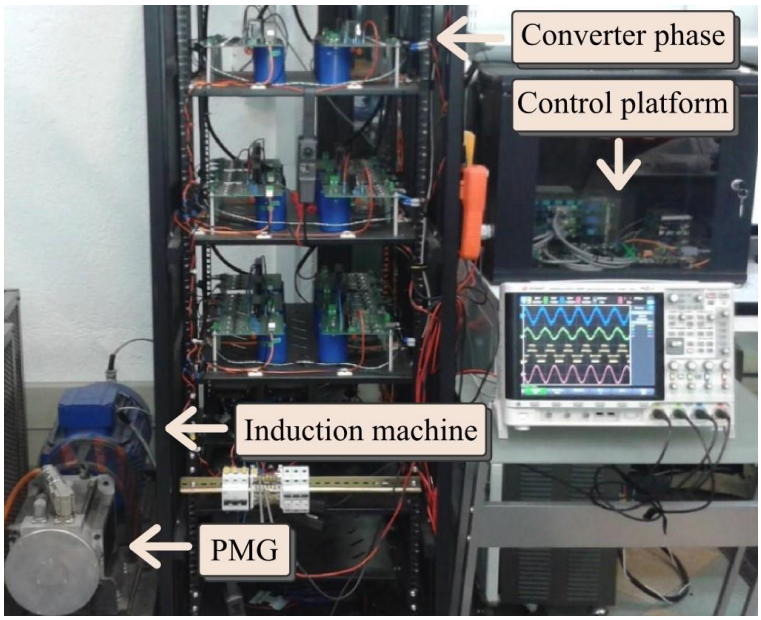

Figure 3.9: Photograph of the laboratory experimental system.

Table 3.1: Set-up parameters for the 18 cells MMC-drive

Parameter	Symbol	Value	Unit
dc-port voltage	E	450	V
Cluster inductor	L	2,5	mH
Cell capacitor	C	4700	μF
Cell dc voltage	$\bar{v}_C^*$	150	V
Cell count per cluster	n	3	–
Carrier frequency	f_s	5000	Hz

system is controlled using a Digital Signal Processor Texas Instrument TMS320C6713 board and 2 Actel ProAsic3 FPGA boards, equipped with a total of 40 14-bit analogue-digital channels. A phase-shifted PWM algorithm generates the 18 switching signals timed via an FPGA platform. Optical fibre connections transmit the switching signals to the gate drivers of the MOSFET switches (model IRFP4868PbF, nominal ratings of 70A, 300V, 32 mΩ on resistance).

3.5.1 Performance for constant speed operation

The performance of the control system has been tested considering fixed rotational speed operation at ω_r=600rpm (i.e. $\omega_e \approx 2\pi 10 \text{rad}\cdot\text{s}^{-1}$). For this experimental test the machine is loaded with a constant torque and the control system is regulating a voltage threshold of $|\tilde{v}_{Cx}^{X*}| \approx 0$V between t=0s to $t \approx 2.5$s (see Fig. 3.10). For $t > 2.5$s to $t \approx 7.5$s, the voltage threshold is changed linearly from 0V to 25V.

As depicted in Fig. 3.10(a), the cell voltage has negligible fluctuations for $t < 2.5$s. The

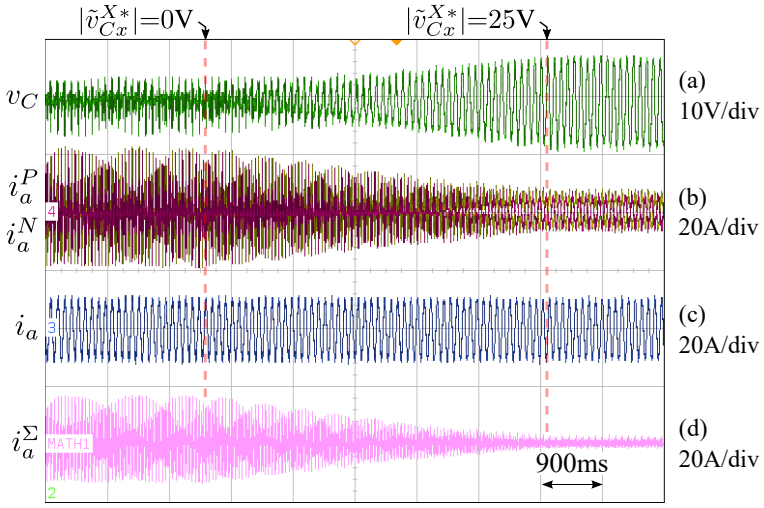

Figure 3.10: MMC variables during constant speed operation. From top to bottom: capacitor voltage v_{Ca1}^P, cluster currents i_a^P and i_a^N, machine current i_a, phase circulating current $i_a^\Sigma = \frac{1}{2}\left(i_a^P + i_a^N\right)$.

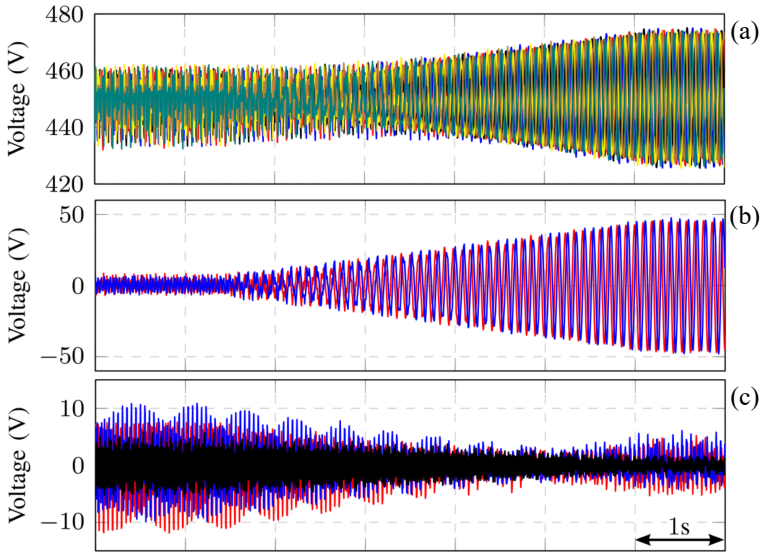

Figure 3.11: Total cluster voltages as a function of $|\tilde{v}_{Cx}^{X*}|$ for a constant speed operation. (a): elements of $\mathbf{V}_{Cabc}^{PN}$, total cluster voltages in $\Sigma\Delta\alpha\beta 0$-coordinates: (b): $v_{C\alpha}^\Delta$ and $v_{C\beta}^\Delta$, (c): $v_{C\alpha}^\Sigma$, $v_{C\beta}^\Sigma$ and v_{C0}^Δ (black signal).

Table 3.2: Nominal induction machine parameters

Parameter	Value	Unit
Rated output power	7.5	kW
Rated rotating speed	3800	rpm
line-to-line rms voltage	380	V
Stator rms current	15	A
i_d Magnetising current	7	A
Pole number	4	–
Rotor resistance	0.724	Ω
Stator resistance	0.660	Ω
Stator inductance	0.141	mH
Rotor inductance	0.141	mH
Mutual inductance	0.138	mH

corresponding cluster currents are shown in Fig. 3.10(b). Notice that the peak-to-peak value of these currents is reduced from approximately 40A to 11A, meanwhile the machine stator current is maintained constant [see Fig. 3.10(c)]. Finally the circulating currents are shown in Fig. 3.10(d). Notice that i_a^{Σ}≈0A at the end of this test, showing the importance of regulating $|\tilde{v}_{Cx}^{X*}|$ to a non-zero value to reduce the currents of the MMC-based drive during LFM.

Other variables, corresponding to the experimental tests depicted in Fig. 3.10, have been captured using the DSP control platform. In Fig. 3.11(a) the total cluster voltages are shown. These are well regulated with fluctuations which are inside the $|\tilde{v}_{Cx}^{X*}|$ threshold. As discussed before, to perform this regulation, the reference value $\mathbf{v}_{Cdq}^{\Delta*}$ has to be calculated on-line and used as the input of the control system depicted in Fig. 3.5. The corresponding amplitudes $v_{C\alpha}^{\Delta}$ and $v_{C\beta}^{\Delta}$ are shown in Fig. 3.11(b). Their peak-to-peak amplitudes are approximately twice the value of $|\tilde{v}_{Cx}^{X*}|$ [see (3.18)]. Finally, the consequences of the high circulating currents, produced when $|\tilde{v}_{Cx}^{X*}|$ is low, are illustrated in Fig. 3.11(c). Notice that the fluctuations in the voltages $v_{C\alpha}^{\Sigma}$, $v_{C\beta}^{\Sigma}$ and v_{C0}^{Δ} become dominant when compared to those obtained in Fig. 3.11(b). This is due to the terms $E\mathbf{i}_{\alpha\beta}^{\Sigma}$ and $\mathbf{v}_{\alpha\beta}(\mathbf{i}_{\alpha\beta}^{\Sigma})^c$ in (3.7a) and (3.7d). When the voltage threshold $|\tilde{v}_{Cx}^{X*}|$ is increased, these oscillations are also reduced.

3.5.2 System performance for different loading conditions

The robustness of the proposed control methodology has been experimentally validated considering different loading conditions. Three experimental tests are shown in Fig. 3.12. These graphics depict, from top to bottom, the induction machine stator currents, the total cluster voltages and the circulating currents, corresponding to a ramp speed variation from 0 to 1200rpm in 6s. The electrical frequency applied to the stator of the induction machine is shown in Fig. 3.13.

To achieve different load conditions, the resistor bank connected to the PMG (see Fig. 3.9) has been adjusted to produce three different i_q values in steady-state operation, as depicted in Fig. 3.12(a)-Fig. 3.12(c). Notice that the peak stator current in Fig. 3.12(a) is ≈ 12A,

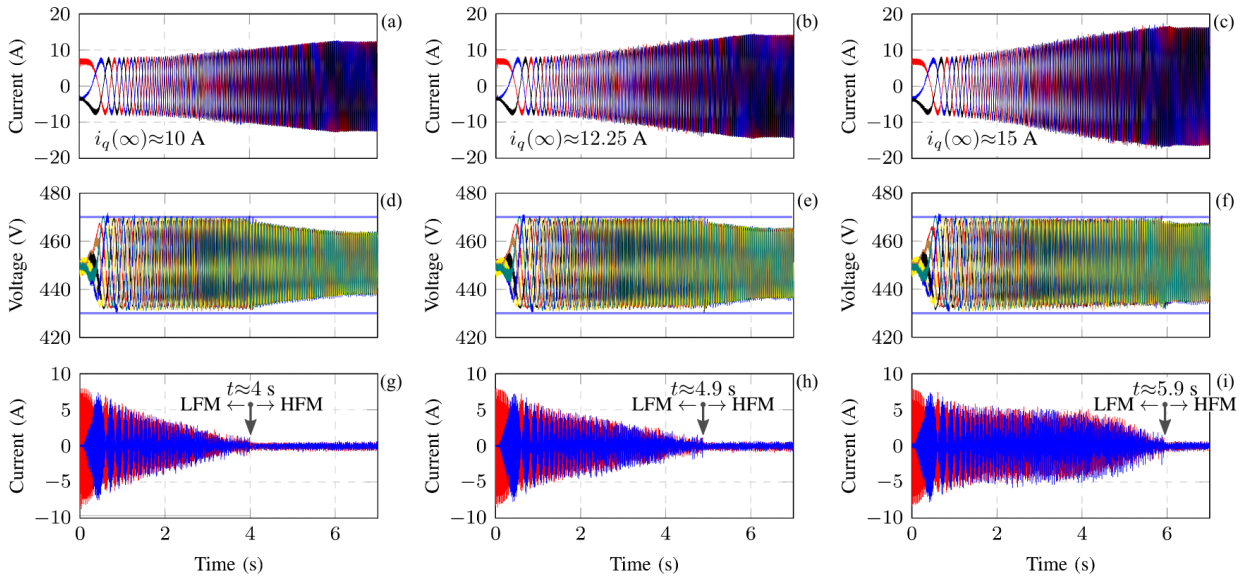

Figure 3.12: Dynamic performance of the proposed control strategy for different loading conditions. Left: low-load, centre: medium-load, right: maximum-load. (a)-(c): Machine currents i_a, i_b, i_c. (d)-(f): Total cluster voltages v_{Ca}^{P}, v_{Ca}^{N}, etc. (g)-(i): Circulating currents i_{α}^{Σ}, i_{β}^{Σ}.

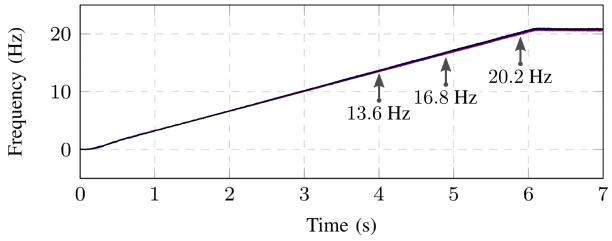

Figure 3.13: Electrical machine frequency for different loading conditions. The transition frequencies are indicated in the figure.

increased by 20% for the experimental test shown in Fig. 3.12(b) and by ≈ 35% for the experimental test shown in Fig. 3.12(c)

The regulation of the total cluster voltage fluctuations during LFM is demonstrated by the results shown in Fig. 3.12(d)-Fig. 3.12(f). As expected, the voltages are well regulated and maintained inside the desired voltage band defined by $\tilde{v}_{Cx}^{X*}$=20V for the three tests (see the blue lines in the corresponding figures). The circulating current required for each of the experimental tests are shown in Fig. 3.12(g)-Fig. 3.12(i). As discussed in Section 3.3.4, the zone where the LFM is applied is dependent on the loading condition (see Fig. 3.4), therefore the transition between LFM and HFM is produced at 4s when operating at low load, up to 5.9s for maximum-load operation; however, notice that in all cases the proposed control strategy ensured low circulating currents in the transition point.

The machine frequency for each of the tests is shown in Fig.3.13. Although the frequencies are practically overlapped, it can be concluded that the transition frequency is automatically modified by the proposed control system to maintain good regulation of the total cluster voltage fluctuations. This transition frequency varies from 13.6 Hz to 20.2 Hz depending

on the machine load [compare Fig. 3.13 with Fig. 3.12(g)-Fig. 3.12(i)]. This experimental result demonstrates the importance of considering more information than that provided by the machine operating frequency alone to change from LFM to HFM. Notice that the use of only the machine operating frequency to switch from LFM to HFM is the conventional approach reported in previous works (see [14, 16, 17]).

3.5.3 Dynamic performance of the proposed control scheme

The proposed control methodology has been validated in the whole frequency (ω_e) range, including zero crossing. Two different operating conditions are considered: nominal flux and flux weakening operation. For both cases, the experimental tests are realised using the same speed profile and mechanical load. In all the figures, the operating range of the LFM is depicted using a green background colour and the voltage threshold, $|\tilde{v}_{Cx}^{X*}|$, is shown using two blue lines. $|\tilde{v}_{Cx}^{X*}|$ has been defined as ≈ 3 times the peak value of the total cluster voltage fluctuation at full load ($\approx 5\%$ of $\bar{v}_C^*$). With this criterion, the LFM was applied over 33% of the frequency range [see Fig. 3.4].

Nominal flux operation

The rotational speed and the d-axis current obtained in this test are shown in Fig. 3.14(a) and 3.14(b), respectively. The speed is changed from ω_r=0rpm to ω_r=2000rpm and then reversed to $\omega_r = -2000$rpm at $t \approx$13s. Although the LFM algorithm considers the fluctuations in the total cluster voltages to calculate $\mathbf{v}_{Cdq}^{\Delta*}$, the individual cell capacitor voltages are well regulated. This is shown in Fig. 3.14(c). Each capacitor voltage is inside the threshold $|\tilde{v}_{Cx}^{X*}|/n$ over the whole frequency range. As discussed in Section 3.3.2, the circulating currents [see Fig. 3.14(f)] decrease as the magnitude of the machine frequency increases, allowing a fast and seamless transition between the operating modes. In fact, the maximum value of $\mathbf{i}_{\alpha\beta}^{\Sigma}$ occurs when $\omega_e \approx 0\text{rad}\cdot\text{s}^{-1}$, because the influence of the vector $\mathbf{p}_m$ is negligible at this point [see (3.12)]. Due to this feature, the clusters can be designed considering the machine nominal current, since the peak value of the cluster currents is obtained at full load, as depicted in Fig. 3.14(d) and 3.14(e).

Flux-weakening operation

In Fig. 3.15 experimental results considering flux-weakening operation are shown. For this test, the same speed and load profile, used to obtain the experimental results shown in Fig. 3.14, are considered. The resulting d-axis current, is depicted in Fig. 3.15(a). Unlike conventional flux-weakening algorithms, in the proposed control system the flux is reduced in the low speed region. Fig. 3.15(b) shows the corresponding regulation of the capacitor voltages which are maintained inside the predefined threshold during the whole operating range. Moreover, the transition between modes is again seamless and achieved with fast dynamics. The main advantage of the proposed flux-weakening algorithm is that the circulating currents are reduced (during LFM operation) by about 50% when the experimental results shown in

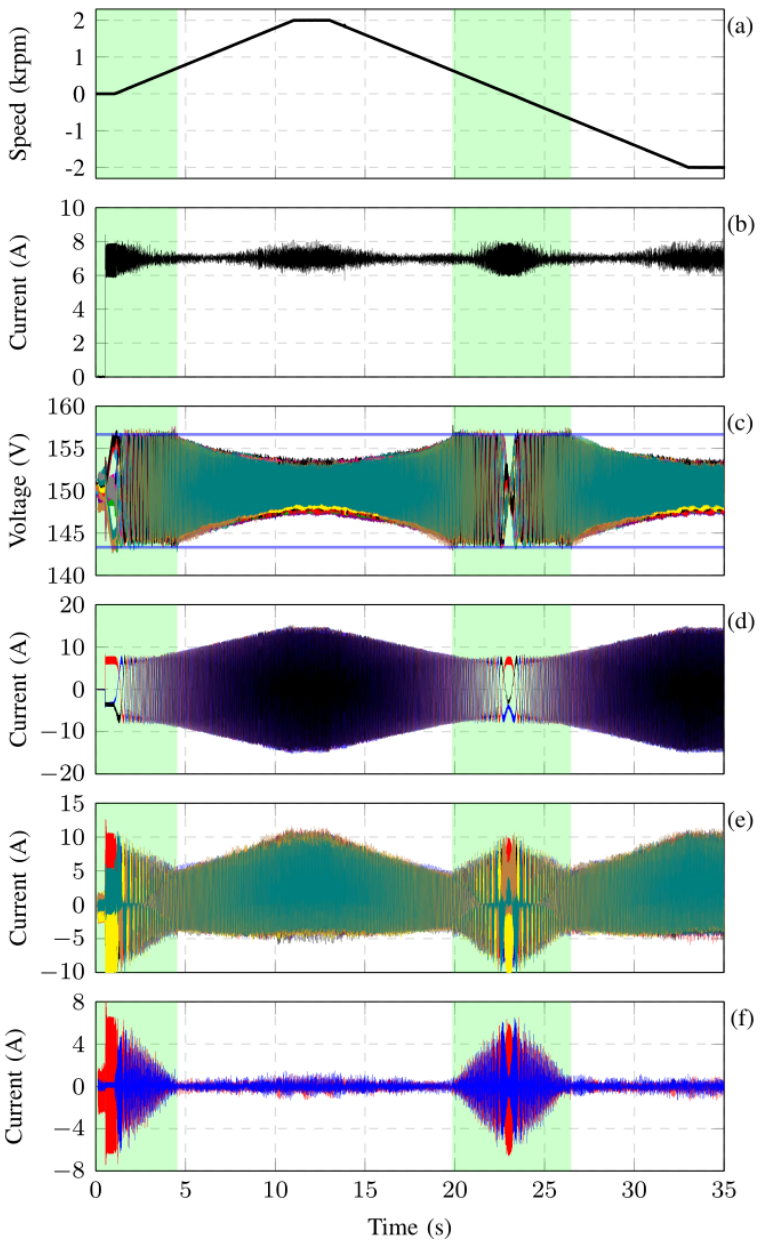

Figure 3.14: Experimental results for nominal flux. (a): machine speed ω_r, (b): d-axis current i_d, (c): capacitor voltages v^P_{Ca1}, v^P_{Ca2}, etc. (the blue lines represent $|\tilde{v}^{X*}_{Cx}|/n$), (d): machine currents i_a, i_b and i_c, (e): cluster currents i^P_a, i^N_a, etc, (f): circulating currents i^Σ_α and i^Σ_β.

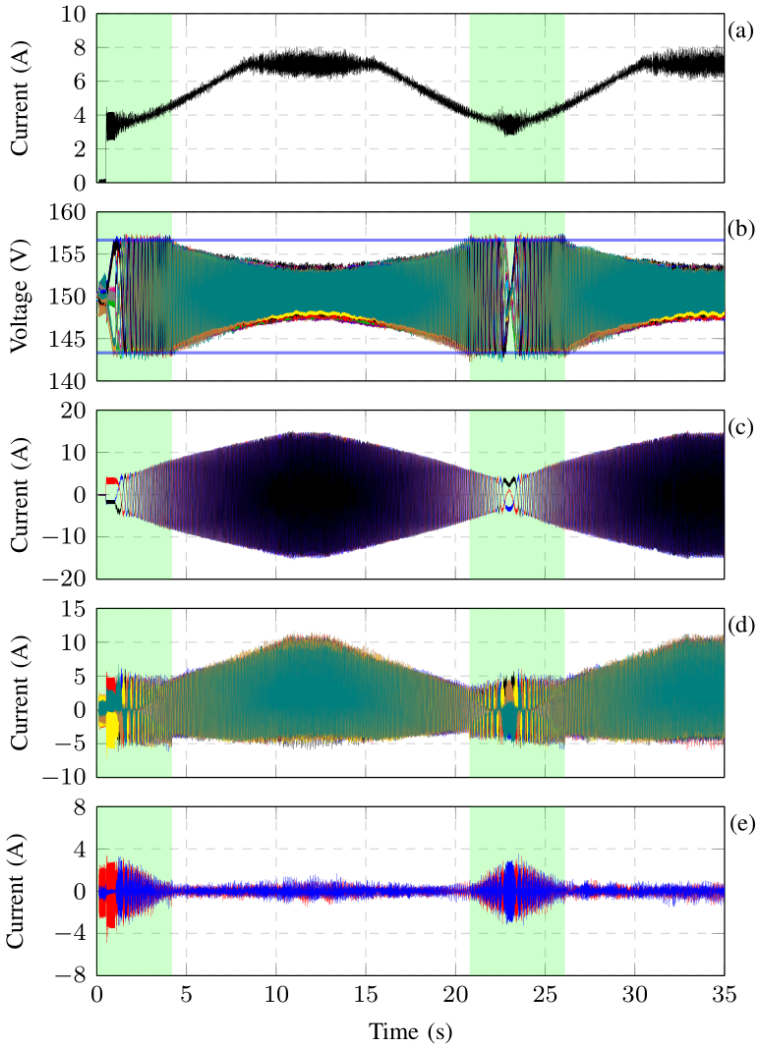

Figure 3.15: Experimental results during flux-weakening operation. (a): d-axis current i_d, (b): capacitor voltages v^P_{Ca1}, v^P_{Ca2}, etc. (the blue lines represent $|\tilde{v}^{X*}_{Cx}|/n$), (c): machine currents i_a, i_b and i_c, (d): cluster currents i^P_a, i^N_a, etc, (e): circulating currents i^Σ_α and i^Σ_β.

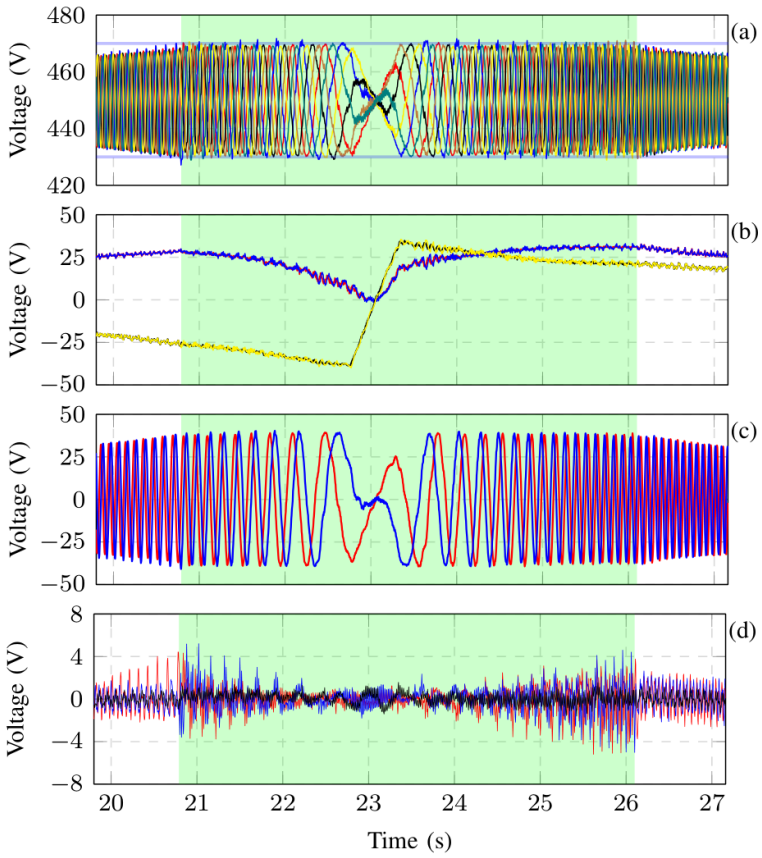

Figure 3.16: Controlled variables during flux-weakening operation. (a): total cluster voltages ($PNabc$-coordinates), total cluster voltages ($\Sigma\Delta\alpha\beta 0$-coordinates) (b): v_{Cd}^{Δ} (red), $v_{Cd}^{\Delta *}$ (blue), v_{Cq}^{Δ} (black) and $v_{Cq}^{\Delta *}$ (yellow), (c): $v_{C\alpha}^{\Delta}$ and $v_{C\beta}^{\Delta}$, (d): $v_{C\alpha}^{\Sigma}$ (red), $v_{C\beta}^{\Sigma}$ (blue) and v_{C0}^{Δ} (black).

Fig. 3.15(e) are compared with those of Fig. 3.14(f). This reduction affects the cluster currents as shown in Fig. 3.15(d). Therefore, the losses in an MMC-based drive could be reduced if flux weakening operation is feasible, such as for quadratic torque-speed profiles. Moreover, the range where the LFM is active has been reduced by 20% (from $\Delta t{\approx}6.62$s to $\Delta t{\approx}5.33$s), implying that a more efficient use of the common-mode voltage v_0 and circulating current $\mathbf{i}_{\alpha\beta}^{\Sigma}$ is achieved during the speed profile shown in Fig. 3.14(a).

In Fig. 3.16, additional results for flux-weakening operation are shown. These correspond to an amplified view of some variables during zero-crossing of the speed (close to t=23s in Fig. 3.15). The total cluster voltages are shown in Fig. 3.16(a). Notice that the voltages are inside the predefined threshold, even during the transition between modes. The regulation of $\mathbf{v}_{Cdq}^{\Delta}$ is shown in Fig. 3.16(b). It is performed with an excellent dynamic response and good tracking of the set-point value $\mathbf{v}_{Cdq}^{\Delta *}$, which has been linearly reduced close to ω_e=0rad·s^{-1} to avoid chattering at low speeds [see (3.19)]. This is not a drawback of the proposed methodology since the influence of $\mathbf{p}_m$ is reduced at $\omega_e{\approx}$0rad·s^{-1}. Finally, as discussed in Section 3.3.2, the fluctuations in the total cluster voltages are dominated by $\mathbf{v}_{C\alpha\beta}^{\Delta}$ [see Fig. 3.16(c)]. The fluctuations in the other $\Sigma\Delta\alpha\beta 0$-voltages are small and are well regulated, as shown in Fig. 3.16(d).

3.6 Conclusions

This paper has demonstrated that a holistic control system design approach, considering the dynamics of the converter and cage induction machine is advantageous to enhance the performance and design of MMC-based drives. Flux weakening operation and the proposed control system to maintain the capacitor voltages inside a predefined threshold, are beneficial as demonstrated in this work. Furthermore, the proposed control scheme allows a seamless transition between the drive operating modes. One of the possible disadvantages of the proposed methodology is higher complexity which is translated into a higher computational burden. For instance, for flux weakening operation the variations in the magnetising inductance and rotor time constant of the induction machine have to be calculated off-line and (e.g.) stored in a look up table, in order to maintain proper rotor flux orientation of the indirect rotor-flux vector control system during the whole speed operating range. However even with this additional complexity, the proposed control system is relatively simple to implement in a modern digital signal processor augmented with FPGA platforms.

Extensive experimental results for a lab prototype have been presented in this work. Steady-state and dynamic experiments in both operating modes have been realised and thoroughly discussed. The performance considering ramp variations in the speed, flux-weakening operation, different loading conditions and zero-crossing speed transitions have been experimentally investigated and good performance has been demonstrated. The experimental results have demonstrated the effectiveness of the proposed strategies.

Bibliography

[1] R. Marquardt, "Stromrichterschaltungen mit verteilten energiespeichern," German Patent DE20 122 923 U1, 2001.

[2] M. Glinka and R. Marquardt, "A new AC/AC-multilevel converter family applied to a single-phase converter," in *The Fifth International Conference on Power Electronics and Drive Systems, 2003. PEDS 2003.*, vol. 1, DOI 10.1109/PEDS.2003.1282669, pp. 16–23 Vol.1, Nov. 2003.

[3] M. Saeedifard and R. Iravani, "Dynamic Performance of a Modular Multilevel Back-to-Back HVDC System," *IEEE Trans. Power Del.*, vol. 25, DOI 10.1109/TPWRD.2010.2050787, no. 4, pp. 2903–2912, Oct. 2010.

[4] Siemens. HVDC PLUS-Basics and Principle of Operation. http://www.energy.siemens.com/br/pool/br/transmissao-de-energia/transformadores/hvdc-plus-basics-and-principle-of-operation.pdf. (2013)

[5] S. Debnath, J. Qin, B. Bahrani, M. Saeedifard, and P. Barbosa, "Operation, Control, and Applications of the Modular Multilevel Converter: A Review," *IEEE Trans. Power Electron.*, vol. 30, DOI 10.1109/TPEL.2014.2309937, no. 1, pp. 37–53, Jan. 2015.

[6] Y. Okazaki, W. Kawamura, M. Hagiwara, H. Akagi, T. Ishida, M. Tsukakoshi, and R. Nakamura, "Experimental Comparisons Between Modular Multilevel DSCC Inverters and TSBC Converters for Medium-Voltage Motor Drives," *IEEE Trans. Power Electron.*, vol. PP, DOI 10.1109/TPEL.2016.2562103, no. 99, pp. 1–1, 2016.

[7] K. Ilves, L. Bessegato, and S. Norrga, "Comparison of cascaded multilevel converter topologies for AC/AC conversion," in *Power Electronics Conference (IPEC-Hiroshima 2014 - ECCE-ASIA), 2014 International*, DOI 10.1109/IPEC.2014.6869722, pp. 1087–1094, May. 2014.

[8] M. Hagiwara, K. Nishimura, and H. Akagi, "A Medium-Voltage Motor Drive With a Modular Multilevel PWM Inverter," *IEEE Trans. Power Electron.*, vol. 25, DOI 10.1109/TPEL.2010.2042303, no. 7, pp. 1786–1799, Jul. 2010.

[9] N. Thitichaiworakorn, M. Hagiwara, and H. Akagi, "Experimental Verification of a Modular Multilevel Cascade Inverter Based on Double-Star Bridge Cells," *IEEE Trans. Ind. Appl.*, vol. 50, DOI 10.1109/TIA.2013.2269896, no. 1, pp. 509–519, Jan. 2014.

[10] M. Hagiwara, I. Hasegawa, and H. Akagi, "Start-Up and Low-Speed Operation of an Electric Motor Driven by a Modular Multilevel Cascade Inverter," *IEEE Trans. Ind. Appl.*, vol. 49, DOI 10.1109/TIA.2013.2256331, no. 4, pp. 1556–1565, July-August 2013.

[11] A. J. Korn, M. Winkelnkemper, and P. Steimer, "Low Output Frequency Operation of the Modular Multi-Level Converter," in *Energy Conversion Congress and Exposition (ECCE), 2010 IEEE*, DOI 10.1109/ECCE.2010.5617802. IEEE, 12-16 September 2010.

[12] A. Antonopoulos, L. Ängquist, S. Norrga, K. Ilves, L. Harnefors, and H.-P. Nee, "Modular Multilevel Converter AC Motor Drives With Constant Torque From Zero to Nominal Speed," *IEEE Trans. Ind. Appl.*, vol. 50, DOI 10.1109/TIA.2013.2286217, no. 3, pp. 1982–1993, May. 2014.

[13] A. Antonopoulos, L. Ängquist, L. Harnefors, and H. P. Nee, "Optimal Selection of the Average Capacitor Voltage for Variable-Speed Drives With Modular Multilevel Converters," *IEEE Trans. Power Electron.*, vol. 30, DOI 10.1109/TPEL.2014.2316273, no. 1, pp. 227–234, Jan. 2015.

[14] J. Kolb, F. Kammerer, M. Gommeringer, and M. Braun, "Cascaded Control System of the Modular Multilevel Converter for Feeding Variable-Speed Drives," *IEEE Trans. Power Electron.*, vol. 30, DOI 10.1109/TPEL.2014.2299894, no. 1, pp. 349–357, Jan. 2015.

[15] M. Espinoza, E. Espina, M. Diaz, A. Mora, and R. Cárdenas, "Improved control strategy of the Modular Multilevel Converter for high power drive applications in low frequency operation," in *Power Electronics and Application (EPE), 2016 18th European Conference on*, DOI 10.1109/EPE.2016.7695557, pp. 5–9, Karlsruhe, Germany, Sep. 2016.

[16] M. Espinoza, R. Cárdenas, M. Díaz, and J. C. Clare, "An Enhanced *dq*-Based Vector Control System for Modular Multilevel Converters Feeding Variable-Speed Drives," *IEEE Trans. Ind. Electron.*, vol. 64, DOI 10.1109/TIE.2016.2637894, no. 4, pp. 2620–2630, Apr. 2017.

[17] B. Li, S. Zhou, D. Xu, R. Yang, D. Xu, C. Buccella, and C. Cecati, "An Improved Circulating Current Injection Method for Modular Multilevel Converters in Variable-Speed Drives," *IEEE Trans. Ind. Electron.*, vol. 63, DOI 10.1109/TIE.2016.2547899, no. 11, pp. 7215–7225, Nov. 2016.

[18] D. E. Soto-Sanchez, R. Pena, R. Cardenas, J. Clare, and P. Wheeler, "A Cascade Multilevel Frequency Changing Converter for High-Power Applications," *IEEE Trans. Ind. Electron.*, vol. 60, DOI 10.1109/TIE.2012.2194971, no. 6, pp. 2118–2130, Jun. 2013.

[19] Siemens. SINAMICS SM120 Cabinet Modules. https://www.industry.siemens.com/drives/global/en/converter/mv-drives/Pages/sinamics-sm120-cm.aspx. (2016, July)

[20] B. Li, S. Zhou, D. Xu, D. Xu, and W. Wang, "Comparative study of the sinusoidal-wave and square-wave circulating current injection methods for low-frequency operation of the modular multilevel converters," in *Energy Conversion Congress and Exposition (ECCE), 2015 IEEE*, DOI 10.1109/ECCE.2015.7310324, pp. 4700–4705, Sep. 2015.

[21] R. Cardenas, R. Pena, G. M. Asher, J. Clare, and R. Blasco-Gimenez, "Control strategies for power smoothing using a flywheel driven by a sensorless vector-controlled induction machine operating in a wide speed range," *IEEE Trans. Ind. Electron.*, vol. 51, DOI 10.1109/TIE.2004.825345, no. 3, pp. 603–614, Jun. 2004.

[22] Y. Okazaki, H. Matsui, M. M. Muhoro, M. Hagiwara, and H. Akagi, "Enhancement on capacitor-voltage-balancing capability of a modular multilevel cascade inverter for medium-voltage synchronous-motor drives," in *2015 IEEE Energy Conversion Congress and Exposition (ECCE)*, DOI 10.1109/ECCE.2015.7310550, pp. 6352–6359, Sep. 2015.

[23] M. Espinoza, R. Cárdenas, M. Diaz, A. Mora, and S. D, "Modelling and Control of the Modular Multilevel Converter in Back to Back Configuration for High Power Induction Machine Drives," in *IEEE Industrial Electronics Society (IECON), 2016 42nd Annual Conference of*, DOI 10.1109/IECON.2016.7793979, pp. 24–27, Florence, Italy, Oct. 2016.

Part III

Journal Paper to be Submitted

Chapter 4

Modelling and Control of the MMC-Based Drive with a Time-Variable dc-Port Voltage

This chapter is based on the paper:

M. Espinoza, R. Cardenas, M. Diaz, F. Donoso, and A. Mora. Modelling and Control of the MMC-Based Drive with a Time-Variable dc-Port Voltage. *IEEE Transactions on Power Electronics*, 2019

which is expected to be submitted to IEEE Transactions on Power Electronics (**Q1 journal paper. Impact Factor: 7.151.**)

Abstract: The Modular Multilevel Converter (MMC) is a topology suitable for high-power medium-voltage variable-speed drives. However, the behaviour of this converter is highly affected by the power fluctuations of its modules. This paper analyses the influence of the dc-port voltage on these power fluctuations. It is demonstrated that the manipulation of this voltage offers several advantages for the operation of the drive. For example, it is possible to reduce: the voltage fluctuations in the capacitors, the capacitance of each cell or the application of mitigating variables during low machine speeds. Additionally, a reduction in the required common-mode voltage during low-speed operation is also feasible. The effectiveness of the proposed control schemes is demonstrated through simulation studies and experimental validation tests conducted with an 18-cell-7.5 kW MMC prototype in the whole frequency range.

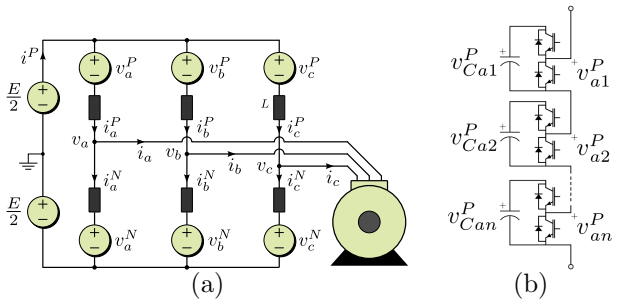

Figure 4.1: MMC-based drive (a): Converter topology. (b): Cluster.

4.1 Introduction

The behaviour of the MMC-based drives is highly affected by the power fluctuations of its clusters. However, the variations of these power fluctuations due to changes in the dc-port voltage, E, have not been analysed extensively due to the most common situation is to work with a constant input voltage, even when a variable voltage can be obtained using active rectifiers [1–4]. This issue has been partially studied in [3–5]. Nonetheless, in most of these works the experimental and simulation results do not included the zero-speed test [3, 4], they are based on open-loop or feed-forward algorithms or there is no discussion regarding the dynamics of the MMC for changes in E [3–5].

In this work, the aforementioned issues are discussed and the MMC response for a varying dc-port voltage is studied. Based on this analysis, the following contributions are given to the state of the art:

1. Three operating schemes are obtained depending on the MMC parameters and applied signals. With them, it is reduced 1) the capacitor voltage fluctuations, 2) the capacitance in each cell, or 3) the duration of the LFM.

2. The proposed control system leads to a reduction of the required common-mode voltage during LFM (i.e. there are mitigated the insulation damage or leakage currents in the machine bearing [6, 7]).

3. A novel model is utilised to analyse the dynamics of the cluster voltages as a function of the dc-port voltage. Consequently, the fluctuations of the cluster voltages are regulated manipulating the dc-port voltage by using a closed loop control system.

Simulations results, as well as an experimental prototype composed of 18 power cells, feeding an induction machine, is used to validate the effectiveness and feasibility of the proposed control strategies.

4.2 Dynamic Modelling and Analysis of the MMC

Representing the output cluster voltages as voltage sources (see Fig. 4.1), the dynamics of the MMC cluster currents are obtained applying the Kirchhoff voltage law as follows:

$$L\frac{d}{dt}\overbrace{\begin{bmatrix} i_a^P & i_b^P & i_c^P \\ i_a^N & i_b^N & i_c^N \end{bmatrix}}^{:=\mathbf{I}_{abc}^{PN}} = -\overbrace{\begin{bmatrix} v_a^P & v_b^P & v_c^P \\ v_a^N & v_b^N & v_c^N \end{bmatrix}}^{:=\mathbf{V}_{abc}^{PN}} - \frac{E}{2}\begin{bmatrix} 1 & 1 & 1 \\ 1 & 1 & 1 \end{bmatrix} + \begin{bmatrix} -v_a & -v_b & -v_c \\ v_a & v_b & v_c \end{bmatrix} \tag{4.1}$$

As is well known, the $\Sigma\Delta\alpha\beta 0$-transformation can be applied to (4.1) to allow a decouple control of the converter currents [8, 9]. Applying this transformation, (4.1) results in:

$$L\frac{d}{dt}\overbrace{\begin{bmatrix} i_\alpha^\Sigma & i_\beta^\Sigma & \frac{1}{3}i^P \\ i_\alpha & i_\beta & 0 \end{bmatrix}}^{:=\mathbf{I}_{\alpha\beta 0}^{\Sigma\Delta}} = -\overbrace{\begin{bmatrix} v_\alpha^\Sigma & v_\beta^\Sigma & v_0^\Sigma \\ v_\alpha^\Delta & v_\beta^\Delta & v_0^\Delta \end{bmatrix}}^{:=\mathbf{V}_{\alpha\beta 0}^{\Sigma\Delta}} - 2\begin{bmatrix} 0 & 0 & -\frac{1}{4}E \\ v_\alpha & v_\beta & v_0 \end{bmatrix} \tag{4.2}$$

where the machine currents (i_α and i_β) and voltages (v_α, v_β and v_0) are expressed in $\alpha\beta 0$-coordinates, i_α^Σ and i_β^Σ are the circulating currents and i^P is the dc-port current.

On the other hand, the relation between the power fluctuations and the addition of the capacitor voltages in a cluster is required to ensure the voltage balancing of the floating capacitors. This relation is given by:

$$C\bar{v}_C\frac{d}{dt}\underbrace{\begin{bmatrix} v_{Ca}^P & v_{Cb}^P & v_{Cc}^P \\ v_{Ca}^N & v_{Cb}^N & v_{Cc}^N \end{bmatrix}}_{:=\mathbf{V}_{Cabc}^{PN}} \approx \underbrace{\begin{bmatrix} p_a^P & p_b^P & p_c^P \\ p_a^N & p_b^N & p_c^N \end{bmatrix}}_{:=\mathbf{P}_{abc}^{PN}=\mathbf{V}_{abc}^{PN}\circ\mathbf{I}_{abc}^{PN}} \tag{4.3}$$

where "$\circ$" denotes the element-by-element multiplication of two matrices and $v_{Ca}^P = \sum_{k=1}^{n} v_{Cak}^P$, etc., are the total cluster voltages. Additionally, it is supposed that the capacitor voltages are maintained around the same value, $\bar{v}_C$, with relatively small ripple. Consequently, applying the $\Sigma\Delta\alpha\beta 0$-transformation to (4.3) yields to:

$$C\bar{v}_C\frac{d}{dt}\underbrace{\begin{bmatrix} v_{C\alpha}^\Sigma & v_{C\beta}^\Sigma & v_{C0}^\Sigma \\ v_{C\alpha}^\Delta & v_{C\beta}^\Delta & v_{C0}^\Delta \end{bmatrix}}_{:=\mathbf{V}_{C\alpha\beta 0}^{\Sigma\Delta}} \approx \underbrace{\begin{bmatrix} p_\alpha^\Sigma & p_\beta^\Sigma & p_0^\Sigma \\ p_\alpha^\Delta & p_\beta^\Delta & p_0^\Delta \end{bmatrix}}_{:=\mathbf{P}_{\alpha\beta 0}^{\Sigma\Delta}} \tag{4.4}$$

However, the vector model of (4.4) results more appropriate for drive applications. Defining the variables as vectors (e.g. $\mathbf{i}_{\alpha\beta}=i_\alpha+ji_\beta$), the vector model of (4.4) results in [9]:

$$C\bar{v}_C\frac{d\mathbf{v}_{C\alpha\beta}^\Sigma}{dt} \approx \frac{1}{2}E\mathbf{i}_{\alpha\beta}^\Sigma - \frac{1}{4}\left(\mathbf{i}_{\alpha\beta}\mathbf{v}_{\alpha\beta}\right)^c - \frac{1}{2}v_0\mathbf{i}_{\alpha\beta} \tag{4.5}$$

$$C\bar{v}_C\frac{d\mathbf{v}_{C\alpha\beta}^\Delta}{dt} \approx \frac{1}{2}E\mathbf{i}_{\alpha\beta} - \frac{2}{3}i^P\mathbf{v}_{\alpha\beta} - \left(\mathbf{v}_{\alpha\beta}\mathbf{i}_{\alpha\beta}^\Sigma\right)^c - 2v_0\mathbf{i}_{\alpha\beta}^\Sigma \tag{4.6}$$

$$C\bar{v}_C\frac{dv_{C0}^\Sigma}{dt} \approx \frac{1}{6}Ei^P - \frac{1}{4}\Re\left[\mathbf{v}_{\alpha\beta}(\mathbf{i}_{\alpha\beta})^c\right] \tag{4.7}$$

$$C\bar{v}_C\frac{dv_{C0}^\Delta}{dt} \approx -\Re\left[\mathbf{v}_{\alpha\beta}(\mathbf{i}_{\alpha\beta}^\Sigma)^c\right] - \frac{2}{3}i^Pv_0 \tag{4.8}$$

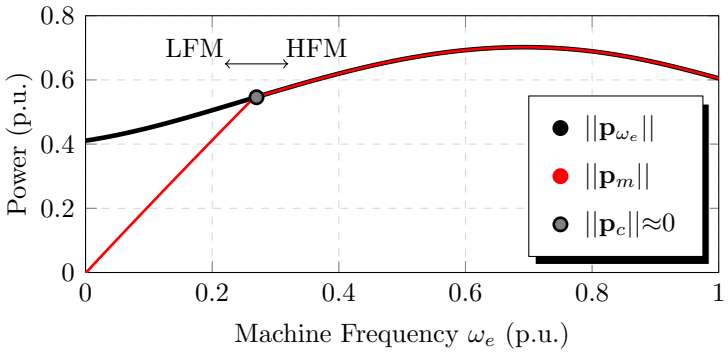

Figure 4.2: $||\mathbf{p}_{\omega_e}||$ and $||\mathbf{p}_m||$ as a function of ω_e for nominal E.

where " ^{c} " represents the complex conjugation operator.

The previous vector representation has several advantages. For example, the regulation of the vector $\mathbf{v}^{\Delta}_{C\alpha\beta}$ can be performed using high dynamic performance vector control systems, which is useful since the amplitude of this vector tends to infinity for low ac-frequencies if no mitigating actions are considered. In this manner, representing (4.6) into a dq-coordinate system rotating at ω_e yields to [9]:

$$C\bar{v}_C \frac{d\mathbf{v}^{\Delta}_{Cdq}}{dt} \approx \underbrace{\tfrac{1}{2}E\mathbf{i}_{dq} - \tfrac{2}{3}i^P\mathbf{v}_{dq}}_{:=\mathbf{p}_{\omega_e}} - \underbrace{jC\bar{v}_C\omega_e\mathbf{v}^{\Delta}_{Cdq}}_{:=\mathbf{p}_m} - \underbrace{2v_0\mathbf{i}^{\Sigma}_{dq}}_{:=\mathbf{p}_c} \tag{4.9}$$

where the term $(\mathbf{v}_{\alpha\beta}\mathbf{i}^{\Sigma}_{\alpha\beta})^c$ in (4.6) has been neglected since it produce low voltage fluctuations in the converter capacitors.

As demonstrated in previous papers, the operating modes of the MMC-based drive are dominated by the power fluctuations defined in (4.9) [10, 11]. Fig. 4.2 depicts the magnitude of the power fluctuations $\mathbf{p}_{\omega_e}$ and $\mathbf{p}_m$ for an MMC driving a machine as the one used in the experimental results of this paper. During LFM, the vector $\mathbf{p}_c$ is required to ensure that the capacitor voltages are within an acceptable value because $||\mathbf{p}_{\omega_e}|| > ||\mathbf{p}_c||$ (the mean value of the three vectors have to add zero to allow a steady-state operation of the MMC). On the other hand, when no mitigation is required, $||\mathbf{p}_c|| \approx 0$ and the converter operates in HFM, producing $||\mathbf{p}_{\omega_e}|| \approx ||\mathbf{p}_c||$.

Additionally, it can be concluded that the fluctuations of the total cluster voltages are mainly affected by the vectors $\mathbf{v}^{\Delta}_{C\alpha\beta}$ and $\mathbf{v}^{\Sigma}_{C\alpha\beta}$. Integrating (4.5)-(4.8) and using the inverse $\Sigma\Delta\alpha\beta 0$-transformation considering that $||\mathbf{v}^{\Delta}_{Cdq}|| = ||\mathbf{v}^{\Delta}_{C\alpha\beta}||$, it is demonstrated that this fluctuation fulfils the following condition [10]:

$$\max[\tilde{v}^X_{Cx}] \leq \tfrac{1}{2}\left\|\mathbf{v}^{\Delta}_{Cdq}\right\| + \left\|\mathbf{v}^{\Sigma}_{C\alpha\beta}\right\| \tag{4.10}$$

where $\tilde{v}^X_{Cx}$ is the oscillating component of the total cluster voltage connected between the points $X = \{P, N\}$ and $x = \{a, b, c\}$ of the MMC shown in Fig. 4.1.

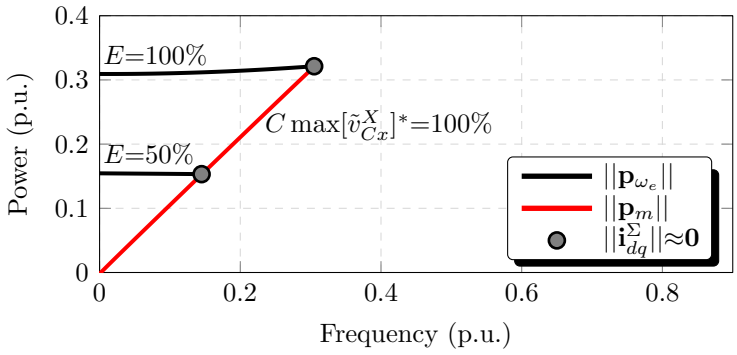

(a) Nominal value of $C\max[\tilde{v}^X_{Cx}]^*$

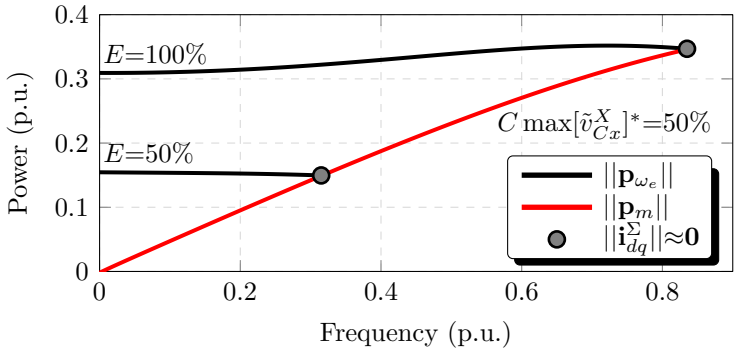

(b) 50% of the nominal value of $C\max[\tilde{v}^X_{Cx}]^*$

Figure 4.3: Influence of the voltage E in LFM

4.3 Effect of the variations of E in the LFM of the MMC-Based Drive

This section analyses the influence of the variations of the dc-port voltage E in the MMC behaviour during LFM. Considering that the power fluctuations $\mathbf{p}_{\omega_e}$ and $\mathbf{p}_m$ are used to perform this analysis, they are simplified as follows:

$$\mathbf{p}_{\omega_e} \approx \frac{1}{2}E\mathbf{i}_{dq} - \Re[\mathbf{v}_{dq}(\mathbf{i}_{dq})^c]\frac{\mathbf{v}_{dq}}{E} \tag{4.11}$$

$$\mathbf{p}_m \approx 2C\bar{v}_C|\omega_e|\left[\max[\tilde{v}^X_{Cx}] - ||\tilde{\mathbf{v}}^{\Sigma}_{C\alpha\beta}||\right]\hat{\mathbf{p}}_{\omega_e} \tag{4.12}$$

where $i^P \approx \frac{3\Re[\mathbf{v}_{dq}(\mathbf{i}_{dq})^c]}{2E}$ (i.e. the converter losses are neglected) and $||\mathbf{v}^{\Delta}_{Cdq}|| \approx 2[\max[\tilde{v}^X_{Cx}] - ||\tilde{\mathbf{v}}^{\Sigma}_{C\alpha\beta}||]$ has been used [see (4.10)]. Additionally, notice that the unitary vector $\hat{\mathbf{p}}_{\omega_e} = \frac{\mathbf{p}_{\omega_e}}{||\mathbf{p}_{\omega_e}||}$ is used in (4.12) to define both, $\mathbf{p}_{\omega_e}$ and $\mathbf{p}_m$, with the same phase-relationship. In this manner, the required mitigating vector $\mathbf{p}_c$ is minimum [see (4.9)].

From (4.11) and (4.12), it is concluded that only the vector $\mathbf{p}_{\omega_e}$ is affected by the voltage E. Based on this fact, three different operating conditions are presented in the following sub-sections. These operating conditions allow a reduction in: 1) the duration of the LFM, 2) the voltage fluctuation in the MMC capacitors or 3) the capacitance of each MMC cell.

4.3.1 Reduction in the duration of the LFM

The first new operating condition is obtained when $||\mathbf{p}_{\omega_e}||$ is modified reducing E but $||\mathbf{p}_m||$ is maintained in its nominal value. To explain this condition, Fig. 4.3(a) shows $||\mathbf{p}_{\omega_e}||$ and $||\mathbf{p}_m||$ as a function of ω_e. The MMC-based drive described in Table 4.2 was used to obtain the figure, and for simplicity, only the LFM is considered (i.e. when $||\mathbf{p}_{\omega_e}||>||\mathbf{p}_m||$). Two values of E are used to calculate $||\mathbf{p}_{\omega_e}||$; E=100% and E=50% of its nominal value. Meanwhile, the nominal cell capacitance and voltage margin are used to calculate $||\mathbf{p}_m||$ (i.e. $C\max[\tilde{v}_{Cx}^X]^*$=100%). Finally, the electrical torque-speed profile is a quadratic-plus-offset profile, defined as:

$$\tau_e(\omega_{e,\text{p.u.}}) = \tau_e(0) + [1 - \tau_e(0)]\,\omega_{e,\text{p.u.}}^2 \tag{4.13}$$

where the starting torque is $\tau_e(0) = 0.2$ p.u. in this case.

Comparing the intersections of $||\mathbf{p}_{\omega_e}||$ and $||\mathbf{p}_m||$ in Fig. 4.3(a), it is concluded that the transition frequency between low- and high-frequency modes decreases from ω_e≈0.30 p.u. to ω_e≈0.15 p.u. when E=50% during all the LFM. Accordingly, the extension of the LFM for E=50% is less than the one obtained for E=100% [see Fig. 4.3(a)]. The reduction of the LFM is a desired goal in Modular Multilevel Converters because: 1) the injection of common-mode voltage might produce insulation damage or leakage currents in the machine bearing [6, 7], and 2) the circulating current can affect the efficiency of the converter [12, 13]. Additionally, notice that a reduction in the LFM leads to an extension of the HFM (e.g., in Fig. 4.3(a) the HFM was extended from 70% to 85% of the total operating range). This extension can be appropriated for high-power applications with low but non-zero speed because the converter could work only in HFM (e.g. wind energy conversion systems).

4.3.2 Effect in the Cell Capacitance or Voltage Fluctuations

The duration of the LFM is not an issue in applications where the drive operates at high speed most of the time, as marine and train applications [14,15]. In these cases, it is proposed to decrease both, E and $||\mathbf{p}_m||$ to provide others advantages in the converter operation. Fig. 4.3(b) shows this possibility presenting the second and the third operating condition when E is modified. In the figure, the values of E=100% and E=50% were also used to calculate $||\mathbf{p}_{\omega_e}||$; nevertheless, in this case the slope of $||\mathbf{p}_m||$ was reduced, affecting the transition points between low- and high-frequency modes. To calculate the slope of $||\mathbf{p}_m||$, it is considered that $\mathbf{v}_{C\alpha\beta}^{\Sigma}$ is low for low- and medium-frequencies, and then $\mathbf{p}_m$ can be approximated as:

$$\mathbf{p}_m \approx 2C\bar{v}_C|\omega_e|\max[\tilde{v}_{Cx}^X]\hat{\mathbf{p}}_{\omega_e} \tag{4.14}$$

Hence, the slope of $||\mathbf{p}_m||$, $\frac{d||\mathbf{p}_m||}{d\omega_e}$, is obtained as follows:

$$\frac{d||\mathbf{p}_m||}{d\omega_e} \approx 2C\bar{v}_C\max[\tilde{v}_{Cx}^X]\text{sign}[\omega_e] \tag{4.15}$$

Therefore, a reduction in $\frac{d||\mathbf{p}_m||}{d\omega_e}$ can be achieved by reducing either C, $\max[\tilde{v}_{Cx}^X]$, or both. To decrease C leads to a reduction in the energy storage requirements in the MMC, which can be associated with smaller capacitors and space savings. This feature is advantageous for applications with constrained space, such as marine and train propulsion systems [16, 17] or off-shore wind energy conversion systems [18, 19]. On the other hand, to reduce $\max[\tilde{v}_{Cx}^X]$ can lead to an increment in the capacitor lifespan related with the reduction of its voltage fluctuations, that is desired for off-shore or mining applications [20, 21]. For example, in the case of Fig. 4.3 and supposing that only one parameter of the expression $C\max[\tilde{v}_{Cx}^X]$ is modified, the expression $C\max[\tilde{v}_{Cx}^X]$=50% means one of these scenarios:

1. The cell capacitance in Fig. 4.3(b) is 50% less than the one required in Fig. 4.3(a); however, the voltage fluctuations in the cell capacitors have the peak value in both cases.

2. In Fig. 4.3(b), the peak value of the voltage fluctuations $\max[\tilde{v}_{Cx}^X]$ is 50% less than the one obtained in Fig. 4.3(a), even when the same cell capacitor is used in both cases.

Comparing Fig. 4.3(a) and Fig. 4.3(b), it is concluded that the same transition frequency is reached for different combinations of $||\mathbf{p}_{\omega_e}||$ and $||\mathbf{p}_m||$. For example, the same transition frequency is achieved for E=100% and $C\max[\tilde{v}_{Cx}^X]^*$=100% in Fig. 4.3(a) and for E=50% and $C\max[\tilde{v}_{Cx}^X]^*$=50% in Fig. 4.3(b). However, not useful scenarios might be obtained for some operating conditions, e.g., a transition frequency of $\omega_e\approx$0.85 p.u. is obtained in Fig. 4.3(b) when E=100% and $C\max[\tilde{v}_{Cx}^X]^*$=50%, which is considered a very large transition frequency.

4.3.3 Influence in the Mitigating Variables During LFM

Based on (4.9), it is concluded that the common-mode voltage and the circulating currents (in dq-coordinates) can be in-phase to manipulate the power $\mathbf{p}_c$, regulating $\mathbf{v}_{Cdq}^{\Delta}$ as required during LFM. To perform this task, fluctuating components with high-frequency are utilised in $\mathbf{i}_{dq}^{\Sigma}$ and v_0 to avoid the generation of any low-frequency power pulsations in (4.5)-(4.8). In steady-state and considering ideal conditions, the set-point values of $\tilde{\mathbf{i}}_{dq}^{\Sigma}$ and $\tilde{v}_0$ are then defined as [10, 11]:

$$\tilde{\mathbf{i}}_{dq}^{\Sigma *} = \frac{1}{2V_0}\left(\mathbf{p}_{\omega_e} - \mathbf{p}_m\right) f(t), \quad \tilde{v}_0^* = V_0\ g(t) \tag{4.16}$$

where the superscript " * " stands for the desired value of a variable, V_0 is the amplitude of the common-mode voltage, the symbol " ˜ " was used to denote the fluctuating behaviour of the variables and the functions $g(t)$ and $f(t)$ are two in-phase high-frequency signals.

Neglecting the inductor voltage drop, the amplitude of the maximum common-mode voltage that can be injected is approximated as [22]:

$$V_0 \approx \frac{1}{2}E - ||\mathbf{v}_{dq}|| \tag{4.17}$$

based on this expression, it is concluded that the maximum value of V_0 is reached at low-frequencies because $||\mathbf{v}_{dq}||\approx\mathbf{0}$, resulting in $\max[V_0]=\frac{1}{2}E$, and then the required common-mode

voltage during LFM decreases with E. As well known, problems such as winding insulation damages, leakage currents in the bearing, etc. are produced by high common-mode voltage in the machines [6,7]. Therefore, low values of E during LFM mitigates these problems because of the reduction in the common-mode voltage.

On the other hand, the maximum value of the circulating currents occurs at the machine start-up if the Margin-based strategies are applied [10, 11, 23]. In this condition, $\mathbf{p}_{\omega_e} \approx \frac{1}{2} E \mathbf{i}_{dq}$ and $\mathbf{p}_m \approx \mathbf{0}$. Therefore, $\mathbf{i}_{dq}^{\Sigma}$ as defined in (4.16) results in:

$$\mathbf{i}_{dq}^{\Sigma}(\omega_e \approx 0) \approx \mathbf{i}_{dq} f(t), \tag{4.18}$$

and then the amplitude of the circulating currents at the machine start-up is not severely affected by E, avoiding a possible over-sizing of the cluster current capability when E is modified, as suggested in this work.

4.4 Effect in the Dynamics of the Voltage Fluctuations During HFM

The previous analysis has demonstrated that to operate the MMC-based drive with a low dc-port voltage is advantageous during LFM. However, the machine voltage increases as the electrical frequency increases and thus the dc-port voltage has to increase as well. For this reason, it is desired to determinate how a change in E modifies the cluster voltages during HFM.

4.4.1 Dynamics of the Non-Fluctuating Components

The non-fluctuating components of the cluster voltages have to be regulated to a null-value to achieve the balancing task of the MMC (except $\bar{v}_{C0}^{\Sigma}$ that has to be regulated to $n\bar{v}_C^*$). The dynamics of these components are described by neglecting all the fluctuating terms of (4.5)-(4.8) (filters are required to filter-out the fluctuating components; then, their dynamics may be added if required). Accordingly, the non-fluctuating terms of the cluster voltages result in:

$$C\bar{v}_C \frac{d\bar{\mathbf{v}}_{C\alpha\beta}^{\Sigma}}{dt} \approx \frac{1}{2} E \mathbf{i}_{\alpha\beta}^{\Sigma} \tag{4.19}$$

$$C\bar{v}_C \frac{d\bar{\mathbf{v}}_{C\alpha\beta}^{\Delta}}{dt} \approx -\left(\mathbf{v}_{\alpha\beta}\mathbf{i}_{\alpha\beta}^{\Sigma}\right)^c - 2v_0 \mathbf{i}_{\alpha\beta}^{\Sigma} \tag{4.20}$$

$$C\bar{v}_C \frac{d\bar{v}_{C0}^{\Sigma}}{dt} \approx \frac{1}{6} E i^P - \frac{1}{4} \Re\left[\mathbf{v}_{\alpha\beta}(\mathbf{i}_{\alpha\beta})^c\right] \tag{4.21}$$

$$C\bar{v}_C \frac{d\bar{v}_{C0}^{\Delta}}{dt} \approx -\Re\left[\mathbf{v}_{\alpha\beta}(\mathbf{i}_{\alpha\beta}^{\Sigma})^c\right] - \frac{2}{3} i^P v_0 \tag{4.22}$$

Inspecting (4.19) and (4.22), it is concluded that the dc-port voltage E modifies only the dynamics of the voltages $\bar{\mathbf{v}}_{C\alpha\beta}^{\Sigma}$ and $\bar{v}_{C0}^{\Sigma}$. From a control point of view, E affects the process gain;

however, these changes can be compensated by using, for instance, gain scheduling methodologies in the balancing control loops of $\bar{\mathbf{v}}^{\Sigma}_{C\alpha\beta}$ and $\bar{v}^{\Sigma}_{C0}$. The application of this methodology in electronic converters is described in [24].

4.4.2 Dynamics of the Fluctuating Components

The dynamics of the fluctuating components of the cluster voltages are calculated by neglecting the non-fluctuating terms of (4.5)-(4.8), resulting in:

$$C\bar{v}_C\frac{d\tilde{\mathbf{v}}^{\Sigma}_{C\alpha\beta}}{dt} \approx -\frac{1}{4}\left(\mathbf{i}_{\alpha\beta}\mathbf{v}_{\alpha\beta}\right)^c - \frac{1}{2}v_0\mathbf{i}_{\alpha\beta} \tag{4.23}$$

$$C\bar{v}_C\frac{d\tilde{\mathbf{v}}^{\Delta}_{C\alpha\beta}}{dt} \approx \frac{1}{2}E\mathbf{i}_{\alpha\beta} - \frac{2}{3}i^P\mathbf{v}_{\alpha\beta} \tag{4.24}$$

$$C\bar{v}_C\frac{d\tilde{v}^{\Sigma}_{C0}}{dt} \approx 0 \tag{4.25}$$

$$C\bar{v}_C\frac{d\tilde{v}^{\Delta}_{C0}}{dt} \approx 0 \tag{4.26}$$

From (4.23)-(4.26), it is concluded that the variations in E only affect the dynamics of the voltage $\tilde{\mathbf{v}}^{\Delta}_{C\alpha\beta}$. Neglecting the converter losses $i^P \approx \frac{3\Re[\mathbf{v}_{\alpha\beta}(\mathbf{i}_{\alpha\beta})^c]}{2E}$, and then the dynamics of $\tilde{\mathbf{v}}^{\Delta}_{C\alpha\beta}$ as a function of E yields to:

$$C\bar{v}_C\frac{d\tilde{\mathbf{v}}^{\Delta}_{C\alpha\beta}}{dt} \approx \frac{1}{2}E\mathbf{i}_{\alpha\beta} - \Re[\mathbf{v}_{\alpha\beta}(\mathbf{i}_{\alpha\beta})^c]\frac{\mathbf{v}_{\alpha\beta}}{E} \tag{4.27}$$

However, it is not straightforward to analyse the influence of E in $\tilde{\mathbf{v}}^{\Delta}_{C\alpha\beta}$ due to the non-linear relationship between them and the fluctuating nature of $\tilde{\mathbf{v}}^{\Delta}_{C\alpha\beta}$. This analysis can be simplified using dq-coordinates considering that the vector $\tilde{\mathbf{v}}^{\Delta}_{C\alpha\beta}$ rotates at ω_e rad·s^{-1}, resulting in:

$$C\bar{v}_C\frac{d\tilde{\mathbf{v}}^{\Delta}_{Cdq}}{dt} \approx \frac{1}{2}E\mathbf{i}_{dq} - \Re[\mathbf{v}_{dq}(\mathbf{i}_{dq})^c]\frac{\mathbf{v}_{dq}}{E} - jC\bar{v}_C\omega_e\tilde{\mathbf{v}}^{\Delta}_{Cdq} \tag{4.28}$$

Additionally, (4.28) can be linearised around an operating point to avoid the non-linear relationship between $\tilde{\mathbf{v}}^{\Delta}_{Cdq}$ and E. Re-ordering (4.28) using a standard complex-state-space representation, it results in:

$$\frac{d\tilde{\mathbf{v}}^{\Delta}_{Cdq}}{dt} \approx \underbrace{-j\omega_e\tilde{\mathbf{v}}^{\Delta}_{Cdq}}_{:=\mathbf{A}} + \underbrace{\frac{\mathbf{i}_{dq}}{2C\bar{v}_C}E - \frac{\Re\{\mathbf{v}_{dq}(\mathbf{i}_{dq})^c\}\mathbf{v}_{dq}}{C\bar{v}_C}\frac{1}{E}}_{:=\mathbf{B}} \tag{4.29}$$

where $\mathbf{A}$ and $\mathbf{B}$ represent the state- and input-complex-functions, respectively, and $\tilde{\mathbf{v}}^{\Delta}_{Cdq}$ is chosen as the state-space complex vector. Hence, using the operator "δ" to denote small changes in a variable and the sub-script "0" to refer to the operating point, the linear approximation of (4.29) yields to:

$$\frac{d\delta\tilde{\mathbf{v}}^{\Delta}_{Cdq}}{dt} \approx \mathbf{A}_0\ \delta\tilde{\mathbf{v}}^{\Delta}_{Cdq} + \mathbf{B}_0\ \delta E \tag{4.30}$$

where:

$$\mathbf{A}_0 := \left.\frac{\partial \mathbf{A}}{\partial \tilde{\mathbf{v}}^{\Delta}_{Cdq}}\right|_0 = -j\omega_{e0} \tag{4.31}$$

$$\mathbf{B}_0 := \left.\frac{\partial \mathbf{B}}{\partial E}\right|_0 = \frac{\mathbf{i}_{dq0}}{2C\bar{v}_{C0}} + \frac{2\Re\{\mathbf{v}_{dq0}(\mathbf{i}_{dq0})^c\}\mathbf{v}_{dq0}}{C\bar{v}_{C0}}\frac{1}{E_0^2} \tag{4.32}$$

Based on (4.30) and (4.31), it is concluded that voltage fluctuations appear in $\tilde{\mathbf{v}}^{\Delta}_{Cdq}$ for sudden changes in E. The frequency of these fluctuations is about to ω_{e0} in dq-coordinates. In the $\alpha\beta$- or $PNabc$-coordinate system, these fluctuations are then reflected as non-fluctuating voltage variations. Consequently, it is not recommended to modify the dc-port voltage without considering its influence in $\tilde{\mathbf{v}}^{\Delta}_{Cdq}$. To solve this issue, next section discusses the regulation of the cluster voltages when E is manipulated.

4.5 Proposed Control System of the MMC Manipulating the dc-Port Voltage

The regulation of $||\tilde{\mathbf{v}}^{\Delta}_{Cdq}||$ (a scalar variable), instead of $\tilde{\mathbf{v}}^{\Delta}_{Cdq}$, is proposed in this work to manipulate E without affecting negatively the cluster voltages during HFM. Consequently, an output equation of the state-space model (SSM) can be defined to relate $||\tilde{\mathbf{v}}^{\Delta}_{Cdq}||$ as a function of the state-space variables of (4.30), yielding to:

$$||\tilde{\mathbf{v}}^{\Delta}_{Cdq}|| = \sqrt{{\tilde{v}^{\Delta}_{Cd}}^2 + {\tilde{v}^{\Delta}_{Cq}}^2} \tag{4.33}$$

and then the linear approximation of $||\tilde{\mathbf{v}}^{\Delta}_{Cdq}||$ results in:

$$\delta||\tilde{\mathbf{v}}^{\Delta}_{Cdq}|| = \Re\left\{\frac{1}{||\tilde{\mathbf{v}}^{\Delta}_{Cdq0}||}\left(\tilde{\mathbf{v}}^{\Delta}_{Cdq0}\right)^c \delta\tilde{\mathbf{v}}^{\Delta}_{Cdq}\right\} \tag{4.34}$$

Based on the state-space model (4.30) and (4.34), it is possible to design novel control systems to manipulate E without affecting negatively the regulation of the cluster voltages. For example, state-space-based control systems, active damping schemes, or PI control systems could be proposed to control $||\tilde{\mathbf{v}}^{\Delta}_{Cdq}||$ by manipulating E. For the sake of simplicity, a PI-based control system is used in this work. For tuning purposes, the transfer function between $\delta||\tilde{\mathbf{v}}^{\Delta}_{Cdq}||$ and δE is required, which is calculated using (4.30) and (4.34) as follows:

$$\frac{\delta||\tilde{\mathbf{v}}^{\Delta}_{Cdq}(s)||}{\delta E(s)} = \Re\left\{\mathbf{C}_0\left(s - \mathbf{A}_0\right)^{-1}\mathbf{B}_0\right\} \tag{4.35}$$

The proposed control system is depicted in Fig. 4.4. The voltage $\mathbf{v}^{\Delta}_{C\alpha\beta}$ is calculated by applying the $\Sigma\Delta\alpha\beta 0$-transformation to the cluster voltages and its fluctuating- and non-fluctuating components are obtained by using low-pass or synchronous filters [9]. The voltage

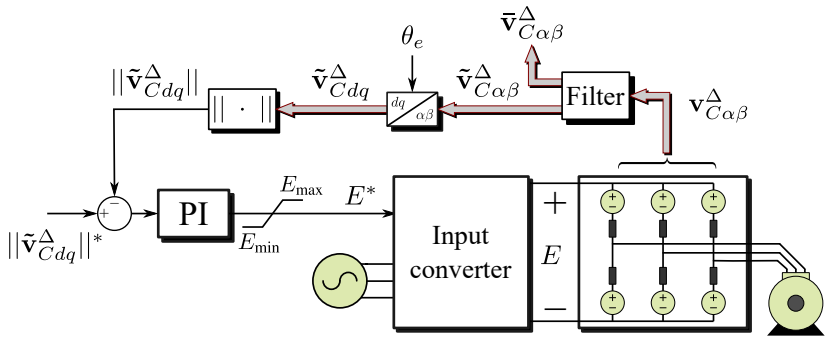

Figure 4.4: Proposed control system to control $\max[\tilde{v}^X_{Cx}]$ manipulating E.

$\bar{\mathbf{v}}^{\Delta}_{C\alpha\beta}$ is regulated by the balancing controller (see [10]). On the other hand, in this case the voltage $\tilde{\mathbf{v}}^{\Delta}_{C\alpha\beta}$ is transformed into a dq-rotating frame using the machine electrical angle, θ_e, which is imposed by the machine control system. A PI controller with an anti-windup algorithm produces the desired dc-port voltage E^* comparing $||\tilde{\mathbf{v}}^{\Delta}_{Cdq}||$ with its reference, $||\tilde{\mathbf{v}}^{\Delta}_{Cdq}||^*$. Notice that the output of the controller has to be limited to ensure a feasible value of E^* during the operation of the MMC. For example, a minimum value has to be ensured to modulate the output voltage properly (i.e. $E_{\min}>2||\mathbf{v}_{\alpha\beta}||$ should be always ensured, even in LFM).

As indicated in (4.10), the amplitude of the cluster voltage fluctuations, $\max[\tilde{v}^X_{Cx}]$, is dominated by the vectors $\mathbf{v}^{\Delta}_{Cdq}$ and $\mathbf{v}^{\Sigma}_{C\alpha\beta}$ and then the set-point value of $||\tilde{\mathbf{v}}^{\Delta}_{Cdq}||$ is related with $\max[\tilde{v}^X_{Cx}]^*$ as follows:

$$||\tilde{\mathbf{v}}^{\Delta}_{Cdq}||^* = 2(\max[\tilde{v}^X_{Cx}]^* - ||\mathbf{v}^{\Sigma}_{C\alpha\beta}||) \tag{4.36}$$

Therefore, if the control system shown in Fig. 4.4 is able to control $||\tilde{\mathbf{v}}^{\Delta}_{Cdq}||$ as given by (4.36), (4.10) results in:

$$\max[\tilde{v}^X_{Cx}] \leq \max[\tilde{v}^X_{Cx}]^* \tag{4.37}$$

and the total cluster voltage fluctuations are regulated within the voltage margin defined by $\max[\tilde{v}^X_{Cx}]^*$, even during HFM.

4.6 Comparison of the Control Methodologies for MMC-Based Drives

Table 4.1 shows a comparison between conventional control strategies and those presented in this work. The control strategies have been classified into the following categories:

1. **Full-mitigation**: were the desired fluctuations of the cluster voltages are set to zero during LFM. This the most conventional control strategy for MMC-base drives [8, 9, 22, 25].

2. **Margin-based**: were a voltage fluctuation is allowed in the cluster voltages during LFM [10, 11, 23].

3. **Variable dc-port voltage**: the control strategies of this chapter are in this category.

Table 4.1 depicts a simulation of the capacitor voltage ($v_C(t)$), as well as the applied voltage $E(t)$ and several comparative variables. The performance indicators are the maximum voltage fluctuation in an MMC capacitor ($\max[v_C]$), the cell capacitance (C), the amplitude of the common-mode voltage (V_0), the maximum value of the circulating currents ($\max[\mathbf{i}^{\Sigma}_{\alpha\beta}]$) and the ratio between the low- and high-frequency modes (LFM/HFM). Additionally, they are classified into "**High**", "**Normal**" and "**Low**". The same loading conditions were used to obtain all the figures (a ramp speed set-point and a quadratic plus offset torque-speed profile). The gray area indicates the LFM. In the case of the Full-mitigation strategy, the transition frequency between low- and high-frequency modes has been defined as the one obtained for the Margin-based strategy, and no transition zone is considered.

As depicted in Table 4.1, the Full-mitigation techniques are less appropriate for MMC-based drives, mainly because the circulating currents increases with the machine frequency in the LFM (see the parameter $\max[\mathbf{i}^{\Sigma}_{\alpha\beta}]$ in Table 4.1) and the ratio between the low- and high-frequency modes is defined arbitrarily by choosing a constant transition frequency (see the parameter LFM/HFM in Table 4.1). Both issues are solved in the Margin-based strategy since the circulating currents decrease as the machine frequency increases and the transition frequency is selected considering the loading conditions (see [10]). Accordingly, the Full-mitigation strategy should not be used in the MMC-based drives.

Table 4.1 also shows that the proposed schemes have attractive features for operating the MMC-based drive. During LFM, the generalised Margin-based strategy ensures the desired peak value of the cluster voltages; however, in this case the mitigating common-mode voltage is reduced in approximately the same ratio that the dc-port voltage, while the peak-value of the circulating currents is not severely modified (see Section 4.3.3, as well as the parameters V_0 and $\max[\mathbf{i}^{\Sigma}_{\alpha\beta}]$ in Table 4.1). During HFM, the control system depicted in Fig. 4.4 ensures the proper regulation of the cluster voltages within the voltage margin defined by $\max[\tilde{v}^{X}_{Cx}]^*$ [i.e. $\max[\tilde{v}^{X}_{Cx}] \leq \max[\tilde{v}^{X}_{Cx}]^*$, see (4.37)]. For example, notice that the peak value of the capacitor voltage fluctuation is practically constant for two of three operating schemes, but the voltage oscillation is different due to the cell capacitance (see the parameter C in Table 4.1). In the last operating scheme, the voltage E is quickly saturated to its maximum value by the anti-windup algorithm of the control system shown in Fig. 4.4 and there are produced similar voltage fluctuations to those obtained for the conventional Margin-based strategy. However, notice that the duration of the LFM is the shortest, as demonstrated in Section 4.3.

Table 4.1: Evolution of the MMC-based drive control strategies

Parameter	Full-mitigation	Margin-based	Variable dc-port voltage		
			Reduced fluctuations	Reduced capacitance	Reduced LFM duration
$v_C(t)$	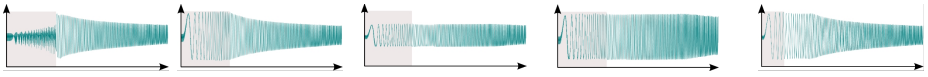				
$E(t)$	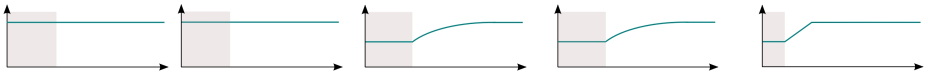				
$\mathbf{v}_{Cdq}^{\Delta*}$ (in LFM)	**0**	$\neq$ **0**	$\neq$ **0**	$\neq$ **0**	$\neq$ **0**
$\max[v_C]$	**Normal**	**Normal**	**Low**	**Normal**	**Normal**
C	**Normal**	**Normal**	**Normal**	**Low**	**Normal**
V_0	**Normal**	**Normal**	**Low**	**Low**	**Low**
$\max[\mathbf{i}_{\alpha\beta}^{\Sigma}]$	**High**	**Low**	**Low**	**Low**	**Low**
LFM/HFM	**High**	**Normal**	**Normal**	**Normal**	**Low**

Table 4.2: Parameters of the simulated MMC-based drive

Parameter	Symbol	Value	Unit
Rated power	p	10	MW
Rated speed	$\omega_{e\text{Nom}}$	1800	rpm
Nominal dc-port voltage	E	11	kV
Cell capacitor	C	8800, 4900	μF
Cells per cluster	n	12	–
Nominal cell dc-voltage	$\bar{v}_C^*$	1000	V

4.7 Simulation and Experimental Results

4.7.1 Comparison of the Proposed Control Schemes

Simulation results of a high-power MMC-based drive have been carried out to compare the proposed control schemes. The parameters of the simulated drive are similar to the one used in [20] (see Table 4.2). In all the tests, the machine was accelerated from 0 to nominal speed in 15 s and a quadratic plus offset (0.3 p.u.) torque-speed profile was implemented. Fig. 4.5 depicts the obtained speed and machine current during the tests. An ideal dc-power supply was utilised as input converter.

The parameters and applied dc-port voltage of the simulated drive have been modified to represent the three proposed control schemes discussed in this work. The results of the simulation are shown in Fig. 4.6. From left to right, the columns of Fig. 4.6 show the control configuration to reduce: the duration of the LFM, the capacitance of each cell, the voltage fluctuation of the MMC capacitors (the speed and currents of the machine are shown in Fig. 4.5). Fig. 4.6(a)-(c) depicts the output voltage of an MMC cluster (black signal), as well as the dc-port voltage (red signal). As demonstrated in Section 4.3, the dc-port voltage is maintained in its minimum value during LFM (50% of the nominal value for these tests); meanwhile, the control system of Fig. 4.4 manipulates E during the HFM to ensure the proper regulation of the cluster voltages. Notice that in Fig. 4.6(a)-(c), the output cluster voltage has a mean value of $\frac{1}{2}E$, which affects the power pulsations of the MMC and then the behaviour of its cluster voltages. Fig. 4.6(d)-(f) demonstrate that the fluctuations of the capacitor voltages are also affected by the cell capacitance and the maximum allowed voltage margin ($\max[\tilde{v}_{Cx}^X]^*$). For example, the values C=8800 μF and $\max[\tilde{v}_{Cx}^X]^*$=1.2 kV (maximum parameters) are used in each cell in the test of Fig. 4.6(d), obtaining the control scheme for a reduction in the duration of the LFM. This reduction can be corroborated comparing the duration of the mitigating variables in Fig. 4.6(g)-(i) or Fig. 4.6(j)-(l),e.g., when compared with the other schemes, the HFM in the test of the left-side of Fig. 4.6 is extended from approximately 71% until 86% of the total drive operation.

When the capacitance or the allowed voltage margin of the cells are decreased, the other control schemes are obtained. As mentioned in Section 4.3 and 4.4, the mitigating variables and the applied dc-port voltage are not modified if the product $C\max[\tilde{v}_{Cx}^X]^*$ is maintained constant, but it is possible to modify the voltage fluctuation of the cluster voltages. In the

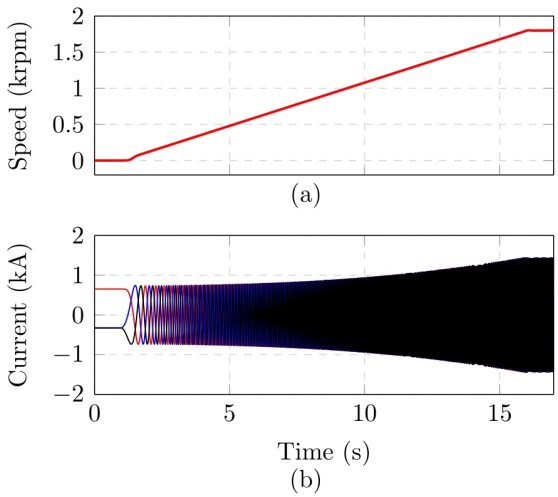

Figure 4.5: Machine speed (a) and currents (b) for the simulated results in Fig. 4.6.

Table 4.3: Set-up parameters for the 18 cells MMC-drive

Parameter	Symbol	Value	Unit
dc-port voltage	E	300	V
Cluster inductor	L	2,5	mH
Cell capacitor	C	4700	μF
Cell dc-voltage	$\bar{v}_C^*$	100	V

central column of Fig. 4.6, the values of C=4900 μF and max$[\tilde{v}_{Cx}^X]^*$=1.2 kV are used in each cell, leading to a decrease of 44% of the required capacitance in each cell, in comparison with the results of the left column of Fig. 4.6. Notice that the generalised Margin-based strategy during LFM, as well as the control system of Fig. 4.4 during HFM, maintain the amplitude of the fluctuations in the cluster voltages within the margin defined by max$[\tilde{v}_{Cx}^X]^*$. As shown in the right column of Fig. 4.6, it is also possible when C=8800 μF and max$[\tilde{v}_{Cx}^X]^*\approx$0.67 kV. However, notice that in this case the fluctuations of the cluster voltages are maintained in their minimum value, the voltage fluctuation for nominal speed and full load.

Finally, notice that the peak value of the mitigating variables is not different between the proposed control schemes. Nonetheless, the required common-mode voltage is reduced when compared with that required for a constant dc-port voltage, as mentioned in Section 4.3.3. Consequently, it was possible to reduce the required common-mode voltage in approximately 50% in the simulation results of Fig. 4.6.

4.7.2 Experimental results

Experimental results for the proposed control methodologies have been obtained using an 18-power cell MMC-based drive. A 12-power cell MMC, operating in boost mode, was used as input converter. A small capacitor is connected in the BTB dc-link to filter the pwm voltage applied to the machine-side MMC. A photograph of the system is presented in Fig. 4.7. The parameters of the machine-side converter are given in Table 4.3. The MMC drives a 7.5 kW

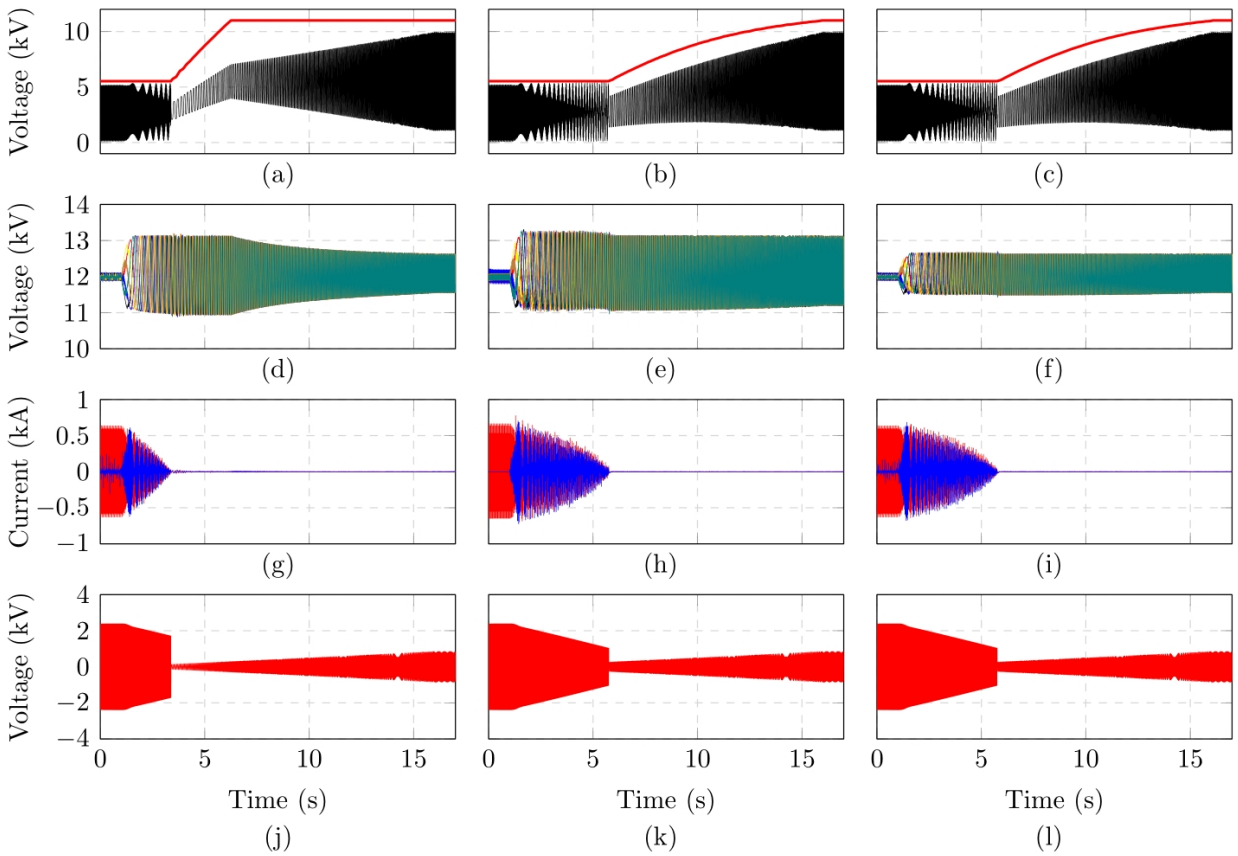

Figure 4.6: Simulation results of the proposed control schemes. From left to right, results of the configuration to reduce: the duration of the LFM, the capacitance of each cell, the voltage fluctuation of the MMC capacitors. (a)-(c): dc-port voltage and output cluster voltage, (d)-(f): cluster voltages, (g)-(i): circulating currents, (j)-(l): common-mode voltage.

vector-controlled induction machine connected to a Permanent Magnet Generator (PMG). A resistor bank has been connected to the PMG output to provide an electrical load. Hall effect transducers are used to measure the dc-port voltage, the capacitor voltages and the cluster currents. A position encoder of 10000 pulses per revolution is affixed to the induction machine. Both systems are controlled using a Digital Signal Processor Texas Instrument TMS320C6713 board and 2 Actel ProAsic3 FPGA boards, equipped with a total of 40 14-bit analogue-digital channels. A phase-shifted PWM algorithm generates the 18 switching signals timed via an FPGA platform. Optical fibre connections transmit the switching signals to the gate drivers of the MOSFET switches (model IRFP4868PbF, nominal ratings of 70A, 300V, 32 mΩ on resistance). Additionally, a SPI communication link has been implemented to communicate the control platforms of both MMC.

Fig. 4.8 depicts the experimental results of the MMC-based drive when two control strategies are used. The compared control strategies are the Margin-Based Strategy [10, 11] (left-side) and the control scheme to reduce the voltage fluctuations of the MMC capacitors (right-side). During the test, the induction machine was accelerated from 0 to 1400 rpm in 15 s. A margin of $\pm$10% of the mean value of the cluster voltages is chosen for the Margin-Based Strategy (i.e. max$[\tilde{v}_{Cx}^{X}]^{*}$=30 V). With this voltage margin and loading conditions, the LFM duration for the Margin-Based Strategy is about 30% of the total drive operating range, which is considered a reasonable value. A similar LFM duration was obtained when the

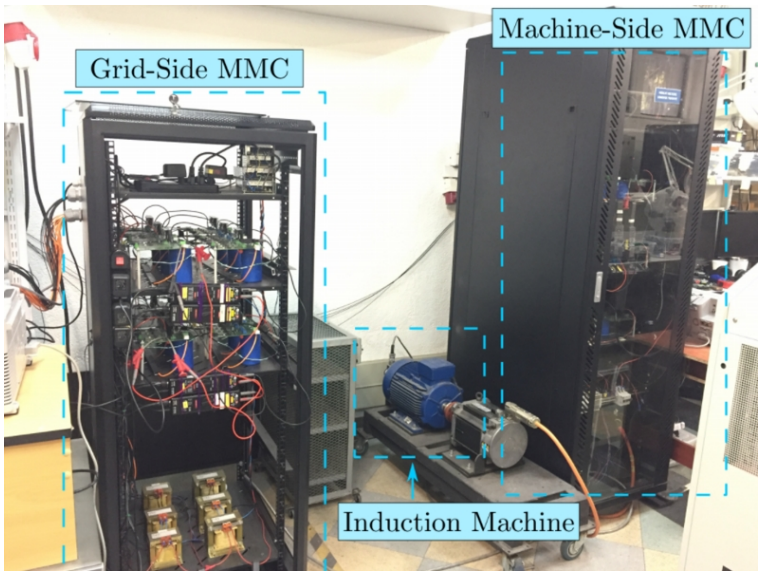

Figure 4.7: Experimental setup

dc-port voltage was modified, as discussed below.

The obtained machine speed and currents are shown in Fig. 4.8(a)-(b) and 4.8(c)-(d), respectively. The applied dc-port voltage (red signal) and the output cluster voltage (black signal) are shown in Fig. 4.8(e)-(f). As shown in the figures, a higher output cluster voltage is required during LFM when the Margin-Based Strategy is applied [compare Fig. 4.8(e) with Fig. 4.8(f)]. Additionally, the mitigating common-mode voltage is reflected in the output cluster voltage, indicating the duration of the LFM for both cases (approximately 30% of the total operating range). The reduction in the required voltage v_0 is also demonstrated.

As expected in the conventional Margin-Based Strategy, the cluster voltages are maintained within the voltage margin defined by $\max[\tilde{v}_{Cx}^{X}]^{*}$=30 V, but their fluctuations decrease until approximately 17 V peak during HFM [see Fig. 4.8(g)]. In the case of the proposed control strategy [see Fig. 4.8(h)], the cluster voltages are within the margin defined by $\max[\tilde{v}_{Cx}^{X}]^{*}$=17 V during the whole operating range (i.e. in both, low- and high-frequency modes). As depicted Fig. 4.8(i) and Fig. 4.8(j), the mitigating currents are not severely affected for the application of a variable dc-port voltage as proposed in this work. When a constant voltage E is utilised [see Fig. 4.8(i)]), the peak value of the circulating currents is approximately 7.9 A, and it increases to approximately 8.5 A when the proposed control strategy is applied [see Fig. 4.8(j)], representing an increase of 7.6%.

4.8 Conclusions

In this work, the influence of the dc-port voltage on the MMC behaviour has been analysed for both, low- and high-frequency modes. During LFM, it has been demonstrated that a low value of E is advantageous for the operation of the machine drive. For example, a low dc-port value could lead to a reduction of three parameters: 1) the voltage fluctuation in

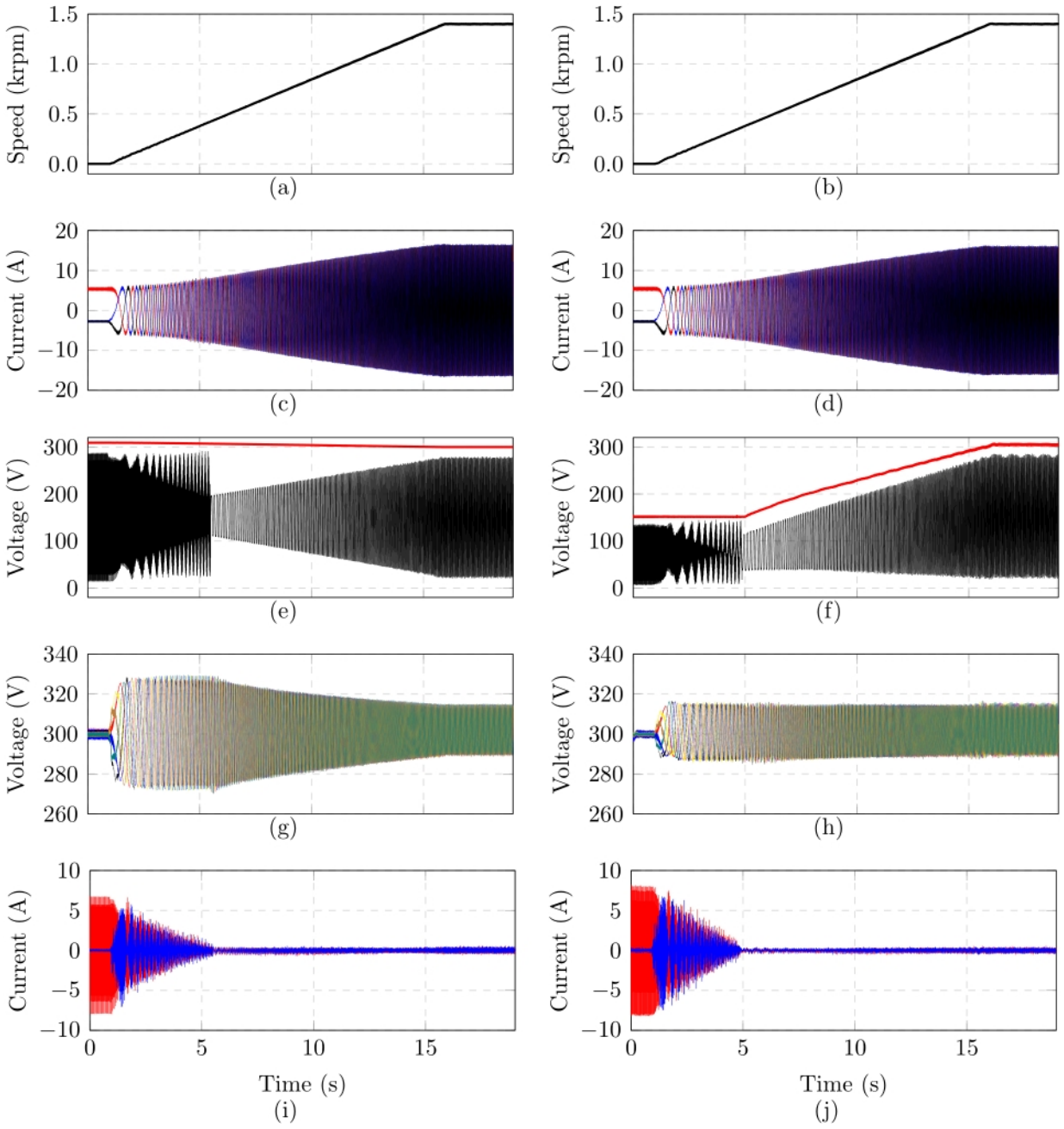

Figure 4.8: Comparison of control strategies. Left: Margin-Based Strategy. Right: Variable dc-Port Strategy. (a)-(b): machine speed, (c)-(d): machine currents, (e)-(f): dc-port voltage, (g)-(h): cluster voltages, (i)-(j): output cluster voltage, (k)-(l): circulating currents.

the MMC capacitors, 2) the cell capacitance or 3) the duration of the LFM. Additionally, a reduction in the mitigating common-mode voltage is achieved when E is reduced (i.e. there are mitigated the insulation damage or leakage currents in the machine bearing). What is more, the peak value of the circulating currents is not affected severely for the proposed control schemes. In HFM, a state-space model was proposed to represent the dynamics of the cluster voltages as a function of the dc-port voltage. It was shown that undesired fluctuations can appear in the cluster voltages for sudden changes in E. Consequently, a closed-loop control system, that manipulates the voltage E, was proposed to regulate the cluster voltages properly. In all the tests and comparisons with the conventional control strategies, the simulated and experimental results of this work show the effectiveness and feasibility of the proposed control schemes. The experimental tests include the operation in the whole whole frequency range (i.e. from 0 to nominal speed).

Bibliography

[1] M. L. Zhang, B. Wu, Y. Xiao, F. A. Dewinter, and R. Sotudeh, "A multilevel buck converter based rectifier with sinusoidal inputs and unity power factor for medium voltage (4160-7200 v) applications," *IEEE Transactions on Power Electronics*, vol. 17, DOI 10.1109/TPEL.2002.805600, no. 6, pp. 853–863, Nov. 2002.

[2] I. Abdelsalam, G. P. Adam, D. Holliday, and B. W. Williams, "Single-stage ac-dc buck-boost converter for medium-voltage high-power applications," *IET Renewable Power Generation*, vol. 10, DOI 10.1049/iet-rpg.2015.0136, no. 2, pp. 184–193, 2016.

[3] M. Guan, B. Li, S. Zhou, Z. Xu, and D. Xu, "Back-to-back hybrid modular multilevel converters for ac motor drive," in *IECON 2017 - 43rd Annual Conference of the IEEE Industrial Electronics Society*, DOI 10.1109/IECON.2017.8216308, pp. 1822–1827, Oct. 2017.

[4] S. Sau and B. G. Fernandes, "Modular multilevel converter based variable speed drives with constant capacitor ripple voltage for wide speed range," in *IECON 2017 - 43rd Annual Conference of the IEEE Industrial Electronics Society*, DOI 10.1109/IECON.2017.8216348, pp. 2073–2078, Oct. 2017.

[5] M. Espinoza, F. Donoso, M. Diaz, A. Letelier, and R. Cardenas, "Control and Operation of the MMC-Based Drive with Reduced Capacitor Voltage Fluctuations," in *Power Electronics, Machines and Drives (PEMD), 9th International Conference on*, Liverpool, UK., 17-19, April 2018.

[6] D. Busse, J. Erdman, R. J. Kerkman, D. Schlegel, and G. Skibinski, "System electrical parameters and their effects on bearing currents," *IEEE Transactions on Industry Applications*, vol. 33, DOI 10.1109/28.568025, no. 2, pp. 577–584, Mar. 1997.

[7] S. Du, B. Wu, and N. R. Zargari, "Common-mode voltage elimination for variable-speed motor drive based on flying-capacitor modular multilevel converter," *IEEE Transactions on Power Electronics*, vol. 33, DOI 10.1109/TPEL.2017.2740782, no. 7, pp. 5621–5628, Jul. 2018.

[8] J. Kolb, F. Kammerer, M. Gommeringer, and M. Braun, "Cascaded Control System of the Modular Multilevel Converter for Feeding Variable-Speed Drives," *IEEE Trans. Power Electron.*, vol. 30, no. 1, pp. 349–357, Jan. 2015.

[9] M. Espinoza, R. Cárdenas, M. Díaz, and J. C. Clare, "An Enhanced *dq*-Based Vector Control System for Modular Multilevel Converters Feeding Variable-Speed Drives," *IEEE Trans. Ind. Electron.*, vol. 64, no. 4, pp. 2620–2630, Apr. 2017.

[10] M. Espinoza, R. Cardenas, J. Clare, D. Soto, M. Diaz, E. Espina, and C. Hackl, "An integrated converter and machine control system for mmc-based high power drives," *IEEE Transactions on Industrial Electronics*, vol. PP, DOI 10.1109/TIE.2018.2801839, no. 99, pp. 1–1, 2018.

[11] M. Espinoza, E. Espina, M. Diaz, and R. Cárdenas, "Control Strategies for Modular Multilevel Converters Driving Cage Machines," in *IEEE 3rd Southern Power Electronics Conference (SPEC), 2017*, pp. 1–6, Puerto Varas, Chile, Diciembre 2017.

[12] K. Ilves, L. Bessegato, and S. Norrga, "Comparison of cascaded multilevel converter topologies for AC/AC conversion," in *Power Electronics Conference (IPEC-Hiroshima 2014 - ECCE-ASIA), 2014 International*, pp. 1087–1094, May. 2014.

[13] Y. Okazaki, W. Kawamura, M. Hagiwara, H. Akagi, T. Ishida, M. Tsukakoshi, and R. Nakamura, "Experimental Comparisons Between Modular Multilevel DSCC Inverters and TSBC Converters for Medium-Voltage Motor Drives," *IEEE Transactions on Power Electronics*, vol. PP, no. 99, pp. 1–1, 2016.

[14] M. Perez, S. Bernet, J. Rodriguez, S. Kouro, and R. Lizana, "Circuit Topologies, Modeling, Control Schemes, and Applications of Modular Multilevel Converters," *IEEE Trans. Power Electron.*, vol. 30, no. 1, pp. 4–17, Jan. 2015.

[15] Allen-Bradley, "Medium Voltage Solutions for Marine Applications: Driving Efficiency Aboard Your Vessel," Rockwell Automation, Inc., Tech. Rep., 2011. [Online]. Available: http://literature.rockwellautomation.com/idc/groups/literature/documents/br/marine-br003_-en-p.pdf

[16] J. Kolb, F. Kammerer, and M. Braun, "Dimensioning and design of a Modular Multilevel Converter for drive applications," in *Power Electronics and Motion Control Conference (EPE/PEMC), 2012 15th International*, pp. LS1a–1.1–1–LS1a–1.1–8, Sep. 2012.

[17] M. Glinka and R. Marquardt, "A new AC/AC multilevel converter family," *IEEE Trans. Ind. Electron.*, vol. 52, no. 3, pp. 662–669, Jun. 2005.

[18] EWEA. Aiming High Rewarding Ambition in Wind Energy. The European Wind Energy Association. (2015, November). [Online]. Available: http://www.ewea.org/fileadmin/files/library/publications/reports/EWEA-Aiming-High.pdf

[19] The European Wind Energy Association. Wind in Power: 2013 European Statistics. The European Wind Energy Association. The European Wind Energy Association. (2014, August). [Online]. Available: http://www.ewea.org/fileadmin/files/library/publications/statistics/EWEA-Annual-Statistics-2013.pdf

[20] P. Himmelmann, M. Hiller, D. Krug, and M. Beuermann, "A new modular multilevel converter for medium voltage high power oil gas motor drive applications," in *2016 18th*

European Conference on Power Electronics and Applications (EPE'16 ECCE Europe), DOI 10.1109/EPE.2016.7695692, pp. 1–11, Sep. 2016.

[21] S. Busse, M. Hiller, K. Kahlen, and P. Himmelmann, "MTBF comparison of cutting edge medium voltage drive topologies for oil gas applications," in *2015 Petroleum and Chemical Industry Conference Europe (PCIC Europe)*, DOI 10.1109/PCICEurope.2015.7790028, pp. 1–13, Jun. 2015.

[22] M. Hagiwara, I. Hasegawa, and H. Akagi, "Start-Up and Low-Speed Operation of an Electric Motor Driven by a Modular Multilevel Cascade Inverter," *IEEE Transactions on Industry Applications*, vol. 49, no. 4, pp. 1556–1565, July-August 2013.

[23] B. Li, S. Zhou, D. Xu, R. Yang, D. Xu, C. Buccella, and C. Cecati, "An Improved Circulating Current Injection Method for Modular Multilevel Converters in Variable-Speed Drives," *IEEE Trans. Ind. Electron.*, vol. 63, no. 11, pp. 7215–7225, Nov. 2016.

[24] H. Kakigano, Y. Miura, and T. Ise, "Distribution voltage control for dc microgrids using fuzzy control and gain-scheduling technique," *IEEE Transactions on Power Electronics*, vol. 28, DOI 10.1109/TPEL.2012.2217353, no. 5, pp. 2246–2258, May. 2013.

[25] A. J. Korn, M. Winkelnkemper, and P. Steimer, "Low Output Frequency Operation of the Modular Multi-Level Converter," in *Energy Conversion Congress and Exposition (ECCE), 2010 IEEE.* IEEE, 12-16 September 2010.

Part IV

Selected Conference Papers

Chapter 5

Improved Control Strategy of the Modular Multilevel Converter for High Power Drive Applications in Low Frequency Operation

This chapter is based on the conference paper:

M. Espinoza, E. Espina, M. Diaz, A. Mora, and R. Cárdenas. Improved control strategy of the Modular Multilevel Converter for high power drive applications in low frequency operation. In *Power Electronics and Application (EPE), 2016 18th European Conference on*, pages 5–9, Karlsruhe, Germany, September 2016

Abstract: Modular Multilevel Converters (MMC) are considered an attractive solution for high power drives. However, its operation during low rotational speeds can produce undesired voltage fluctuations in the MMC capacitors. In this paper, two methodologies to improve the converter performance in this speed range are analysed and tested. The first strategy proposes the control of the inner converter currents combining a synchronous *dq* rotating frame and resonant controllers to improve the current tracking and to reduce the voltage fluctuations. The second strategy achieves the reduction of the voltage fluctuations by adjusting the DC Port voltage as a function of the machine frequency. Both methods are validated by simulation and experimental work, where a 18 cell MMC prototype is applied to drive an induction machine.

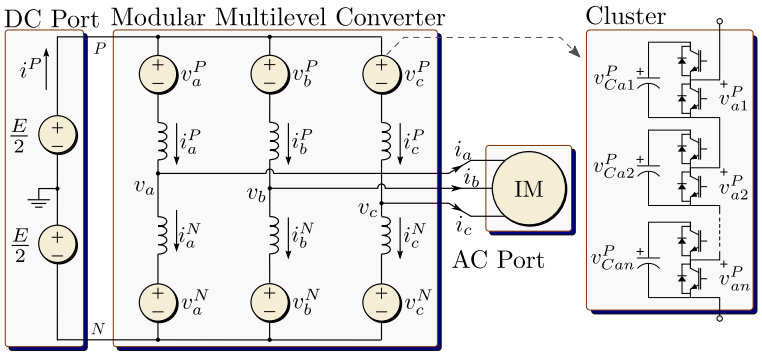

Figure 5.1: Modular Multilevel Converter for drive applications

5.1 Introduction

The Modular Multilevel Converter (M^2C) was firstly proposed in [1, 2]. In these papers, this topology was recommended for High Voltage DC transmission systems (HVDC), offshore wind farms and drive applications, the latter being widely validated with laboratory prototypes in [3, 4, 5, 6]. Moreover, the M^2C has been compared with others multilevel topologies, concluding that the M^2C in Back to Back (BTB) configuration is the optimal choice for a synchronous operation [7] and it is also more suitable for quadratic torque-to-speed loads [8]. As a consequence, the application of the M^2C could be well suited for industrial drive application of high power machines.

The M^2C is shown in Fig. 5.1 and consists of a DC Port, an AC Port and six clusters. Each cluster has n cells connected in cascade and is attached to a Port with an inductor L. The cell is composed of a half bridge circuit and a flying capacitor C. Therefore, the control of the M^2C must involve the regulation of the AC signals, as well as maintaining the voltage in each cell bounded in an acceptable range. This control target is particularly difficult to achieve when the electrical machine is operating at low rotational speed, since the voltage fluctuations in the M^2C capacitors increases considerably [3].

At low frequency operation, the power delivered by the circulating currents and the common mode voltage is conventionally used to mitigate the voltage fluctuations in the cluster capacitors, being a circulating current a current that has not emergence at the AC Port [9]. The waveforms proposed in the literature for the set-point value of the common mode voltage and the circulating currents are sinusoidal signals with or without third harmonic injection [3, 5], square waves [5] (a comparative study of some of these signals is performed in [10, 5]) and hybrid mitigation signals [11]. However, although a good dynamic performance of the control systems of the circulating current controllers is mandatory for low frequency, only P or PI controllers have been proposed in the literature to control these currents. As it is well known, these controllers cannot regulated with zero steady state error currents of sinusoidal nature.

In this paper, two novel alternatives to improve the operation of the M^2C at low frequency are discussed. Firstly, a novel circulating current control scheme is proposed. The control algorithm is implemented in a synchronous rotating frame and resonant controllers are used

to regulate the resultant currents. This control structure is applicable to several mitigating methods discussed above, and has been validated with a laboratory prototype controlling an induction machine for dynamic and steady state conditions. Secondly, a novel low frequency mode, that modifies the DC Port voltage as a function of the AC port frequency is studied. This approach could be specially useful for cases where a periodical duty cycle of the machine is required, since this methodology achieves a low frequency operation without injecting extra circulating currents or high common mode voltage. Simulation results are used to validate the effectiveness of this control strategy.

5.2 Modelling of the Modular Multilevel Converter

Using Fig. 5.1, the following dynamic relations for the M^{2}C can be derived:

$$\frac{E}{2}\begin{bmatrix}1&1&1\\1&1&1\end{bmatrix}=\underbrace{\begin{bmatrix}v_a^P&v_b^P&v_c^P\\v_a^N&v_b^N&v_c^N\end{bmatrix}}_{\boldsymbol{V}_{abc}^{PN}}+L\frac{d}{dt}\underbrace{\begin{bmatrix}i_a^P&i_b^P&i_c^P\\i_a^N&i_b^N&i_c^N\end{bmatrix}}_{\boldsymbol{I}_{abc}^{PN}}+\begin{bmatrix}v_a&v_b&v_c\\-v_a&-v_b&-v_c\end{bmatrix} \tag{5.1}$$

$$\underbrace{\begin{bmatrix}v_{Ca}^P&v_{Cb}^P&v_{Cc}^P\\v_{Ca}^N&v_{Cb}^N&v_{Cc}^N\end{bmatrix}}_{\boldsymbol{V}_{Cabc}^{PN}}\approx\frac{1}{Cv_C^*}\int\underbrace{\begin{bmatrix}p_a^P&p_b^P&p_c^P\\p_a^N&p_b^N&p_c^N\end{bmatrix}}_{\boldsymbol{P}_{abc}^{PN}=\boldsymbol{V}_{abc}^{PN}\circ\boldsymbol{I}_{abc}^{PN}}dt \tag{5.2}$$

where (5.1) is based on the Kirchhoff's voltage law and (5.2) relates the sum of the capacitor voltages and the power flow of each cluster, being v_C^* the desired capacitor voltage and "$\circ$" the Hadamard product.

Analysing (5.1) and (5.2), it is not simple to define a control methodology to regulate the voltages $\boldsymbol{V}_{abc}^{PN}$ to control the port currents and to balance the energy/voltage of the M^{2}C. Consequently, (5.1) and (5.2) could be transformed to obtain a decoupled model of the M^{2}C. This objective is performed applying the $\Sigma\Delta\alpha\beta0$ transformation [6, 11], which transforms a matrix $\boldsymbol{X}_{abc}^{PN}$ into a matrix $\boldsymbol{X}_{\alpha\beta0}^{\Sigma\Delta}$ as follows:

$$\boldsymbol{X}_{\alpha\beta0}^{\Sigma\Delta}=\begin{bmatrix}\frac{1}{2}&\frac{1}{2}\\1&-1\end{bmatrix}\cdot\boldsymbol{X}_{abc}^{PN}\cdot\begin{bmatrix}\frac{2}{3}&-\frac{1}{3}&-\frac{1}{3}\\0&\frac{1}{\sqrt{3}}&-\frac{1}{\sqrt{3}}\\\frac{1}{3}&\frac{1}{3}&\frac{1}{3}\end{bmatrix}^{\mathsf{T}} \tag{5.3}$$

With this transformation, the pole variables in a same M^{2}C phase are related using the first matrix of the right member of (5.3). Subsequently, the last matrix of the right member of (5.3) relates the resultant variables among the converter phases. Then, applying (5.3) to (5.1) and (5.2) and simplifying yields:

$$\begin{bmatrix}0&0&\frac{E}{2}\\0&0&0\end{bmatrix}=\begin{bmatrix}v_\alpha^\Sigma&v_\beta^\Sigma&v_0^\Sigma\\v_\alpha^\Delta&v_\beta^\Delta&v_0^\Delta\end{bmatrix}+L\frac{d}{dt}\begin{bmatrix}i_\alpha^\Sigma&i_\beta^\Sigma&\frac{1}{3}i^P\\i_\alpha&i_\beta&0\end{bmatrix}+2\begin{bmatrix}0&0&0\\v_\alpha&v_\beta&v_0\end{bmatrix} \tag{5.4}$$

$$\underbrace{\begin{bmatrix}v_{C\alpha}^\Sigma&v_{C\beta}^\Sigma&v_{C0}^\Sigma\\v_{C\alpha}^\Delta&v_{C\beta}^\Delta&v_{C0}^\Delta\end{bmatrix}}_{\boldsymbol{V}_{C\alpha\beta0}^{\Sigma\Delta}}\approx\frac{1}{Cv_C^*}\int\underbrace{\begin{bmatrix}p_\alpha^\Sigma&p_\beta^\Sigma&p_0^\Sigma\\p_\alpha^\Delta&p_\beta^\Delta&p_0^\Delta\end{bmatrix}}_{\boldsymbol{P}_{\alpha\beta0}^{\Sigma\Delta}}dt \tag{5.5}$$

where v_α, v_β, v_0, i_α and i_β are the AC Port voltages and currents in $\alpha\beta 0$ coordinates. Therefore, (5.4) shows that the port and circulating currents (i_α^Σ and i_β^Σ) have been decoupled and each one can be controlled by using only one cluster voltage in the $\Sigma\Delta\alpha\beta 0$ domain. Moreover, the matrix $\boldsymbol{P}_{\alpha\beta 0}^{\Sigma\Delta}$ can be manipulated to control the matrix $\boldsymbol{V}_{C\alpha\beta 0}^{\Sigma\Delta}$. The elements of $\boldsymbol{P}_{\alpha\beta 0}^{\Sigma\Delta}$ are defined as in [6, 11]:

$$p_\alpha^\Sigma = \tfrac{1}{2}Ei_\alpha^\Sigma - \tfrac{1}{4}i_\alpha v_\alpha + \tfrac{1}{4}i_\beta v_\beta - \tfrac{1}{2}i_\alpha v_0 \tag{5.6}$$

$$p_\beta^\Sigma = \tfrac{1}{2}Ei_\beta^\Sigma + \tfrac{1}{4}i_\beta v_\alpha + \tfrac{1}{4}i_\alpha v_\beta - \tfrac{1}{2}i_\beta v_0 \tag{5.7}$$

$$p_0^\Sigma = \tfrac{1}{6}Ei^P - \tfrac{1}{4}i_\alpha v_\alpha - \tfrac{1}{4}i_\beta v_\beta \tag{5.8}$$

$$p_\alpha^\Delta = \tfrac{1}{2}Ei_\alpha - \tfrac{2}{3}i^P v_\alpha - i_\alpha^\Sigma v_\alpha + i_\beta^\Sigma v_\beta - 2i_\alpha^\Sigma v_0 \tag{5.9}$$

$$p_\beta^\Delta = \tfrac{1}{2}Ei_\beta - \tfrac{2}{3}i^P v_\beta + i_\beta^\Sigma v_\alpha + i_\alpha^\Sigma v_\beta - 2i_\beta^\Sigma v_0 \tag{5.10}$$

$$p_0^\Delta = -i_\alpha^\Sigma v_\alpha - i_\beta^\Sigma v_\beta - \tfrac{2}{3}i^P v_0 \tag{5.11}$$

5.3 Analysis of the M^{2}C model

To achieve perfect regulation of the capacitor voltages in the M^{2}C drive depicted in Fig. 5.1, all capacitor voltages must be equal to v_C^*. With this condition, the set-point value of the matrix $\boldsymbol{V}_{C\alpha\beta 0}^{\Sigma\Delta}$ is:

$$\boldsymbol{V}_{C\alpha\beta 0}^{\Sigma\Delta *} = \begin{bmatrix} v_{C\alpha}^{\Sigma *} & v_{C\beta}^{\Sigma *} & v_{C0}^{\Sigma *} \\ v_{C\alpha}^{\Delta *} & v_{C\beta}^{\Delta *} & v_{C0}^{\Delta *} \end{bmatrix} = \begin{bmatrix} 0 & 0 & nv_C^* \\ 0 & 0 & 0 \end{bmatrix} \tag{5.12}$$

Hence, the voltage v_{C0}^Σ must be regulated to the desired total cluster voltage (nv_C^*), while the others five voltages may be regulated to zero. However, in a practical implementation, these five voltages have oscillations produced by the power flows through the clusters (see (5.5)) and only their mean value have to be null. To achieve the balance of the previous six voltages, it is necessary to create a manipulable power flow in (5.6)-(5.11). Defining $\bar{x}$ as the DC part of the variable x, and $\tilde{x}$ as its AC component (i.e. $x = \tilde{x} + \bar{x}$), is possible to prove that the power flow $E\bar{i}_\alpha^\Sigma$ could by used to regulate $v_{C\alpha}^\Sigma$, while $v_0\tilde{i}_\alpha^\Sigma$ is a power flow that modifies $v_{C\alpha}^\Delta$. The same analysis is valid for the β-variables. Furthermore, the power flow $E\bar{i}^P$ may be used to regulate v_{C0}^Σ, while the power flow $v_0\tilde{i}^P$ is able to control v_{C0}^Δ. See [11] for details regarding this control strategy and [6] for another suitable control scheme.

Nevertheless, in addition to the balancing task described previously, the amplitude of the voltage oscillations in the matrix $\boldsymbol{V}_{C\alpha\beta 0}^{\Sigma\Delta}$ have to be bounded to avoid extra voltage fluctuations in the M^{2}C capacitors. Analysing (5.6)-(5.11), it is concluded that most of the high oscillations are produced in $v_{C\alpha}^\Delta$ and $v_{C\beta}^\Delta$. As an example for $v_{C\alpha}^\Delta$, consider (5.9) and (5.5) when there is not circulating currents (the balancing currents tends to zero if the balancing controller is properly implemented); then, the voltage $v_{C\alpha}^\Delta$ yields:

$$v_{C\alpha}^\Delta \approx \tfrac{1}{Cv_C^*}\int \left(\tfrac{1}{2}Ei_\alpha - \tfrac{2}{3}i^P v_\alpha\right)dt \tag{5.13}$$

Additionally, if $v_\alpha = V\sin(\omega_e t)$ and $i_\alpha = I\sin(\omega_e t + \theta)$, (5.13) results:

$$v_{C\alpha}^\Delta \approx -\frac{EI}{2Cv_C^*\omega_e}\cos(\omega_e t + \theta) + \frac{2i^P V}{3Cv_C^*\omega_e}\cos(\omega_e t) \tag{5.14}$$

It should be noted that the voltage $v_{C\alpha}^{\Delta}$ is inversely proportional to the electrical AC Port frequency ω_e; then, large voltage oscillations are expected at low frequencies, being these oscillations reduced as the frequency increases. Consequently, the M^{2}C operation is divided into two operational modes: the Low Frequency Mode (LFM), where any low frequency term in the cluster power flow is eliminated to avoid the extra oscillations in the capacitor voltages, and the High Frequency Mode (HFM), where these oscillations are bounded inside an acceptable range (typically $\pm 10\%$ of v_C^*) [3].

5.4 Proposed control system at low AC frequencies in the M^{2}C

The contribution of this paper is focused on an improved control strategy of the M^{2}C at LFM. Specifically, two different methods to cancel or reduce the voltage fluctuations in the cell capacitors of the M^{2}C are developed. The first one is implemented by using a novel control scheme that combines dq and resonant control theories to regulate the circulating currents to cancel any low frequency term in the cluster power flows. The second one, shows that modifying the DC Port voltage is possible to avoid the use of circulating currents, at the same time that the voltage oscillations in the M^{2}C capacitors are reduced. This methodology is also valid for nominal frequencies. Both operative methods are described below.

5.4.1 Low Frequency Mode with circulating currents controlled in a rotating frame

Notice that i_α^Σ, i_β^Σ and v_0 are degrees of freedom that can be modified without change the machine currents and voltages, implying that each circulating current could be divided into two components: the balancing and the mitigating component. The first one is defined as was analysed in previous section, and its purpose is to balance the total cluster voltages. The second one is an extra current flow that reduces the low frequency terms in (5.9) and (5.10). Several waveforms for the mitigating component have been compared for this purpose [5, 3, 11]. However, if the $\Sigma\Delta\alpha\beta 0$ transformation is used, the set-point value for the mitigation circulating currents can be generalized as follows:

$$i_{\alpha m}^{\Sigma *}=\left(\tfrac{1}{2}Ei_\alpha-\tfrac{2}{3}i^P v_\alpha\right)\tfrac{f(t)}{2V_0},\qquad i_{\beta m}^{\Sigma *}=\left(\tfrac{1}{2}Ei_\beta-\tfrac{2}{3}i^P v_\beta\right)\tfrac{f(t)}{2V_0},\qquad v_0^*=V_0 g(t) \tag{5.15}$$

being $f(t)$ and $g(t)$ the Mitigation Functions and V_0 the maximum value of the common mode voltage.

Supposing $i_\alpha^\Sigma = i_{\alpha m}^{\Sigma *}$, $i_\beta^\Sigma = i_{\beta m}^{\Sigma *}$, $v_0 = v_0^*$ and replacing (5.15) into (5.9) and (5.10) yields:

$$p_\alpha^\Delta \approx \left(\tfrac{1}{2}Ei_\alpha - \tfrac{2}{3}i^P v_\alpha\right)\left[1-f(t)g(t)\right],\qquad p_\beta^\Delta \approx \left(\tfrac{1}{2}Ei_\beta - \tfrac{2}{3}i^P v_\beta\right)\left[1-f(t)g(t)\right] \tag{5.16}$$

Hence, the low frequency power flow in the clusters is cancelled if the mean value of $f(t)g(t)$ is 1. In (5.16) were neglected the relative high frequency components of p_α^Δ and p_β^Δ, due to

Table 5.1: Mitigation Functions for several mitigating methods

Method	$f(t)$	$g(t)$
Sinusoidal-Wave [3]	$2\sin(\omega_m t)$	$\sin(\omega_m t)$
Third-Order Harmonic [5]	$1.68\left[\sin(\omega_m t) + 0.16\sin(3\omega_m t)\right]$	$1.15\left[\sin(\omega_m t) + 0.16\sin(3\omega_m t)\right]$
Square-Wave [5]	$\sum_{k=1}^{\infty} \frac{4}{\pi k}\sin(k\omega_m t)$	$\sum_{k=1}^{\infty} \frac{4}{\pi k}\sin(k\omega_m t)$
Hybrid n-Order [11]	$\sum_{k=1}^{n} A_k \sin(k\omega_m t)$	$\sum_{k=1}^{\infty} \frac{4}{\pi k}\sin(k\omega_m t)$

Table 5.2: Optimal parameters of $f_n(t)$

n	A_1	A_3	A_5	A_7	max
1	1.571	0	0	0	1.571
3	1.473	0.295	0	0	1.282
5	1.425	0.362	0.125	0	1.187
∞	1.273	0.424	0.255	0.182	1

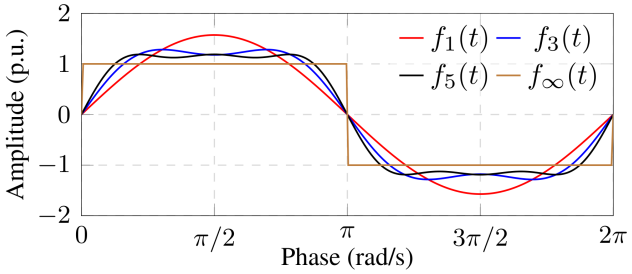

Figure 5.2: Graphical representation of $f_n(t)$

the fact that very high frequency oscillations are easily filtered out by the capacitors of each cell.

In Table 5.1 are shown expressions of $f(t)$ and $g(t)$ for the mitigating methods presented in [5, 3, 11], being ω_m the Mitigating Frequency, which must be as high as possible. Further, considering that the circulating currents are proportional to $f(t)$ (see (5.15)), the coefficients A_k in the Hybrid Method presented in Table 5.2 are obtained to reduce its peak value by solving the constrained optimization problem:

$$\min_{t} \max_{A_k} \left[f_n(t)\right], \quad \text{such that: } \frac{\omega_m}{2\pi}\int_0^{\frac{2\pi}{\omega_m}} \left[f_n(t)g(t)\right] dt = 1 \tag{5.17}$$

Table 5.2 shows the non-zero A_k optimal coefficients of $f(t)$ as a function of n (i.e. $f_n(t)$) and its maximum value. Additionally, in Fig. 5.2 is depicted the graphical representation of $f_n(t)$. Noticed that for $n \to \infty$, the Hybrid Method is equivalent to the Square-Wave Method [5]. Nevertheless, it is impossible to achieve a perfect current tracking for a square set-point waveform, because it requires infinity bandwidth. Moreover, considering the Sinusoidal-Wave Method as a comparative reference, with Table 5.1 and 5.2 it is proved that the peak value of the set-point circulating currents is reduced by 27% when the Third-Order Harmonic Method is used, by 21% for $n = 1$, 36% for $n = 3$ and 40% for $n = 5$ for the Hybrid Method and for 50% if the Square-Wave Method could be successfully implemented.

Although the mitigating methods allow to reduce the extra voltage oscillations in the LFM, this reduction is effective only if the circulating current controllers produces a good current tracking. The set-point value of these variables has several frequency components depending on n, ω_m and ω_e, which is a dynamic variable for drive systems (see (5.15)). Hence, P or PI controllers are not able to produce zero tracking error, degrading the performance of the mitigating task.

To solve the aforementioned problem, this paper proposes the implementation of the circulating current controllers in a rotating frame oriented with the electrical angle θ_e. Considering (5.4) and (5.15) and using vector relations ($\boldsymbol{v}^{\Sigma}_{\alpha\beta} = v^{\Sigma}_{\alpha} + jv^{\Sigma}_{\beta}$, $\boldsymbol{i}^{\Sigma}_{\alpha\beta m} = i^{\Sigma}_{\alpha m} + ji^{\Sigma}_{\beta m}$, etc.) results:

$$\boldsymbol{i}^{\Sigma*}_{\alpha\beta m} = \left[\tfrac{1}{2}E\boldsymbol{i}_{\alpha\beta} - \tfrac{2}{3}i^{P}\boldsymbol{v}_{\alpha\beta}\right]\tfrac{f(t)}{2V_0} \Rightarrow \boldsymbol{i}^{\Sigma*}_{dqm} = \left[\tfrac{1}{2}E\boldsymbol{i}_{dq} - \tfrac{2}{3}i^{P}\boldsymbol{v}_{dq}\right]\tfrac{f(t)}{2V_0} \tag{5.18a}$$

$$\boldsymbol{v}^{\Sigma}_{\alpha\beta} = -L\tfrac{d}{dt}\boldsymbol{i}^{\Sigma}_{\alpha\beta} \Rightarrow \boldsymbol{v}^{\Sigma}_{dq} = -L\tfrac{d}{dt}\boldsymbol{i}^{\Sigma}_{dqm} - j\omega_e\boldsymbol{i}^{\Sigma}_{dqm} \tag{5.18b}$$

Therefore, based on (5.18a), $\boldsymbol{i}^{\Sigma*}_{dqm}$ has only the frequency components of $f(t)$ (since the dq components of the M^{2}C ports are DC variables). Then, if the Hybrid Method is considered, only $n+1$ resonant controllers have to be implemented to regulate $\boldsymbol{i}^{\Sigma}_{dqm}$ (instead of $2(n+1)$ adaptive resonant controllers in a stationary frame). However, this control structure is also valid for the Sinusoidal-Wave and Third-Order Harmonic methods, because the function $f(t)$ is composed by sinusoidal signals. Fig. 5.3 (a) shows the proposed control system based on (5.18b), where the multi-resonant controllers are given by:

$$C_r(z) = K_r \prod_{k=1}^{n} \frac{z^2 - 2r_k\cos\left(k\omega_m T_s\right)z + r_k^2}{z^2 - 2\cos\left(k\omega_m T_s\right)z + 1} \tag{5.19}$$

where T_s is the sample time and $k \in \{1, 3, 5...\}$. In the diagram, the set-point value of the circulating currents is conformed by the mitigating and the balancing component. The dynamic of the second component is slow in comparison with the first one; then, the controllers allow a suitable current tracking.

Considering the high number of parameters in the proposed controller, in this paper is used an optimal tuning for them. The tuning criteria takes into account the performance/robustness trade-off of the control loop by solving the following optimization problem:

$$\min_{K_r, r_k} \sum_{h=0}^{\infty} |e(hT_s)| \text{ such that: } M_S^* = \max_{\omega} \left|\frac{1}{\underbrace{C_r(\omega)P(\omega)}_{H(z)} + 1}\right| = 2 \tag{5.20}$$

being $e(hT_s)$ the tracking error, $P(\omega)$ the discrete process model (including the total time delay) and M_s the peak of the sensitivity function. Graphically, M_S represents the inverse of the shortest distance from the Nyquist curve to the critical point $\langle -1, j0\rangle$, as is shown in Fig. 5.3 (b). Additionally, the gain margin A_m and the phase margin ϕ_m fulfil the following expressions:

$$A_m \geq \frac{M_S}{M_S - 1}, \quad \phi_m \geq 2\sin^{-1}\left(\frac{1}{2M_S}\right) \tag{5.21}$$

Thus, the system stability is guaranteed for changes in the process nominal model. It is common to consider $M_S \leq 2$ as a good robustness indicator, resulting in $A_m \geq 2$ and $\phi_m \geq 28.9°$ [12].

5.4.2 Low frequency mode applying a dynamic DC Port voltage

Even though the mitigating methods allow the operation of the M^{2}C at LFM, it is necessary an extra current through the clusters. This situation becomes extreme when the LFM is

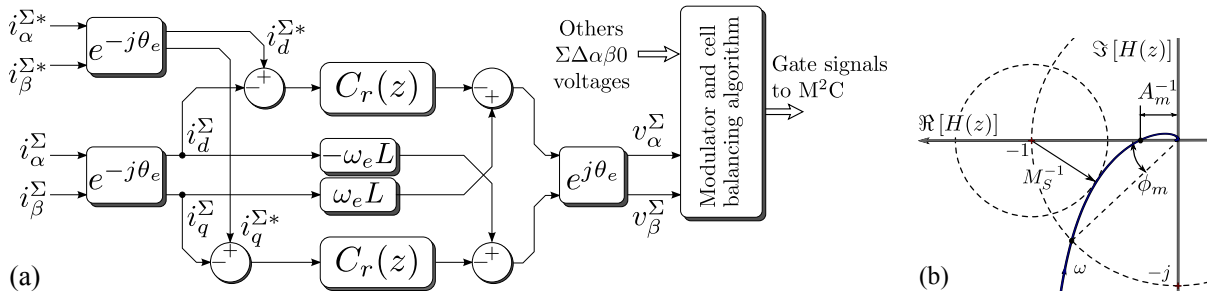

Figure 5.3: (a) Proposed circulating current controller in a rotating frame, (b) robust tuning criteria.

extended enough to generate a high voltage in the AC port, since the amplitude of the term $1/V_0$ tends towards infinity because V_0 must be reduced to generate the AC port voltage (see (5.15)) [7, 8]. To avoid this negative effect and to maintain the cluster current bounded, it is necessary to reduce the available output torque, limiting the type of loads that the M^{2}C can handle to quadratic torque-speed profiles, as was reported in [6, 8]. However, to eliminate the extra capacitor voltage oscillations at LFM without using circulating currents, this paper introduces a novel alternative, which is to regulate the DC Port voltage according to the AC Port frequency. This procedure is explained using the voltage $v_{C\alpha}^{\Delta}$ as a representative example.

Consider $i_\alpha = I\sin(\omega_e t + \theta)$ and $v_\alpha \approx k_v \omega_e \sin(\omega_e t)$ (as occurs if a vector control scheme is used and for non-zero speeds), being k_v a constant that is function of the rotor flux and the machine number of poles. Additionally, if the DC Port voltage is defined as $E = k_E \omega_e$ being k_E a constant, (5.13) results:

$$v_{C\alpha}^{\Delta} \approx -\frac{I k_E}{2 C v_C^*}\cos(\omega_e t + \theta) + \frac{2 i^P k_v}{3 C v_C^*}\cos(\omega_e t) \tag{5.22}$$

Comparing (5.14) and (5.22), it is clear that the adverse impact in the amplitude of $v_{C\alpha}^{\Delta}$ is not presented when the DC Port voltage is proportional to the electrical frequency ω_e. In fact, the amplitude of the voltage $v_{C\alpha}^{\Delta}$ is a function of the amplitude of the AC and DC Port currents; then, it remains bounded for any torque-speed profile and there is no requirement of mitigating power flows.

It is evident that this method is not applied to the overall frequency range since the instantaneous DC Port voltage can not be zero for a M^{2}C topology and a voltage margin must be guaranteed for control purposes. Additionally, an extra device is required to adapt the dynamic DC Port voltage to the grid. However, this methodology allows a reduction of the conventional LFM of the M^{2}C, reducing the current flow through the clusters and the common mode voltage, improving the converter efficiency. These features can be beneficial for systems where the operation of the M^{2}C is bounded between a non-zero speed range in normal operation, as in Wind Energy Conversion Systems (WECSs), where a high quality of the voltage and current injected to the grid is mandatory and a Back-to-Back scheme is recommended [13].

Table 5.3: Experimental set-up parameters

Parameter	Symbol	Value	Unit
DC Port voltage	E	450	V
Cells per cluster	n	3	-
Cluster inductor	L	2,5	mH
Cell capacitor	C	4700	μF
Cell DC voltage	v_C^*	160	V
Switching frequency	f_s	5000	Hz
Mitigating frequency	ω_m	314	rad/s

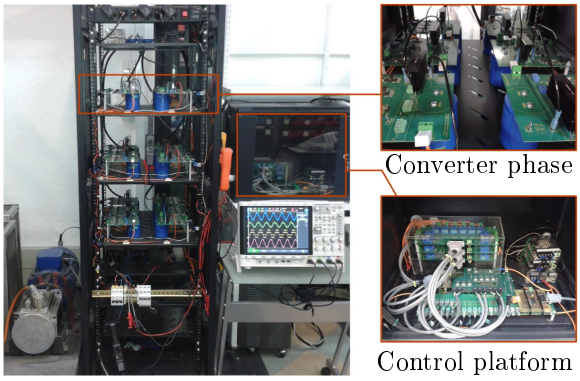

Figure 5.4: Experimental set-up

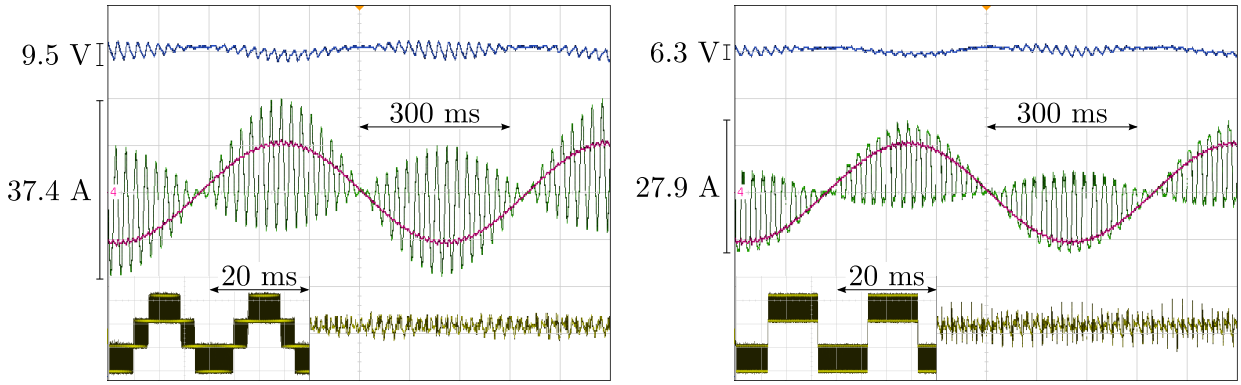

(a) Sinusoidal-Wave [3]

(b) Hybrid Method for $n = 3$ [11]

Figure 5.5: Comparative performance of mitigating methods. Blue: capacitor voltage (20 V/Div, 160 V mean value), red: machine current (10 A/Div), green: cluster current (10 A/Div), yellow: DC Port current (10 A/Div), zoom yellow: cluster voltage (150 V/Div).

5.5 Experimental and simulation results

The effectiveness of the proposed control strategies has been determined using experimental and simulation work. The novel circulating current controller is validated with a laboratory prototype of the M^{2}C driving an induction motor controlled by field oriented control. Fig. 5.4 shows the experimental set-up, where the feedback signals are measured by two FPGAs (Actel ProAsic3E) and processed by a DSP (TMS320C6713). The system parameters are summarized in Table 5.3. Otherwise, the manipulation of the DC Port voltage and its effect on the M^{2}C drive is analysed by using a simulation of the same experimental system. In both cases the control scheme presented in [11] was implemented, changing the circulating current controller by the proposed in this work.

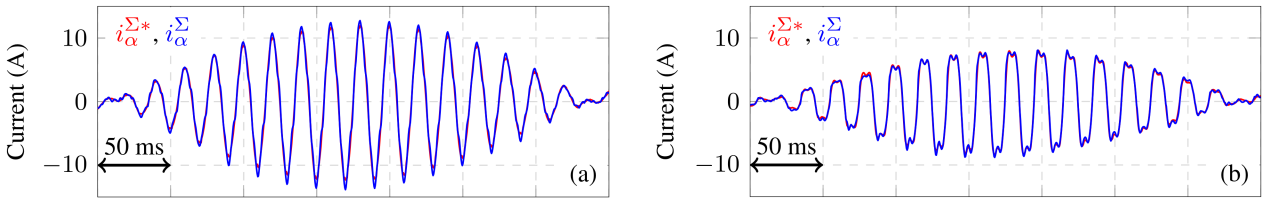

Figure 5.6: Current control. (a) Sinusoidal-Wave [3], (b) Hybrid Method (n=3) [11].

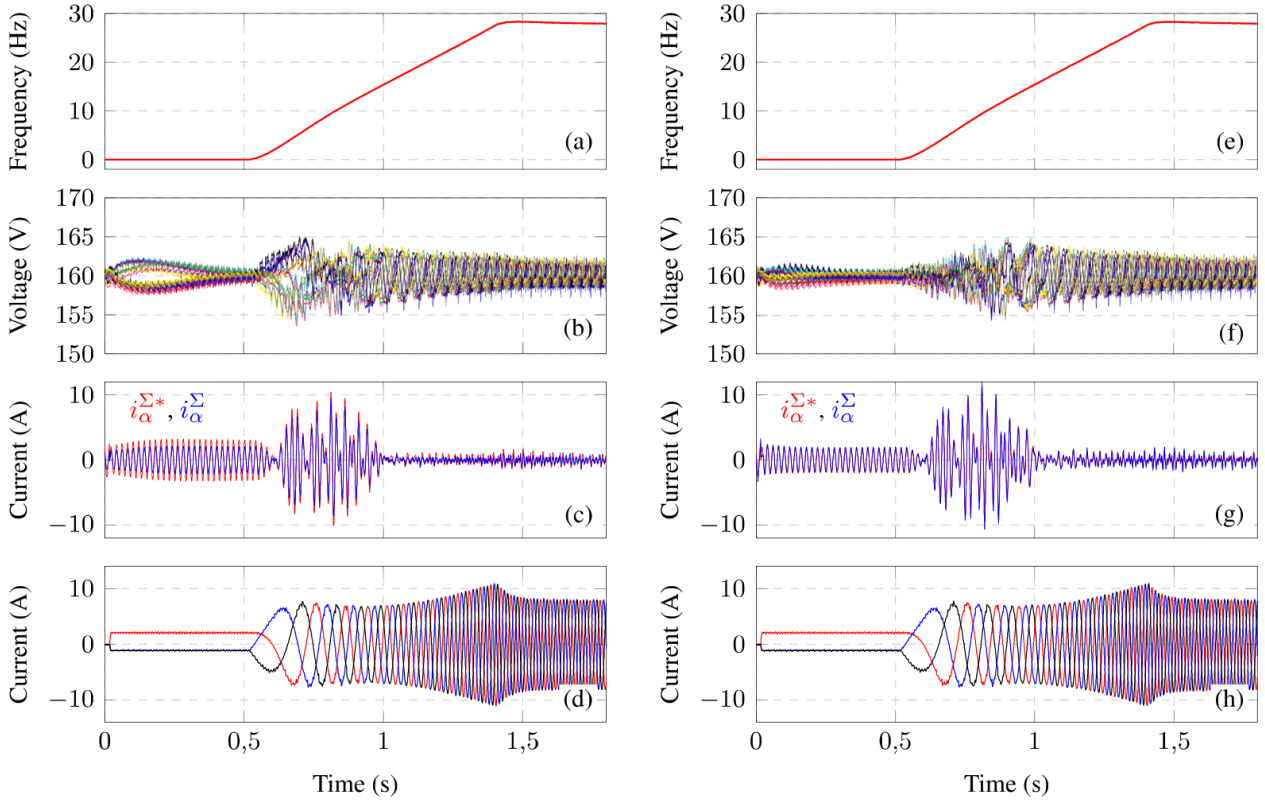

Figure 5.7: Dynamic system performance. Left: proportional controller, right: proposed controller.

5.5.1 Control of the circulating currents in a rotating frame

The performance of the novel circulating current controller has been compared for two mitigating methods: the Sinusoidal-Wave and the Hybrid Method for $n = 3$. This comparison is illustrated in Fig. 5.5 and Fig. 5.6. In the test, the induction machine shaft is blocked and the torque current is regulated to 10 A; then, the electrical stator frequency is the slip frequency (near to 1.53 Hz). Fig. 5.5 shows that, in comparison with the Sinusoidal-Wave Method, the Hybrid Method is able to reduce the cluster current in 25% and the capacitor voltage oscillation in 34%. However, to achieve this reduction a square wave common mode voltage is required, as is reflected in the DC Port current and the cluster voltage (this is also discussed in [10]). The circulating current for both methods is shown in Fig. 5.6. Notice that the set-point value of the circulating currents is composed by balancing and mitigating components. Therefore, low variations from the nominal value given in (5.15) are expected. Although, the controller is able to perform a suitable current tracking, having the peak value

of the set-point signal for both methods a difference of 33% (3% of error with respect to the theoretical value calculated above).

Fig. 5.7 shows the comparison of the proposed control topology and the conventional control P. Both controllers were tuned by using the rule defined in (5.20). In this test the induction machine is accelerated from 0 rpm to 1600 rpm and a permanent magnet generator with load resistors has been affixed to its shaft, creating a quadratic torque-speed load. As is depicted in Fig. 5.7 (a) and (d) and Fig. 5.7 (e) and (h), the electrical machine frequency and its currents are similar; hence, any difference in the capacitor voltages will be mainly produced by the circulating currents. It is clear from Fig. 5.7 (c) that the proportional controller is not able to achieve a suitable current tracking, producing extra oscillations in the 18 capacitor voltages (see Fig. 5.7 (b)). It is important to note that if a better current tracking is needed, the controller gain must be increased, degrading the relative stability of the control loop. However, if the proposed controller is used, the current tracking is improved and there is not a noticeable phase shift between the set-point value and the feedback signal, producing a decrease in the oscillations of the capacitor voltages. Finally, notice that the proposed controller is also suitable for the HFM, where the mitigation signals are disabled and only the balancing components of the circulating current have to be regulated.

5.5.2 Dynamic variation of the DC Port voltage

In Fig. 5.8 are shown the simulated variables of the M^2C drive for quadratic (left) and constant (right) torque-speed profiles when the DC Port voltage is dynamically changed. In the simulation the machine start-up is achieved by using the conventional LFM strategy, since the DC Port voltage can not be zero. However, after $3,8$ s, the machine speed and the DC Port voltage are periodically changed, respectively from 100% to 10% and from 100% to 33% of their nominal value (see Fig. 5.8(a) and (f)).

Notice from Fig. 5.8(d) and (i) that the mean value of the duty cycle of the M^2C cells is affected by the DC Port voltage, modifying the power delivered by the cells and the capacitor voltages. As depicted in Fig. 5.8(b), the voltage oscillation is properly bounded for quadratic torque-speed profiles. For the constant torque load, these oscillations are also bounded and their peak-to-peak value when the DC Port voltage is minimised is similar to the obtained for a 70% of the electrical frequency for the conventional LFM [see Fig. 5.8(g) and (f)]. Moreover, as shown in Fig. 5.8(c) and (h), in both cases the cluster currents are composed only by the AC and DC components of the port and balancing currents, reducing the current flow through the cluster (particularly for a constant torque load).

5.6 Conclusions

This paper has presented several improvements to the LFM of the M^2C-based machine drive control. It has been shown that the circulating currents expressed in a rotating dq-frame can be controlled by using resonant controllers, improving the current tracking and reducing he

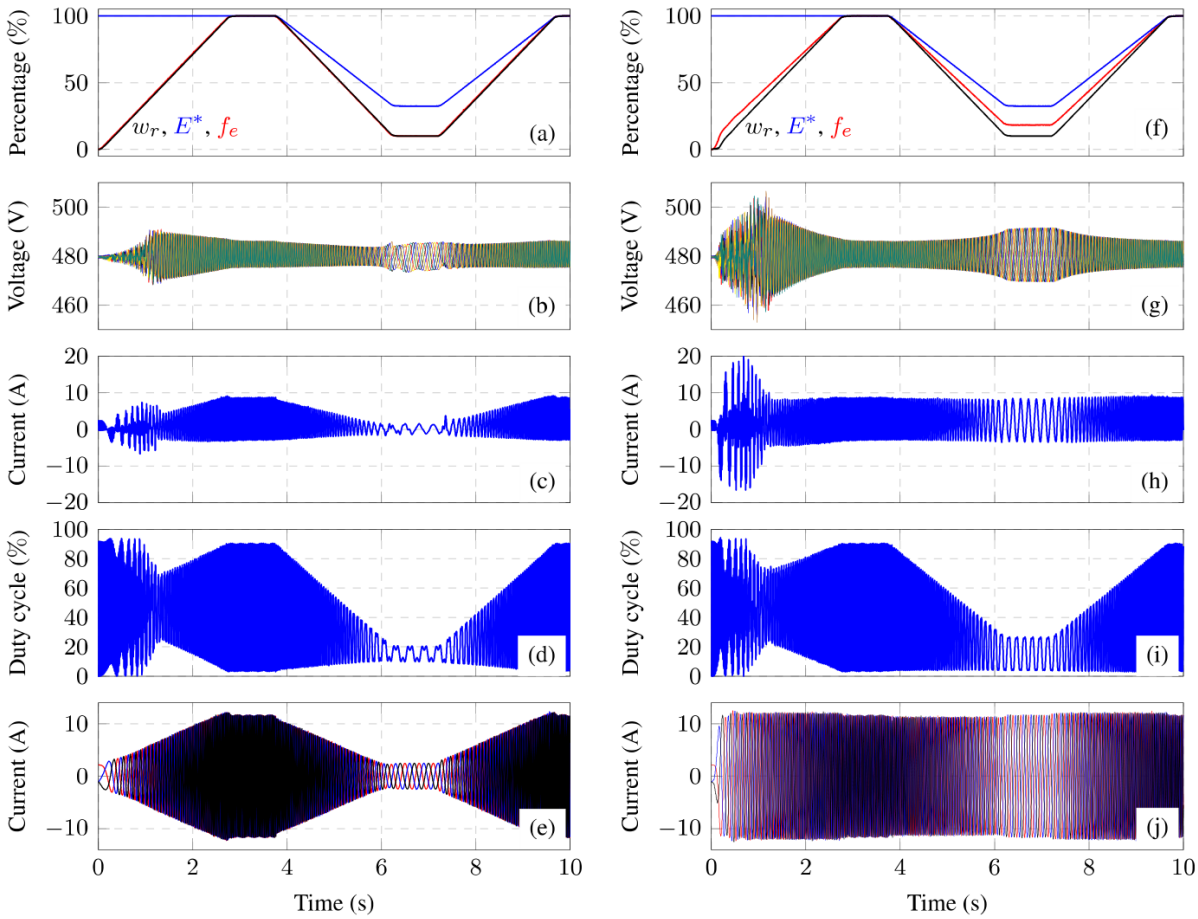

Figure 5.8: Effect of the torque-speed profile and dynamic DC Port voltage. Left: quadratic, right: constant.

voltage fluctuations in the M^{2}C capacitors. Analysing experimental results, it is evident that the proposed control scheme is applied to different mitigation methods, and its performance is high in comparison with conventional control topologies. Additionally, it is proposed a novel methodology, based on the variation of the DC Port voltage as a function of the AC Port frequency, to allow the low frequency operation of the M^{2}C drive without circulating currents injection (even for nominal AC Port current). The proposed method is suitable for high power machines with not-nominal torque at start-up, or for applications where the operation of the M^{2}C is bounded between a non-zero speed, i.e., sag mills and wind energy applications. Simulation results shown that the proposed DC Port voltage control is applicable to constant and quadratic torque-speed profiles, allowing a stable operation to low speeds and keeping bounded the M^{2}C capacitor voltages without mitigating currents.

Bibliography

[1] R. Marquardt, "Stromrichterschaltungen mit verteilten energiespeichern," German Patent DE20 122 923 U1, 2001.

[2] M. Glinka and R. Marquardt, "A new AC/AC multilevel converter family," *Industrial Electronics, IEEE Transactions on*, vol. 52, no. 3, pp. 662–669, June 2005.

[3] A. J. Korn, M. Winkelnkemper, and P. Steimer, "Low Output Frequency Operation of the Modular Multi-Level Converter," in *Energy Conversion Congress and Exposition (ECCE), 2010 IEEE*. IEEE, 12-16 September 2010.

[4] A. Antonopoulos, L. Angquist, S. Norrga, K. Ilves, L. Harnefors, and H.-P. Nee, "Modular Multilevel Converter AC Motor Drives With Constant Torque From Zero to Nominal Speed," *Industry Applications, IEEE Transactions on*, vol. 50, no. 3, pp. 1982–1993, May 2014.

[5] M. Hagiwara, I. Hasegawa, and H. Akagi, "Start-Up and Low-Speed Operation of an Electric Motor Driven by a Modular Multilevel Cascade Inverter," *IEEE Transactions on Industry Applications*, vol. 49, no. 4, pp. 1556–1565, July-August 2013.

[6] J. Kolb, F. Kammerer, M. Gommeringer, and M. Braun, "Cascaded Control System of the Modular Multilevel Converter for Feeding Variable-Speed Drives," *Power Electronics, IEEE Transactions on*, vol. 30, no. 1, pp. 349–357, Jan 2015.

[7] K. Ilves, L. Bessegato, and S. Norrga, "Comparison of cascaded multilevel converter topologies for ac/ac conversion," in *Power Electronics Conference (IPEC-Hiroshima 2014 - ECCE-ASIA), 2014 International*, May 2014, pp. 1087–1094.

[8] Y. Okazaki, W. Kawamura, M. Hagiwara, H. Akagi, T. Ishida, M. Tsukakoshi, and R. Nakamura, "Which is more suitable for MMCC-based medium-voltage motor drives, a DSCC inverter or a TSBC converter?" in *Power Electronics and ECCE Asia (ICPE-ECCE Asia), 2015 9th International Conference on*, June 2015, pp. 1053–1060.

[9] Y. Wan, S. Liu, and J. Jiang, "Generalised analytical methods and current-energy control design for modular multilevel cascade converter," *Power Electronics, IET*, vol. 6, no. 3, pp. 495–504, March 2013.

[10] B. Li, S. Zhou, D. Xu, D. Xu, and W. Wang, "Comparative study of the sinusoidal-

wave and square-wave circulating current injection methods for low-frequency operation of the modular multilevel converters," in *2015 IEEE Energy Conversion Congress and Exposition (ECCE)*, Sept 2015, pp. 4700–4705.

[11] M. Espinoza, A. Mora, M. Diaz, and R. Cárdenas, "Balancing energy and low frequency operation of the Modular Multilevel Converter in Back to Back configuration," in *Ecological Vehicles and Renewable Energies (EVER), 2015 International Conference on*, March 2015, pp. 1–9.

[12] M. Espinoza, J. D. Rojas, R. Vilanova, and O. Arrieta, "Robustness/performance tradeoff for anisochronic plants with two degrees of freedom PID controllers," in *2015 IEEE Conference on Control Applications (CCA)*, Sept 2015, pp. 1230–1235.

[13] J. Dorn, H. Gambach, J. Strauss, T. Westerweller, and J. Alligan, "Trans bay cable-A breakthrough of VSC multilevel converters in HVDC transmission," in *CIGRE San Francisco Colloq.*, 2012.

Chapter 6

Modelling and Control of the Modular Multilevel Converter in Back to Back Configuration for High Power Induction Machine Drives

This chapter is based on the conference paper:

M. Espinoza, R. Cárdenas, M. Diaz, A. Mora, and Soto. D. Modelling and Control of the Modular Multilevel Converter in Back to Back Configuration for High Power Induction Machine Drives. In *IEEE Industrial Electronics Society (IECON), 2016 42nd Annual Conference of*, pages 24–27, Florence, Italy, October 2016

Abstract: Drives based on modular multilevel topologies are the next generation of high-power/voltage converters. In this paper, the Modular Multilevel Converter model is extended to the Back to Back scheme, allowing its control as an unique system, instead two separated converters. Additionally, the proposed control strategy is able to regulate the ac ports and to perform the voltage balancing in both converters by using circulating currents and common mode voltage, providing independence between the converters and the ac ports. Extensive computer simulation and a laboratory prototype of a Modular Multilevel Converter with eighteen power cells feeding an induction machine validate the effectiveness of the presented control algorithm.

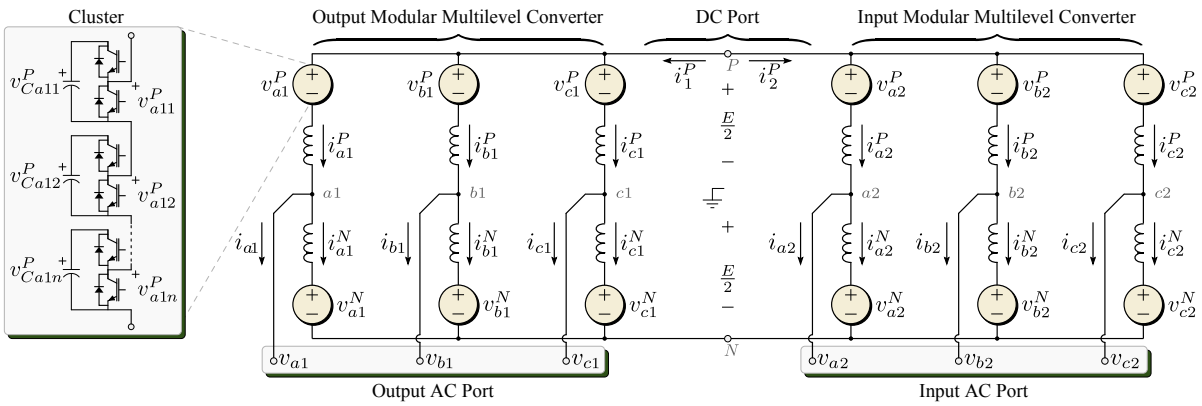

Figure 6.1: Modular Multilevel Converter in Back to Back configuration.

6.1 Introduction

Since the invention of the Modular Multilevel Converter (MMC) this topology has been proposed for rail train and energy conversion applications, such that high voltage dc transmission (HVDC), where a MMC in Back to Back (BTB) configuration is implemented [1,2]. However, the application of the MMC in motor drives has been amply researched and validated with laboratory prototypes [3–5]. As a consequence, the emergence of BTB-MMC based drives may be possible.

The topology of the BTB-MMC is shown in Fig. 6.1. This converter consists of two MMC connected by their dc port, allowing an ac/dc/ac conversion between both ac ports. Each one of the six "clusters" that form an MMC has n cells connected in cascade and one inductor L. The cell is composed of a half bridge circuit and a "flying" capacitor C. Therefore, the control of the BTB-MMC does not involve only the regulation of ac signals, since the voltage in each cell must be bounded between an acceptable range, even for low frequency operation in the ac ports, which cause high voltage fluctuations in the cell capacitor voltages [6]. For this reason, the converter has at least two modes of operation: High Frequency Mode (HFM) and Low Frequency Mode (LFM).

Several control schemes for HFM have been developed in [4,7]. However, these approaches do not use a decoupled methodology to control the MMC, forcing interactions among control loops that could degraded the dynamic performance. In [5] a control system for each port performing a decoupled balancing is presented. Nevertheless, the control algorithm did not consider the BTB scheme and used the machine voltages to balance the converter energy, over simplifying the control problem for variable speed applications.

At LFM, the power delivered by the circulating currents and the common mode voltage is used to mitigate the voltage fluctuations in the MMC capacitors. A circulating current is a current that has not emergence at the ac port [8]. However, if a BTB-MMC is implemented as motor drive, only the machine-side MMC will enter in LFM at the motor start-up since the grid-side MMC has a constant frequency in its ac port. Consequently, in comparison with other modular multilevel topologies for ac/ac operation, the capacitor cell and the current rating of the grid-side MMC can be reduced [9, 10].

Summarizing, a control scheme for the BTB-MMC must fulfil the following requirements:

1. To balance the capacitor voltages in the converter clusters.
2. Independence of the ac ports and the balancing control.
3. To take the BTB scheme as a complete unit.
4. Optimal design of the mitigation signals to avoid extra current stress at LFM in the Machine MMC.

In this paper, the control scheme that complies the aforementioned requirements for the BTB MMC drive is proposed. The paper is divided as follows: Section 6.2 presents the model of the MMC in BTB scheme. The control system based on this model is presented in Section 6.3. Extensive simulations and experimental results to validate the effectiveness of the control strategy are analysed in Section 6.4. Finally, the conclusions of this work are presented in Section 6.5.

6.2 Analysis of the MMC

6.2.1 Decoupled model of the MMC

Considering Fig. 6.1 and neglecting the subscripts "1" and "2" due to the Back to Back symmetry, it is possible to obtain the following dynamic relations for each MMC:

$$\frac{E}{2}\begin{bmatrix} 1 & 1 & 1 \\ 1 & 1 & 1 \end{bmatrix} = \underbrace{\begin{bmatrix} v_a^P & v_b^P & v_c^P \\ v_a^N & v_b^N & v_c^N \end{bmatrix}}_{\boldsymbol{V}_{abc}^{PN}} + L\frac{d}{dt}\underbrace{\begin{bmatrix} i_a^P & i_b^P & i_c^P \\ i_a^N & i_b^N & i_c^N \end{bmatrix}}_{\boldsymbol{I}_{abc}^{PN}} + \begin{bmatrix} v_a & v_b & v_c \\ \text{-}v_a & \text{-}v_b & \text{-}v_c \end{bmatrix} \tag{6.1}$$

$$\frac{d}{dt}\underbrace{\begin{bmatrix} v_{Ca}^P & v_{Cb}^P & v_{Cc}^P \\ v_{Ca}^N & v_{Cb}^N & v_{Cc}^N \end{bmatrix}}_{\boldsymbol{V}_{Cabc}^{PN}} \approx \frac{1}{Cv_C^*}\underbrace{\begin{bmatrix} p_a^P & p_b^P & p_c^P \\ p_a^N & p_b^N & p_c^N \end{bmatrix}}_{\boldsymbol{P}_{abc}^{PN}=\boldsymbol{V}_{abc}^{PN}\circ\boldsymbol{I}_{abc}^{PN}} \tag{6.2}$$

where (6.1) results to applying the Kirchhoff's voltage law and (6.2) is the relation between the available voltage and the power flow of each cluster, being v_C^* the desired voltage in each cell and "$\circ$" the Hadamard product of two matrices.

Analysing (6.1)-(6.2), it is not simple to understand how the matrix $\boldsymbol{V}_{abc}^{PN}$ should be manipulated to control the converter ports and to regulate the available voltage among the converter clusters. Consequently, (6.1)-(6.2) has to be transformed to obtain a decoupled model of each MMC. This objective is performed applying the $\Sigma\Delta\alpha\beta0$ transformation [5,11], which transforms a matrix $\boldsymbol{X}_{abc}^{PN}$ into a matrix $\boldsymbol{X}_{\alpha\beta0}^{\Sigma\Delta}$ as follows:

$$\boldsymbol{X}_{\alpha\beta0}^{\Sigma\Delta} = \begin{bmatrix} \frac{1}{2} & \frac{1}{2} \\ 1 & -1 \end{bmatrix} \cdot \boldsymbol{X}_{abc}^{PN} \cdot \begin{bmatrix} \frac{2}{3} & -\frac{1}{3} & -\frac{1}{3} \\ 0 & \frac{1}{\sqrt{3}} & -\frac{1}{\sqrt{3}} \\ \frac{1}{3} & \frac{1}{3} & \frac{1}{3} \end{bmatrix}^{\mathsf{T}} \tag{6.3}$$

Then, applying (6.3) to (6.1)-(6.2) and simplifying yields:

$$\begin{bmatrix} 0 & 0 & \frac{E}{2} \\ 0 & 0 & 0 \end{bmatrix} = \begin{bmatrix} v_\alpha^\Sigma & v_\beta^\Sigma & v_0^\Sigma \\ v_\alpha^\Delta & v_\beta^\Delta & v_0^\Delta \end{bmatrix} + L\frac{d}{dt}\begin{bmatrix} i_\alpha^\Sigma & i_\beta^\Sigma & \frac{1}{3}i^P \\ i_\alpha & i_\beta & 0 \end{bmatrix} + 2\begin{bmatrix} 0 & 0 & 0 \\ v_\alpha & v_\beta & v_0 \end{bmatrix} \tag{6.4}$$

$$\frac{d}{dt}\underbrace{\begin{bmatrix} v_{C\alpha}^\Sigma & v_{C\beta}^\Sigma & v_{C0}^\Sigma \\ v_{C\alpha}^\Delta & v_{C\beta}^\Delta & v_{C0}^\Delta \end{bmatrix}}_{\boldsymbol{V}_{C\alpha\beta0}^{\Sigma\Delta}} \approx \frac{1}{Cv_C^*}\underbrace{\begin{bmatrix} p_\alpha^\Sigma & p_\beta^\Sigma & p_0^\Sigma \\ p_\alpha^\Delta & p_\beta^\Delta & p_0^\Delta \end{bmatrix}}_{\boldsymbol{P}_{\alpha\beta0}^{\Sigma\Delta}} \tag{6.5}$$

where v_α, v_β, v_0, i_α and i_β are the ac port voltages and currents in $\alpha\beta0$ coordinates. Therefore, (6.4) shows that the port and circulating currents (i_α^Σ and i_β^Σ) have been decoupled. Moreover, $\boldsymbol{V}_{C\alpha\beta0}^{\Sigma\Delta}$ can be controlled by manipulating $\boldsymbol{P}_{\alpha\beta0}^{\Sigma\Delta}$. The elements of $\boldsymbol{P}_{\alpha\beta0}^{\Sigma\Delta}$ are defined as in [5]:

$$p_\alpha^\Sigma = \tfrac{1}{2}Ei_\alpha^\Sigma - \tfrac{1}{4}i_\alpha v_\alpha + \tfrac{1}{4}i_\beta v_\beta - \tfrac{1}{2}i_\alpha v_0 \tag{6.6}$$

$$p_\beta^\Sigma = \tfrac{1}{2}Ei_\beta^\Sigma + \tfrac{1}{4}i_\beta v_\alpha + \tfrac{1}{4}i_\alpha v_\beta - \tfrac{1}{2}i_\beta v_0 \tag{6.7}$$

$$p_0^\Sigma = \tfrac{1}{6}Ei^P - \tfrac{1}{4}i_\alpha v_\alpha - \tfrac{1}{4}i_\beta v_\beta \tag{6.8}$$

$$p_\alpha^\Delta = \tfrac{1}{2}Ei_\alpha - \tfrac{2}{3}i^P v_\alpha - i_\alpha^\Sigma v_\alpha + i_\beta^\Sigma v_\beta - 2i_\alpha^\Sigma v_0 \tag{6.9}$$

$$p_\beta^\Delta = \tfrac{1}{2}Ei_\beta - \tfrac{1}{3}2i^P v_\beta + i_\beta^\Sigma v_\alpha + i_\alpha^\Sigma v_\beta - 2i_\beta^\Sigma v_0 \tag{6.10}$$

$$p_0^\Delta = -i_\alpha^\Sigma v_\alpha - i_\beta^\Sigma v_\beta - \tfrac{2}{3}i^P v_0 \tag{6.11}$$

and the set-point of $\boldsymbol{V}_{C\alpha\beta0}^{\Sigma\Delta}$ is calculated considering that all capacitor voltages are equal to v_C^* (balance condition):

$$\begin{bmatrix} v_{C\alpha}^{\Sigma*} & v_{C\beta}^{\Sigma*} & v_{C0}^{\Sigma*} \\ v_{C\alpha}^{\Delta*} & v_{C\beta}^{\Delta*} & v_{C0}^{\Delta*} \end{bmatrix} = \begin{bmatrix} 0 & 0 & nv_C^* \\ 0 & 0 & 0 \end{bmatrix} \tag{6.12}$$

6.2.2 Model of the MMC in Back to Back configuration

The MMC connection in a BTB scheme is made through the dc port; therefore, adapting (6.4) to Fig. 6.1 and considering that $-i_2^P = i_1^P = i^P$ results:

$$\tfrac{1}{3}L\frac{d}{dt}i^P = \tfrac{1}{2}E - v_{01}^\Sigma, \qquad -\tfrac{1}{3}L\frac{d}{dt}i^P = \tfrac{1}{2}E - v_{02}^\Sigma \tag{6.13}$$

Hence, solving (6.13) for i^P and E results,

$$\tfrac{2}{3}L\frac{d}{dt}i^P = -v_{01}^\Sigma + v_{02}^\Sigma = u_1^\Sigma, \quad E = v_{01}^\Sigma + v_{02}^\Sigma = u_2^\Sigma \tag{6.14}$$

Consequently, the complete BTB model is achieved considering (6.4)-(6.5) for each MMC and (6.14). Notice that the dc port voltage E is directly imposed by using the signals v_{01}^Σ and v_{02}^Σ. Hence, based on an analysis of the $\Sigma\Delta\alpha\beta0$ transform, the dc port voltage results proportional to the sum of all cell voltages. Moreover, the dc port current i^P is manipulated by the difference of the average value of the cells in both MMC.

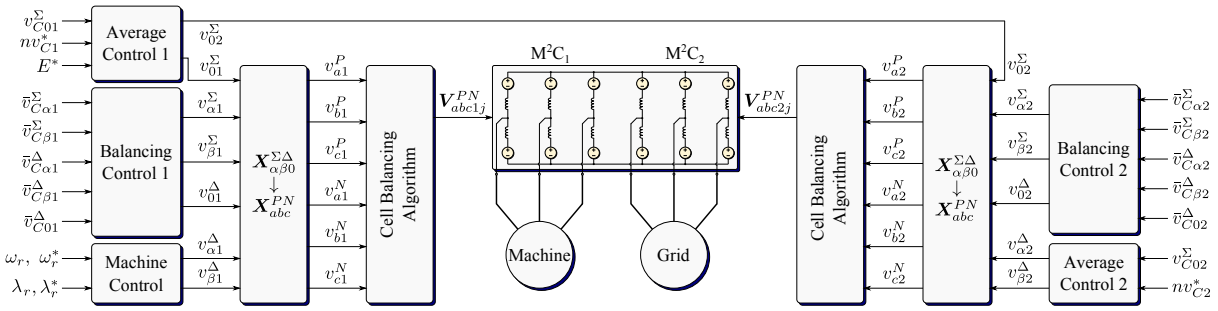

Figure 6.2: Overall control system for the MMC

6.3 Proposed control system for the BTB MMC

The block diagram of the proposed control system for the BTB MMC is depicted in Fig. 6.2. Particularly, this diagram considers a cascade structure, where the outer controllers balance the available cluster voltage and the inner controllers control the converter currents. The former controllers are tuned considering (6.5) and (6.6)-(6.11), while the latter controllers are based on (6.4). For a description of the cell balancing algorithm see [12]. In the following subsections the internal structure and objective of each subordinated control system is presented.

6.3.1 Machine Control

The dq vector model of the ac port variables of (6.4) results:

$$-\boldsymbol{v}_{dq1}^{\Delta} = L\frac{d}{dt}\boldsymbol{i}_{dq1} + j\omega_{e1}L\boldsymbol{i}_{dq1} + 2\boldsymbol{v}_{dq1} \tag{6.15}$$

On the other hand, the stator dynamic model of an induction machine applying rotor-field oriented control and supposing constant rotor flux, with $\boldsymbol{\psi}_r = \psi_{rd1} = L_0 i_{sd1}$ is [13]:

$$\boldsymbol{v}_{dq1}{=}R_s\boldsymbol{i}_{dq1} + \sigma L_s\frac{d}{dt}\boldsymbol{i}_{dq1} + j\omega_{e1}\left(\sigma L_s\boldsymbol{i}_{dq1}{+}\frac{L_0}{L_r}\boldsymbol{\psi}_r\right) \tag{6.16}$$

where R_s is the stator resistance, σ is the total leakage factor and L_s, L_r and L_0 are the stator, rotor and mutual inductances. Hence, from (6.15) and (6.16) defining $L' = L + 2\sigma L_s$ yields:

$$-\boldsymbol{v}_{dq1}^{\Delta}{=}2R_s\boldsymbol{i}_{dq1}{+}L'\frac{d}{dt}\boldsymbol{i}_{dq1}{+}j\omega_{e1}\left(L'\boldsymbol{i}_{dq1}{+}2\frac{L_0}{L_r}\boldsymbol{\psi}_r\right) \tag{6.17}$$

Fig. 6.3 shows the corresponding control diagram, where the outer controllers define the desired value of the torque and flux currents. Notice that the decouple terms u_{fd1}^{Δ} and u_{fq1}^{Δ} are the last terms of (6.17). Further, the manipulated voltages into $\alpha\beta 0$ coordinates, are v_{d1}^{Δ} and v_{q1}^{Δ}, instead of the machine voltages, due to the inductor voltage drop must be considered.

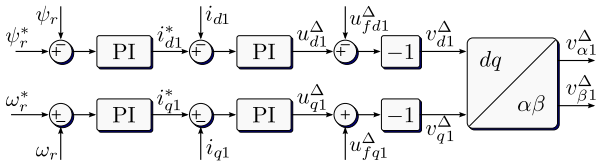

Figure 6.3: Machine control system

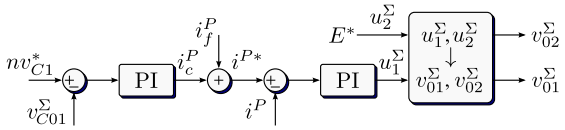

(a) Machine MMC

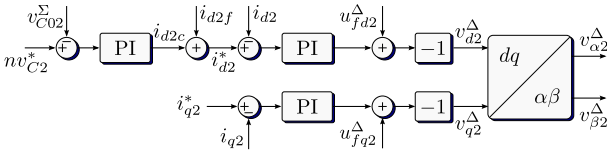

(b) Grid MMC (*dq* scheme)

Figure 6.4: Average control systems for the BTB MMC

6.3.2 Average Control

The objective of this control is to ensure the desired average voltage value for each MMC manipulating the current of its input port; therefore, its implementation depends on the MMC.

Average Control 1 (Machine MMC)

its block diagram is shown in Fig. 6.4a. The outer controller defines the set point value of the dc port current i_c^P comparing v_{C01}^{Σ} with nv_{C1}^* (see (6.12)). The transfer function for i_c^P and v_{C01}^{Σ} and the feed-forward current i_f^P can be straightforward obtained from (6.8) and (6.5).

Additionally, the inner dc port current controller and the set point value of the dc port voltage E^* are used to define the voltages v_{01}^{Σ} and v_{02}^{Σ} (see (6.14)).

Average Control 2 (Grid MMC)

(6.4) suggests that the ac port currents $i_{\alpha 2}$ and $i_{\beta 2}$ can be controlled by using a *dq* scheme as the presented in Fig. 6.4b, where the rotating frame has been oriented with the grid voltage (i.e $v_{q2} = 0$). Hence, i_{d2} defines the active power to the Grid MMC and i_{q2} defines the reactive power (typically i_{q2}^*=0 for drive applications). The transfer function for the outer controller and the feedforward current i_{d2f} are calculated based on (6.8) and (6.5). Additionally, the decouple terms u_{fd2}^{Δ} and u_{fq2}^{Δ} can be obtained from (6.15), changing the converter sub-index.

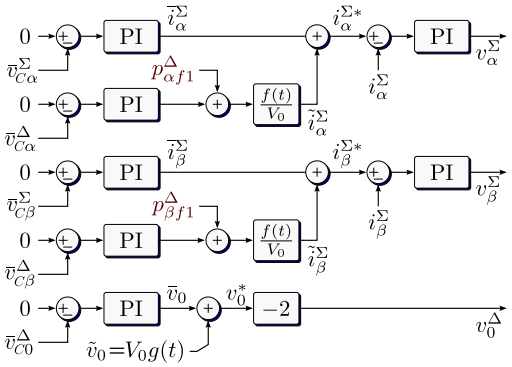

Figure 6.5: Balancing controller for both MMC ($p^{\Delta}_{\alpha 1 f}$ and $p^{\Delta}_{\beta 1 f}$ are used only for the machine converter in LFM)

6.3.3 Balancing Control

Considering (6.5) and (6.6)-(6.11), it is possible to prove that a dc component in i^{Σ}_{α} ($\bar{i}^{\Sigma}_{\alpha}$) will produce a power flow able to regulate $v^{\Sigma}_{C\alpha}$, while its ac component ($\tilde{i}^{\Sigma}_{\alpha}$) in phase with v_0 will generate a power flow that modifies $v^{\Delta}_{C\alpha}$. The same analysis can be made for the β-variables. Further, v^{Δ}_{C0} can be regulated at HFM with a dc component in the common mode voltage ($\bar{v}^{\Delta}_{C0}$), while at LFM this can be performed using an ac component in the dc port current in phase with v_0.

Accordingly, Fig. 6.5 shows the Balancing Control system for both MMC, where the components mentioned above are defined by PI controllers. The indicative sub-index for each converter has been omitted due to their similar behaviour. Additionally, only the dc components of the voltage signals are regulated to zero (see (6.12)) to decrease the use of the circulating currents in steady state. The ac component of the common mode voltage $\tilde{v}_0 = V_0 g(t)$ and $f(t)$ create the ac components and are defined considering the operating point of each MMC.

Balancing Control for HFM

In HFM V_0, $f(t)$ and $g(t)$ are defined to maximise the modulation index of each MMC by the third harmonic injection method, then:

$$f(t)=2\sin(3\theta^{\Delta}_{\alpha\beta}),\;\; g(t)=\tfrac{1}{2}f(t),\;\; V_0=\tfrac{1}{6}\left|\boldsymbol{v}^{\Delta}_{\alpha\beta}\right| \tag{6.18}$$

being $\theta^{\Delta}_{\alpha\beta}$ the electrical angle of the vector $\boldsymbol{v}^{\Delta}_{\alpha\beta} = v^{\Delta}_{\alpha} + jv^{\Delta}_{\beta}$. It is important to clarify that, unlike traditional converters, the electrical angle of the common mode voltage is not the machine electrical angle θ_e, because the voltage drop in the inductor cluster must be considered.

Table 6.1: Simulation parameters

Parameter	Symbol	M^2C_1	M^2C_2	Unit
ac port voltage	v_{rms}	4100	4100	V
dc port voltage	E	6500	6500	V
Cells per cluster	n	6	6	-
Cluster inductor	L	2,5	2.5	mH
Cell capacitor	C	3000	1500	μF
Cell dc voltage	v_C^*	1085	1085	V
Mitigating frequency	ω_m	314	-	rad/s

Balancing Control for LFM

Only the Machine MMC has this condition at the motor start-up, where any low frequency term in $p_{\alpha 1}^{\Delta}$ and $p_{\beta 1}^{\Delta}$ has to be eliminated in order to bound the capacitor voltages [6]. This task is carry out by using the feedback signals in the control system of Fig. 6.5:

$$p_{\alpha 1 f}^{\Delta}=\tfrac{1}{2}Ei_{\alpha 1}-\tfrac{2}{3}i^P v_{\alpha 1},\quad p_{\beta 1 f}^{\Delta}=\tfrac{1}{2}Ei_{\beta 1}-\tfrac{2}{3}i^P v_{\beta 1} \tag{6.19}$$

Moreover, the functions $f(t)$, $g(t)$ and V_0 are defined applying the Hybrid Mitigation as [11], i.e:

$$f(t)=0.786\sin(\omega_m t),\quad g(t)=\text{sgn}\left[f(t)\right],\quad V_0=V_{0\,\max} \tag{6.20}$$

where ω_m is the mitigating frequency (as higher as possible), sgn is the sign function, $V_{0\,\max}$ is the highest common mode voltage that can be synthesized and $f(t)$ is calculated to decrease the peak value of the circulating currents. With the previous definition, the low frequency terms in $p_{\alpha 1}^{\Delta}$ and $p_{\beta 1}^{\Delta}$ are cancelled and the circulating currents can be reduced they are inversely proportional to V_0.

Transition between modes

A simple method is used to switch between the values of the functions $\tilde{v}_0$ and $f(t)$ from LFM to HFM. Assuming that ω_l is the highest frequency at which the LFM is used and the transition zone is from ω_l to ω_h, the following weighting factors are defined:

$$k_l=1-k_h=\begin{cases}1 & \text{if } |\omega_e|<\omega_l\\ \frac{\omega_h-|\omega_e|}{\omega_h-\omega_l} & \text{if } \omega_l\leq\ |\omega_e|\ \leq\omega_h\\ 0 & \text{if } \omega_h<|\omega_e|\end{cases} \tag{6.21}$$

6.4 Simulation and experimental results

The validation of the proposed control scheme has been divided into simulation and experimental work. The simulation of the BTB-MMC drive was performed to feed a 1000hp induction machine with quadratic torque-speed profile. The converter parameters are shown in

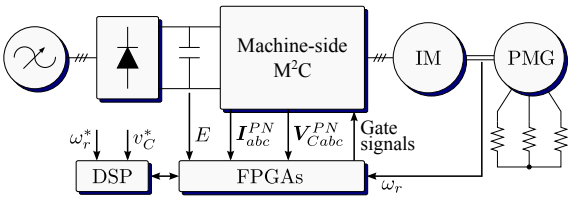

(a) Configuration

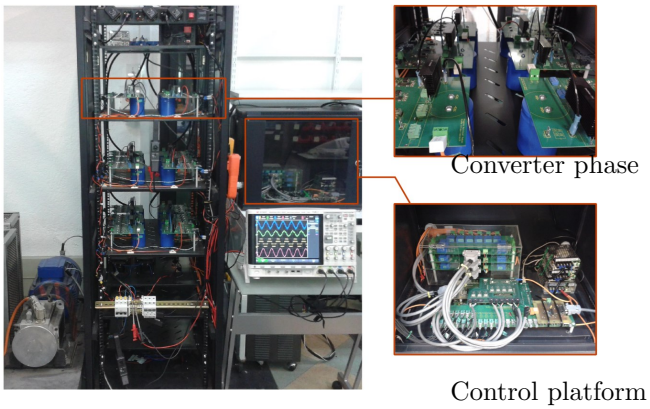

(b) Photograph

Figure 6.6: Experimental system

Table 6.2: Experimental set-up parameters

Parameter	Symbol	Value	Unit
dc port voltage	E	420	V
Cells per cluster	n	3	-
Cluster inductor	L_1	2,5	mH
Cell capacitor	C	4700	μF
Cell dc voltage	V_C	160	V
Mitigating frequency	ω_m	314	rad/s

Table 6.1. The experimental results have been obtained using a prototype of the machine-side MMC driving an induction machine. Fig. 6.6(a) shows the configuration of the experimental system and its photograph is presented in Fig. 6.6(b). The MMC is fed by a dc-link created by a six pulse diode rectifier bridge and filter capacitors. The MMC output port is connected to a 2-pole vector-controlled induction machine driving a Permanent Magnet Generator (PMG). The PMG is feeding a 3ϕ resistor bank emulating a quadratic torque-speed load. To control the system a platform based on two FPGA boards (Actel ProASIC3), 40 14-bit AD channels and the DSP Texas Instrument TMS320C6713 is used. The experimental parameters are summarized in Table 6.2.

6.4.1 Simulation results for a BTB scheme

Fig. 6.7 shows the simulation results of the BTB-MMC drive. After 1.25s, the motor is accelerated from 0rpm to ±900rpm, as is shown in Fig. 6.7(a). The LFM is enabled when

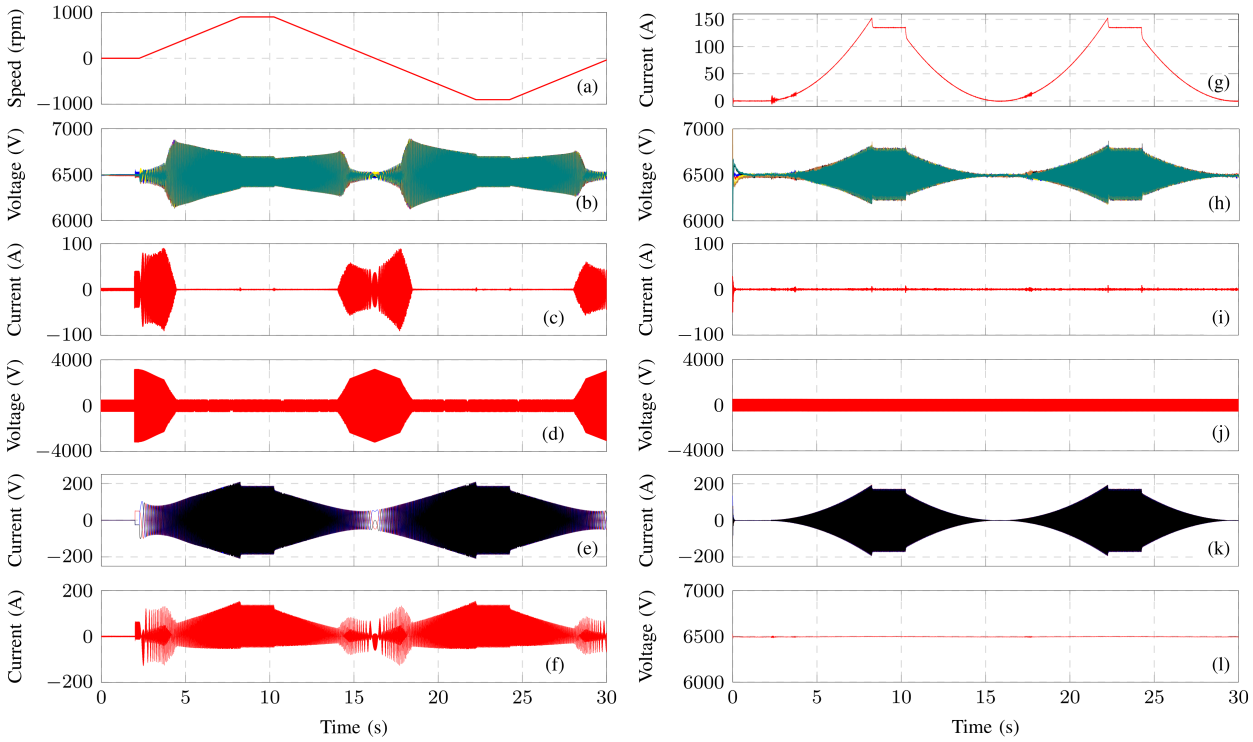

Figure 6.7: Simulation results for the BTB system. Left Machine MMC variables: (a) Machine speed, (b) Available cluster voltages, (c) Circulating current i_{α}^{Σ}, (d) Common mode voltage, (e) ac port current, (f) Cluster current i_{a}^{P}. Right Grid MMC variables: (g) dc port current, (h) Available cluster voltages, (i) Circulating current i_{α}^{Σ}, (j) Common mode voltage, (k) ac port current, (l) Filtered dc port voltage.

$|f_e| < 10$Hz (150rpm). Therefore, the circulating currents and the common mode voltage regulate the available cluster voltages within an acceptable range, producing a variation of $\pm$400V around the nominal value of 6500V [see Fig. 6.7(b)]. In Fig. 6.7(c) is shown that at HFM the circulating currents are used only to balance the converters and its amplitude is approximately zero. In this region, the dc component of the common mode voltage is also low [see Fig. 6.7 (d)], while its ac component decreases the cluster peak voltage at nominal speed. Additionally, the cluster current peak value occurs at HFM, since the selected torque-speed profile is a quadratic function; hence, the cluster size is dependant on the nominal load.

To ensure the power flow from the grid to the machine, the dc and ac port currents of the grid-side MMC are automatically modified when the machine power changes [Fig. 6.7(g) and (k)]. Although the capacitance ratio of both MMC is 2:1, the oscillations in the capacitor voltages have similar magnitudes [see Fig. 6.7(h)]. Moreover, the amplitude of the circulating currents of this converter is low in the overall machine frequency range. Therefore, its cluster current capability can be defined only for the nominal machine power. The common mode voltage of the grid-side MMC is shown in Fig. 6.7(j), showing that the dc component is low, while its ac component is defined to maximise the modulation index at nominal speed. Finally, the filtered dc port voltage is depicted in Fig. 6.7(l), it shows that its mean value is regulated to the desired value.

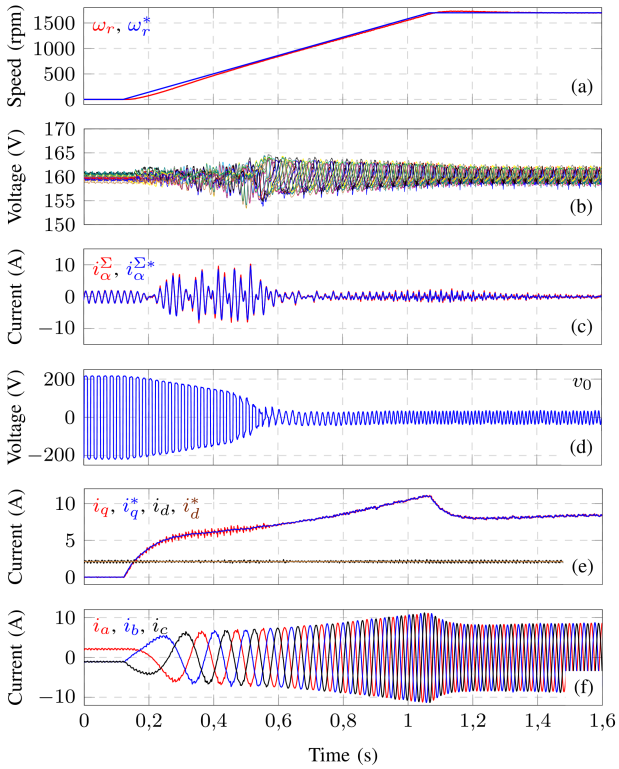

Figure 6.8: Induction machine start-up. (a) Machine speed, (b) Capacitor voltages, (c) Common mode voltage, (d) Circulating current, (e) Machine currents (dq-frame), (f) Machine currents (abc-frame).

6.4.2 Experimental results: machine-side MMC

The operation of the experimental system is shown in Fig. 6.8. As is depicted in Fig. 6.8(a), the machine speed was linearly increased until 1700rpm in approximately 1s. The LFM mode was enabled when $f_e < 10$Hz (close to 500 rpm). In this mode, the control scheme is able to regulate the 18 capacitor voltages, maintaining them bounded and balanced, with maximum oscillation of $\pm$10V (at the transition zone) and an average value of 160V, as is shown in Fig. 6.8(b). The transition zone was selected to operate from 10Hz to 15Hz. The effectiveness of the filters to eliminate the ac components of the control feedback is demonstrated since the circulating currents are low in the HFM and only a low dc component is presented in the common mode voltage [see Fig. 6.8(c) and (d)]. Finally, the indirect vector control performance is evaluated by the high quality tracking in the currents [see Fig. 6.8(e) and (f)].

6.5 Conclusion

This paper has described a suitable model of the BTB-MMC drive. Additionally, the control algorithms to ensure the operation of the converter have been proposed and validated by simulation and experimental results, controlling an induction machine with an eighteen power

cells MMC. The proposed control algorithm is not dependent on the machine variables to balance the converter, increasing the converter robustness for sudden load changes in the machine. At LFM, an hybrid mitigating algorithm was performed and experimentally validated to allow the machine start-up, keeping bounded the voltage of the BTB-MMC capacitors. Simulation results show that the BTB-MMC drive is balanced in HFM, even for zero-crossing speed, and requiring low circulating currents flowing into its clusters. Further, for quadratic torque-speed profiles, it has been shown that the current capability of a BTB-MMC can be designed considering nominal conditions and the capacitors of both MMC can achieve a ratio of 2:1.

Bibliography

[1] R. Marquardt, "Stromrichterschaltungen mit verteilten energiespeichern," German Patent DE20 122 923 U1, 2001.

[2] M. Glinka and R. Marquardt, "A new AC/AC multilevel converter family," *Industrial Electronics, IEEE Transactions on*, vol. 52, no. 3, pp. 662–669, June 2005.

[3] A. Antonopoulos, L. Angquist, S. Norrga, K. Ilves, L. Harnefors, and H.-P. Nee, "Modular Multilevel Converter AC Motor Drives With Constant Torque From Zero to Nominal Speed," *Industry Applications, IEEE Transactions on*, vol. 50, no. 3, pp. 1982–1993, May 2014.

[4] M. Hagiwara, I. Hasegawa, and H. Akagi, "Start-Up and Low-Speed Operation of an Electric Motor Driven by a Modular Multilevel Cascade Inverter," *IEEE Transactions on Industry Applications*, vol. 49, no. 4, pp. 1556–1565, July-August 2013.

[5] J. Kolb, F. Kammerer, M. Gommeringer, and M. Braun, "Cascaded Control System of the Modular Multilevel Converter for Feeding Variable-Speed Drives," *Power Electronics, IEEE Transactions on*, vol. 30, no. 1, pp. 349–357, Jan 2015.

[6] A. J. Korn, M. Winkelnkemper, and P. Steimer, "Low Output Frequency Operation of the Modular Multi-Level Converter," in *Energy Conversion Congress and Exposition (ECCE), 2010 IEEE*. IEEE, 12-16 September 2010.

[7] M. Hagiwara, R. Maeda, and H. Akagi, "Control and Analysis of the Modular Multilevel Cascade Converter Based on Double-Star Chopper-Cells (MMCC-DSCC)," *Power Electronics, IEEE Transactions on*, vol. 26, no. 6, pp. 1649–1658, June 2011.

[8] Y. Wan, S. Liu, and J. Jiang, "Generalised analytical methods and current-energy control design for modular multilevel cascade converter," *Power Electronics, IET*, vol. 6, no. 3, pp. 495–504, March 2013.

[9] K. Ilves, L. Bessegato, and S. Norrga, "Comparison of cascaded multilevel converter topologies for AC/AC conversion," in *Power Electronics Conference (IPEC-Hiroshima 2014 - ECCE-ASIA), 2014 International*, May 2014, pp. 1087–1094.

[10] Y. Okazaki, W. Kawamura, M. Hagiwara, H. Akagi, T. Ishida, M. Tsukakoshi, and R. Nakamura, "Experimental Comparisons Between Modular Multilevel DSCC Inverters

and TSBC Converters for Medium-Voltage Motor Drives," *IEEE Transactions on Power Electronics*, vol. PP, no. 99, pp. 1–1, 2016.

[11] M. Espinoza, A. Mora, M. Diaz, and R. Cárdenas, "Balancing energy and low frequency operation of the Modular Multilevel Converter in Back to Back configuration," in *Ecological Vehicles and Renewable Energies (EVER), 2015 International Conference on*, March 2015, pp. 1–9.

[12] Y. Okazaki, H. Matsui, M. M. Muhoro, M. Hagiwara, and H. Akagi, "Enhancement on capacitor-voltage-balancing capability of a modular multilevel cascade inverter for medium-voltage synchronous-motor drives," in *2015 IEEE Energy Conversion Congress and Exposition (ECCE)*, Sept 2015, pp. 6352–6359.

[13] R. Cardenas, R. Pena, J. Clare, and P. Wheeler, "Analytical and Experimental Evaluation of a WECS Based on a Cage Induction Generator Fed by a Matrix Converter," *IEEE Transactions on Energy Conversion*, vol. 26, no. 1, pp. 204–215, March 2011.

Chapter 7

Control and Operation of the MMC-Based Drive with Reduced Capacitor Voltage Fluctuations

This chapter is based on the conference paper:

M. Espinoza, F. Donoso, M. Diaz, A. Letelier, and R. Cardenas. Control and Operation of the MMC-Based Drive with Reduced Capacitor Voltage Fluctuations. In *Power Electronics, Machines and Drives (PEMD), 9th International Conference on*, Liverpool, UK., 17-19, April 2018

Abstract: The Modular Multilevel Converter has emerged as a suitable topology for high power drive applications. However, the voltage fluctuations of its floating capacitors increase the control complexity of the converter. In this paper, the MMC dc-port voltage is manipulated to regulate the amplitude of these fluctuations to a constant value during the whole frequency range. The proposed approach has several advantages when compared with the conventional ones since it minimises the voltage fluctuation in the capacitor cells. Additionally, it decreases the common-mode voltage at low-frequencies and the capacitor rms current, increasing their expected lifespan and reducing the winding insulation damages and the leakage currents in the bearing of the machine. The effectiveness of the proposed control strategy is validated with a laboratory-based prototype composed of eighteen power cells, feeding a vector-controlled induction machine.

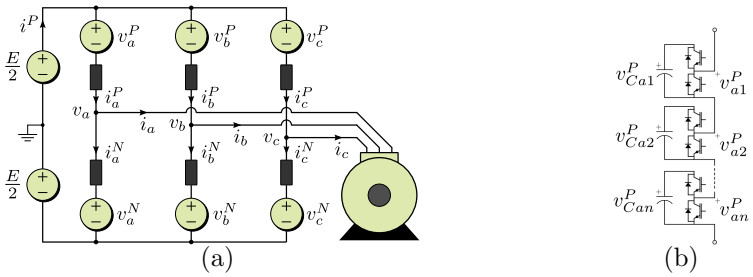

Figure 7.1: MMC-based drive (a): Converter topology. (b): Cluster.

7.1 Introduction

Since the invention of the Modular Multilevel Converter (MMC), this topology has been proposed for applications such as rail train [1], high voltage dc transmission (HVDC) [2] and machine drives [3–16]. Although the MMC has several advantages over others high power modular converters (mainly for quadratic torque-speed profile loads [3,4]), significant efforts are still required to improve its performance for drive applications. The MMC topology is shown in Fig. 7.1. The converter is composed of six "clusters" connected to form an ac-port that feeds the machine and a dc port. Each cluster has an inductor L and n cascaded half bridge modules. The energy in each cell is stored by a "flying" capacitor C.

Consequently, the proper operation of the MMC-based drive requires a control system to maintain the capacitor voltage balanced. This target is complex to achieve when the machine is operating at low speed because large voltage fluctuations occur in the capacitors. For this reason, in the so-called "Low-Frequency Mode" (LFM), mitigating variables (circulating currents and common-mode voltage) are used to reduce the voltage fluctuations, maintaining them within an acceptable margin [7, 8, 13, 17]. On the other hand, when the mitigating signals are not longer required, the "High-Frequency Mode" (HFM) is enabled.

As is well known, the lifetime of electrolytic capacitors is nominally below semiconductors lifetime. Regarding reliability, this fact represents a significant drawback of MMC family because its capacitors are always subjected to voltage fluctuations. In consequence, several control strategies have been proposed to decrease the voltage capacitor oscillations. Another approach is developing new dielectric material capacitors, such as film capacitors, to extend the lifespan of cell capacitors, and there is an important ongoing research being carried out and new material capacitors, such as film capacitors, represent an excellent alternative to extending the lifetime of the cell capacitors [18, 19].

A novel control system for the MMC-based drive is proposed to solve the problems mentioned above. This new control scheme considers the manipulation of the dc-port voltage as a function of the capacitor voltage fluctuations. The major advantage of this methodology is that the capacitor voltage fluctuations is regulated within a predefined margin during the whole frequency range. Accordingly, contrary to the conventional approaches, the amplitude of the capacitor fluctuations is not dependant on the machine frequency, and it can be minimised as much as possible, reducing the rms current in the capacitors and increasing their expected lifespan. What is more, this work shows that the common-mode voltage and

circulating currents are reduced at the start-up of the machine when the dc-port voltage is regulated as proposed, eliminating problems such as winding insulation damages, leakage currents in the bearing, etc.

The remainder of this paper is organized as follows. The modelling and analysis of the MMC-based drive is discussed in Section 7.2, while the effect of apply a dynamic dc-port voltage to the MMC-based drive is discussed in Section 7.3. Several experimental results are presented in Section 7.4 by using a vector-controlled induction machine being fed by a MMC in the whole frequency range, including start-up and zero crossing speed. Finally, Section 7.5 presents the conclusions of this work.

7.2 Dynamic Modelling and Analysis of the MMC

Recently, a modelling approach for the MMC has been reported in [12, 14]. In these papers, the $\Sigma\Delta\alpha\beta 0$-transformation is used to represent the cluster currents and total capacitor voltages (the sum of the capacitor voltages in a cluster) into a new coordinate system, allowing a decoupled control of each variable. To perform this modelling, the dynamics of these signals are derived as follows (see Fig. 7.1):

$$L\frac{d}{dt}\overbrace{\begin{bmatrix} i_a^P & i_b^P & i_c^P \\ i_a^N & i_b^N & i_c^N \end{bmatrix}}^{:=\mathbf{I}_{abc}^{PN}} = -\overbrace{\begin{bmatrix} v_a^P & v_b^P & v_c^P \\ v_a^N & v_b^N & v_c^N \end{bmatrix}}^{:=\mathbf{V}_{abc}^{PN}} - \frac{E}{2}\begin{bmatrix} 1 & 1 & 1 \\ 1 & 1 & 1 \end{bmatrix} + \begin{bmatrix} -v_a & -v_b & -v_c \\ v_a & v_b & v_c \end{bmatrix} \tag{7.1}$$

$$C\bar{v}_C\frac{d}{dt}\underbrace{\begin{bmatrix} v_{Ca}^P & v_{Cb}^P & v_{Cc}^P \\ v_{Ca}^N & v_{Cb}^N & v_{Cc}^N \end{bmatrix}}_{:=\mathbf{V}_{Cabc}^{PN}} \approx \underbrace{\begin{bmatrix} p_a^P & p_b^P & p_c^P \\ p_a^N & p_b^N & p_c^N \end{bmatrix}}_{:=\mathbf{P}_{abc}^{PN}}, \tag{7.2}$$

where $\bar{v}_C$ is the algebraic mean value of the voltage in all capacitors of the MMC, $p_a^P{=}i_a^P v_a^P$, $p_b^P{=}i_b^P v_b^P$, etc., are the cluster power flows and $v_{Ca}^P{=}v_{Ca1}^P{+}v_{Ca2}^P{+}...{+}v_{Can}^P$, $v_{Ca}^N{=}v_{Ca1}^N{+}v_{Ca2}^N{+}...{+}v_{Can}^N$, etc, are the total cluster voltages. Expression (7.1) is based on the Kirchhoff's voltage law applied into the converter depicted in Fig. 7.1. On the other hand, (7.2) denotes the energy balance in the MMC clusters, assuming that the total cluster voltages are close to an operating point, as is in a well controlled MMC.

As discussed before, to achieve a decoupled control of the converter currents and voltages, the $\Sigma\Delta\alpha\beta 0$-transformation is utilised. This transformation is given by:

$$\boldsymbol{X}_{\alpha\beta 0}^{\Sigma\Delta} := \mathbf{C}^{\Sigma\Delta}\cdot\boldsymbol{X}_{abc}^{PN}\cdot\mathbf{C}_{\alpha\beta 0}^{\intercal} \tag{7.3}$$

where $\boldsymbol{X}_{abc}^{PN}$ represents the matrix to be transformed (e.g. $\boldsymbol{I}_{abc}^{PN}$ or $\boldsymbol{V}_{abc}^{PN}$) and the matrices $\mathbf{C}^{\Sigma\Delta}$ and $\mathbf{C}_{\alpha\beta 0}^{\intercal}$ are:

$$\mathbf{C}^{\Sigma\Delta} = \begin{bmatrix} \frac{1}{2} & \frac{1}{2} \\ 1 & -1 \end{bmatrix}, \quad \mathbf{C}_{\alpha\beta 0}^{\intercal} = \begin{bmatrix} \frac{2}{3} & \frac{-1}{3} & \frac{-1}{3} \\ 0 & \frac{1}{\sqrt{3}} & \frac{-1}{\sqrt{3}} \\ \frac{1}{3} & \frac{1}{3} & \frac{1}{3} \end{bmatrix}^{\intercal} \tag{7.4}$$

Hence, applying (7.3) to (7.1) and (7.2) and simplifying leads to:

$$L\frac{d}{dt}\overbrace{\begin{bmatrix} i_\alpha^\Sigma & i_\beta^\Sigma & \frac{1}{3}i^P \\ i_\alpha & i_\beta & 0 \end{bmatrix}}^{:=\mathbf{I}_{\alpha\beta0}^{\Sigma\Delta}} = -\overbrace{\begin{bmatrix} v_\alpha^\Sigma & v_\beta^\Sigma & v_0^\Sigma \\ v_\alpha^\Delta & v_\beta^\Delta & v_0^\Delta \end{bmatrix}}^{:=\mathbf{V}_{\alpha\beta0}^{\Sigma\Delta}} - 2\begin{bmatrix} 0 & 0 & -\frac{1}{4}E \\ v_\alpha & v_\beta & v_0 \end{bmatrix} \tag{7.5}$$

$$C\bar{v}_C\frac{d}{dt}\underbrace{\begin{bmatrix} v_{C\alpha}^\Sigma & v_{C\beta}^\Sigma & v_{C0}^\Sigma \\ v_{C\alpha}^\Delta & v_{C\beta}^\Delta & v_{C0}^\Delta \end{bmatrix}}_{:=\mathbf{V}_{C\alpha\beta0}^{\Sigma\Delta}} \approx \underbrace{\begin{bmatrix} p_\alpha^\Sigma & p_\beta^\Sigma & p_0^\Sigma \\ p_\alpha^\Delta & p_\beta^\Delta & p_0^\Delta \end{bmatrix}}_{:=\mathbf{P}_{\alpha\beta0}^{\Sigma\Delta}}, \tag{7.6}$$

where the machine currents (i_α and i_β) and voltages (v_α, v_β and v_0) are expressed in $\alpha\beta0$-coordinates, i_α^Σ and i_β^Σ are the circulating currents and i^P is the dc port current. Based on (7.5), each current can be easily controlled manipulating only one voltage in the matrix $\mathbf{V}_{\alpha\beta0}^{\Sigma\Delta}$, achieving a decoupled control.

As discussed in [14], the vector representation of (7.6) improves the implementation of high-dynamic control strategies using vector control algorithms. Specifically, defining the power flows and the total cluster voltages as vectors (e.g. $\mathbf{p}_{\alpha\beta}^\Sigma{=}p_\alpha^\Sigma + jp_\beta^\Sigma$, $\mathbf{v}_{C\alpha\beta}^\Sigma{=}v_{C\alpha}^\Sigma + jv_{C\beta}^\Sigma$, etc.), the vector model of (7.6) is obtained as (see [14] and Appendix 7.6 for details):

$$C\bar{v}_C\frac{d\mathbf{v}_{C\alpha\beta}^\Sigma}{dt} \approx \mathbf{p}_{\alpha\beta}^\Sigma \approx \frac{1}{2}E\mathbf{i}_{\alpha\beta}^\Sigma - \frac{1}{4}(\mathbf{i}_{\alpha\beta}\mathbf{v}_{\alpha\beta})^c - \frac{1}{2}v_0\mathbf{i}_{\alpha\beta} \tag{7.7a}$$

$$C\bar{v}_C\frac{d\mathbf{v}_{C\alpha\beta}^\Delta}{dt} \approx \mathbf{p}_{\alpha\beta}^\Delta \approx \tfrac{1}{2}E\mathbf{i}_{\alpha\beta} - \tfrac{2}{3}i^P\mathbf{v}_{\alpha\beta} - (\mathbf{v}_{\alpha\beta}\mathbf{i}_{\alpha\beta}^\Sigma)^c - 2v_0\mathbf{i}_{\alpha\beta}^\Sigma \tag{7.7b}$$

$$C\bar{v}_C\frac{dv_{C0}^\Sigma}{dt} \approx p_0^\Sigma \approx \frac{1}{6}Ei^P - \frac{1}{4}\Re\left[\mathbf{v}_{\alpha\beta}\left(\mathbf{i}_{\alpha\beta}\right)^c\right] \tag{7.7c}$$

$$C\bar{v}_C\frac{dv_{C0}^\Delta}{dt} \approx p_0^\Delta \approx -\Re\left[\mathbf{v}_{\alpha\beta}\left(\mathbf{i}_{\alpha\beta}^\Sigma\right)^c\right] - \frac{2}{3}i^Pv_0 \tag{7.7d}$$

where the superscript " ^{c} " stands for the complex conjugated operator.

For a proper operation of the MMC, the oscillations of the total cluster voltages (indicated by the super-script " ˜ ") have to be within an acceptable value. In previous works it has been shown that the term $\tilde{\mathbf{v}}_{C\alpha\beta}^\Delta$ produces a fundamental ω_e fluctuation, which amplitude is proportional to ω_e^{-1}, $\tilde{\mathbf{v}}_{C\alpha\beta}^\Sigma$ produces a double frequency oscillation and $\tilde{v}_{C0}^\Sigma$, as well as $\tilde{v}_{C0}^\Sigma$, do not produce fluctuations in the MMC capacitors. It straightforward to demonstrate setting the signals $\mathbf{i}_{\alpha\beta}^\Sigma$ and v_0 to zero and integrating (7.7a)-(7.7d), resulting in:

$$\tilde{\mathbf{v}}_{C\alpha\beta}^\Sigma \approx \frac{-1}{j8\omega_eC\bar{v}_C}\left(\mathbf{i}_{\alpha\beta}\mathbf{v}_{\alpha\beta}\right)^c \tag{7.8a}$$

$$\tilde{\mathbf{v}}_{C\alpha\beta}^\Delta \approx \frac{1}{j\omega_eC\bar{v}_C}\left(\tfrac{1}{2}E\mathbf{i}_{\alpha\beta} - \tfrac{2}{3}i^P\mathbf{v}_{\alpha\beta}\right) \tag{7.8b}$$

$$\tilde{v}_{C0}^\Sigma \approx n\bar{v}_C, \quad \tilde{v}_{C0}^\Sigma \approx 0 \tag{7.8c}$$

Based on the inverse $\Sigma\Delta\alpha\beta0$-transformation, the total capacitor voltages in $PNabc$ coordinates can be expressed using the vector voltages of (7.6). For example, the voltages v_{Ca}^P and

v_{Ca}^{N} are expressed as follows:

$$v_{Ca}^{P} = \frac{1}{2}\Re\left[\mathbf{v}_{C\alpha\beta}^{\Delta}\right] + \Re\left[\mathbf{v}_{C\alpha\beta}^{\Sigma}\right] + \frac{1}{2}v_{C0}^{\Delta} + v_{C0}^{\Sigma} \tag{7.9a}$$

$$v_{Ca}^{N} = -\frac{1}{2}\Re\left[\mathbf{v}_{C\alpha\beta}^{\Delta}\right] + \Re\left[\mathbf{v}_{C\alpha\beta}^{\Sigma}\right] - \frac{1}{2}v_{C0}^{\Delta} + v_{C0}^{\Sigma} \tag{7.9b}$$

Consequently, the maximum amplitude of the oscillating component of the total cluster voltages, $|\tilde{v}_{Cx}^{X}|$, can be approximated with the vector voltages $\mathbf{v}_{C\alpha\beta}^{\Delta}$ and $\mathbf{v}_{C\alpha\beta}^{\Sigma}$ as follows:

$$|\tilde{v}_{Cx}^{X}| \approx \frac{1}{2}||\mathbf{v}_{C\alpha\beta}^{\Delta}|| + ||\mathbf{v}_{C\alpha\beta}^{\Sigma}|| \tag{7.10}$$

where $x=\{a,b,c\}$ and $X=\{P,N\}$. Notice that (7.10) represents the worst case situation for $|\tilde{v}_{Cx}^{X}|$, since the amplitude of $\mathbf{v}_{C\alpha\beta}^{\Delta}$ and $\mathbf{v}_{C\alpha\beta}^{\Sigma}$ are summed.

7.3 Influence of the dc-port voltage E in the MMC electrical variables

In this paper, a new control methodology is proposed to operate the MMC as a machine drive. This strategy manipulates the dc-port voltage E to maintain the fluctuations of the total cluster voltages within a voltage margin in the whole frequency range. The effect of modifying the dc-port voltage E is analysed below.

7.3.1 During low-frequency mode

In the LFM circulating currents and common-mode voltage are needed to maintain the fluctuations of the vector voltage $\mathbf{v}_{C\alpha\beta}^{\Delta}$ within an acceptable value. Due to its oscillating frequency ω_e, it is straghtforward to analyse the regulation of $\mathbf{v}_{C\alpha\beta}^{\Delta}$ representing (7.7b) into a dq-coordinate frame rotating at ω_e rad·s^{-1} as follows:

$$C\bar{v}_C\frac{d\mathbf{v}_{Cdq}^{\Delta}}{dt} \approx \underbrace{\frac{1}{2}E\mathbf{i}_{dq} - \frac{2}{3}i^{P}\mathbf{v}_{dq}}_{:=\mathbf{p}_{\omega_e}} - \underbrace{jC\bar{v}_C\omega_e\mathbf{v}_{Cdq}^{\Delta}}_{:=\mathbf{p}_m} - \underbrace{2v_0\mathbf{i}_{dq}^{\Sigma}}_{:=\mathbf{p}_c} \tag{7.11}$$

Considering ideal conditions, the set-point values of $\tilde{\mathbf{i}}_{\alpha\beta}^{\Sigma}$ and $\tilde{v}_0$ can be defined as:

$$\tilde{\mathbf{i}}_{dq}^{\Sigma *} = \frac{1}{2V_0}\left(\mathbf{p}_{\omega_e} - \mathbf{p}_m\right) f(t), \tag{7.12}$$

$$\tilde{v}_0^{*} = V_0 \text{sign}\left[f(t)\right] \tag{7.13}$$

where V_0 is the amplitude of the common-mode voltage. Consequently, the power term $\mathbf{p}_c$ can be expressed as:

$$\mathbf{p}_c = \left(\mathbf{p}_{\omega_e} - \mathbf{p}_m\right)|f(t)| \tag{7.14}$$

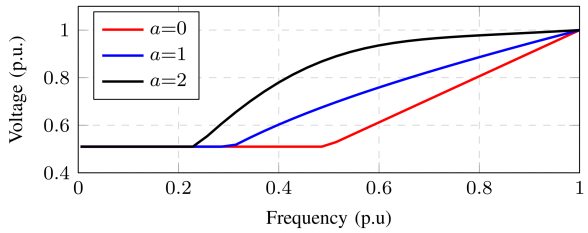

Figure 7.2: Required value of the voltage E to regulate $|\tilde{v}_{Cx}^{X}|$ to a constant value.

Hence, $\mathbf{p}_{\omega_e}$ and $\mathbf{p}_m$ are eliminated from (7.11) if $f(t)$ is a high frequency signal compared to ω_e during LFM, such that the mean value of $|f(t)|$=1 (considering one period of $f(t)$ see [7,8,13]). Notice that if $\mathbf{p}_m$ is defined as a non-zero vector (i.e. a fundamental oscillation is allowed in $\mathbf{v}_{C\alpha\beta}^{\Delta}$) the circulating currents decrease as the machine frequency increases [see $\mathbf{p}_m$ in (7.11)]. A discussion regarding this methodology is addressed in [20].

Based on (7.12), it is concluded that the mitigating circulating currents are inversely proportional to V_0. Neglecting the inductor voltage drop and considering that the output cluster voltages has to be positive, it is straightforward to demonstrate that the maximum amplitude of the common-mode voltage can be approximated as [see (7.1)]:

$$V_0 \approx \frac{1}{2}E - ||\mathbf{v}_{dq}|| \tag{7.15}$$

where $\mathbf{v}_{dq}$ is the machine voltage in a dq-rotating frame. At the machine start-up, $\omega_e \approx 0$ rad·s^{-1} and $||\mathbf{v}_{dq}|| \approx 0$ V; therefore, $\tilde{\mathbf{i}}_{dq}^{\Sigma *}$ and $\tilde{v}_0^*$ as defined in (7.12)-(7.13) results in:

$$\tilde{\mathbf{i}}_{dq}^{\Sigma *}(\omega_e \approx 0) \approx \mathbf{i}_{dq} f(t), \tag{7.16}$$

$$V_0(\omega_e \approx 0) \approx \frac{1}{2}E \tag{7.17}$$

The importance of this result is that the amplitude of the circulating currents is not affected by variations in the dc-port voltage E or the voltage $\mathbf{v}_{C\alpha\beta}^{\Delta}$ during the machine start-up. However, the amplitude of the common-mode voltage is modified at the same ratio of the dc-port voltage. In this manner, it is an attractive solution to maintain a low value of the dc-port voltage during the LFM to reduce the required common-mode voltage to eliminate the high-voltage fluctuations in the MMC capacitors.

7.3.2 During high-frequency mode

The voltage E cannot be maintained in a low value during the whole frequency range because the output cluster voltage would reach negative values as ω_e increases. For this reason, E has to be manipulated from its minimum value in LFM, $E_{\min}$, until its maximum/nominal value in HFM, $E_{\max}$.

In this paper, a simple method to achieve this task is proposed. What is more, the presented methodology ensures a constant voltage fluctuation in the total cluster voltages during the HFM. Of all the possible values for this fluctuation, the minimum value is preferred since

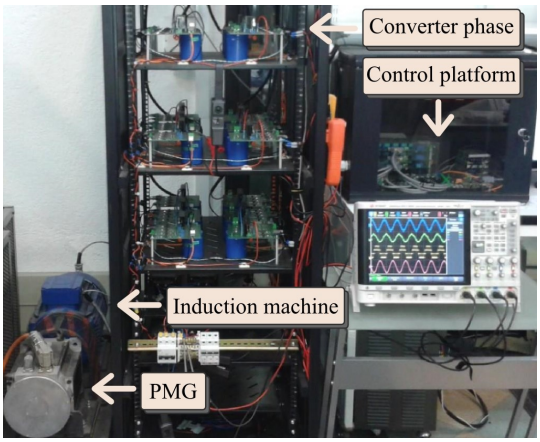

Figure 7.3: Photograph of the laboratory experimental system.

it increases the lifespan of the MMC capacitors. Consequently, the value of $|\tilde{v}_{Cx}^{X*}|$ can be determined using (7.10) for the nominal machine conditions.

From (7.11), the HFM is enable when $||\mathbf{p}_c||\approx 0$ (i.e. the mitigating variables are no longer required to reduce the voltage fluctuations of $\mathbf{v}_{C\alpha\beta}^{\Delta}$). Therefore, in steady-state conditions $\mathbf{p}_{\omega_e}=\mathbf{p}_m$. Supposing that the MMC is balanced (i.e. $\mathbf{v}_{C\alpha\beta}^{\Sigma}=\tilde{\mathbf{v}}_{C\alpha\beta}^{\Sigma}$ and $i^P\approx\frac{3}{2E}\Re\{\mathbf{v}_{dq}\mathbf{i}_{dq}^c\}$), the amplitude of the power fluctuations $\mathbf{p}_{\omega_e}$ and $\mathbf{p}_m$ can be expressed as follows:

$$||\mathbf{p}_{\omega_e}(E)|| = \left|\left|\frac{1}{2}E\mathbf{i}_{dq} - \Re\{\mathbf{v}_{dq}\mathbf{i}_{dq}^c\}\frac{\mathbf{v}_{dq}}{E}\right|\right| \tag{7.18}$$

$$||\mathbf{p}_m(|\tilde{v}_{Cx}^{X*}|)|| = 2C\bar{v}_C\omega_e(|\tilde{v}_{Cx}^{X*}| - ||\mathbf{v}_{C\alpha\beta}^{\Sigma}||) \tag{7.19}$$

where $||\mathbf{v}_{Cdq}^{\Delta}||=||\mathbf{v}_{C\alpha\beta}^{\Delta}||$ has been written as a function of $||\mathbf{v}_{C\alpha\beta}^{\Sigma}||$ and $|\tilde{v}_{Cx}^{X*}|$ by using (7.10). Finally, based on (7.18) and (7.19), it can be concluded that the dc-port voltage E can be manipulated to achieve a desired value of $|\tilde{v}_{Cx}^{X}|$, $|\tilde{v}_{Cx}^{X*}|$.

Fig. 7.2 shows the dc-port voltage E as a function of ω_e to achieve the minimum value of $|\tilde{v}_{Cx}^{X}|$ during the whole frequency range in an MMC as the one utilised in the experimental results of this paper. In the figure, the electrical torque was defined as:

$$T_e(\omega_e) = T_{e0} + (T_{e\text{Nom}} - T_{e0})\left(\frac{\omega_e}{\omega_{e\text{Nom}}}\right)^a \tag{7.20}$$

where T_{e0} is the starting-torque, $T_{e\text{Nom}}$ is the nominal torque, $\omega_{e\text{Nom}}$ is nominal machine frequency and a is a parameter to define the machine torque-speed profile.

7.4 Experimental results and set-up

Experimental results of the proposed control methodology have been obtained using an 18-power cell MMC-based drive. The experimental set-up is shown in Fig. 7.3, while its parameters are given in Table 7.1. The MMC is driving a 7.5 kW vector-controlled induction

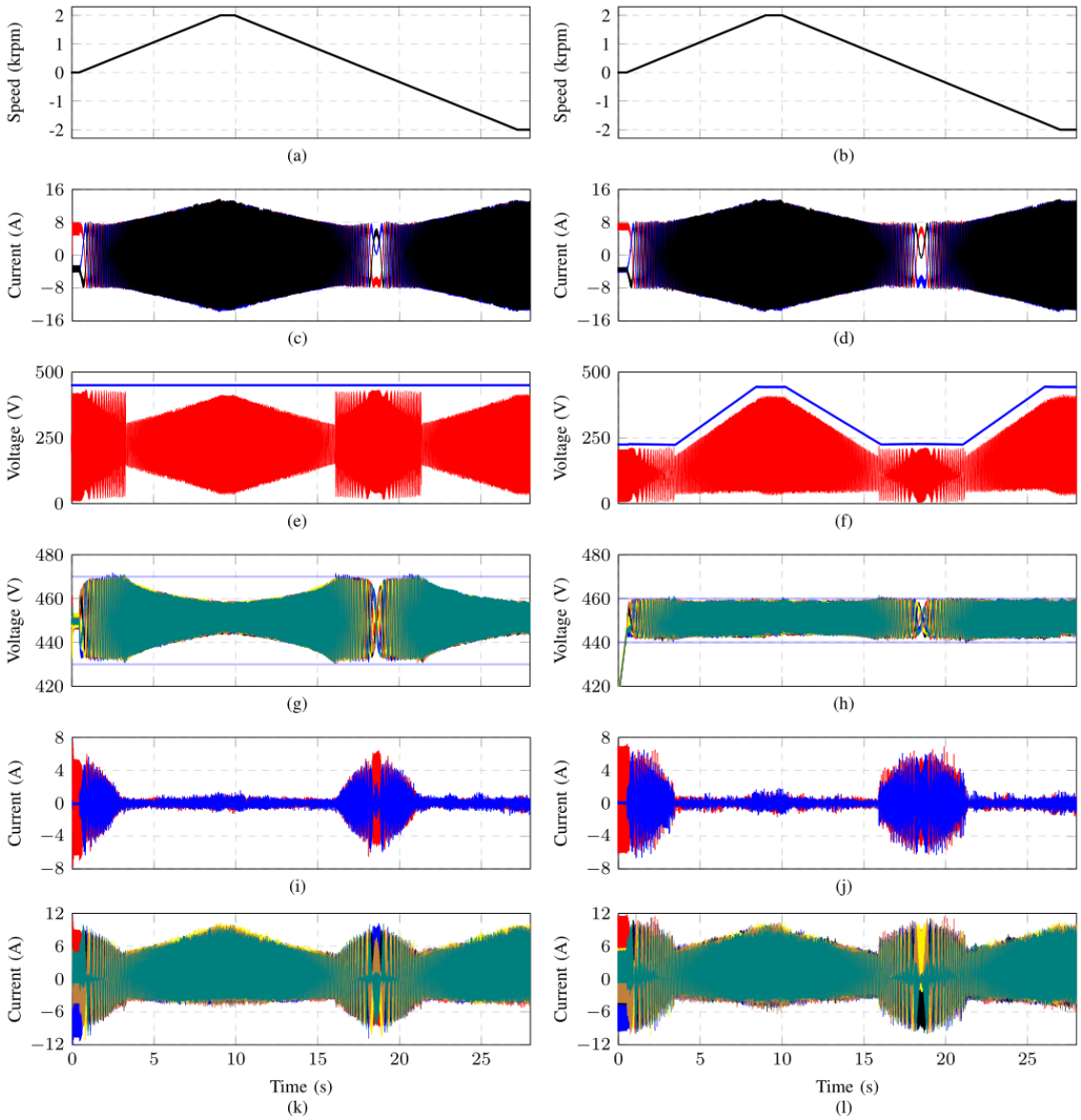

Figure 7.4: Comparison of the dynamic performance of the MMC-based drive for constant (left) and manipulated (right) dc-port voltage. (a)-(b) Machine speed, (c)-(d) Machine currents, (e)-(f) dc-port voltage E (blue line) and desired output cluster voltage (red), (g)-(h) Total cluster voltages, (i)-(j) Circulating currents, (k)-(l) Cluster currents.

Parameter	Symbol	Value	Unit
dc port voltage	E	450	V
Cluster inductor	L	2,5	mH
Cell capacitor	C	4700	μF
Cell dc voltage	v_C^*	150	V
Switching frequency per cell	f_s	5000	Hz

Table 7.1: Set-up parameters for the 18 cells MMC-drive

machine connected to a Permanent Magnet Generator (PMG). A resistor bank has been connected to the PMG output providing a 4 kW load at nominal speed. Hall effect transducers are used to measure the dc port voltage, the capacitor voltages and the cluster currents. To control the system, a platform based on two FPGA boards (Actel ProASIC3) and a DSP (TI TMS320C6713) is used. A programmable AMETEK power supply model CSW5550 generates the dc-port voltage as discussed in Section 7.3. In a commercial implementation, this voltage can be generated using a medium voltage source as those presented in [21, 22] or another MMC with full-bridge cells [23, 24].

Considering that the contribution of this paper is to analyse and show the effect of a dynamic variation of the dc-port voltage in the MMC-based drive, the converter cluster voltages and machine currents have been controlled by using conventional control strategies [12, 14, 20]. The vector voltage $\mathbf{v}_{C\alpha\beta}^{\Delta}$ is regulated in a dq-rotating frame during LFM. This task is carried out by using an ac-component in the circulating currents that creates a power flow with the common-mode voltage [see the term $-2v_0\mathbf{i}_{\alpha\beta}^{\Sigma}$ in (7.11)]. During HFM, this ac-component creates a power flow with the machine voltages to regulate $\mathbf{v}_{C\alpha\beta}^{\Delta}$ [see the term $(\mathbf{v}_{\alpha\beta}\mathbf{i}_{\alpha\beta}^{\Sigma})^c$ in (7.7b)]. Additionally, the vector voltage $\mathbf{v}_{C\alpha\beta}^{\Sigma}$ is controlled by adding a dc-component in the circulating currents for both, low- and high- frequency modes to manipulate the power flow $\frac{1}{2}E\mathbf{i}_{\alpha\beta}^{\Sigma}$ in (7.7a). On the other hand, the dc-port current i^P is manipulated during LFM to regulate v_{C0}^{Δ} by using an ac-component in-phase with the common-mode voltage [see (7.7d)]. In HFM, the power flow $-\Re[\mathbf{v}_{\alpha\beta}(\mathbf{i}_{\alpha\beta}^{\Sigma})^c]$ in (7.7d) regulates v_{C0}^{Δ}. A complete description of the control diagrams utilised in this work can be found in [12, 14, 20].

Fig. 7.4 depicts the dynamic performance when the MMC drives the induction machine from 0 rpm to 2000 rpm for constant (left) and manipulated (right) dc-port voltage. The speed profile for both test is shown in Fig. 7.4(a) and Fig. 7.4(b). Notice that this profile includes the machine start-up and the zero-crossing condition, what represents the worst case situation for an MMC-based drive. The machine currents are shown in Fig. 7.4(c) and Fig. 7.4(d), demonstrating that the same mechanical load was applied during the tests.

The dc-port voltage (blue line) and the desired output voltage of a cluster (red line) are depicted in Fig. 7.4(e) and Fig. 7.4(f). As shown, the MMC cluster has to synthesise a high common-mode voltage during the LFM because the nominal dc-port voltage is applied during the machine operation. This is concluded based on the high-frequency signals of the output cluster voltage at low-frequencies [see (7.17)]. However, the required common-mode voltage is naturally lower when the dc-port voltage is reduced as in Fig. 7.4(f). Notice that in this experimental results the voltage E was regulated to a 50% of its nominal value in

LFM, which represent a feasible reduction for the aforementioned input converters [21–24].

The total cluster voltages are shown in Fig. 7.4(g) and Fig. 7.4(h). As discussed in Section 7.3, a margin-based control strategy maintains their amplitudes constant during LFM [20]. Notice that their peak-to-peak value for a constant dc-port voltage is 40 V; however, it is possible to reduce this fluctuation to 20 V peak-to-peak applying a manipulated dc-port voltage, increasing the expected lifespan of the capacitor cells and decreasing their rms current [23]. What is more, this amplitude is maintained constant by manipulating E as the machine speed increases in HFM. Fig. 7.4(i) and Fig. 7.4(j) depict the obtained circulating currents during these tests. It is important to mention that the peak value of both currents is similar, and then the converter current rating has not to be increased when the proposed strategy is implemented, as demonstrated in Fig. 7.4(k) and Fig. 7.4(l), where it is shown that the cluster currents have a similar peak-value for both tests.

7.5 Conclusions

This paper has demonstrated that the dc-port voltage of an MMC can be manipulated to maintain constant the amplitude of the capacitor voltage fluctuations in drive applications. It has been shown that this methodology allows a reduction in both, the rms current and voltage fluctuation of the capacitor cells, increasing its expected lifespan. Additionally, a low common-mode voltage at the machine start-up is required since the dc-port voltage is reduced with the proposed scheme; therefore, problems such as winding insulation damages, leakage currents in the bearing, etc. are also minimised.

Extensive experimental results for a laboratory prototype have been presented in this work. Dynamic experiments in both operating modes (high- and low- frequency modes) have been realized and thoroughly discussed. The performance considering ramp variations in the speed and zero-crossing speed transitions have been experimentally investigated and good performance has been demonstrated. The experimental results have demonstrated the effectiveness of the proposed strategies.

Bibliography

[1] R. Marquardt, "Stromrichterschaltungen mit verteilten energiespeichern," German Patent DE20 122 923 U1, 2001.

[2] Siemens. HVDC PLUS-Basics and Principle of Operation. http://www.energy.siemens.com/br/pool/br/transmissao-de-energia/transformadores/hvdc-plus-basics-and-principle-of-operation.pdf. (2013)

[3] Y. Okazaki, W. Kawamura, M. Hagiwara, H. Akagi, T. Ishida, M. Tsukakoshi, and R. Nakamura, "Experimental Comparisons Between Modular Multilevel DSCC Inverters and TSBC Converters for Medium-Voltage Motor Drives," *IEEE Transactions on Power Electronics*, vol. PP, no. 99, pp. 1–1, 2016.

[4] K. Ilves, L. Bessegato, and S. Norrga, "Comparison of cascaded multilevel converter topologies for AC/AC conversion," in *Power Electronics Conference (IPEC-Hiroshima 2014 - ECCE-ASIA), 2014 International*, pp. 1087–1094, May. 2014.

[5] M. Hagiwara, K. Nishimura, and H. Akagi, "A Medium-Voltage Motor Drive With a Modular Multilevel PWM Inverter," *IEEE Transactions on Power Electronics*, vol. 25, no. 7, pp. 1786–1799, Jul. 2010.

[6] N. Thitichaiworakorn, M. Hagiwara, and H. Akagi, "Experimental Verification of a Modular Multilevel Cascade Inverter Based on Double-Star Bridge Cells," *IEEE Transactions on Industry Applications*, vol. 50, no. 1, pp. 509–519, Jan. 2014.

[7] M. Hagiwara, I. Hasegawa, and H. Akagi, "Start-Up and Low-Speed Operation of an Electric Motor Driven by a Modular Multilevel Cascade Inverter," *IEEE Transactions on Industry Applications*, vol. 49, no. 4, pp. 1556–1565, July-August 2013.

[8] A. J. Korn, M. Winkelnkemper, and P. Steimer, "Low Output Frequency Operation of the Modular Multi-Level Converter," in *Energy Conversion Congress and Exposition (ECCE), 2010 IEEE*. IEEE, 12-16 September 2010.

[9] A. Antonopoulos, L. Ängquist, S. Norrga, K. Ilves, L. Harnefors, and H.-P. Nee, "Modular Multilevel Converter AC Motor Drives With Constant Torque From Zero to Nominal Speed," *IEEE Trans. Ind. Appl.*, vol. 50, no. 3, pp. 1982–1993, May. 2014.

[10] S. Debnath, J. Qin, B. Bahrani, M. Saeedifard, and P. Barbosa, "Operation, Control,

and Applications of the Modular Multilevel Converter: A Review," *IEEE Transactions on Power Electronics*, vol. 30, no. 1, pp. 37–53, Jan. 2015.

[11] A. Antonopoulos, L. Ängquist, L. Harnefors, and H. P. Nee, "Optimal Selection of the Average Capacitor Voltage for Variable-Speed Drives With Modular Multilevel Converters," *IEEE Transactions on Power Electronics*, vol. 30, no. 1, pp. 227–234, Jan. 2015.

[12] J. Kolb, F. Kammerer, M. Gommeringer, and M. Braun, "Cascaded Control System of the Modular Multilevel Converter for Feeding Variable-Speed Drives," *IEEE Trans. Power Electron.*, vol. 30, no. 1, pp. 349–357, Jan. 2015.

[13] M. Espinoza, E. Espina, M. Diaz, A. Mora, and R. Cárdenas, "Improved control strategy of the Modular Multilevel Converter for high power drive applications in low frequency operation," in *Power Electronics and Application (EPE), 2016 18th European Conference on*, pp. 5–9, Karlsruhe, Germany, Sep. 2016.

[14] M. Espinoza, R. Cárdenas, M. Díaz, and J. C. Clare, "An Enhanced *dq*-Based Vector Control System for Modular Multilevel Converters Feeding Variable-Speed Drives," *IEEE Trans. Ind. Electron.*, vol. 64, no. 4, pp. 2620–2630, Apr. 2017.

[15] B. Li, S. Zhou, D. Xu, R. Yang, D. Xu, C. Buccella, and C. Cecati, "An Improved Circulating Current Injection Method for Modular Multilevel Converters in Variable-Speed Drives," *IEEE Trans. Ind. Electron.*, vol. 63, no. 11, pp. 7215–7225, Nov. 2016.

[16] Siemens. SINAMICS SM120 Cabinet Modules. https://www.industry.siemens.com/drives/global/en/converter/mv-drives/Pages/sinamics-sm120-cm.aspx. (2016, July)

[17] B. Li, S. Zhou, D. Xu, D. Xu, and W. Wang, "Comparative study of the sinusoidal-wave and square-wave circulating current injection methods for low-frequency operation of the modular multilevel converters," in *Energy Conversion Congress and Exposition (ECCE), 2015 IEEE*, pp. 4700–4705, Sep. 2015.

[18] B. Karanayil, V. G. Agelidis, and J. Pou, "Performance Evaluation of Three-Phase Grid-Connected Photovoltaic Inverters Using Electrolytic or Polypropylene Film Capacitors," *IEEE Transactions on Sustainable Energy*, vol. 5, DOI 10.1109/TSTE.2014.2347967, no. 4, pp. 1297–1306, Oct. 2014.

[19] H. Wang and F. Blaabjerg, "Reliability of Capacitors for DC-Link Applications in Power Electronic Converters: An Overview," *IEEE Transactions on Industry Applications*, vol. 50, DOI 10.1109/TIA.2014.2308357, no. 5, pp. 3569–3578, Sep. 2014.

[20] M. Espinoza, E. Espina, M. Diaz, and R. Cárdenas, "Control Strategies for Modular Multilevel Converters Driving Cage Machines," in *IEEE 3rd Southern Power Electronics Conference (SPEC), 2017*, pp. 1–6, Puerto Varas, Chile, Diciembre 2017.

[21] M. L. Zhang, B. Wu, Y. Xiao, F. A. Dewinter, and R. Sotudeh, "A multilevel buck converter based rectifier with sinusoidal inputs and unity power factor for medium voltage (4160-7200 v) applications," *IEEE Transactions on Power Electronics*, vol. 17, DOI

10.1109/TPEL.2002.805600, no. 6, pp. 853–863, Nov. 2002.

[22] I. Abdelsalam, G. P. Adam, D. Holliday, and B. W. Williams, "Single-stage ac-dc buck-boost converter for medium-voltage high-power applications," *IET Renewable Power Generation*, vol. 10, DOI 10.1049/iet-rpg.2015.0136, no. 2, pp. 184–193, 2016.

[23] S. Sau and B. G. Fernandes, "Modular multilevel converter based variable speed drives with constant capacitor ripple voltage for wide speed range," in *IECON 2017 - 43rd Annual Conference of the IEEE Industrial Electronics Society*, DOI 10.1109/IECON.2017.8216348, pp. 2073–2078, Oct. 2017.

[24] Y. S. Kumar and G. Poddar, "Medium-voltage vector control induction motor drive at zero frequency using modular multilevel converter," *IEEE Transactions on Industrial Electronics*, vol. 65, DOI 10.1109/TIE.2017.2721927, no. 1, pp. 125–132, Jan. 2018.

7.6 Derivation of the power flows in $\Sigma\Delta\alpha\beta 0$-coordinates

The power flows of the MMC in $\Sigma\Delta\alpha\beta 0$-coordinates are derived in this appendix. Based on the definition of the $\Sigma\Delta\alpha\beta 0$-transformation:

$$\begin{aligned}\mathbf{P}_{\alpha\beta 0}^{\Sigma\Delta} &= \mathbf{C}^{\Sigma\Delta}\cdot\mathbf{P}_{abc}^{PN}\cdot\mathbf{C}_{\alpha\beta 0}^{\intercal}\\ &= \mathbf{C}^{\Sigma\Delta}\cdot\left[\mathbf{V}_{abc}^{PN}\circ\mathbf{I}_{abc}^{PN}\right]\cdot\mathbf{C}_{\alpha\beta 0}^{\intercal}\end{aligned}\tag{7.21}$$

where " $\circ$ " denotes the element-by-element multiplication of two matrices. Moreover, the inverse $\Sigma\Delta\alpha\beta 0$-transformation of $\mathbf{V}_{\alpha\beta 0}^{\Sigma\Delta}$ and $\mathbf{I}_{\alpha\beta 0}^{\Sigma\Delta}$ is given by:

$$\mathbf{V}_{abc}^{PN} = (\mathbf{C}^{\Sigma\Delta})^{-1}\cdot\mathbf{V}_{\alpha\beta 0}^{\Sigma\Delta}\cdot(\mathbf{C}_{\alpha\beta 0}^{\intercal})^{-1}\tag{7.22}$$

$$\mathbf{I}_{abc}^{PN} = (\mathbf{C}^{\Sigma\Delta})^{-1}\cdot\mathbf{I}_{\alpha\beta 0}^{\Sigma\Delta}\cdot(\mathbf{C}_{\alpha\beta 0}^{\intercal})^{-1}.\tag{7.23}$$

$\mathbf{V}_{\alpha\beta 0}^{\Sigma\Delta}$ is approximated in (7.5) by neglecting the inductor voltage droop, i.e.:

$$\mathbf{V}_{\alpha\beta 0}^{\Sigma\Delta} = \begin{bmatrix} v_{\alpha}^{\Sigma} & v_{\beta}^{\Sigma} & v_{0}^{\Sigma} \\ v_{\alpha}^{\Delta} & v_{\beta}^{\Delta} & v_{0}^{\Delta} \end{bmatrix} \approx 2\begin{bmatrix} 0 & 0 & -\frac{1}{4}E \\ v_{\alpha} & v_{\beta} & v_{0} \end{bmatrix}\tag{7.24}$$

Finally, inserting (7.24), (7.23) and (7.22) into (7.21) and rewriting the result in vector form, the power flows of the MMC are derived as the those presented in (7.7a)-(7.7d).

Part V

Appendices

Chapter 8

Experimental System Implementation

8.1 Introduction

In this chapter, the experimental system implemented to experimentally validate the proposed control strategies is discussed. Section 8.2 describes an overview of the experimental system. The control platform used to process all the measurements as well as to generate the gate signals of the transistors is presented in Section 8.3. Finally, the summary of this chapter is presented in Section 8.5

8.2 System Overview

In Fig. 8.1 the experimental system implemented in this Ph.D. project is shown. The MMC output port is connected to a 7.5 kW, 3800 rpm, 2-pole vector-controlled induction machine driving a Permanent Magnet Generator (PMG) of 4 kW and 2000 rpm. The PMG is feeding a resistor bank emulating a linear torque-speed load. For the implementation of the indirect vector-control system, a position encoder of 10.000 pulses per revolution is affixed to the induction machine. Hall effect transducers are used to measure the dc-port voltage, the capacitor voltage of the 18 cells and the cluster currents. To control the system a platform based on two Field-Programmable Gate Array (FPGA) boards (Actel ProASIC3), 40 14-bit AD channels and the Digital Signal Processor (DSP) Texas Instrument TMS320C6713 is used.

Table 8.1: Set-up parameters for the 18 cells MMC-drive

Parameter	Symbol	Value	Unit
Cluster inductor	L_1	2,5	mH
Cell capacitor	C	4700	μF
Switching frequency	f_s	5000	Hz
Mitigating frequency	ω_m	314	rad/s

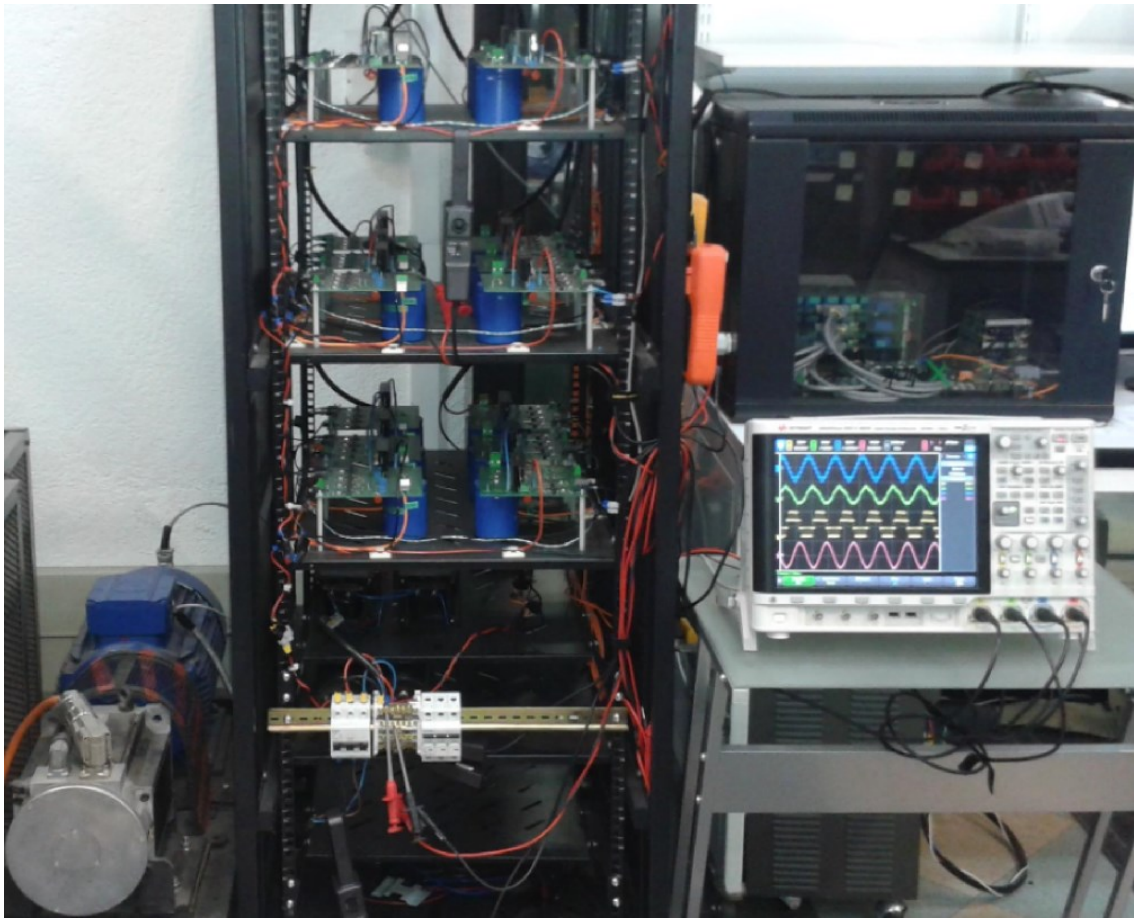

Figure 8.1: Laboratory prototype

Optical fibres have been implemented to transmit the switching signals for the MOSFET switches (model IRFP4868PbF, nominal ratings of 70 A, 300 V, 32 mΩ on resistance).

8.3 Control Platform

The control platform comprises a TMS320C6713 Texas Instrument Digital Signal Processor (DSP), two FPGA boards, an external analogue-digital board, and interface board with fibre optic transmitters and an HPI (Host Port Interface) daughter board. A photograph of the control platform mounted in the experimental set-up is shown in Fig. 8.2 and a description of its components is presented in the following Subsections. Furthermore, a photograph of each of the control platform main components is shown in Fig. 8.3.

The control platform must be able to measure all the electrical variables of the MMC to implement the feedback control proposed in the previous chapters. These measurement requirements are summarised in Table 8.2, where is shown that 26 signals have to be processed by the control system of the MMC to measure capacitor voltages, cluster currents, the speed of the induction machine and the dc-port voltage (for feed-forward purposes). It is important to mention that the input and output currents are not directly measured because they are

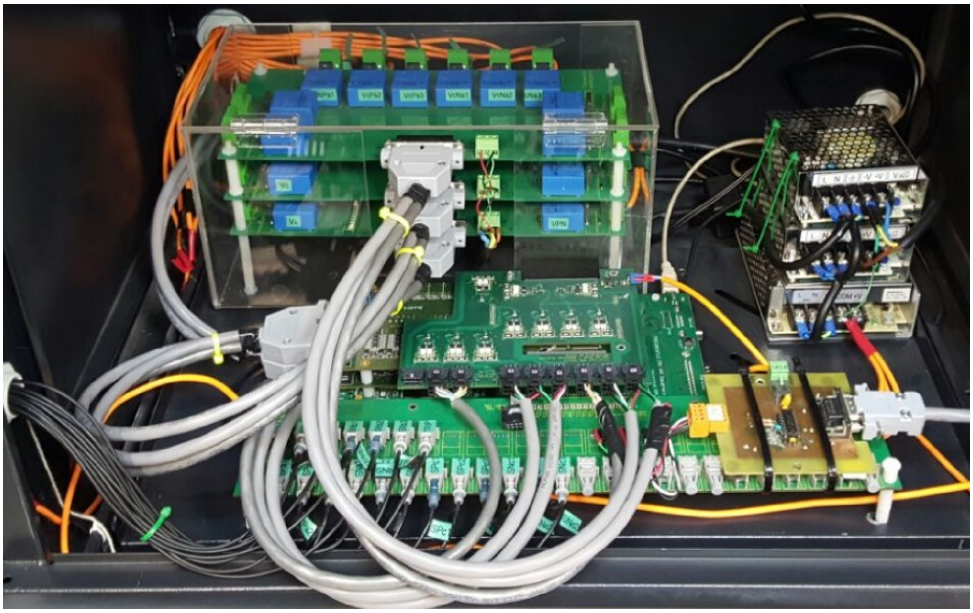

Figure 8.2: Control platform used in this project

dependent on the cluster currents.

Measurements	Quantity
Capacitor voltages	18
Cluster currents	6
dc-port voltage (optional)	1
speed encoder	1

Table 8.2: Signals to be measured by the Control Platform of the experimental MMC

On the other hand, a MMC with three cells per cluster implies that at least 3x6=18 gate-drive signals have to be switched (there are 36 MOSFETs in total). Accordingly, the control platform shall be able to measure 26 signals and to synthesise 19 gate-drive signals (a trip signal is also generated for security purposes).

8.3.1 Digital Signal Processor

The TMS320C6713 is a 32-bit floating point DSP able to process 1350 million of floating point instructions per second, which runs at 225 MHz. This DSP can be programmed in C using Code Composer Studio from Texas Instruments and it is used for the real-time implementation of all the control structures proposed in this thesis. One of the major advantages of this development kit is that the External Memory Interface (EMIF) supports 64 MB of on board SDRAM memory, Flash ROM, and I/O port but also expands the memory interface through an connector for a daughter board. Then, the FPGAs are mapped into the DSK's memory using EMIF connectors on the DSK. The DSP has four dedicated address spaces which allow both the on-board devices and the expansion memory interface to be selected.

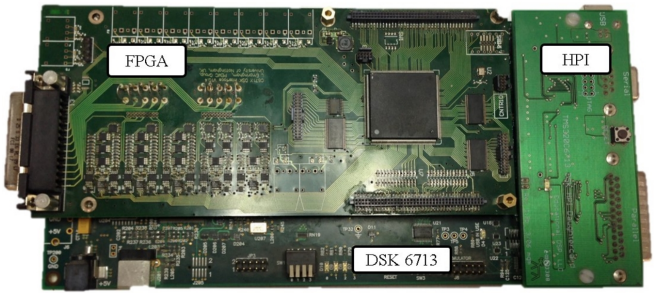

(a) Control platform designed by the PEMC

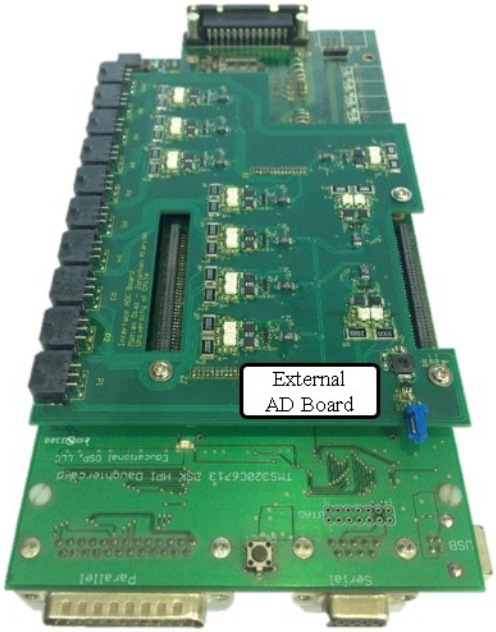

(b) Control Platform with the external A/D board

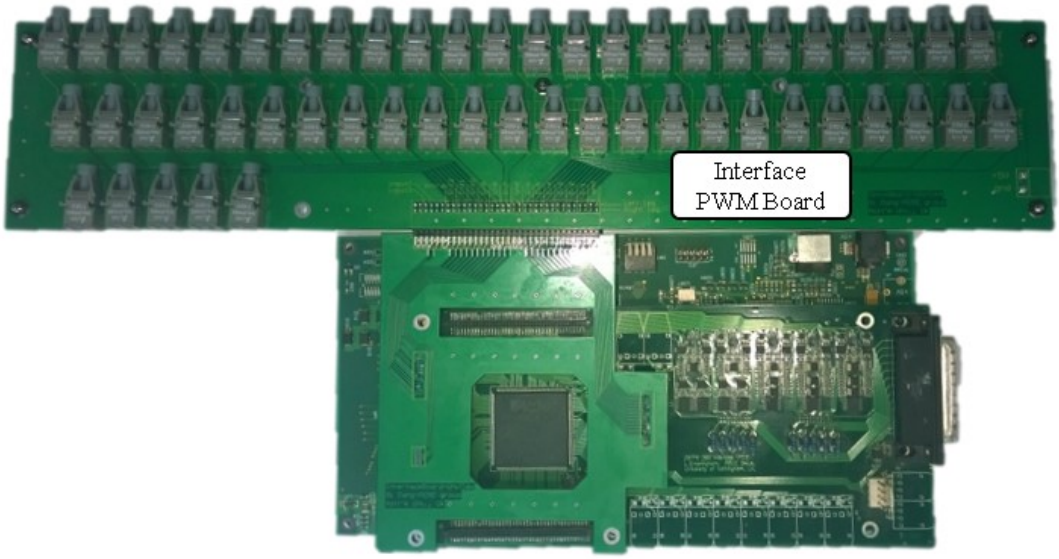

(c) Control Platform with the Interface PWM board on top

Figure 8.3: Components of the Control Platform.

The access to the EMIF is clocked at up to 100 MHz while the CPU is clocked at 225 MHz.

8.3.2 HPI daughter board

The HPI daughter board provides an HPI between the host PC and the DSP without interrupting the central processor unit, providing serial, parallel and USB access to the HPI port in the DSK. With this access in place, a MATLAB application can be used, and also stand/Alone applications can be developed to permit a PC host to download software to the DSP and then control its operation. Fig. 8.3 shows the HPI daughter board mounted on the DSP.

8.3.3 FPGA board

The FPGA board employed in this project was developed by the PEMC Group of the University of Nottingham, and it has proved to be a very flexible and versatile tool for several power electronics applications. This board features a ProASIC3 chip capable up to one million system gates, ten 14-bit A/D converters to measure analogue signals, three connectors with 52 digital input/output ports, connectors for DSP-FPGA data transmission, hardware comparators for over-current and/or over-voltage protection, optical transmitters for the PWM gate drive signals, etc. Among other functions, the FPGA boards are used to:

- Interruption signal generation.
- A/D and D/A conversion and data acquisition.
- DSP memory interface.
- Phase-shifter modulation implementation.
- Trip generator.

Due to the complexity of MMC, two FPGA boards (a master and one slave FPGA boards), one External A/D board and one Interface PWM board have been connected and synchronised to handle the 26 measurements and 19 switching signals required for the experimental prototype. The master FPGA generates an interrupt signal for the DSP and the slave FPGA at 5 kHz. This interrupt signal triggers the execution of the interrupt service routine in the DSP and the execution of the Phase-Shifted PWM modules. Non-stop communication between the DSP and the FPGA is ensured using the watchdog timer. Whenever there is loss of communication between the DSP and the master FPGA, the watchdog service generates a trip signal which halts converter operation by setting all gate-signals to zero.

The Trip Generator features the watchdog, software and hardware trip decisions. Watchdog trip and hardware trip are implemented in the master FPGS board due to they require high-speed processing. The software trip which acts as a backup trip and it is implemented in the DSP code.

8.3.4 Measurement boards

As mentioned in previously, 26 signals have to be measured to control the MMC. Therefore, several voltage and current transducers are considered in the experimental set-up. Current transducers model LEM LA 55-P and the voltage transducers model LV 25-P are mounted on PCB boards, as shown in Figure 8.4. These two models are Hall effect transducers that present excellent accuracy, good linearity and a wide frequency bandwidth.

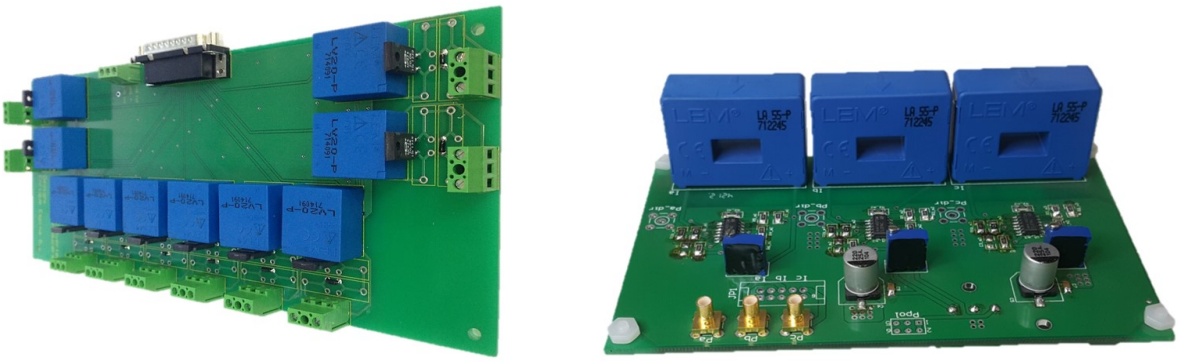

(a) (b)

Figure 8.4: Measurement Boards

8.4 Half-Bridge Power Cells

Fig. 8.5(a) shows the Half-Bridge power cell that was designed and built during this Ph.D. project. Each power cell considers two MOSFET modules IRFP4868PBF from International Rectifier. The MOSFETs are rated for a nominal voltage of 300 V and a nominal current of 70 A. The schematic of the Half-Bridge power cell is shown in 8.5(b). This design considers an optic-electric stage to receive the optic signals from the FPGAs and transform them into electrical signals. A delay circuit composed of a trimmer and a capacitor is included to add dead time to the drive signals. Moreover, an optocoupler stage is implemented using the HCPL-3120 optocoupler, which is specifically designed for gate driver applications. Furthermore, an isolated ± 15 V power supply is used to achieve the required isolation in the gate circuit. Finally, two Zener diodes Dz1 and Dz2 are used to prevent transient over-voltage of the MOSFETs gate signals and the pull-down resistor R10 connected between gate and emitter of the MOSFET ensures that the semiconductor remains off during the power-up sequence of the gate driver.

8.5 Summary

This chapter has described the components of a 18 power cells MMC-based drive. This converter is used to validate the nested control systems proposed in chapters 2-7. The

design, functions and components of the control platform have been described, focusing on the experimental MMC requirements, such as electrical variables to be measured and gate drive switching signals.

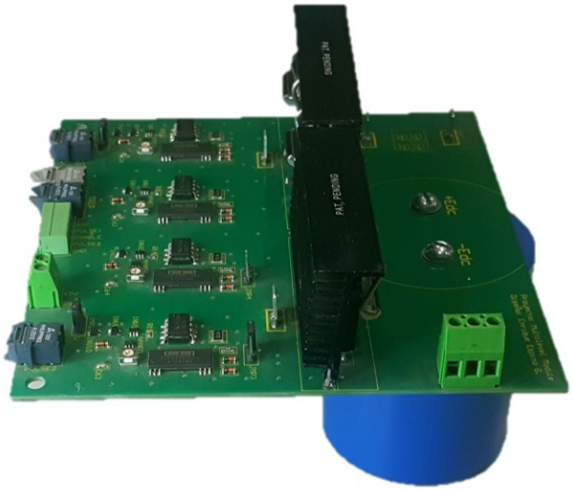

(a) Half-Bridge Power Cell

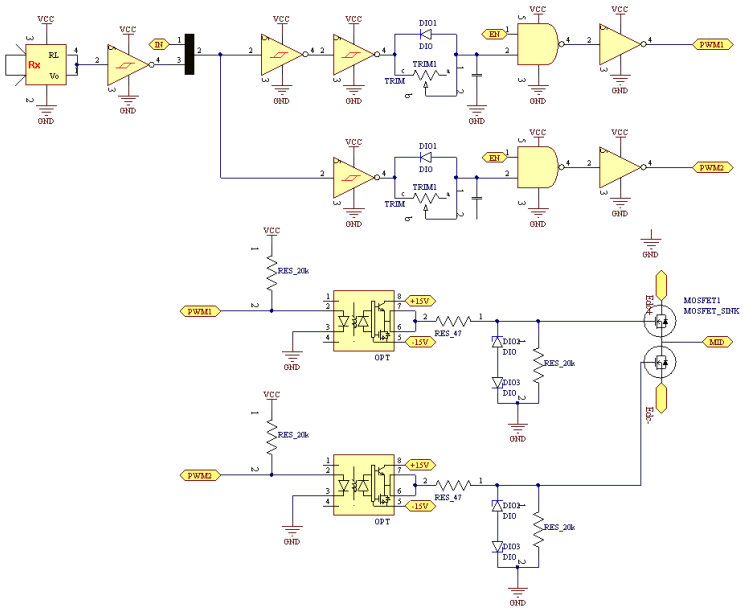

(b) Gate-Drive Circuit

Figure 8.5: Half-Bridge Power Cells